Role of Surface Chemistry to Regulate the Anodic Behaviour, Charge Transport and Reactivity: A Computational Study

A Thesis
Submitted for the Degree of
Doctor of Philosophy
in the Faculty of Science

by

Swastika Banerjee

New Chemistry Unit
Jawaharlal Nehru Centre for Advanced Scientific Research
(A Deemed University)
Bangalore-560064

August 2016

To my Parents and Teachers

DECLARATION

I hereby declare that the matter embodied in the thesis entitled "**Role of Surface Chemistry to Regulate the Anodic Behaviour, Charge Transport and Reactivity: A Computational Study**" is the result of investigations carried out by me at the New Chemistry Unit, Jawaharlal Nehru Centre for Advanced Scientific Research, Bangalore, India under the supervision of Prof. Swapan K. Pati and that it has not been submitted elsewhere for the award of any degree or diploma.

In keeping with the general practice in reporting scientific observations, due acknowledgement has been made whenever the work described is based on the findings of other investigators.

Swastika Banerjee

Swastika Banerjee

CERTIFICATE

I hereby certify that the matter embodied in this thesis entitled "**Role of Surface Chemistry to Regulate the Anodic Behaviour, Charge Transport and Reactivity: A Computational Study**" has been carried out by Ms. Swastika Banerjee at the New Chemistry Unit, Jawaharlal Nehru Centre for Advanced Scientific Research, Bangalore, India under my supervision and that it has not been submitted elsewhere for the award of any degree or diploma.

Prof. Swapan K. Pati
(Research Supervisor)

Acknowledgements

I take this opportunity to express my sincere gratitude to my advisor Prof. Swapan K. Pati for enormous freedom, constant motivation and excellent guidance throughout my Ph.D. Working with him has been a thoroughly enjoyable experience. His valuable comments and instructions in scientific communications have helped me immensely. I am extremely grateful for his kindness, endless support and encouragement during my stay at JNC. I also convey my heartfelt gratitude for excellent computational resources he has provided for the group and the great help during writing this thesis. I shall always cherish fond memories of my association with him.

My heartfelt gratitude to Prof. C. N. R. Rao for his vision about JNC. His presence & speeches are truly very inspiring.

I would like to express my sincere gratitude to Prof. Pratim K. Chattaraj (IIT-Kharagpur). I would also like to thank Dr. Kanishka Biswas, Dr. Sebastian C. Peter, Dr. Subi J. George, Prof. S. C. Lee, Dr. Ganga, Dr. Siam, Dr. Sumanta, Satya and Ananya for the interesting and fruitful scientific discussions.

I would also like to thank all my course instructors: Prof. Swapan K Pati, Prof. S. Balasubramanian, Prof. N. S. Vidhyadiraja, Prof. Shobhana Narasimhan, Prof.

Umesh V. Waghmare and Prof. Aloknath Chakraborty.

I am thankful to my present and past lab mates Ayan, Sairam, Sudipta, Sasmita, Meera, Ganga, Alex, Ershaad, Wasim, Nabanita, Madhuri, Amrit, Ashutosh, Silvia. I thank Prakash, Arun, Pralok, Dibya, Arkamita, Sharma, Siam sir, Pallavi, Bradraj, Soma, Shubhajit, Abhiroop, Madhulika, Neha and Nisheal for making the work place memorable. I have no word to thank PP, Pralok da, Manna da and Dibya for their supportive attitude. My special thanks to Abhiroop for various technical helps during writing this thesis.

I extend my sincere thanks to Dr. Ganga Periyasamy who has been kind and cooperative whenever I approached her for any help.

I thank all the academic, administrative, library, complab and hostel staff for providing the facilities in JNC. I especially thank CCMS staff (Amit, Vijay, Anand and Bharti) for their support.

I would like to thank all my IIT-mates and college-mates. I express my heartfelt thanks to Priya and Rajat, their friendship have left an indelible impression on me. I sincerely thank Samya da, for many fruitful suggestions and discussion.

I thank all my friends in JNC & IISc: Satya, Rajkumar, Sumanta, Debarati, Samya, Anirban, Pallabi, Debopreeti, Tumpa, Debdyuti, Arpan, Debabrata, Sudip, Prakash, Ritesh, Kaushik, Chandan Kumar, Sisir, Sutapa, Jia, Saikat, Subhajit, Debdipta, Rajib, Manoj, Mohini, Anaranya, Krishnendu, Chandradhish, Jiaul, Sujoy, Prabhas, Ananya, Sohini, Soumyabrata, Syamantak, Tarak, Sudip, Moumita, Nivedita, Papri, Shreya, Anindita, Saibal, Monodeep, Manisha, Subhajit, Satya (junior), Saurav, Swagatam, Niloyendu, Ranjan, Aritra, Shreyan and many more. My stay in JNC would not have been wonderful and enjoyable without their presence.

I extend my sincere thanks to the entire Academic and Administrative staff of JNCASR for their efficiency and helpfulness. Special thanks are due to the members of computer laboratory and library.

I would also like to thank the Hostel staff, Mess workers and Dining Hall for keeping me well fed.

I would like to express my sincere regards to Anusooya ma'am and Sohan for their endless support, love & affection. I've really no word to thank my dear Anu ma'am, for everything during my stay at JNC.

Last but not the least, my parents (Maa & Baba) for their unending support and encouragement. My brother Shibendu, without whom I can't think of my footsteps since my childhood. They have always believed in me, and never tied me down in any of my endeavors. I thank Rana who has been my friend, philosopher and guide in academic and non-academic affairs and has supported me throughout.

Synopsis

Electrochemical energy storage and designing transport devices largely relies on the properties of the electrode-properties and charge-storage/transport through systems. On the other hand, photochemical energy storage in molecular systems depends on the nature of two photo-switchable states. Chemo-selectivity is also important for molecular chemistry which fundamentally determines the reactivity. However, the common factor is the sensitivity towards surface-chemistry. To this end, understanding the impact of surface on the electrode-behaviour and charge-transport properties of materials is a crucial factor. In addition, experimental advancement on control over the surface-structure of materials allows material scientists to tailor the material properties for improved reliability and functionality. We focus on Bisphenol A (BPA) based molecular systems which are the widely used component of polycarbonate plastics and epoxy epoxy resins. They accumulate in nature without degradation and causes serious health-hazard. Hence, understanding the detail chemistry and photo-response of BPA-systems are not only of fundamental interest but also of environmental issues. Finally, we establish the role of surface structure in periodic as well as molecular systems to determine the chemical reactivity, electrochemical and charge-transport properties. We under-

stand various properties as well as responses of materials to the external stimuli with the help of theoretical and computational methods. Most importantly, such studies provide access to atomistic details which is not readily accessible to experiments.

Thesis begins with introduction in chapter 1 which is followed by three main sections. The first part consisting of chapter 2, 3 and 4 focuses on designing an anode material in rechargeable battery and capacitor. The second part consisting of chapter 5 and 6 explores the transport behaviour of 2D/quasi-2D systems, such as $B_xC_yN_z$ and black phosphorus. In third part consisting of chapter 7, 8 and 9, we study the photo-response of Bisphenol A based molecular systems and their stereo-chemical properties which are not only of technological relevance but also deserves attention for environmental issues.

Chapter 1 introduces the materials of our interest along with theoretical and computational details. The periodic systems of our interest falls in the category of van der Waals solids, namely, black phosphorus (BP), borocarbonitride (BCN) and metal chalcogenides which exhibit many fold benefits for application as anode in rechargeable battery, active material for transistor and photodetector. We focus on Bisphenol A (BPA) based molecular system for better understanding of their photo-response and chemical transformations. We provide a general description of theoretical models and computational approaches which have been extensively used in this thesis. We have used first principles calculations coupled with semiclassical Boltzmann Transport formalism (for periodic systems) and charge-transfer theory for molecular systems. We also give a brief introduction to the properties which have been studied in subsequent chapters.

In Chapter 2, We investigate the possibility of 2D boron sheets (BSs) as an

anode in lithium ion batteries (LIBs). Among the α, α_1, and $\eta_{4/28}$ metallic BSs, planarity is retained for the α_1, and $\eta_{4/28}$ polymorphs after the formation of the layered structures. The α_1 and α_1-AA polymorphs have been found to show optimum anodic behaviour based on their electronic structural and Li adsorption/desorption properties. The highly symmetric "H" site is energetically favored for Li adsorption at both 0 and 298 K. Li migration occurs from one "H" site to another via the top of a B atom, with a 0.66 eV and 0.39 eV energy barrier at 0 and 298 K respectively. Li-saturation confers the theoretical estimate of the capacity as 383 $mAhg^{-1}$, which is higher than that of the conventional graphitic electrode. All of these characteristics suggest the appropriateness of α_1-AA as the lightest possible anode material for LIBs.

We show that variation in the shape of the B_xN_z-domain and B-N charge-imbalance in $B_xC_yN_z$ layers results in tunable anodic properties in chapter 3. Two-dimensional $B_xC_yN_z$ with nitrogen-excess trigonal B_xN_z-domain (T_N) meets the requirements for a superior anode for Sodium ion Battery (SIB). Monolayer T_N-sheet can store Na(Li) up to $Na_{2.2}S_6(Li_{1.8}T_6)$ composition, which corresponds to a specific capacity as high as 810(668) $mAhg^{-1}$ for SIB(LIB). The average open circuit voltage is found to be 1.25 V vs. Na/Na^+ for a wide range of chemical stoichiometries of Na_xT_N. The enhanced electronic transport and fast diffusion kinetics of the Na-ions is particularly found in the T_N-anode, which in turn results in high power efficiency in SIB, even better than that of graphite electrode in conventional LIB. Charge-storage upon layer-wise accumulation of Na-ions on the T_N-surface is also appealing for application to sodium-ion capacitors, as an alternative to lithium-ion capacitors.

Chapter 4 demonstrates Black phosphorous as anode in Magnesium-ion Battery. Multivalent electrochemistry involving magnesium ion has immense impor-

tance to achieve higher energy storage in rechargeable battery compared to conventional one electron redox process, as present in LIB and SIB. However, anode in Mg-ion battery suffers from two key factors: (1) structural instability of metallic Mg-anode during charging-discharging cycle, and (2) very slow diffusion of Mg^{2+}-ion within insertion-type anode. In this chapter, light has been shed on the appropriateness of black phosphorus (P) based anode in Mg-ion Battery. Mg-ion storage within covalent P-anode optimises the anodic voltage and reduces the Mg-diffusion barrier, thereby can overcome the bottleneck in Mg-battery technology.

Chapter 5 describes the role on BN and C domains controlling the transport property of ternary Borocarbonitrides. 2D nano-hybrid system (Borocarbonitrides) have been modelled and transport properties have been calculated using *ab-initio* DFT-based computation combined with Boltzmann transport formalism. It is shown that conduction polarity can be controlled by atomically engineered surface topology. The principles for maximising mobility and possibility for obtaining particular (electron/hole) conduction polarity for borocarbonitrides of any stoichiometric proportion has also been discussed. Such an extraordinary transport efficiency can find applications in modern transistors.

Chapter 6 focuses on effect of puckered structure of Elemental Black Phosphorene on its transport property. Black Phosphorus in its bulk form as well as layered structures are not only the good electrode in Mg-ion battery as discussed in chapter 4, they are being used as an active material in diverse areas of electronics. In this chapter, the critical dependence of the number of layers in controlling the charge-transport property has been studied based on DFT-based computation combined with Boltzmann transport theory. We find that, tri-layer black phosphorus offers itself as appropriate anisotropic material which possesses both the directional as well as electron-hole anisotropy. The systematic scheme described

here, helps to understand the fundamentals on anisotropy associated with carrier scattering process for any such complex quasi-2D materials which indeed has significant potential to design and optimise the advanced transport (logical) devices.

Chapter 7 aims to shed light on the potential mechanism for metabolic activation of 2, 2′-bis (4-hydroxyphenyl) propane (BPA) producing two different metabolites: 4-methyl-2,4-bis(p-hydroxyphenyl)pent-2-ene (M-1) and 4-methyl-2, 4-bis (4-hydroxyphenyl) pent-1-ene (M-2). Selectivity toward M-1(nontoxic)/M-2 (toxic) formation can be controlled by varying the polarity of the reaction medium. The reversal of thermodynamic stability for M-1/M-2 in response to the static polarization of the medium has been found. Moreover, stereocontrol of biologically active M-2 with static polarization as the switch (0.005 au) might affect the receptor binding. This analysis may be useful in dictating the prevention of the harmful action of BPA and its metabolites.

Chapter 8 shed light on the potential of selective surfaces in view of detection and extraction of bis-phenol based pollutants (BPA, M-1 and M-2). It is found that, graphene and MoS_2 surfaces are capable of removing these toxic molecules from environment, in particular, from water contamination. Layered graphene supports very strong surface adsorption and assures complete removal of EDCs, while they physisorb on MoS_2 surface. In particular, optical response of the EDCs gets tuned upon adsorption on graphene. Hence, understanding the surface adsorption and modulation of the electronic structure would reveal possible means for extraction and photodegradation of a major class of environmental pollutants by specific choice of surface.

Chapter 9 discusses the photo-conversion of Bisphenol A (BPA)-based molecular architectures. Conformational flexibility helps in photochemical energy storage

through excitation energy transfer, where M-1 exhibits maximum storage efficiency (0.97 eV/mol) compared to BPA and M-2. Through first-principles analysis coupled with electron transfer theory, it has been shown that, B-1 bridge in M-1-structure acts as an asymmetric wire and leads to photo-induced switching between two conformers (S-1 and S-2). These two conformers follow dissimilar charge-storage/transport mechanism with detectable optical responses. Finally, the origin of photo-stability of EDCs are discussed with a special emphasis on the M-1-like molecular configuration as an excellent motif for light-energy-conversion.

List of publications

1. "Black Phosphorus as Anode for Magnesium-ion Battery: The Significance of Mg-P Bond-synergy", **Swastika Banerjee** and Swapan K Pati, Chem. Commun., 52, 8381-8384 (2016).

2. "Microscopic Understanding on Transport Anisotropy in Trilayer Phosphorene", **Swastika Banerjee** and Swapan K. Pati, Phys. Chem. Chem. Phys. **18**, 16345-16352 (2016).

3. "Photo-switchability and Photochemical Energy Storage of Bisphenol A Derivatives Through Geometrically Deformed State: Insights from First Principles Study", **Swastika Banerjee** and Swapan K. Pati (2016), (Submitted).

4. "Origin of Order-disordered Phase Transition and Anomalous Change of Thermopower in $AgBiS_2$ Nanocrystals: A Combined Experimental and Theoretical Study", Satya N. Guin, **Swastika Banerjee**, Dirtha Sanyal, Swapan K. Pati and Kanishka Biswas, Inorg. Chem., DOI: 10.1021/acs.inorgchem.6b00997 (2016).

5. "Synthetically Tuned Structural Variations in Ce_2PdGe_3 Towards Magnetic Exchange Bias and Other Physical Properties", Sumanta Sarkar, **Swastika**

Banerjee, Pramod Halappa, Deepti Kalsi, Swapan K. Pati, Somnath Ghara, A. Sundaresan, Ivan da Silva, Rajeev Rawat, Sudhindra Rayaprol, Boby Joseph and Sebastian C. Peter, (2016), (Under revision in Inorg. Chem.).

6. "First-principles Design of a Borocarbonitride Based Anode for Superior Performance in Sodium-ion Battery and Capacitor", **Swastika Banerjee**, Siam Khanthang Neihsial, and Swapan K. Pati, J. Mater. Chem. A, 4, 5517-5527 (2016).

7. "$Eu_3Ir_2In_{15}$: A Mixed-Valent and Vacancy-Filled Variant of the $Sc_5Co_4Si_{10}$ Structure Type with Anomalous Magnetic Properties", Sumanta Sarkar, **Swastika Banerjee**, Rajkumar Jana, Ramesh Siva, Swapan K Pati, Mahalingam Balasubramanian, Sebastian C Peter, Inorg. chem., 54 (22), 10855-10864 (2015).

8. "Surface-Mediated Extraction and Photoresponse Modulation of Bisphenol A Derivatives: A Computational Study", **Swastika Banerjee** and Swapan K. Pati, ACS Applied Materials & Interfaces, 7 (43), 23893-23901 (2015).

9. "Criticality of Surface Topology for Charge-carrier Transport Characteristics in Two-Dimensional Borocarbonitrides: Design Principle of an Efficient Electronic Material", **Swastika Banerjee** and Swapan K. Pati, Nanoscale, 6, 13430-13434 (2014).

10. "Formation Mechanism and Possible Stereo Control of Bisphenol A derivatives: A Computational Study", **Swastika Banerjee**, Ganga Periyasamy and Swapan K. Pati, J. Phys. Chem. B, 118, 9258-9262 (2014).

11. "Possible Application of 2D-Boron Sheets as Anode Material in Lithium Ion Battery: A DFT and AIMD study", **Swastika Banerjee**, Ganga Periyasamy and Swapan K. Pati, J. Mater. Chem. A, 2, 3856-3864 (2014).

12. "Structural, Optical and Hydrogen Adsorption Properties of B_9/Metal-B_9 Clusters: A Density Functional Theoretical Study", **Swastika Banerjee**, Ganga Periyasamy and Swapan K. Pati, Phys. Chem. Chem. Phys., 15, 8303-8310 (2013).

13. "Role of Lithium Decoration on Hydrogen Storage Potential", Sudip Pan, **Swastika Banerjee**, Pratim Kumar Chattaraj, J. Mex. Chem. Soc. 56, 3, 229-240 (2012).

List of Figures

List of Tables

Contents

1 Introduction

1.1 A Brief Overview

Research endeavour towards energy-storage and controlling environmental pollution has drawn the most attention since the advent of science and technology. Technological developments are led by the discovery of materials with exotic properties. Designing material for grid storage as well as transport devices are of utmost interest in recent days, where the efficiency largely relies on the electrode-properties and charge-storage/transport through systems. To this end, materials science plays a crucial role in modern technology.

However, pollution appears as bi-product of various technological developments. Plastic-pollution is one of such example. Bisphenol A (BPA) based molecular systems are the widely used component of polycarbonate plastics and epoxy resins. They accumulate in nature without degradation and cause serious health-hazard. Hence, understanding the detail chemistry and photo-response of BPA-systems are not only of fundamental interest but also deserves attention for solving environmental issues.

Notably, stereochemistry of BPA-compounds play an important role to determine their toxicity. Similar to the stereo-isomerism present in molecular systems,

extended systems exhibit isomerism, such as, different polymorphs and allotropes for a single chemical composition. Consequently, surface chemistry which influence the electronic, optical, mechanical and transport properties, dictate the behaviour of materials (see Figure 1.1).

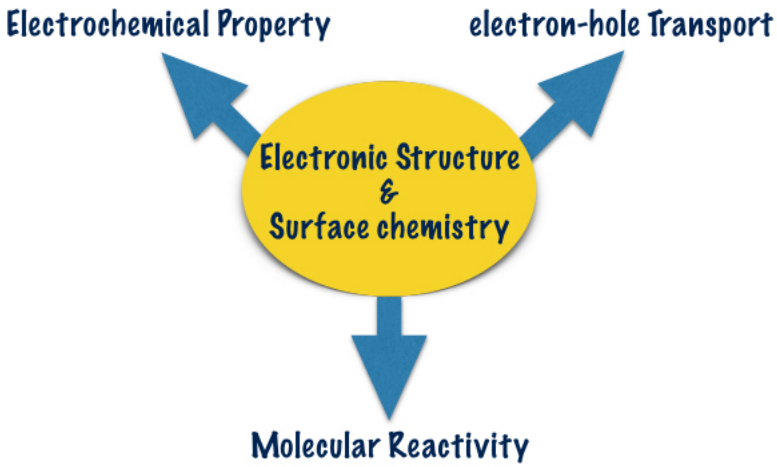

Figure 1.1: Coupling between surface chemistry and various properties in a material.

The aim of the study presented in this thesis is to establish the role of surface chemistry in periodic as well as molecular systems to determine the chemical reactivity, electrochemical and charge-transport properties (see Figure 1.2). With advances in theoretical and computational methods, various properties as well as responses of materials to the external stimuli have been determined. In this regard, first-principles Density Functional Theory (DFT) have become the most widely used tools for estimation of materials' properties. Result of the simulation can be applied to evaluate the efficiency of the material in devices as well. Most importantly, such studies provide access to atomistic details which is not readily accessible to experiments. In addition, experimental advancement on control over the surface-structure of materials allows material scientists to tailor the material properties for improved reliability and functionality for various applications (see Figure 1.2).

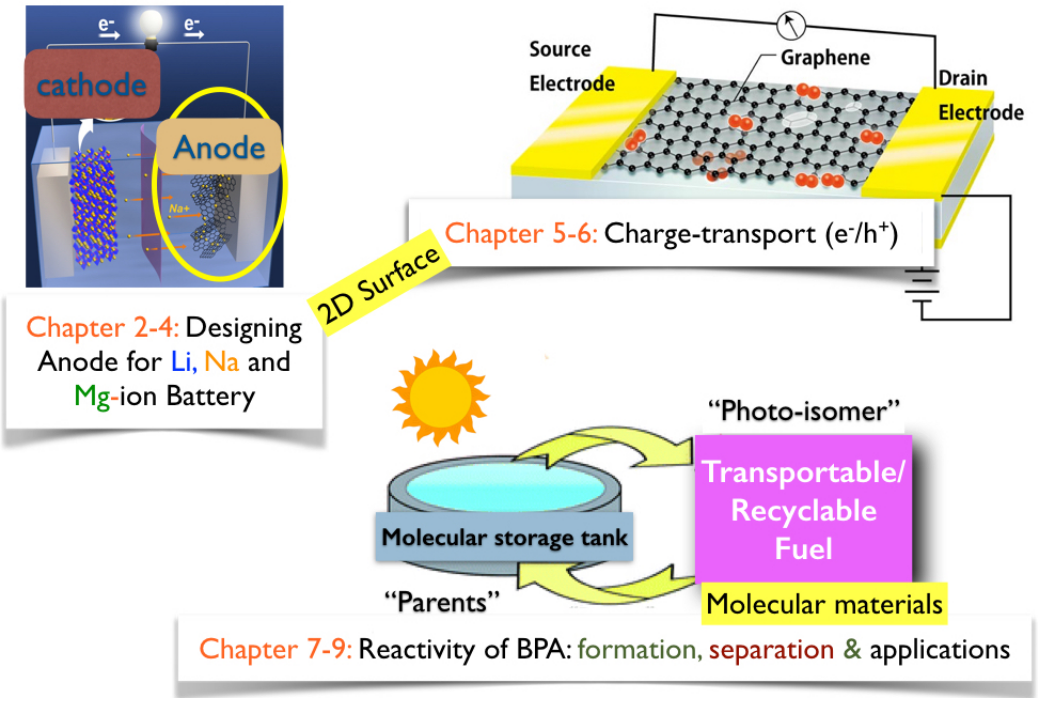

Figure 1.2: Schematic of main theme of the thesis focusing on designing material with efficient anodic behaviour, desired charge-transport property and regulation of chemical reactivity.

Remainder of this introductory chapter is arranged as follows: in section 1.2, we provide a general description of the systems of our interest. In section 1.3, we give a brief introduction to the properties which have been studied in subsequent chapters. This is followed by a detail discussion on the theoretical models and computational approaches which are extensively used to understand the materials' properties, in section 1.4. We also provide a short discussion on the softwares used, in section 1.5. With this brief introduction, we give an outline of the studies (in section 1.6) presented in this thesis which have been elaborated chapter-wise, subsequently.

1.2 Introduction to Materials of Interest

The materials of interest for electrochemical energy storage and electronic device application falls mostly in the category of van der Waals solids. In this thesis, we also focus on the similar materials, namely, boron sheet (BS), black phosphorus (BP), borocarbonitride ($B_xC_yN_z$) and metal dichalcogenides (MoS_2) which exhibit many fold benefits for application as anode in rechargeable battery and active material for transistor and photodetector. On the other hand, BPA-compounds are of environmental interests. Here, we introduce the materials of our interest more pictorially in Figure 1.3 which is followed by brief descriptions on each.

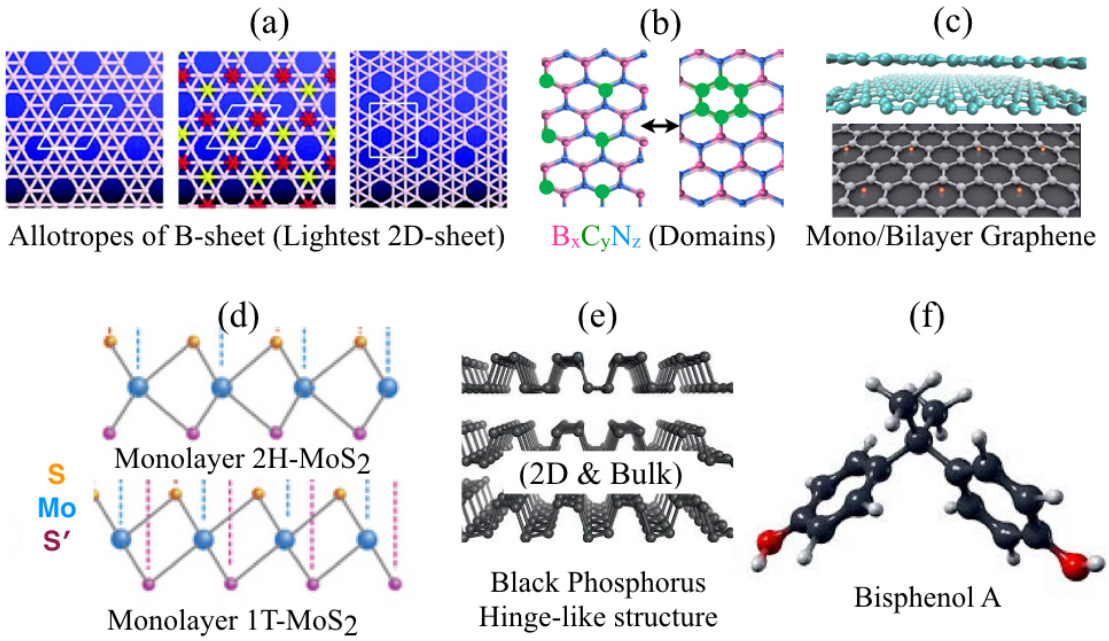

Figure 1.3: Systems of our interest: surface structures of various two dimensional and bulk materials as well as BPA-based molecular system are shown.

1.2.1 Boron-sheet

Boron is the member in periodic table residing as carbon's neighbour. However, graphene-like structures with a honeycomb hexagonal framework does not form

with elemental boron due to its electron deficient nature. Combined experimental[1,2] and computational studies[3,4] suggest that extended boron sheets can be formed with partially filled hexagonal holes. There can be various possible surface structures of the atom-thin boron nano-structures (see Figure 1.3a) exhibiting polymorphism in 2D boron-sheet.[5]

1.2.2 Graphene and Borocarbonitride

Various forms of carbon allotropes have received considerable attention due to their diverse application in many fields.[6,7] Graphene, the 2D form of carbon has drawn the most attention due to excellent electronic structural and transport property.[8–11] However, graphene is a zero band-gap semi-metal. Recently, there has been some effort to investigate graphene-substitute, such as, borocarbonitrides ($B_xC_yN_z$), comprising of carbon and the two elements on either sides of carbon, B and N (see Figure 1.3b and c). Unlike graphene, $B_xC_yN_z$ network exhibit finite electronic band-gap,[12–15] and display many exotic electronic properties depending on their chemical compositions and bonding nature. In principle, many plausible $B_xC_yN_z$ structures can be constructed by varying B:C:N stoichiometry as well as altering shapes, sizes and grain boundaries of BN/C domains (see Figure 1.3b). Thus, understanding the effect of surface engineering on the electronic and transport property, is of utmost interest for practical application of $B_xC_yN_z$.

1.2.3 Metal dichalcogenide (MoS_2)

Two-dimensional (2D) semiconducting materials obtained from transition metal dichalcogenides (TMDs) are highly promising in electronic devices, such as, channel material for field effect transistors (FETs).[16–19] Single-layer molybdenum disulfide (MoS_2) has attracted much attention recently.[20,21] Their ultra-thin structure, excellent electrostatics, and planar nature facilitates easy fabrication com-

pared to one-dimensional structures (such as nanowires and nanotubes). These properties make them appropriate for absorbing surface medium and for device application.

There are two kinds of MoS_2-polytypes: 2H and 1T (see Figure 1.3d). 2H-MoS_2 is a semiconductor with a hexagonal layered structure. Each Mo atom is prismatically coordinated by six S atoms. Another polytype is the metallic 1T-MoS_2, in which the Mo coordination becomes octahedral.

1.2.4 Black Phosphorous

The most recently introduced elemental 2D-sheet is the phosphorene, made up of phosphorus. Such extended P-system has been proposed as a promising candidate with an atom-thick layer and a natural band gap associated with high electron-hole mobility. In addition, puckered nature of the phosphorene sheet differentiates it from other 2D electronic materials, like graphene, borocarbonitrides, hexagonal boron nitrides, etc. Among various allotropes of phosphorus, black phosphorus (Black-P or BP, see Figure 1.3e) is the most stable form at ambient condition. Unlike the symmetric buckling of six-membered rings as found in blue phosphorene (P-allotrope: Blue-P)[22] and silicene.[23], there is asymmetric buckling present in BP. Such structural asymmetry along two in-plane directions imparts anisotropy in the electronic and optical responses of BP.[24–26]

1.2.5 Molecular Materials: BPA Compounds

2′-bis (4-hydroxyphenyl) propane (Bisphenol A or BPA, see Figure 1.3f), is one of the highest volume chemicals produced worldwide, as well as released into the atmosphere by yearly production.[27] BPA is the building block of polycarbonate plastic. Metallic food cans are protected from rusting and corrosion by the application of epoxy resins as inner coatings. Many of these resins are synthe-

sized by the condensation of BPA with epichlorhydrin to create BPA diglycidyl ether.[28] When incomplete polymerization occurs, residual BPA leaches from the epoxy resin and has the potential to contaminate stored foods. BPA along with its derivatives (metabolites) act as environmental micro-pollutant.[29] Two well characterised metabolites of BPA are M-1: 4-methyl-2,4-bis(p-hydroxyphenyl)pent-2-ene (Biologically inactive), and M-2 : 4-methyl-2, 4-bis (4-hydroxyphenyl) pent-1-ene (Biologically active).

1.3 Overview of the Materials Properties and Their Applications

The topics covered in this thesis can be broadly divided into three domains. In the first part consisting of chapter 2, 3 and 4, we focus on designing an anode material in rechargeable metal-ion battery and capacitor. The second part consisting of chapter 5 and 6 explores the transport behaviour of 2D/quasi-2D systems. In third part consisting of chapter 7, 8 and 9, we study the stereo-chemical properties and photo-response of BPA-based molecular systems. In the following subsections, we give a brief introduction to the properties we have studied:

1.3.1 Principles of Rechargeable Metal(M)-ion Battery and Conventional Anodes

Batteries have distinct advantages over other energy storage systems due to their ability to convert chemical energy into electrical energy and vice versa.[30–32] Today, the dominant form of battery being used in consumer electronics is the rechargeable lithium-ion battery (LIB).[33–37] Simply, LIB is a device that functions on the basis of the reversible transport of Li^+ ions. It offers the highest energy densities among all known battery technologies, thus, LIBs are finding their applications starting

from portable electronics to electric vehicles and grid storage. Despite the great success in Li-ion technology, concerns regarding the abundance and cost of lithium motivates the upcoming research in rechargeable sodium-ion batteries,[38–44] which function on the same basic principle but with Na^+ as active ion instead of Li^+. Figure 1.4 shows schematic representation of a rechargeable M-ion battery (M = Li, Na, Mg etc.) which consists of electrode (anode and cathode) and electrolyte components. The anode (cathode) in a M-ion battery is the source (sink) of M-

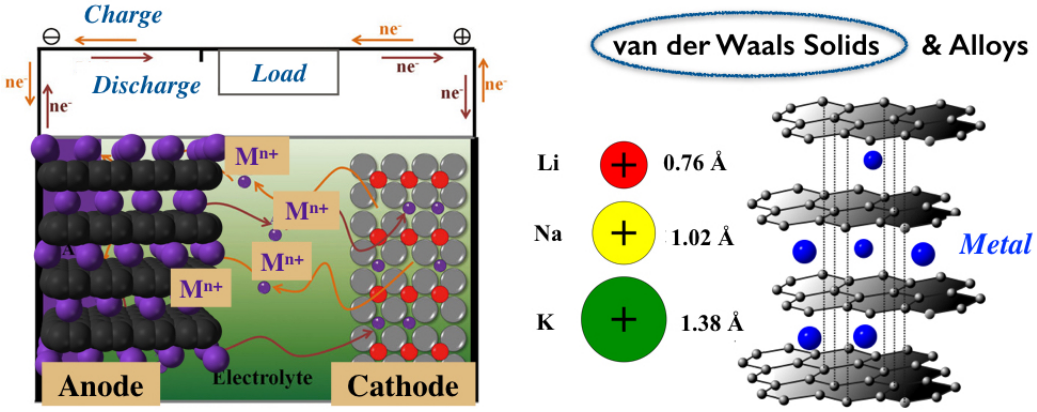

Figure 1.4: Schematic representation of M-ion rechargeable battery (M = Li, Na, Mg etc) is shown in left subfigure. Design of an insertion-type anode: graphite is shown as model anode (right).

ions. The electrolyte provides the path for ionic transport. During discharge, M^+ ions are transported from the anode, through the electrolyte and into the cathode. The reverse process happens during charge. In this thesis, we mainly focus on anode component in rechargeable M-ion battery (M = Li, Na and Mg) and analyse the electrochemistry in details. Anode materials are chosen by optimising a number of parameters determined by the basic thermodynamics and kinetics of the electrochemical cell.

1.3.1.1 Basic Thermodynamics and Kinetic Aspect in Battery Set-up

Thermodynamics

The amount of energy stored and the charging/discharging rate performance of batteries rely completely on the thermodynamic and kinetic formulations of chemical reactions.[45] Change in Gibbs free energy for a reversible electrochemical reaction is given by,

$$\Delta G = \Delta H - T\Delta S \tag{1.1}$$

where, ΔG is the the available energy in a reaction for useful work. Thus, the net available electrical energy from a reaction in a electrochemical cell, is given by,

$$\Delta G = -nFE \tag{1.2}$$

where n is the number of electrons involved in reaction for one mol of the reactants, F is the Faraday constant, and E is the voltage of the cell. Equation 1.2 represents a balance between the chemical and electrical driving forces upon the ions under open circuit conditions. Hence, E refers to the open circuit potential (V_{oc}) of a cell when there is no flow of current (see Figure 1.5). The voltage of the cell is unique for each reaction couple. ΔH is the enthalpy released by the reaction, ΔS is the entropy, and T is the absolute temperature. $T\Delta S$ is the heat associated with the reaction. The terms ΔG , ΔH and ΔS depend only on the initial and final states of the reactions at electrode materials, since these are state functions.

While the electrolyte acts as a perfect filter that allows the only passage of ionic species, but not electrons, the cell voltage is determined by the difference in the chemical potential of the electrodes (see Figure 1.5). The amount of electricity produced in battery is given by nF, which is determined by the total amount of materials available for reaction. Thus, storage of ions within electrode host can be thought of as a capacity factor; the voltage can be considered to be an

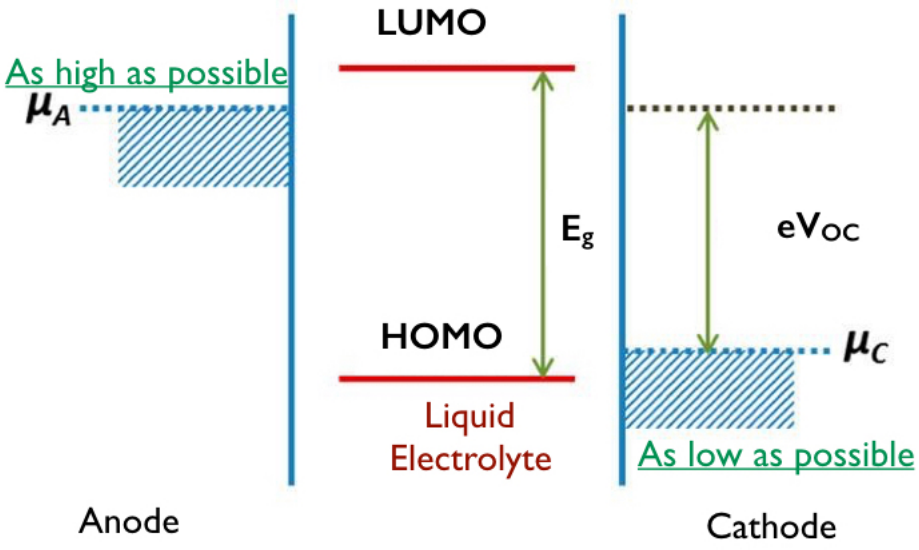

Figure 1.5: Schematic representation of electrolytic window and electrochemical potentials of electrodes.

intensity factor.[46] The change of free energy for a given species 'i' defines the chemical potential. The chemical potential, μ_i, for species 'i' is related to another thermodynamic quantity, the activity (a_i), by

$$\mu_i = \mu_i^0 + RTlna_i \tag{1.3}$$

where μ_i^0 is the value of the chemical potential of species 'i' in its standard state. R is the gas constant, and T is absolute temperature. Consider an electrochemical cell in which the activity of species 'i' is different in the negative and positive electrode ($a_i(-) \neq a_i(+)$). The difference between the chemical potential on the positive side and that on the negative side is written as,

$$\mu_i(+) - \mu_i(-) = RTln[a_i(+)/a_i(-)] \tag{1.4}$$

Then according to the relation balancing chemical potential difference by electro-

static energy (see Equation 1.2), we have,

$$E = -\frac{RT}{nF} ln \left[\frac{a_i(+)}{a_i(-)}\right] \tag{1.5}$$

The above relation is the well known Nernst equation, which relates the measurable cell voltage to the chemical difference across an electrochemical cell. [45]

Kinetics

Thermodynamic quantities as discussed above describe the reactions at equilibrium and determines the maximum energy available for a given reaction. In contrast, when current is drawn from the battery, voltage drops off compared to the open circuit potential (V_{oc}) at equilibrium state. This is because of the kinetic limitations of reactions. Figure 1.6a shows a typical discharge curve of a battery. [46,47] Fundamentally, three different kinetics-effects for polarization are considered (see Figure 1.6a): (1) kinetics of the charge-transfer reaction taking place at the elec-

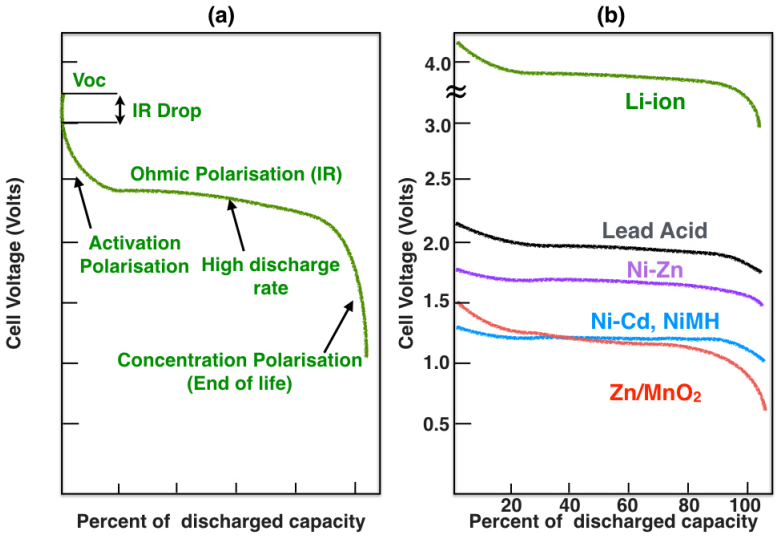

Figure 1.6: (a) Typical discharge curve of a battery, (b) Various cell characteristics normalised as a percentage of cell capacity versus supplied voltage.

trode/electrolyte interface which is defined as activation polarization; (2) resis-

tance due to contact problem between the cell components and resistance of individual cell components leads to ohmic polarization; (3) mass transport limitations during cell operation results in concentration polarization.[47] In comparison with various battery set-up, the supply voltage stays reasonably constant throughout the discharge cycle (state-of-charge) for modern Lithium Ion cells (see Figure 1.6b), and perform better.

In this scenario, it is worth to understand the electrochemical reaction kinetics which follows the same considerations as in bulk chemical reactions. However, the electrode reactions often involve a series of steps, including charge-transfer and charge-transport reactions. Rates of these elementary steps determine the kinetics of the electrode reaction. Kinetics based on activation is best understood using transition-state theory. The current flow is often described by the Butler-Volmer equation. Ohmic polarization appears or disappears instantaneously when current flows or ceases. Typically the linear Ohm's law relates the current and potential. As the redox reactions proceed, the availability of the active species at the electrode/electrolyte interface varies. Concentration polarization arises from limited diffusion of active species to and from the electrode surface. Such polarization usually becomes the rate-limiting step at the completion of charge/discharge.

1.3.1.2 Principles to Achieve Efficient Anodic Behaviour

The key requirements for a material to be successfully used as a anode in a rechargeable battery are as follows:

(1) it must contain light elements, thus, can exhibit high gravimetric ratio after accommodation of fairly large amounts of Li per formula unit. Li-intercalatation capacity of graphite can be up to the composition LiC_6, as stage-I intercalation product is found, meaning that a Li atom (Li ion + electron) is present between every layer of the host graphite lattice.[48–50] This gives rise to a theoretical capacity

of 372 $mAhg^{-1}$. However, efforts to increase the Li content in LiC_6 and high reversible cycle-life have not been successful.

(2) Li-storage potential should be low (less free energy of reaction); must show a potential as close to that of Li metal as possible (see Figure 1.5). This is because, when combined with a 4 V cathode, the overall working voltage of the LIB will not be much lower than 4 V. For graphite electrode, the anodic potential is 0.15-0.25 V vs Li metal.[48–50]

(3) Electrode should be stable in the solvent of the electrolyte medium and must not chemically react with the salt too. However, it is found that chemical reaction of Li with ethylene carbonate-based solvents forms a protective film named as solid electrolyte interphase (SEI) on the external surfaces of the graphite particles during the first few cycles of discharge/charge reactions. Such SEI prevents excessive solvent co-intercalation and acts as a good Li-ion conductor and enables facile Li cycling.[51–53] Furthermore, SEI protects the charged graphite (LiC_6) which is a strong reducing agent, thus, suppresses the unwanted side reactions.

(4) The anode material should be less expensive and environmentally benign.

(6) Most importantly, an ideal anode should be a good conductor for electrons and ions ('mixed conduction'), so that the electrode will have small impedance for current pick-up and for the motion of the Li-ions within the active material.[54] While graphite is a semiconductor (conductivity (σ_{300K}) $\approx 10^{-2}$ to 10^{-3} S cm^{-1}), LiC_6 is an excellent mixed conductor and, as a matter of fact, shows metallic-type electronic conductivity ($\sigma_{300K} \approx 10^2$ to 10^3 S cm^{-1}) and a high Li ion mobility (D_{Li^+} at 300 K $\approx 10^{-8}$ *to* 10^{-10} cm^2s^{-1}).[55]

Taking all the points into consideration, graphitic carbon is the most widely used anode till date, which is also considered as the benchmark. So, the properties of a newly proposed anode material for LIB is always compared with those exhibited by the conventional graphite anode.

1.3.1.3 Anode Materials for Li-ion Battery

Most of the research endeavours and commercialisation of anode materials have centred on four classes of materials.

1. Layered compounds as anodes based on Li intercalation-deintercalation reaction: examples are graphite, binary oxides such as, TiO_2, vanadium, molibdenum and niobium oxides. There are ternary oxides like: $Li_4Ti_5O_{12}$ (LTO), $MgTi_2O_5$, $LiTiNbO_5$, $TiNb_2O_7$ and other oxides.

2. Anode based on alloying-dealloying reaction: binary tin oxides: SnO, SnO_2, ternary tin oxides: M_2SnO_4 (M = Metal), $ASnO_3$ (A = Ca, Sr, Ba, Co, and Mg), Li_2SnO_3, SnP_2O_7 etc. Amorphous tin composite oxides (ATCOs), antimony oxides and mixed oxides, other group IV oxides have also been explored.

3. Anodes based on conversion (redox) reaction: binary oxides with rock salt (MO; M = Mn, Fe, Co, Ni, or Cu), and spinel (M_3O_4, M = Co, Fe, or Mn) structure.

4. Anodes based on both alloying-dealloying and conversion reaction involves oxides with spinel structure: ZnM_2O_4 (M = Co, Fe) and $CdFe_2O_4$, oxides of Sn and metal oxysalts: carbonates and oxalates.

1.3.1.4 Limitations of Li-ion Technology

- Scarcity of ingredient & high price: impossible for bulk scale application.
- Operational temperature: consumer grade lithium-ion batteries cannot be charged below 0°C (32°F).
- Safety issue: formation of dendrites which can penetrate the microporous separator and can give rise to short-circuiting of the LIB.
- Li is Class 9 miscellaneous hazardous material.

1.3.1.5 Solution

- Appropriate insertion-type anode is a safer option.
- Post-Li technology based on more abundant Na-ion is potential for large scale application
- Multivalent redox chemistry leads to a concomitant increase in the energy density

We have utilised available computational methods for finding suitable intercalation anode host (van der Waals layered materials) in M-ion battery (M = Li and Na). The characteristics focused in chapter 2 and 3 include both lithium and sodium ion chemistries. We have also studied the appropriate anode for multivalent chemistries involving Mg^{2+} as active ion, subsequently in chapter 4.

1.3.2 Charge-carrier Transport in Molecular and Periodic Systems

Van der Waals solids which have been the focus of our interest as intercalation anode-host, are of tremendous importance for their applications in transport devices as well.[56] Charge-transport characteristics are mainly determined by three primary types of carrier action in material. (1) Drift: carrier transport in presence of applied field which tune the current flow in metal oxide semiconductor field effect transistor (MOSFET),[57,58] (2) diffusion is the carrier motion due to concentration gradient,[59,60] and (3) recombination-generation process, where low mobility compacts exciton, thus, helps in light emitting diode configuration.[61] On the other hand, high carrier mobility and weakly bound exciton helps in photocurrent generation in solar cell configuration.[62,63] We focus on the designing of material with high e-h mobility and try to understand the transport property of 2D/Quasi-2D systems.

1.3.2.1 Transport Regimes

In a pure semiconductor, electron wavelengths are delocalized and can spread over large distances (large $\lambda \rightarrow$ small k). For such cases, transport occurs in the bands, this regime of transport is called band transport. For low field regime, the transport proceeds by scattering from impurities. For high field regime, there are optical phonon emissions, but all transport occur in the conduction (or valence) band. If there is a lot of disorder in a semiconductor (say polycrystalline semiconductor with grain boundaries), then there will be small localized pockets of carriers which will have to surmount the potential barriers between them to carry current. This process requires an activation energy, and the activation energy can be measured. This form of transport is very different from band transport and is called 'activated' or 'hopping' transport because the carriers hop from one localized state to the other. Theoretical treatment of transport in such disordered systems requires percolation theory and sophisticated techniques such as Green's functions.

1.3.2.2 Charge Transport in Organic Molecular Crystals

Understanding the basic charge transport mechanism in organic semiconductors is of immense importance for flexible electronics, yet the knowledge is incomplete till date. The time-of-flight experiments by Karl and co-workers[64,65] (with ultrapure crystals of naphthalene and anthracene) have demonstrated that charge transport in organic crystals is characterized by a rapid decrease of the carrier mobility with increasing temperature and there is a pronounced anisotropy of the mobility along different crystallographic directions. Such decrease in mobility originates from enhanced scattering processes by lattice phonons. The complexity arises from polaronic nature of charge carriers and the strong electron-vibration interactions. However, the coupling between electrons and vibrations cannot be treated as a perturbation,[66,67] which becomes a challenge for theoreticians to develop a

model that describes transport as a function of temperature.[66,67] Recently, significant attention is being paid to highly ordered semiconductors and their frequency decomposed carrier-vibronic coupling elements.

1.3.2.3 Charge-carrier Mobility in Materials

We start with the definition of the carrier mobility which is followed by a short description of charge transport.

Mobility, μ, is related to the conductivity, σ, according to:

$$\sigma = ne\mu \tag{1.6}$$

where n indicates the density of the charge carriers and e is the elementary charge. The mobility of the charge carriers in solids is often described in terms of the linear response formalism. In this case, the Kubo formula provides a general starting point for a semiclassical or fully quantum-mechanical description of the mobility. For charge carriers at thermal equilibrium moving in an electric field, the mobility is given by (according to Kubo's formula):

$$\mu(\omega) = -\frac{e\omega^2}{2K_BT}\int_0^\infty \frac{\langle|r(t) - r(0)|^2\rangle}{d} e^{-i\omega t}dt \tag{1.7}$$

with K_B as Boltzmann constant, T the temperature, t the time, ω the radial frequency of the electric field, r the total displacement vector, and $d = 1, 2, 3$ the dimensionality of the system. The brackets imply averaging over a large number of charge carriers at thermal equilibrium. Calculation of the charge carrier mobility on the basis of Equation 1.7 requires an evaluation of the average of the square displacement for all the charge carriers contributing to the conductivity. This averaging involves the contribution of all states of the charge carriers. The charge

carrier states can be obtained from the Hamiltonian of the system, given by:

$$H = H_e + H_{ph} + H_{e-ph} \tag{1.8}$$

where, H_e is the electronic Hamiltonian and H_{ph} is the phonon Hamiltonian. The H_{e-ph} term describes the interactions between electrons and phonons, which are associated with the dynamic fluctuations of the material. Such fluctuations correspond to nuclear vibrations of the molecule or to motions of the entire molecular unit. In the case of normal Gaussian diffusion, the mean square displacement of a charge eventually increases with time according to:

$$\left\langle |r(t) - r(0)|^2 \right\rangle = 2dDt \tag{1.9}$$

with D representing the diffusion constant, d the dimensionality of the system, and t the time. Substitution of Equation 1.9 into Equation 1.7 gives the Einstein relation for the mobility:

$$\mu = \frac{e}{K_B T} D \tag{1.10}$$

The mobility in Equation 1.10 is frequency independent and the imaginary component is zero.

1.3.3 Photochemical Energy Storage in Molecular Systems

Photochromic molecules which can undergo reversible photo-triggered isomerization between (at least) two (meta)stable states, are of immense importance as solar fuel (see Figure 1.7). Different states originate from various factors: E/Z isomerization, valence isomerization, cyclo-additions, tautomerizations etc. A variety of such molecular systems have been designed and synthesized. The system absorbs sunlight which leads to different type of chemical processes such

as: (1) pericyclic reactions; (2) photo-induced bond cleavages; (3) E/Z isomerizations; (4) intramolecular hydrogen/group transfers; (5) electron transfers (redox).[68] The most widely used photochromic molecules are azobenzenes[69], diarylethenes[70], spiropyrans/-oxazines[71] and stilbenes[72]. Diarylethenes can be switched between the two states photochemically or electrochemically, whereas the other three molecules can be reverted either photochemically or thermally. The switching behaviour, including rate of the isomerization and stability of the different isomers, depends on several factors such as their surrounding environment, chemical functionalisation etc. .

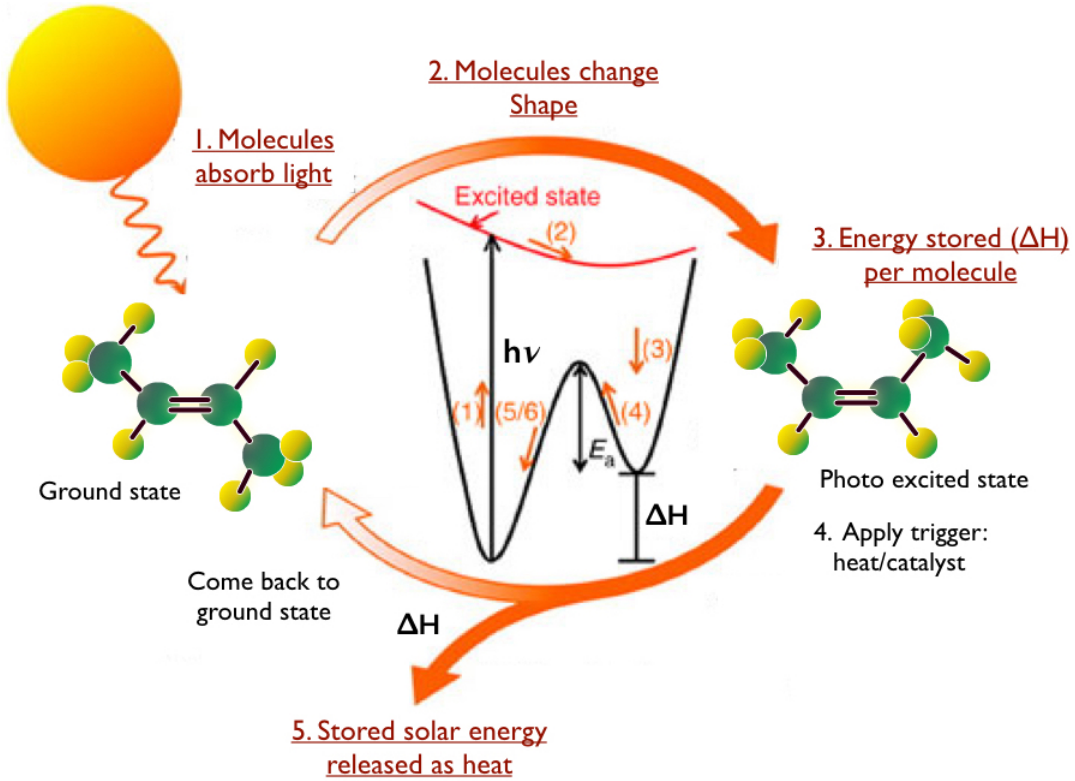

Figure 1.7: Mechanism of solar thermal fuels based on cis-trans isomerisation in butene system.

There are some basic requirements for such optoelectronic responses[73,74]: molecule should have (1) wide fundamental gaps preventing the thermal generation of free charge carriers; (2) no permanent charges; (3) avoid undesired photo-

decomposition processes. (4) Electronic structures of donor-bridge-acceptor (D-B-A) molecules are known for efficient light energy conversion process through reversible photo-switchability, where the bridge would be an asymmetric wire or "diode".[75] Bridge fundamentally acts as a rectifier that promotes electron transfer (ET) from donor to acceptor but resist ET in the reverse direction suppressing the charge recombination process.[76,77] In that scenario, if the photo-transformed state is a bound state and maintains a finite energy difference with the ground state, this can effectively result in photochemical energy storage (see Figure 1.7).[78]

1.3.4 Reactivity of Bisphenol A Based Molecular Systems and Their Stereochemistry

Plastics and pesticides are the products that contain estrogenic endocrine disrupting chemicals (EDCs), which mimics the action of the hormone oestradiol[79], thus, interfere with mammalian development. Bisphenol A, which was initially synthesized as a chemical oestrogen,[80] is now used as the monomer for the production of polycarbonate plastics[81] and causes toxicity. Low levels of BPA are detected in 90% of human urine samples, indicating the widespread exposure to BPA. It has been established that BPA monoglucuronide is the predominant metabolite of BPA, which is an inactive estrogen.[82] Hence, BPA-compounds (see Figure 1.8) and their potential health issues demand our understanding of the underlying mechanism behind its toxicity. Notably, when glucuronidation is unable to work as a detoxification pathway of BPA, metabolic activation occurs,[83] thereby producing two constitutional (structural) isomers (M-1 and M-2) with molecular formula $C_{18}H_{20}O_2$ (see Figure 1.8). Importantly, recent endeavors[84,85] emphasize the fact that neither BPA nor M-1 but M-2 is the potential environmental estrogen because of its activity at nM concentration. In fact, stereochemistry plays an important role. Appropriate spacing of two terminal phenolic moieties through

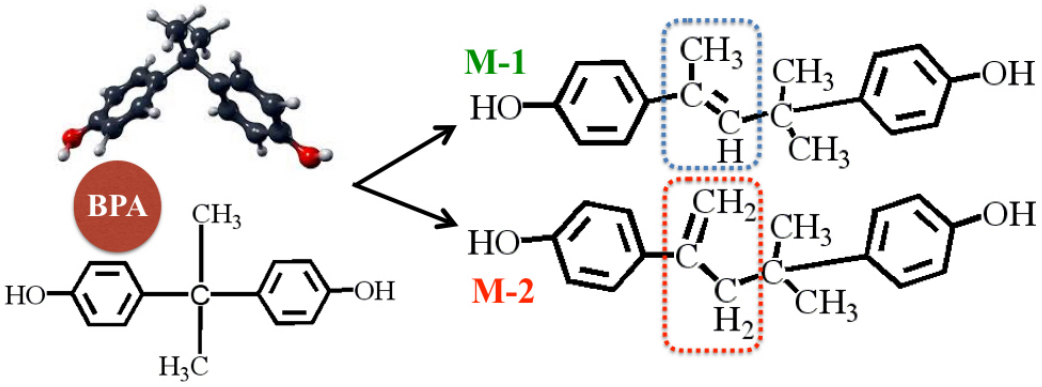

Figure 1.8: Molecular structure of (Bisphenol A; BPA) and its metabolites: 4-methyl-2,4-bis(p-hydroxyphenyl)pent-2-ene (M-1) and 4-methyl-2,4-bis(4-hydroxyphenyl)pent-1-ene (M-2).

aliphatic spacer group triggers M-2 to act as a potential disruptor toward the estrogen receptors ($ER\alpha$ and $ER\beta$).[86]

1.4 Computational Methods

1.4.1 Density Functional Theory (DFT)

DFT is the most widely used quantum mechanical approach for calculating the ground state properties of a wide range of systems; from molecules to bulk materials. Various ground state properties, such as, optimized geometry, vibrational frequency, atomization energy, ionization energy, electronic property, one-particle magnetic states, optical property, reaction pathway etc. can be predicted very accurately. With gradual advancement, it has also been modified for molecular dynamics, spin dependent study, investigation at non-zero temperature, time dependent phenomena etc.

According to the Schrödinger equation, the non-relativistic wavefunction, $\Psi(r)$, is calculated with the external potential due to the nuclei, $V_{ext}(r)$, where,

$$\left[-\frac{\hbar^2\nabla^2}{2m} + V_{ext}(r)\right]\Psi(r) = \epsilon\Psi(r) \tag{1.11}$$

To treat many electron systems, the equation can be modified as follows,

$$\left[\sum_{i}^{n}\left(-\frac{\hbar^2\nabla_i^2}{2m}+v(r_i)\right)+\sum_{i<j}U(r_i,r_j)\right]\Psi(r_1,r_2\ldots,r_N)=E\Psi(r_1,r_2\ldots,r_N) \tag{1.12}$$

where n is the number of electrons in the system and $U(r_i, r_j)$ is the electron-electron interaction. It is evident that only through U term, simple single-body quantum mechanics of Equation 1.11 differs from the complex many-body problem of Equation 1.12. However, the computational resources required for solving Schrödinger equation by many-body methods is exceedingly large even for modest system sizes. Here comes the superior performance of Density Functional Theory which successfully map the many-body problem of interacting particles in a potential, onto one of non-interacting particles in an effective potential. Accordingly, it reduces the many-body problem to a one-electron problem.

Hohenberg-Kohn theorems are the basics of DFT method.[87] The two theorems which were constituted can be stated as follows:

Theorem 1: External potential, $V_{ext}(r)$, of an interacting gas of electrons can be uniquely determined by ground state particle density $\rho(r)$.

Theorem 2: A universal functional for the energy $E[\rho]$ can be defined in terms of the density $\rho(r)$, for any external potential $V_{ext}(r)$. For a given $V_{ext}(r)$, the exact ground state energy of the system is the global minimum of $E[\rho]$, and the density that minimizes it is the exact ground state density, $\rho_0(r)$. Thus, conceptually DFT is exact. However, approximation arises due to inherent difficulty in efficiently evaluating many-body interactions.

Based on the above two theorems, we can see that the problem of functions of 3n number of variables in equation 1.12 has been reduced to functions of only 3 variables in $\rho(r)$. Within DFT formalism, the total energy functional, $E_{HK}[\rho]$,

can be expressed as,

$$\begin{aligned} E_{HK}[\rho] &= T[\rho] + E_{e-e}[\rho] + \int drV_{ext}(r)\rho(r) + E_{ion-ion} \\ &= F_{HK}[\rho] + \int drV_{ext}(r)\rho(r) + E_{ion-ion} \end{aligned} \tag{1.13}$$

can be expressed where, $T[\rho]$ and $E_{e-e}[\rho]$ are the kinetic and potential energies of electrons, respectively, and $E_{ion-ion}$ is the Coulomb ion-ion interaction energy. The functional F_{HK} is universal. Soon after this formulation, here comes an anstaz proposed by Kohn and Sham in 1965 to determine the ground state density $\rho_0(r)$.[88]

1.4.1.1 Kohn-Sham ansatz

The most extensively used implementation of DFT is the Kohn-Sham approach[88]. Kohn and Sham gave a formalism to map a given system with interacting electrons onto one of non-interacting electrons in an effective potential with exactly the same ground state density. So, solution of the non-interacting problem gives the ground state charge density of the real system, which can be used to determine its total energy and thus, physical properties. In the Kohn-Sham formulation, the total energy functional can be written as,

$$\begin{aligned} E_{KS}[\rho] &= T_s[\rho] + \int drdr' \frac{\rho(r)\rho(r')}{|r-r'|} + \int drV_{ext}(r)\rho(r) + E_{XC}[\rho] + E_{ion-ion} \\ &= T_s[\rho] + E_{Hartree}[\rho] + \int drV_{ext}(r)\rho(r) + E_{XC}[\rho] + E_{ion-ion} \end{aligned} \tag{1.14}$$

where, $E_{Hartree}$ and E_{XC} are the Hartree and exchange correlation contributions to the total energy. E_{XC} term accounts for the many body effects of exchange and correlation. The charge density $\rho(r)$ is given by,

$$\rho(r) = \rho_s(r) = \sum_{i=1}^{n} |\phi_i(r)|^2, and, n = \int dr\rho(r) \tag{1.15}$$

and, $T_s[\rho(r)] = -\frac{\hbar^2}{2m}\sum_{i=1}^{N}\int \phi_i^*(\mathbf{r})\nabla^2\phi_i(r)dr$, is the non-interacting kinetic energy. After comparing 1.13 and 1.14, we get

$E_{XC}[\rho] = T[\rho] + E_{e-e} - T_s[\rho] - E_{Hartee}$

$V_{XC} = \frac{\delta E_{XC}[\rho(r)]}{\delta\rho(r)}$, is the exchange-correlation potential.

Finally, solving the Kohn-Sham equation is done in a self-consistent manner following the scheme illustrated in Figure 1.9. First, an initial guess for $\rho_0(r)$ is

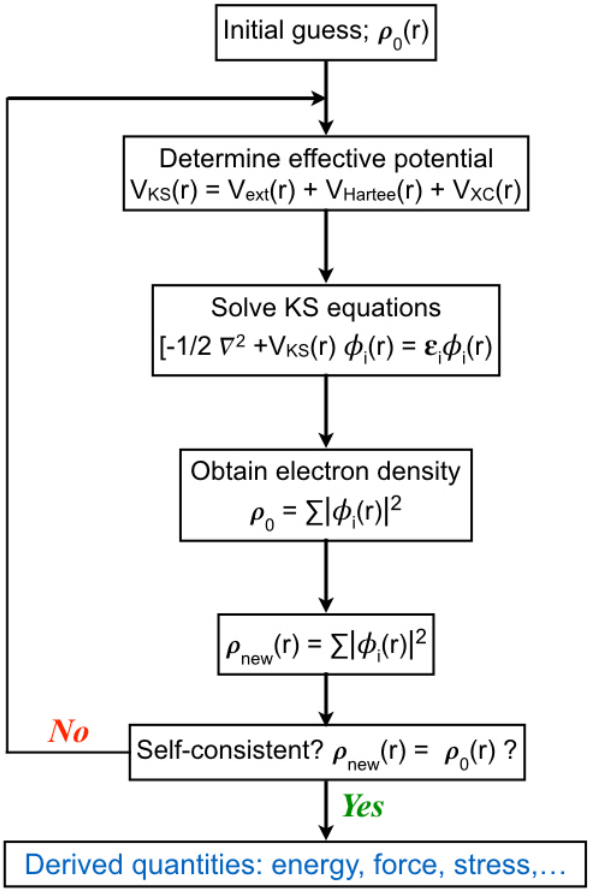

Figure 1.9: Scheme to solve the Kohn-Sham equations in a self consistent way.

considered and then the corresponding V_{KS} is calculated. After that, $\{\phi_i(r)\}$ can be calculated by solving the Kohn-Sham equations. From these $\{\phi_i(r)\}$, one can calculate a new density and the process starts all over again. This procedure is then continued until a convergence is reached (see Scheme 1.9).

1.4.1.2 Exchange and Correlation Functionals

Here we discuss some of the exchange and correlation energy functionals (E_{XC}), which have been used extensively among wide variety of approximations. The exchange correlation energy functional (E_{XC}) is not exactly known, and the accuracy of finding the ground state density is limited by the approximations made in the formulation of the functional. Local density approximation (LDA) and generalized gradient approximations (GGA) are the two commonly used approximations that determine the accuracy of a solution.

1.4.1.2.1 Local Density Approximation (LDA): LDA is the simplest approximation to the exchange-correlation energy functional, $E_{XC}[\rho(r)]$ [89] which is defined as:

$$E_{XC}^{LDA}[\rho] = \int dr \epsilon_{xc}[\rho(r)] \cdot \rho(r) \tag{1.16}$$

where $\epsilon_{xc}[\rho(r)]$ is the exchange-correlation energy per electron of the homogeneous electron gas with density $\rho(r)$. In this approach, it is considered that the electronic density, $\rho(r)$, is a smooth and homogeneous function in space.

1.4.1.2.2 Generalized Gradient Approximation (GGA): GGA functional is a modified version of LDA functional with inhomogeneous charge densities. As the exchange-correlation energy in GGA approximation depend on the gradients of charge density (apart from the local electron densities), it has shown the improvement in result over LDA for the systems where the charge density is slowly varying. There are a variety of formalism for GGA approximation. [90–95]. The exchange-correlation energy is defined as,

$$E_{XC}^{GGA}[\rho, \vec{\bigtriangledown}\rho] = \int d\mathbf{r} \epsilon_{xc}[\rho, \vec{\bigtriangledown}\rho] \cdot \rho(r) \tag{1.17}$$

while, for spin polarized systems, the exchange-correlation energy is defined as,

$$E_{XC}^{GSGA}[\rho_\uparrow, \rho_\downarrow, \vec{\nabla}\rho_\uparrow, \vec{\nabla}\rho_\downarrow] = \int dr \epsilon_{xc}[\rho_\uparrow, \rho_\downarrow, \vec{\nabla}\rho_\uparrow, \vec{\nabla}\rho_\downarrow] \cdot \rho(r) \tag{1.18}$$

1.4.1.2.3 Hybrid Functionals: In hybrid functionals, the exchange-correlation energy includes a mixture of Hartree-Fock exchange with exchange and correlation from different sources, often including various forms of LDA and GGA. For example, in case of B3LYP (Becke 3-parameter Lee-Yang-Parr),[96] one mixes the Hatree-Fock exchange with both LDA (VWN exchange) and GGA (Becke88 exchange) exchange and employs LYP correlation functional. B3LYP exchange-correlation functional is given by:

$$E_{XC}^{B3LYP} = E_x^{LDA} + a_0[E_x^{HF} - E_x^{LDA}] + a_x[E_x^{GGA} - E_x^{LDA}] + a_c[E_c^{GGA} - E_c^{LDA}] + E_c^{LDA} \tag{1.19}$$

where, $a_0 = 0.20$, $a_x = 0.72$ and $a_c = 0.81$.

1.4.1.2.4 Long range corrected functionals: The non-coulomb part of exchange functionals typically die off very rapidly and become less accurate at large distances. Therefore, it is not accurate for modelling processes such as electron excitations to higher energy orbitals. Various types of formalisms have been adopted to handle the systems with significant dispersive interactions. CAM-B3LYP[97] and ωb97xd[98] are the most commonly used long range corrected functionals.

1.4.1.3 Pseudopotentials and Numerical Orbitals

Pseudopotentials are used as an approximation for the simplified description of wavefunction in computational physics and chemistry. Such approximation is used for (a) reduction of basis set size, (b) reduction of effective number of electrons

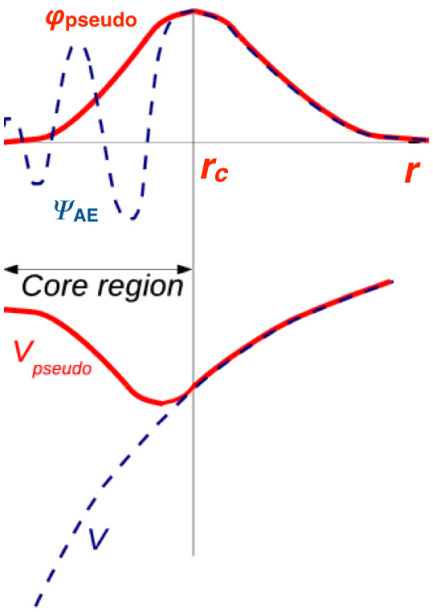

Figure 1.10: Comparison of a wave function in the Coulomb potential of the nucleus (dashed line) to the one in the pseudopotential (continuous line).[101] The real and the pseudo wave function and potentials match above a certain cutoff radius r_c.

for explicit consideration and (c) inclusion of relativistic and other effects. Pseudopotentials are obtained by constructing smoother wave functions in which the oscillations of the valence wave function in the core region are removed.[99,100] The pseudo wave function and all electron wave function becomes comparable with each other beyond a particular value of radial distance, which is after the last node in the all electron wave function; this is called the cutoff radius, r_c. A good pseudopotential needs to fulfil the following conditions:

- The lowest pseudo wave function generated by the pseudopotential generalization method should not contain any nodes.
- The normalized atomic radial pseudo wave function with an angular momentum l should be equal to the normalized radial all-electron (AE) wave function outside a given cut-off radius, r_c (Fig. 1.10):

$$R_i^{PP}(r) = R_i^{AE}(r) \ (r > r_c) \tag{1.20}$$

- Norm conservation: The charge inside of r_c has to be the same for both wave functions,

$$\int_0^{r_c} |R_i^{PP}(r)|^2 r^2 dr = \int_0^{r_c} |R_i^{AE}(r)|^2 r^2 dr \tag{1.21}$$

- The eigenvalues of both wave functions should be the same.

1.4.1.3.1 Sources of Errors and Limitations in Density Functional Theory based calculations:

- Pseudopotential: Accuracy of the results obtained using a plane wave basis code, is limited by the accuracy of the treatment used for the core electrons. In general, Projector Augmented Wave method (PAW) produces more accurate results than any pseudopotential method, since it reconstructs the exact valence wavefunctions, with all nodes in the core region.

- Exchange-Correlation potential: Two major errors arise from the inappropriate choice exchange-correlation functional. Firstly, the bandgap is (usually) strongly reduced compared to experiment. Secondly, exchange-correlation related error is also found while determining the formation energy or adsorption affinity. LDA overbinds all bonds, while GGA underbinds them. An exact solution lie somewhere in between the DFT formation energies.

- Large scale simulation: The computational cost in ab initio calculation increases rapidly with the size of problem N (number of atoms or electrons, basis size). The scaling with N is governed by several factors and is generally $\sim N^3$ in both DFT and HF-based realizations. The methods, which rely on the short-ranged nature of electronic structure, can allow accurate, ab initio simulations of systems of larger size. We have used the SIESTA method for

ab initio order-N materials simulation which uses numerical linear combination of atomic orbitals basis set including multiple-zeta and polarization orbitals. Exchange and correlation are treated with the generalized gradient approximations.

1.4.2 Density Functional Perturbation Theory

Density Functional Perturbation Theory (DFPT) is a linear response technique for computing the second derivatives of the ground state energy with respect to external perturbation $\lambda \equiv \{\lambda_i\}$. The first and second derivatives of the ground-state energy are

$$\frac{\partial E}{\partial \lambda_i} = \frac{\partial E_{ion-ion}}{\partial \lambda_i} + \int dr \frac{\partial V_{ext}(r)}{\partial \lambda_i} \rho(r) \tag{1.22}$$

and

$$\frac{\partial^2 E}{\partial \lambda_i \lambda_j} = \frac{\partial^2 E_{ion-ion}}{\partial \lambda_i \lambda_j} + \int dr \frac{\partial^2 V_{ext}(r)}{\partial \lambda_i \lambda_j} \rho(r) + \int dr \frac{\partial \rho(r)}{\partial \lambda_i} \frac{\partial V_{ext}(r)}{\partial \lambda_j} \tag{1.23}$$

In Equation 1.23, $\frac{\partial \rho(r)}{\partial \lambda_i}$ is the induced charge-density by the first order perturbation, which is the new quantity to derive and defined as,

$$\frac{\partial \rho(r)}{\partial \lambda_i} = \sum_i \frac{\partial \phi_i^*(r)}{\partial \lambda} \phi_i(r) + \phi_i^*(r) \frac{\partial \phi_i(r)}{\partial \lambda} \tag{1.24}$$

In the linear approximation, $\frac{\partial \rho(r)}{\partial \lambda_i} = \Delta\rho(r)$ where, $\Delta\rho(r)$ can be expressed as,

$$\Delta\rho(r) = \sum_i^N \phi_i^*(r) \Delta\phi(r) \tag{1.25}$$

$$\left[-\frac{\hbar^2\nabla^2}{2m} + V_{KS}(r)\right]\phi_i(r) = \epsilon_i\phi_i(r) \tag{1.26}$$

$V_{KS}(r) = V_{loc}(r) + V_H(r) + V_{XC}(r).V_{KS}(r,\lambda)$,
V_{KS} depends on λ, as a result, $\phi_i(\mathbf{r},\lambda)$ and $\epsilon_i(\lambda)$ are the function of λ. Hence, after the first order derivative with respect to λ, we get,

$$\left[-\frac{\hbar^2\nabla^2}{2m} + V_{KS}(r) - \epsilon_i\right]\frac{\partial\phi_i}{\partial\lambda}\phi_i(r) = -\frac{\partial V_{KS}(r)}{\partial\lambda}\phi_i(r) + \frac{\partial\epsilon_i}{\partial\lambda}\phi_i(r) \tag{1.27}$$

where,

$$\frac{\partial V_{KS}(r)}{\partial\lambda_i} = \frac{\partial V_{local}(r)}{\partial\lambda_i} + \frac{\partial V_H(r)}{\partial\lambda_i} + \frac{\partial V_{XC}(r)}{\partial\lambda_i} \tag{1.28}$$

and

$$\frac{\partial V_H(r)}{\partial\lambda_i} = \int\frac{1}{|r-r'|}\frac{\partial\rho(r')}{\partial\lambda}d^3r' \tag{1.29}$$

$$\frac{\partial V_{XC}(r)}{\partial\lambda_i} = \frac{dV_{XC}}{d\rho}\frac{\partial\rho(r)}{\partial\lambda} \tag{1.30}$$

So, the variation in Kohn-Sham potential is given by,

$$\frac{\partial V_{XC}(r)}{\partial\lambda_i} = \frac{dV_{XC}}{d\rho}\frac{\partial\rho(r)}{\partial\lambda} \tag{1.31}$$

Equation 1.27, 1.29 and 1.31 depend on the induced (by perturbation) charge density in self-consistent manner.

Hence, the variation in the wave function, $\Delta\phi(r)$, as mentioned in Equation 1.25, can be obtained by first-order perturbation theory (see Equation 1.32

and 1.33):

$$(H - \epsilon_i) |\Delta\phi_i\rangle = -(\Delta V_{ext}(r) - \Delta\epsilon_i) |\phi_i\rangle \tag{1.32}$$

$$(H - \epsilon_i) |\Delta\phi_i\rangle = -\widehat{P}_{empty} \Delta V_{ext}(r) |\phi_i\rangle \tag{1.33}$$

$\widehat{P}_{empty}$ is the projector onto the empty states, thus,

$$\widehat{P}_{empty} = 1 - \widehat{P}_{occupied} = 1 - \sum_i |\phi_i\rangle \langle\phi_i| \tag{1.34}$$

Change in effective potential, $\Delta V_{ext}(r)$ is obtained self-consistently by solving Equation 1.27, 1.29 and 1.31

$\Delta\epsilon_i = \langle\phi_i|\Delta V_{ext}(r)|\phi_i\rangle$

Hence, self-consistent solution of the set of linear equations 1.32, 1.33 and 1.28, $\Delta\rho$ can be evaluated with reasonable accuracy. $\Delta\rho$ is used in Equation 1.23, to find the second derivative of the total energy. Following this procedure, DFPT method is applied to evaluate the phonon frequencies by evaluating the second derivatives of energy with respect to atomic positions (displacement of ions is the perturbation).

Advantages of the DFPT method are: (1) it avoids the use of supercell, (2) allows the calculation of phonon frequencies at arbitrary phonon wave vector (q), and (3) makes the intensity of the calculation independent of the phonon wavelength.

1.4.3 Time Dependent Density Functional Theory (TDDFT)

Excited state wave-function, energy and related properties are hard to understand from ground state method like DFT. However, one may use DFT to calculate

the excited state energies in certain scenarios such as when the excited state is of different spin-multiplicity (like triplet) or it belongs to a different space group when compared to the ground state. These methods are called Δ methods. However, their use is very limited. For example, one cannot calculate the excited state energy if both the ground and excited states belong to the same symmetry or space-group which indeed is the case for general systems of interest. Thus, one needs a different formalism to explore excited states. Wave-function based methods include configuration interaction (CI), time dependent HF etc. and density functional based methods include TD-DFT, TD-DFTB etc. CI and TD-HF are also known as Tamn-Dancoff approximation and random phase approximation (RPA).[102] Time dependent density functional theory (TDDFT) extends the basic ideas of ground-state density functional theory (DFT) to the treatment of excitations or more general time-dependent phenomena.[103] TDDFT can be viewed as an alternative formulation of time-dependent quantum mechanical approach based on wave-functions and the many-body Schrödinger equation. The basic variable in TDDFT is the time-dependent electron density, $\rho(r,t)$. Thus, a many-body wave-function and 3N-dimensional space (where N is the number of electrons in the system) is simplified by 3 variables, x, y and z. The standard way to obtain $\rho(r,t)$ is with the help of a fictitious system of non-interacting electrons, as described in the Kohn-Sham formalism. Electrons feel an effective potential, the time-dependent Kohn-Sham potential. In the time-dependent case, these Kohn-Sham electrons obey the time-dependent Schrödinger equation

$$i\frac{\partial}{\partial t}\psi_i(r,t) = \left[-\frac{\hbar^2}{2m}\nabla_i^2 + \hat{V}_{KS}(r,t)\right]\psi_i(r,t) \tag{1.35}$$

The density of the interacting system can be obtained from the time-dependent Kohn-Sham orbitals

$$\rho(r,t) = \sum_{i}^{occ} \psi_i(r,t) \tag{1.36}$$

1.4.4 *ab initio* Molecular Dynamics

Predicting the material properties can be achieved quite accurately though usage of relativistic time-dependent Schrödinger equation. However, this method has serious limitation towards treating large and complex materials. To treat large systems, one need to find other suitable methods. In this regard, molecular dynamics (MD) simulations are quite reliable and computationally affordable to gain detailed structural and conformational aspects on a realistic time scale and atomic level[104]. Simulating systems by MD, we can obtain ensemble-averaged properties, such as binding energy, relative stability of molecular conformations etc. by averaging over representative statistical ensembles of structures.

Basically, we need to obtain the numerical solution of Newton's equation of motion for all the nuclei within a system. In classical MD, the force (F_i) on a atom 'i' with mass M_i is formulated as follows,

$$\overrightarrow{F_i} = M_i \frac{\partial^2 \overrightarrow{r_i}}{\partial t^2} \tag{1.37}$$

The vector notations in forces F_i and positions r_i, *i.e.* in three dimensions the whole system is described by 3N coordinates. The forces on a atom 'i' is calculated as the negative derivative of the potential U, describing the interactions between the particles. And it can be written as,

$$\overrightarrow{F_i} = -\frac{\partial U}{\partial \overrightarrow{x_i}} \tag{1.38}$$

where, U, the inter-atomic potential, is a function of many degrees of freedom corresponding to all nuclei. The major challenge in MD simulations is calculating interatomic forces accurately[105]. In classical MD, forces are calculated from "predefined potentials", which are either based on empirical data or on independent electronic structure calculations[104]. Although, these empirical potentials have been modified over time to make them reliable, transferability is still the major issue. Moreover, classical MD cannot capture the bond-reformation processes taking place in many dynamic systems. To overcome these limitations, first-principle based approach *i.e.* ab-initio molecular dynamics (AIMD) has been developed by various groups[106]. Here, the forces are calculated on-the-fly from accurate electronic structure calculations. However, the better accuracy and reliable predictive power of AIMD simulations demands significant increase in computational effort. Thus, till now, DFT is the most commonly applied method for electronic structure calculation during AIMD simulations. Notably, evaluation of interatomic forces in AIMD does not depend on any adjustable parameters but only on position of nuclei. Depending upon the way of solving the electronic structures in every AIMD steps, there are different approaches developed by the researchers. These are Ehrenfest molecular dynamics, Born-Oppenheimer molecular dynamics (BOMD), Car-Parrinello molecular dynamics (CPMD) etc. For the works presented in this thesis, we have extensively used BOMD simulations to investigate structural evaluation of various low-dimensional as well as bulk systems at finite temperatures.

1.4.4.1 Born-Oppenheimer Molecular Dynamics

BOMD simulation is based on the direct solution of the static electronic structure problem in each molecular dynamics step, given the set of fixed nuclear positions at any instance of time. Hence, electronic structure part is tackled by

solving the time-independent Schrödinger equation and then propagating the nuclei via classical molecular dynamics. Note that, unlike other AIMD methods, the time-dependence of the electronic structure is a consequence of nuclear motion for BOMD simulations. One can define the force ($F_i = M_i\ddot{R}_i(t)$) on a atom 'i' with mass M_i, as follows within the BOMD framework,

$$M_i\ddot{R}_i(t) = \nabla_i \min_{\psi_0} <\psi_0|H_e|\psi_0> \tag{1.39}$$

thus, the electronic ground state can be determined.

1.4.5 Transition State Theory and Nudged Elastic Band Method

Ionic diffusion can be modelled using a lattice model, where the atoms diffusing on the surface spend most of their time at well-defined equilibrium sites and only a small fraction of time along paths connecting adjacent sites. This leads to diffusion which is simply the migration or 'hopping' of an ion from one site to a neighbouring vacant site via an activated state, called Transition State (TS). TS is defined as the maximum energy point along the minimum energy path between the end points of the hop. The activation barrier ΔE_{diff} is then given by

$$\Delta E_{diff} = E_{TS} - E_{initial} \tag{1.40}$$

where E_{TS} is the enthalpy in the activated state and $E_{initial}$ is the enthalpy in the initial state. The frequency ν at which a hop occurs is then given by transition state theory[107] as

$$\nu = \nu_{pre} exp(\frac{\Delta S}{k_B}) exp(-\frac{\Delta E_{diff}}{k_B T}) \tag{1.41}$$

where, ν_{pre} is denoted as attempt frequency, ΔS is the activation entropy, k_B is the Boltzmann constant and T is the temperature. Within the harmonic approximation, this equation can be simplified as follows:

$$\nu = \nu_{pre}^{'} exp(-\frac{\Delta E_{diff}}{k_B T}) \tag{1.42}$$

where $\nu_{pre}^{'}$ can be estimated by the ratio of the product of the normal-mode frequencies of the initial state to the product of the normal-mode frequencies of the activated state.

In studies of Li, Na and Mg ion diffusion as discussed in this thesis, the nudged elastic band (NEB) method[108] has been used to determine the barriers for alkali migration paths for a specific nuclei configuration. In this method, a number of intermediate images along the migration path is considered maintaining spacing between neighbouring images and subsequently optimised to find the lowest possible energy. This is a constrained optimisation by adding 'spring' forces along the band between images and projecting out the component of the force due to the potential perpendicular to the band. Such a calculation would typically involve the following steps: (1) geometry optimisation of the host material with the ion in their (initial and final) equilibrium positions, (2) generation of a series of 'images' along the migration path through interpolation between the starting and end points. (3) Determination of the lowest energy path along the saddle points through NEB calculation. In principle, the NEB method is applicable to determine the barrier of any migration event. However, the identification of the migration events in many solid electrolytes exhibiting alkali-ion disorder and coordinated multi-ion motion is highly challenging. In practice, NEB calculations are usually pretty good at the dilute limits, that is, considering the migration of a single vacancy or a single ion. To obtain an actual diffusivity number, the prefactor ($\nu_{pre}^{'}$) in Equation 1.42 must be calculated. Typically, $\nu_{pre}^{'} = 1013$ is used, which can

also be estimated via first-principles calculations.

1.4.6 Transport Theory for Periodic Lattice Model

1.4.6.1 Boltzmann Transport Equation

Boltzmann Transport Equation is a very powerful tool to understand the transport properties of materials. In this formalism, all kinds of carrier scattering processes can be simply introduced by relaxation time approximation. Within the anisotropic relaxation time (τ) approximation, $\tau(i,k)$ is determined upon varying the k states of the i^{th} band in the first Brillouin zone. Probability of occupation of an electron at time t at r with wavevectors lying between k,k+dk is defined through a distribution-function $f(k,r,t)$. Under equilibrium (E = B = $\nabla_r f$ = $\nabla_T f = 0$), *i.e.*, no external electric (E) or magnetic (B) field and no spatial and thermal gradients), the distribution function is found from quantum-statistical analysis to be given by the Fermi-Dirac function for fermions

$$f_0(\varepsilon) = \frac{1}{1 + e^{\frac{\varepsilon_k - \mu}{k_B T}}} \tag{1.43}$$

where, ε_k is the energy of the electron, μ is the Fermi energy, and k_B is the Boltzmann constant. Any external perturbation drives the distribution function away from the equilibrium; and Boltzmann-transport equation (BTE) governs the shift of the distribution function from equilibrium. It may be written formally as,

$$\frac{df}{dt} = \frac{F_t}{\hbar} \cdot \nabla_k f(k) + v \cdot \nabla_r f(k) + \frac{\partial f}{\partial t} \tag{1.44}$$

where, on the right hand side, the first term reflects the change in distribution function due to the total field force $F_t = E + v \times B$, the second term is the change due to concentration gradients, and the last term is the local change in the

distribution function. Since the total number of carriers in the crystal is constant, the total rate of change of the distribution is identically zero by Liouville's theorem. Hence the local change in the distribution function is written as,

$$\frac{\partial f}{\partial t} = \frac{\partial f}{\partial t}|_{coll} - \frac{F_t}{\hbar} \cdot \nabla_k f(k) - v \cdot \nabla_r f(k) + \frac{\partial f}{\partial t} \tag{1.45}$$

where, the first term has been split off from the field term since collision effects are not easily described by fields. The second term is due to applied field only and the third is due to concentration gradients. Denoting the scattering rate (see Figure 1.11) from state $k \rightarrow k'$ as $S(k, k')$, the collision term is given by,

$$\frac{\partial f(k)}{\partial t}|_{coll} = \sum_{k'} [S(k', k) f(k')[1 - f(k)] - S(k, k') f(k)[1 - f(k')]] \tag{1.46}$$

At equilibrium ($f = f_0$), the 'principle of detailed balance' (see Figure 1.11) enforces the condition

$$S(k', k) f_0(k')[1 - f_0(k)] = S(k, k') f_0(k)[1 - f_0(k')] \tag{1.47}$$

which translates to

$$S(k', k) e^{\frac{\varepsilon_k}{k_B T}} = S(k, k') e^{\frac{\varepsilon_{k'}}{k_B T}} \tag{1.48}$$

In the special case of elastic scattering, $\varepsilon_{k'} = \varepsilon_k$, and as a result, $S(k, k') = S(k', k)$ irrespective of the nature of the distribution function. Using this, one rewrites the collision term as

$$\frac{\partial f(k)}{\partial t}|_{coll} = \sum_{k'} S(k, k')[f(k') - f(k)] \tag{1.49}$$

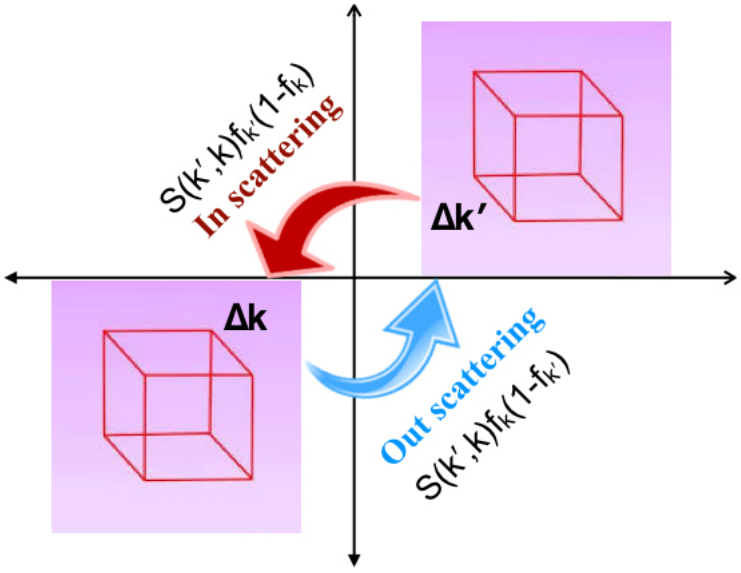

Figure 1.11: Visual representation of the scattering term of Boltzmann transport equation depicting the inflow and outflow of the distribution function.

One can rewrite this collision equation as

$$\frac{df(k)}{dt} + \frac{f(k)}{\tau_q(k)} = \sum_{k'} S(k,k')f(k') \tag{1.50}$$

where, the quantum scattering time is defined as

$$\frac{1}{\tau_q(k)} = \sum_{k'} S(k,k') \tag{1.51}$$

A particle prepared in state $|k\rangle$ at time $t = 0$ by an external perturbation will be scattered into other states $|k'\rangle$ due to collisions, and the distribution function in that state will approach the equilibrium distribution exponentially fast with the time constant τ_q(k) upon the removal of the applied field. The quantum scattering time τ_q(k) may be viewed as a 'lifetime' of the particle in the state $|k\rangle$. Let us now assume that the external fields and gradients have been turned on for a long time. They have driven the distribution function to a steady state value f from f_0. The perturbation is assumed to be small, *i.e.*, distribution function is assumed not to

deviate far from its equilibrium value of f_0. Under this condition, it is common practice to assume that

$$\frac{\partial f(k)}{\partial t} = \frac{\partial f(k)}{\partial t}|_{coll} = -\frac{f - f_0}{\tau} \tag{1.52}$$

where τ is a time scale characterizing the relaxation of the distribution. This is the relaxation time approximation, which is crucial for getting a solution of the Boltzmann transport equation. When the distribution function reaches a steady state, the Boltzmann transport equation may be written as

$$\frac{\partial f(k)}{\partial t} = -\frac{f - f_0}{\tau} - \frac{F_t}{\hbar} \cdot \nabla_k f(k) + v \cdot \nabla_r f(k) = 0 \tag{1.53}$$

where, the relaxation time approximation to the collision term has been used. In absence of any concentration gradients, the distribution function is given by,

$$f(k) = f_0(k) - \tau \frac{F_t}{\hbar} \cdot \nabla_k f \tag{1.54}$$

Using the definition of the velocity $v = 1/\hbar(\partial\varepsilon_k/\partial k)$, the distribution function becomes

$$f(k) = f_0(k) - \tau F_t \cdot v \frac{\partial f(k)}{\partial \varepsilon} \tag{1.55}$$

and, since the distribution function is assumed to be close to f_0, we can make the replacement $f(k)$ to $f_0(k)$, then distribution function

$$f(k) = f_0(k) - \tau F_t \cdot v \frac{\partial f_0(k)}{\partial \varepsilon} \tag{1.56}$$

is the solution of BTE for a perturbing force F_t.[109–111]

1.4.6.2 Mobility: Basic Theory

We will now arrive at a general expression for the drift mobility of carriers of arbitrary degeneracy confined in 'd' spatial dimensions. 'd' may be 1,2 or 3; for d = 0, the carrier in principle does not move in response to a field. Let the electric field be applied along the i^{th} spatial dimension, ($E = E_{ii}$) and the magnetic field B = 0. Starting from the Boltzmann equation for the distribution function of carriers $f(k, r, t)$, and using the relaxation-time approximation solution, we write the distribution function as

$$f(k) = f_0(k) + eF_i\tau(k)v_i\frac{\partial f_0}{\partial \varepsilon} \tag{1.57}$$

where $\tau(k)$ is the momentum relaxation time and v_i is the velocity of carriers in the i^{th} direction in response to the field. The current in response to the electric field along the i^{th} direction is given by

$$J = 2e\int \frac{d^dk}{(2\pi)^d}vf(k) \tag{1.58}$$

Using the distribution function from the solution of the BTE, we see that the f_0 term integrates out to zero, and only the second term contributes to a current. For a particle moving in d-dimensions the total kinetic energy (ε) is related to the average squared velocity $\langle v_i^2\rangle$ along one direction by the expression $\langle v_i^2\rangle = 2\varepsilon/dm^*$. Using this result, we re-write the expression for current as,

$$J_i = ne\left(-\frac{2e}{dm^*}\frac{\int d\varepsilon\tau_m\varepsilon^{\frac{d}{2}}\frac{\partial f_0}{\partial\varepsilon}}{\int d\varepsilon f_0(\varepsilon)\varepsilon^{\frac{d}{2}-1}}\right)E_i \tag{1.59}$$

where the term within bracket in equation 1.59 is the mobility in the d-dimensional case. Here, τ_m is the momentum relaxation time due to scattering events calculated in the Born approximation by Fermi's golden rule using the scattering potential,

turns out to depend on the energy of the mobile carrier and the temperature.

1.4.7 Charge Transfer Theory for Molecular Systems

The most commonly used charge transfer mechanisms in molecular systems is the hopping model introduced by R. A. Marcus.[112,113] In this mechanism, the charge hops between sites over a small distance and hopping rate is estimated from charge-coupling values. The same mechanism is also used to estimate transport characteristics in ultra pure organic molecular crystals. The coupling constant is obtained from the splitting of the frontier orbitals when molecular dimers are considered. The same is also estimated from 1D Holstein molecular model.[114,115] According to these models, the total mobility can be expressed to a good approximation as a sum of two contributions:

$$\mu = \mu_{tunnelling} + \mu_{hopping} \tag{1.60}$$

Here, the first term corresponds to coherent electron transfer (electron tunneling) and dominates transport at low temperatures; the second term is related to incoherent electron transfer (hopping motion) which becomes dominant at higher temperatures. The relative contribution of these two mechanism determines the microscopic parameters, such as electron-phonon coupling, electronic and phonon bandwidths, and phonon energy. According to the standard Holstein-type polaron model, the resulting energy after solving the Hamiltonian for a single charge carrier in the lattice is given by,

$$E_m = \varepsilon_m^{(0)} - \frac{1}{N}\sum_{kj} \hbar\omega_{kj} |g_m k, j|^2 + \sum_{kj} \hbar\omega_{kj} \left(n_{kj} + \frac{1}{2} \right) \tag{1.61}$$

where N denotes the total number of unit cells, and $g_m(k, j)$ the corresponding local electron-phonon coupling constant for a phonon of branch j and wavevector

k. The middle term in Equation 1.61 is the polaron binding energy ($E_{polaron}$) which is the measure of stabilization of electron (hole) localized on a single lattice site. $E_{polaron}$ originates from the deformations in geometry due to localisation of charge-carrier on a given site. This quantity is thus related to the reorganisation energy term in electron-transfer theories. Figure 1.12 reveals that potential energy

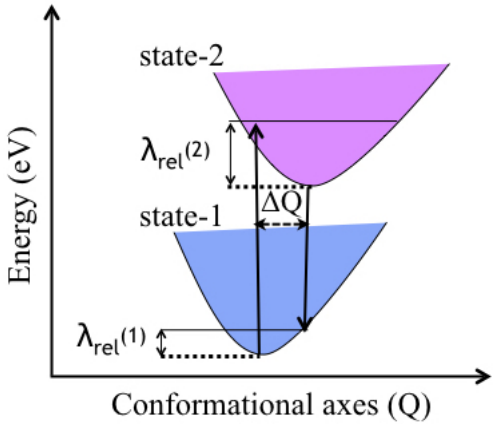

Figure 1.12: Potential energy surfaces for the neutral (state 1) and charged state (state-2), showing the vertical transitions, the normal-mode displacement ΔQ, and the relaxation energies $\lambda_{rel}^{(1)}$ and $\lambda_{rel}^{(2)}$.

surfaces for two electronic states (1 and 2): the ground state (neutral) and charged state; the geometry relaxation energies upon vertical transition from the neutral state to the charged state and vice versa ($\lambda_{rel}^{(1)}$ and $\lambda_{rel}^{(2)}$) are given by:

$$\lambda_{rel} = \sum_j \lambda_j = \sum_j \frac{V(j)^2}{2M_j\omega_j^2} \tag{1.62}$$

Notably, $E_{polaron} = \lambda_{rel}$

Commonly, the reorganisation energy (λ_{rel}) is expressed as the sum of inner and outer contributions. The inner (intramolecular) reorganization energy represents the change in equilibrium geometry of the donor and acceptor sites after the gain or loss of an electronic charge upon an electron transfer (ET) process. The outer (intermolecular) reorganization energy arises from the electronic and

nuclear polarization of the surrounding medium. Due to the weakness of the van der Waals interactions, it is possible to separate the reorganization energy into its inter- and intramolecular contributions in molecular systems to a good approximation. Within this approximation, the intramolecular reorganization energy (λ_{reorg}) is given by:

$$\lambda_{reorg} = \lambda_{rel}^{(1)} + \lambda_{rel}^{(2)} \tag{1.63}$$

and $E_{polaron} = \lambda_{reorg}/2$

There is an alternate approach to calculate λ_{reorg} and the contribution of vibrational modes to λ_{rel} through expanding the potential energy expression of neutral and charged states in power series of normal-mode coordinates. Where,

$$E_{polaron} = \lambda_{rel} = \sum_j \lambda_j = \sum \frac{M_j \omega_j^2 \Delta Q_j^2}{2} \tag{1.64}$$

$$\lambda_j = \frac{k_j}{2} \Delta Q_j^2, \tag{1.65}$$

$$S_j = \frac{\lambda_j}{\hbar \omega_j} \tag{1.66}$$

where ΔQ_j represents the displacement along normal-mode j between the equilibrium geometries of the neutral and charged molecules. k_j and ω_j are the corresponding force constants and vibrational frequencies; and S_j denotes the Huang-Rhys factor. The λ_j term is commonly used to estimate the electron(hole)-vibration coupling constant of a particular normal-mode. The addition of all coupling constants for a given molecular system represents the so-called vibronic coupling. We note that normal modes of the neutral and charged states, Q_1 and Q_2, are in general different and are related by the Duschinsky matrix, Z, as:[116]

$$Q_1 = JQ_2 + \Delta Q \tag{1.67}$$

Calculations of the Duschinsky matrices have been carried out with the gaussian suit of program.[117,118] The ionization bands has been determined in the framework of the Born-Oppenheimer and Franck-Condon (FC) approximations.[119]

1.5 Softwares Used

There are many packages for the self-consistent calculations of electronic structure using Hartree-Fock and DFT methods. DFT calculations on atoms, molecules or nanomaterials as reported in this thesis were carried out using Gaussian suite of code[117]. A combination of atom centered basis functions with pseudopotentials make an ideal choice for studying large systems. This has been implemented in the Spanish Initiative for Electronic Simulations with Thousands of Atoms (SIESTA) package,[120] making it an ideal choice for studying realistic systems of large sizes. We have also applied mixed Gaussian-Planewave (GPW) formalism with GTH (Goedecer-Tetter-Hutter) potential as implemented in CP2K[121]. For plane wave basis set, we have also used Quantum ESPRESSO[122] and Vienna Ab-initio Simulations Packages (VASP).[123] We have carried out Ab initio molecular dynamics simulations as implemented in CP2K (for molecular system) and VASP (for periodic systems). Xmgrace[124] and gnuplot[125] packages were used for plotting. Visualizations and graphical analyses were done using GaussView[126], Xcrysden[127], jmol[128] and VMD[129] visualization softwares. Many of the results were analyzed using home developed scripts/codes. The work reported in this thesis required computational calculations which were performed on dedicated home clusters as well as from the resources available in central facilities at Center for Computational Materials Science (CCMS), JNCASR.

1.6 Outline of Thesis

In the next chapter (second), we investigate the possibility of 2D boron sheets (BSs) as an anode in lithium ion batteries (LIBs). Among the α, α_1, and $\eta_{4/28}$ metallic BSs, α_1 polymorph has been found to be an optimum anode based on their electronic structural, Li adsorption/desorption, and Li-diffusion properties. At the Li-saturation limit, theoretical estimate of the capacity appears to be 383 $mAhg^{-1}$, which is higher than that of the conventional graphitic electrode. All of these characteristics suggest the appropriateness of α_1-boron sheet as the lightest possible anode material for LIBs.

In third chapter, we show that variation in the shape of the B_xN_z-domain and B-N charge-imbalance in $B_xC_yN_z$ layers results in tunable anodic properties. Two-dimensional $B_xC_yN_z$ with trigonal B_xN_z-domain (T_N with nitrogen-excess) meets the requirements for a superior anode for Sodium ion Battery (SIB). Charge-storage upon layer-wise accumulation of Na-ions on the T_N-surface is also appealing for application to sodium-ion capacitors, as an alternative to lithium-ion capacitors.

In fourth chapter, we investigate for an appropriate anode for multivalent electrochemistry involving magnesium ion which has immense importance to achieve higher energy storage in rechargeable battery compared to conventional one electron redox process, as present in LIB and SIB. We demonstrate that black phosphorus (P) based anode can overcome two overcome the major complications in Mg-battery set-up: (1) structural instability of metallic Mg-anode during charging-discharging cycle, and (2) very slow diffusion of Mg^{2+}-ion. Notably, Mg-ion storage within covalent P-anode optimises the anodic voltage and reduces the Mg-diffusion barrier, thereby can overcome the bottleneck in Mg-battery technology.

In chapter 5, we focus on 2D nano-hybrid systems namely Borocarbonitrides, which is a semiconducting graphene analogue. We study the role on BN and C domains in controlling the transport property of ternary Borocarbonitrides using *ab-initio* DFT-based computation combined with Boltzmann transport formalism. It is shown that atomically engineered surface topology and control over the stoichiometric proportion of B:C:N can control the conduction polarity (electron/hole) and maximise the mobility. Such an extraordinary transport efficiency can find applications in modern transistors.

Chapter 6 focuses on effect of puckered structure of Elemental Black Phosphorene on its transport property. In this chapter, we study the critical dependence of the number of layers in controlling the charge-transport property. We find that, tri-layer black phosphorus offers itself as appropriate anisotropic material which possesses both the directional as well as electron-hole anisotropy.The systematic scheme described here, helps to understand the fundamentals on anisotropy associated with carrier scattering process for any such complex quasi-2D materials which indeed has significant potential to design and optimise the advanced transport (logical) devices.

Chapter 7 discusses the effect of molecular surface chemistry to control the reactivity and stability of 2, 2′-bis (4-hydroxyphenyl) propane (BPA)-based systems. Here, we discuss the mechanism for metabolic activation of BPA, producing two metabolites: 4-methyl-2,4-bis (p-hydroxyphenyl) pent-2-ene (M-1) and 4-methyl-2, 4-bis (4-hydroxyphenyl) pent-1-ene (M-2) which are stereoisomer of each other. Possible way for selectivity toward M-1(nontoxic)/M-2(toxic) formation has been proposed. Moreover, stereo-control of biologically active M-2 with static polarization as the switch might affect the receptor binding. This analysis may be useful

in dictating the prevention of the harmful action of BPA and its metabolites.

Chapter 8 sheds light on the choice of appropriate surfaces in view of detection and extraction of bis-phenol based pollutants (EDCs: BPA, M-1 and M-2). Layered graphene supports very strong surface adsorption and assures complete removal of EDCs, while they get physisorbed on MoS_2 surface. In particular, understanding the modulation of the electronic structure and optical response upon surface adsorption can be exploited as possible means for isolation, detection and photo-degradation by specific choice of surface.

Chapter 9 discusses the photo-conversion of Bisphenol A (BPA)-based molecular architectures. Again, the specific stereochemical feature becomes important to attain the conformational flexibility and photochemical energy storage through excitation energy transfer. Through first-principles analysis coupled with electron transfer theory, we emphasize on the M-1-like molecular configuration as an excellent motif for light-energy-conversion.

Thus, a diverse background of materials chemistry and knowledge of first-principles methods coupled with modern charge-transport theory has built a solid ground to establish the importance of surface-chemistry in materials deigning as well as controlling the chemical reactivity.

References

[1] A. N. Alexandrova, A. I. Boldyrev, H.-J. Zhai, and L.-S. Wang, Coordination Chemistry Reviews **250**, 2811 (2006).

[2] A. P. Sergeeva, D. Y. Zubarev, H.-J. Zhai, A. I. Boldyrev, and L.-S. Wang,

Journal of the American Chemical Society **130**, 7244 (2008).

[3] D. L. Prasad and E. D. Jemmis, Physical Review Letters **100**, 165504 (2008).

[4] S. De, A. Willand, M. Amsler, P. Pochet, L. Genovese, and S. Goedecker, Physical Review Letters **106**, 225502 (2011).

[5] E. S. Penev, S. Bhowmick, A. Sadrzadeh, and B. I. Yakobson, Nano Letters **12**, 2441 (2012).

[6] M. J. Oconnell, *Carbon nanotubes: properties and applications* (CRC press, 2006).

[7] L. Britnell, R. Gorbachev, R. Jalil, B. Belle, F. Schedin, A. Mishchenko, T. Georgiou, M. Katsnelson, L. Eaves, S. Morozov, et al., Science **335**, 947 (2012).

[8] Y. Zhang, Y.-W. Tan, H. L. Stormer, and P. Kim, Nature **438**, 201 (2005).

[9] K. Novoselov, A. K. Geim, S. Morozov, D. Jiang, M. Katsnelson, I. Grigorieva, S. Dubonos, and A. Firsov, Nature **438**, 197 (2005).

[10] A. K. Geim and K. S. Novoselov, Nature Materials **6**, 183 (2007).

[11] S. Dutta and S. K. Pati, Journal of Materials Chemistry **20**, 8207 (2010).

[12] S. Z. Butler, S. M. Hollen, L. Cao, Y. Cui, J. A. Gupta, H. R. Gutiérrez, T. F. Heinz, S. S. Hong, J. Huang, A. F. Ismach, et al., ACS Nano **7**, 2898 (2013).

[13] L. Song, L. Ci, H. Lu, P. B. Sorokin, C. Jin, J. Ni, A. G. Kvashnin, D. G. Kvashnin, J. Lou, B. I. Yakobson, et al., Nano Letters **10**, 3209 (2010).

[14] M. Xu, T. Liang, M. Shi, and H. Chen, Chemical Reviews **113**, 3766 (2013).

[15] A. Ismach, H. Chou, D. A. Ferrer, Y. Wu, S. McDonnell, H. C. Floresca, A. Covacevich, C. Pope, R. Piner, M. J. Kim, et al., ACS Nano **6**, 6378 (2012).

[16] C.-H. Lee, G.-H. Lee, A. M. Van Der Zande, W. Chen, Y. Li, M. Han, X. Cui, G. Arefe, C. Nuckolls, T. F. Heinz, et al., Nature Nanotechnology **9**, 676 (2014).

[17] Q. H. Wang, K. Kalantar-Zadeh, A. Kis, J. N. Coleman, and M. S. Strano, Nature Nanotechnology **7**, 699 (2012).

[18] W. Liu, J. Kang, D. Sarkar, Y. Khatami, D. Jena, and K. Banerjee, Nano Letters **13**, 1983 (2013).

[19] H. Fang, S. Chuang, T. C. Chang, K. Takei, T. Takahashi, and A. Javey, Nano Letters **12**, 3788 (2012).

[20] B. Radisavljevic, A. Radenovic, J. Brivio, i. V. Giacometti, and A. Kis, Nature Nanotechnology **6**, 147 (2011).

[21] K. F. Mak, C. Lee, J. Hone, J. Shan, and T. F. Heinz, Physical Review Letters **105**, 136805 (2010).

[22] C. Chowdhury, S. Jahiruddin, and A. Datta, The Journal of Physical Chemistry Letters **7**, 1288 (2016).

[23] D. Jose and A. Datta, Accounts of Chemical Research **47**, 593 (2013).

[24] J. Qiao, X. Kong, Z.-X. Hu, F. Yang, and W. Ji, Nature Communications **5** (2014).

[25] M. Buscema, D. J. Groenendijk, S. I. Blanter, G. A. Steele, H. S. van der Zant, and A. Castellanos-Gomez, Nano Letters **14**, 3347 (2014).

[26] Y. Cai, Q. Ke, G. Zhang, Y. P. Feng, V. B. Shenoy, and Y.-W. Zhang, Advanced Functional Materials **25**, 2230 (2015).

[27] L. N. Vandenberg, R. Hauser, M. Marcus, N. Olea, and W. V. Welshons, Reproductive toxicology **24**, 139 (2007).

[28] L. N. Vandenberg, M. V. Maffini, C. Sonnenschein, B. S. Rubin, and A. M. Soto, Endocrine Reviews **30**, 75 (2009).

[29] H. H. Le, E. M. Carlson, J. P. Chua, and S. M. Belcher, Toxicology Letters **176**, 149 (2008).

[30] H. Chen, T. N. Cong, W. Yang, C. Tan, Y. Li, and Y. Ding, Progress in Natural Science **19**, 291 (2009).

[31] B. E. Conway, *Electrochemical supercapacitors: scientific fundamentals and technological applications* (Springer Science & Business Media, 2013).

[32] B. Dunn, H. Kamath, and J.-M. Tarascon, Science **334**, 928 (2011).

[33] M. S. Whittingham, Science **192**, 1126 (1976).

[34] M. S. Whittingham, Chemical Reviews **114**, 11414 (2014).

[35] K. Mizushima, P. Jones, P. Wiseman, and J. Goodenough, Materials Research Bulletin **15**, 783 (1980).

[36] N. K. Padhi, A and J. Goodenough, Journal of the Electrochemical Society **144**, 1188 (1997).

[37] M. S. Whittingham, Chemical Reviews **104**, 4271 (2004).

[38] M. S. Whittingham, Progress in Solid State Chemistry **12**, 41 (1978).

[39] A. S. Nagelberg and W. L. Worrell, Journal of Solid State Chemistry **29**, 345 (1979).

[40] C. Delmas, J.-J. Braconnier, C. Fouassier, and P. Hagenmuller, Solid State Ionics **3**, 165 (1981).

[41] J. Zhao, J. He, X. Ding, J. Zhou, S. Wu, R. Huang, et al., Journal of Power Sources **195**, 6854 (2010).

[42] J. Whitacre, A. Tevar, and S. Sharma, Electrochemistry Communications **12**, 463 (2010).

[43] S. P. Ong, V. L. Chevrier, G. Hautier, A. Jain, C. Moore, S. Kim, X. Ma, and G. Ceder, Energy & Environmental Science **4**, 3680 (2011).

[44] N. Yabuuchi, M. Kajiyama, J. Iwatate, H. Nishikawa, S. Hitomi, R. Okuyama, R. Usui, Y. Yamada, and S. Komaba, Nature Materials **11**, 512 (2012).

[45] R. Huggins, *Advanced batteries: materials science aspects* (Springer Science & Business Media, 2008).

[46] M. Winter and R. J. Brodd, Chemical Reviews **104**, 4245 (2004).

[47] D. Linden, New York, McGraw-Hill Book Co., 1984, 1075 p. No individual items are abstracted in this volume. **1** (1984).

[48] M. Winter, J. O. Besenhard, M. E. Spahr, and P. Novak, Advanced Materials **10**, 725 (1998).

[49] D. Aurbach, B. Markovsky, I. Weissman, E. Levi, and Y. Ein-Eli, Electrochimica Acta **45**, 67 (1999).

[50] S. Flandrois and B. Simon, Carbon **37**, 165 (1999).

[51] A. S. Arico, P. Bruce, B. Scrosati, J.-M. Tarascon, and W. Van Schalkwijk, Nature Materials **4**, 366 (2005).

[52] K. E. Aifantis, S. A. Hackney, and R. V. Kumar, *High energy density lithium batteries: materials, engineering, applications* (John Wiley & Sons, 2010).

[53] P. Verma, P. Maire, and P. Novák, Electrochimica Acta **55**, 6332 (2010).

[54] Y. Tang, Y. Zhang, W. Li, B. Ma, and X. Chen, Chemical Society Reviews **44**, 5926 (2015).

[55] G. V. S. R. M. V. Reddy and B. V. R. Chowdari, Chemical Reviews **113**, 5364 (2013).

[56] Y. Liu, N. O. Weiss, X. Duan, H.-C. Cheng, Y. Huang, and X. Duan, Nature Reviews Materials pp. 16042–16045 (2016).

[57] Y.-M. Lin, K. A. Jenkins, A. Valdes-Garcia, J. P. Small, D. B. Farmer, and P. Avouris, Nano Letters **9**, 422 (2008).

[58] F. Schwierz, Nature Nanotechnology **5**, 487 (2010).

[59] G.-J. A. Wetzelaer and P. W. Blom, NPG Asia Materials **6**, e110 (2014).

[60] Z. Guo, J. S. Manser, Y. Wan, P. V. Kamat, and L. Huang, Nature Communications **6** (2015).

[61] H.-S. Kim, C.-R. Lee, J.-H. Im, K.-B. Lee, T. Moehl, A. Marchioro, S.-J. Moon, R. Humphry-Baker, J.-H. Yum, J. E. Moser, et al., Scientific Reports **2**, 591 (2012).

[62] J. Burschka, N. Pellet, S.-J. Moon, R. Humphry-Baker, P. Gao, M. K. Nazeeruddin, and M. Grätzel, Nature **499**, 316 (2013).

[63] L. K. G. H. T. M. Brenner, D. A. Egger and D. Cahen, Nature Reviews Materials **1**, 15007 (2016).

[64] N. Karl, Synthetic Metals **133**, 649 (2003).

[65] N. Karl and J. Marktanner, Molecular Crystals and Liquid Crystals **355**, 149 (2001).

[66] M. Pope and C. E. Swenberg, *Electronic processes in organic crystals and polymers* (Oxford University Press on Demand, 1999).

[67] E. Sili? and V. Capek, *Organic molecular crystals: interaction, localization, and transport phenomena* (American Institute of Physics, 1994).

[68] H. Bouas-Laurent and H. Dürr, Pure and Applied Chemistry **73**, 639 (2001).

[69] X. Zhang, L. Hou, and P. Samorì, Nature Communications **7** (2016).

[70] H. Tian and S. Yang, Chemical Society Reviews **33**, 85 (2004).

[71] B. Lukyanov and M. Lukyanova, Chemistry of Heterocyclic Compounds **41**, 281 (2005).

[72] J. d. Oudar, The Journal of Chemical Physics **67**, 446 (1977).

[73] K. Vandewal, A. Gadisa, W. D. Oosterbaan, S. Bertho, F. Banishoeib, I. Van Severen, L. Lutsen, T. J. Cleij, D. Vanderzande, and J. V. Manca, Advanced Functional Materials **18**, 2064 (2008).

[74] M. Lenes, M. Morana, C. J. Brabec, and P. W. Blom, Advanced Functional Materials **19**, 1106 (2009).

[75] D. Gust, T. A. Moore, and A. L. Moore, Accounts of Chemical Research **34**, 40 (2001).

[76] R. M. Metzger, Chemical Reviews **103**, 3803 (2003).

[77] J. R. Heath and M. A. Ratner (2003).

[78] M.-M. Russew and S. Hecht, Advanced Materials **22**, 3348 (2010).

[79] T. Colborn, F. S. vom Saal, and A. M. Soto, Environmental Health Perspectives **101**, 378 (1993).

[80] E. Dodds and W. Lawson, Nature **137**, 996 (1936).

[81] Y. Takao, H. C. Lee, Y. Ishibashi, S. Kohra, N. Tominaga, and K. Arizono, Journal of Health Science **45** (1999).

[82] J. B. Matthews, K. Twomey, and T. R. Zacharewski, Chemical Research in Toxicology **14**, 149 (2001).

[83] S. Yoshihara, T. Mizutare, M. Makishima, N. Suzuki, N. Fujimoto, K. Igarashi, and S. Ohta, Toxicological Sciences **78**, 50 (2004).

[84] X. Mu, C. V. Rider, G. S. Hwang, H. Hoy, and G. A. LeBlanc, Environmental Toxicology and Chemistry **24**, 146 (2005).

[85] M. E. Baker and C. Chandsawangbhuwana, PloS one **7**, e46078 (2012).

[86] K. Pettersson and J.-Å. Gustafsson, Annual Review of Physiology **63**, 165 (2001).

[87] P. Hohenberg and W. Kohn, Physical Review **136**, B864 (1964).

[88] W. Kohn and L. J. Sham, Physical Reviews. **140**, A1133 (1965).

[89] D. Ceperley and B. Alder, Physical Review Letters **45**, 566 (1980).

[90] J. P. Perdew, K. Burke, and M. Ernzerhof, Physical Review Letters **77**, 3865 (1996).

[91] J. P. Perdew and Y. Wang, Physical Review B **45**, 13244 (1992).

[92] J. P. Perdew, J. Chevary, S. Vosko, K. A. Jackson, M. R. Pederson, D. Singh, and C. Fiolhais, Physical Review B **46**, 6671 (1992).

[93] A. D. Becke, Physical Review A **38**, 3098 (1988).

[94] F. A. Hamprecht, A. J. Cohen, D. J. Tozer, and N. C. Handy, Journal of Chemical Physics **109**, 6264 (1998).

[95] A. D. Boese, N. L. Doltsinis, N. C. Handy, and M. Sprik, Journal Chemical Physics **112**, 1670 (2000).

[96] A. D. Becke, Journal of Chemical Physics **98**, 5648 (1993).

[97] T. Yanai, D. P. Tew, and N. C. Handy, Chemical Physics Letters **393**, 51 (2004).

[98] J.-D. Chai and M. Head-Gordon, Physical Chemisrty Chemical Physics **10**, 6615 (2008).

[99] G. Bachelet, D. Hamann, and M. Schlüter, Physical Review B **26**, 4199 (1982).

[100] D. Vanderbilt, Physical Review B **41**, 7892 (1990).

[101] Wikipedia, *Pseudopotential — wikipedia, the free encyclopedia* (2015), [Online; accessed 9-August-2015], URL `https://en.wikipedia.org/w/index.php?title=Pseudopotential&oldid=650715630`.

[102] A. Dreuw and M. Head-Gordon, Chemical Reviews **105**, 4009 (2005).

[103] F. Jensen, *Introduction to computational chemistry* (John Wiley & Sons, 2013).

[104] D. Frenkel and B. Smit, *Understanding molecular simulation: from algorithms to applications*, vol. 1 (Academic press, 2001).

[105] M. P. Allen and D. J. Tildesley, *Computer simulation of liquids* (Oxford university press, 1989).

[106] D. Marx and J. Hutter, Modern methods and algorithms of quantum chemistry **1**, 141 (2000).

[107] G. H. Vineyard, Journal of Physics and Chemistry of Solids **3**, 121 (1957).

[108] G. Mills, W. Jacobsen, et al. (1998).

[109] K. Seeger, in *Semiconductor Physics* (Springer, 1991), pp. 156–216.

[110] C. M. Wolfe, N. Holonyak Jr, and G. E. Stillman, *Physical properties of semiconductors* (Prentice-Hall, Inc., 1988).

[111] J. H. Davies, *The physics of low-dimensional semiconductors: an introduction* (Cambridge university press, 1997).

[112] R. A. Marcus, Angewandte Chemie International Edition in English **32**, 1111 (1993).

[113] R. A. Marcus, Reviews of Modern Physics **65**, 599 (1993).

[114] T. Holstein, Annals of Physics **8**, 325 (1959).

[115] T. Holstein, Annals of Physics **8**, 343 (1959).

[116] J. R. Reimers, The Journal of Chemical Physics **115**, 9103 (2001).

[117] M. Frisch, G. Trucks, H. B. Schlegel, G. Scuseria, M. Robb, J. Cheeseman, G. Scalmani, V. Barone, B. Mennucci, G. Petersson, et al., Gaussian Inc., Wallingford (2009).

[118] M. Frisch, G. Trucks, H. Schlegel, G. Scuseria, M. Robb, J. Cheeseman, G. Scalmani, V. Barone, B. Mennucci, and G. Petersson, Inc., Wallingford, CT **2**, 4 (2009).

[119] M. Malagoli, V. Coropceanu, D. A. da Silva Filho, and J.-L. Brédas, The Journal of Chemical Physics **120**, 7490 (2004).

[120] J. M. Soler, E. Artacho, J. D. Gale, A. García, J. Junquera, P. Ordejón, and D. Sánchez-Portal, Journal of Physics: Condensed Matter **14**, 2745 (2002).

[121] J. Hutter, M. Iannuzzi, F. Schiffmann, and J. VandeVondele, WIREs Computatinal Molecular Sciences **4**, 15 (2014), URL `http://dx.doi.org/10.1002/wcms.1159`.

[122] P. Giannozzi, S. Baroni, N. Bonini, M. Calandra, R. Car, C. Cavazzoni, D. Ceresoli, G. L. Chiarotti, M. Cococcioni, I. Dabo, et al., Journal of Physics: Condensed Matter **21**, 395502 (2009).

[123] http://www.vasp.at/, URL `http://www.vasp.at/`.

[124] GRaphing, Advanced Computation and Exploration of data, http://plasma-gate.weizmann.ac.il/Grace/ (2015).

[125] T. Williams, C. Kelley, et al., Official gnuplot documentation, http://sourceforge. net/projects/gnuplot (2010).

[126] R. Dennington, T. Keith, and J. Millam, Semichem Inc.: Shawnee Mission, KS (2009).

[127] A. Kokalj, Journal of Molecular Graphics and Modelling **17**, 176 (1999).

[128] Jmol: an open-source Java viewer for chemical structures in 3D. http://www.jmol.org/ (2015).

[129] W. Humphrey, A. Dalke, and K. Schulten, Journal of Molecular Graphics **14**, 33 (1996).

2 Boron-sheet as Anode in Lithium-ion Battery*

2.1 Introduction

Among various recheargeable battery technologies, Lithium-ion batteries (LIBs) are one of the most advanced battery technology, because of their higher efficiency towards energy conversion and storage.[1,2] High power and energy densities, as well as longer cycle and shelf life of LIBs, are also appreciable.[3–5] However, scaling up LIBs for larger-scale applications such as electric vehicles has encountered numerous challenges relating to energy/power densities, cost and safety.[6,7] In general, LIBs have three components, graphitic material as the 'anode',[8–11] a transition metal oxide 'cathode'[5,12–16] and an electrolyte medium with an appropriate solvent.[17–20] The first commercial lithium ion batteries (LIBs), have been developed more than 20 years ago by Sony. Initial set-up uses layer-type compounds, such as, lithium cobalt oxide ($LiCoO_2$) as the cathode (positive electrode) and graphite (C) as the anode (negative electrode) material. A nonaqueous Li-ion conducting

*Work reported in this chapter is published in: Swastika Banerjee, Ganga Periyasamy, and Swapan K. Pati, J. Mater. Chem. A, **2**, 3856-3864(2014)

medium acts as the electrolyte. The principle of operation involves intercalation/deintercalation of Li ions to and from the electrodes, to store and deliver dc electrical energy during the charge and discharge process, respectively. The principle reaction is $LiCoO_2 + 6C \rightleftharpoons Li_{1-x}CoO_2 + Li_xC_6(0 < x \leq 1)$. Charge neutrality for $x \neq 0$ is maintained by the oxidation of Co^{3+} to Co^{4+} ion in the cathode. Similarly, the graphite lattice will be in reduced valency state. The LIBs are assembled in the discharged state. During charging by an external dc source, the electrical energy is converted to chemical energy in the form of charged products, $Li_{1-x}CoO_2$ and Li_xC_6, whereas during discharge, under a load, the reverse reaction occurs. Studies have shown that for $0 < x \leq 0.5$ in $Li_{1-x}CoO_2$ and for $0 < x \leq 1.0$ in Li_xC_6, the system is completely reversible for a large number of charge/discharge cycles.

To improve the efficiency of LIBs, the aforementioned constituents should be optimised. As the electrodes, 2D layered materials have advantages over bulk materials due to their higher exposure to the electrolyte, which leads to a higher charge/discharge rate and the ability to form a regular stacking arrangement.[10] Based on that, we have tried to find a more appropriate 2D-anodic material for LIBs. The performance of the graphitic anode material has a practical limitation of low capacity at higher operating current rates (e.g. a reversible capacity of 270 $mAhg^1$ becomes 100 $mAhg^1$ when operating at a higher current rate).[21] This might be rectified by using 2D nanosheets made up of electron deficient atoms, such that the atoms do not get the fulfilment of their octet at their common valence state (e.g. trivalent boron) compared to carbon atoms. Then the inclusion of electrons will be facilitated due to their electron deficiency, and their common valence state will permit to release the extra electrons. This property can be exploited for easy charging/discharging. Moreover, the highly conductive nature of single-walled boron nanotubes[22] (SWBNTs) and multi-walled boron nanotubes[23] (MWBNTs) has already been proved, using various experimental

and theoretical studies.[24,25] Note that BNTs are highly conducting, even more than carbon nanotubes (CNTs), irrespective of their lattice structures and chiralities.[26] Although BNT structures have been well characterized, until now, the microscopic details of the exact arrangement of boron atoms in the nanosheet has not been determined experimentally.[24] Few theoretical studies have been devoted to understanding the buckled and unbuckled crystalline structures of hexagonal ($\alpha-, \beta-, g_{1/8}$-, and $g_{2/15}$-sheets) and twin-hexagonal (η) sheets in the elementary and binary forms.[24,27–30]Among the many polymorphs, α, α_1 and η are predicted to energitically more stable.[30] However, their electrochemical performances have not yet been studied, which are important to determine their application in LIBs.

In this chapter, we focus on the efficiency of boron sheets (BSs) towards electrochemical performance based on energy density and power density, in order to bring it into play as an anode material in LIBs. In general, apart from the voltage dependence, at electrochemical equilibrium, energy density depends on the Li storage capacity, whereas the power density is related to the diffusion of Li over the sheet. Density Functional Theory (DFT) investigations on the electronic properties of three highly stable metallic BS-polymorphs (α, α_1 and η) have been performed to evaluate the above mentioned systems' electrochemical performances. Theoretical aspects on the lithium storage efficiency, reversible lithiation/delithiation and diffusion barrier have also been investigated. In addition, the finite temperature (300 K) sustainability of the material upon lithiation has been investigated using ab initio molecular dynamics (AIMD) simulations. The diffusion barrier for Li migration at finite temperature (300 K) and the dynamics of the diffused Li on the BSs have been compared with the results obtained without the inclusion of the thermal effect. The feasibility of lithium insertion, de-insertion, saturation as well as diffusion phenomena gives insights into the potential of BSs as an anode material in LIBs.

2.2 Computational Details

Electronic structures of all three polymorphic (α, α_1 and $\eta_{4/28}$) BSs were computed using density functional theory (DFT) methods. Three sheets were optimized with their respective supercell size, which are 2 x 2 with 32 atoms for α, 2 x 2 with 56 atoms for α_1, and 1 x 2 with 48 atoms for $\eta_{4/28}$ (see Figure 2.1). Calculations were performed by using the GPW formalism with the Perdew-Burke-Ernzerhof (PBE) functional[31] in the Quickstep module of the CP2K program package.[32–34] CP2K uses a mixed basis set in which the core electrons and nuclei are represented using the analytical dual-space pseudo-potential recommended by Goedecker, Teter and Hutter (GTH),[35,36,36,37] and the valence electrons are handled using the triple-zeta valence (TZV) basis set. In addition, as the non-covalent interactions are important for the present study, empirical van der Waals corrections, as prescribed by Grimme, were employed.[38]

Geometry optimizations have been carried out using the Broyden-Fletcher-Goldfarb-Shanno (BFGS) minimization algorithm,[39–43] with the convergence threshold of 1 x 10^{-4} Hartree for energy and 1 x 10^{-4} Hartree per Bohr for force and atomic displacements lower than 3 x 10^{-3} Bohr. A reasonable mesh cutoff of 480 Ry for the grid integration is utilised to represent the charge density. Furthermore, the DIMER method,[44,45] as implemented in CP2K, was used to optimize the transition state.[46,47] In addition to the CP2K calculations, we performed spin-polarized first principles computations to obtain all of the electronic band structures, density of states (DOS) as well as the projected density of states (pDOS) of the systems, using the double-z polarized (DZP) basis set for all of the atoms and a real space mesh cut-off of 400 Ry. The exchange-correlation is based on the Perdew-Burke-Ernzerhof functional[48] within the Generalized Gradient Approximation (GGA), as implemented in the SIESTA package.[49] The Brillouin zone was represented by the Monkhorst-Pack special k-point mesh for electronic struc-

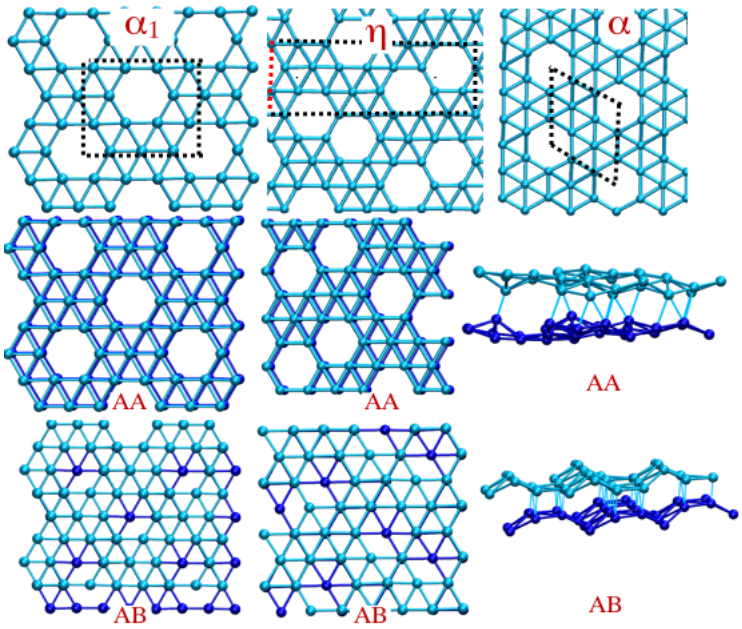

Figure 2.1: Optimized geometries of the monolayer, AA and AB bilayer configurations of α, α_1 and η BSs. The unit shells are represented by dotted lines. In order to differentiate the layers in bilayers, two different colour codings are used: cyan for the top layer and blue for the bottom layer. Note that $\alpha - AA$ and $\alpha - AB$ form covalent-like bonds between two layers.

ture computations. In order to compare the three sheets, all of the quantitative values regarding energetic stability were normalized with respect to the number of B atoms in the sheet. This method and models are validated by corroborating the structural parameters and electronic nature of the monolayer of BSs, α and α_1 bilayers with the reported results.[50,51] The inter-layer interaction energies (IL-IE) per atom are calculated as,

$$IL - IE = \frac{E_{bilayer-BS} - 2E_{monolayer-BS}}{n_B} \tag{2.1}$$

where $E_{bilayer-BS}$ and $E_{monolayer-BS}$ are the total energies of the bilayer and monolayer boron sheets. n_B is the total number of boron atoms in supercell geometries (see Figure 2.1). Note that the number of atoms in the bilayer supercell will be twice that of the monolayer. The electrochemical properties are studied by relax-

ing the geometries with N and $N \pm 1$ electrons, and their energies are considered for adiabatic ionization potential (AIP) and electronic affinity (AEA) computations. For an N-electron system with energy $E(N)$,
$AIP = E(N-1) - E(N)$ and $AEA = E(N) - E(N+1)$. The adsorption energies (AE) per atom (lithium) are calculated following the equation,

$$AE = \left(\frac{E_{Li_n@BS} - (E_{BS} + n_{Li} \times E_{Li})}{n_{Li}} \right) \tag{2.2}$$

where E_{BS}, E_{Li}, and $E_{Li_n@BS}$ are the total energy of bare boron sheets (BS), isolated lithium atoms, and lithium adsorbed boron sheets, and n_{Li} indicates the number of adsorbed Li atoms. In order to introduce thermal effects, *ab initio* molecular dynamic (AIMD) simulations have been carried out at 300 K and 1 atm pressure using CP2K, with the same level of theory as applied for the geometry optimisation. The temperature was maintained at 300 K using a Nose-Hoover thermostat. A time step of 1 femto-second was used to integrate the equations of motion. 5 ps trajectory was generated and used for analysis. This time scale is comparable with the reported time scale for the simulation of Li diffusion in electrolytes.[52]

2.3 Results and Discussions

2.3.1 Electronic Structure

We discuss first the electronic structure of various 2D-boron sheet (BS) polymorphs (α, α_1 and η) in monolayers and bilayers in the zero charge states in order to validate our methods. In this study, the three lowest energy conformers of BS, α, α_1 (elementary) and η (binary) sheets are considered, as shown in Figure 2.1. The computed B-B bond distances (see Table 2.1) of the α_1 sheet are comparable with the reported bond distance range of 1.66-1.70 $\mathring{A}$. Among the three sheets,

Table 2.1: Computed average B-B distances (d_{B-B}) and inter-layer distances (ID), in $\mathring{A}$, for various optimized geometries of the α_1, α_1-AA, α_1-AB, η, η-AA and η-AB configurations. The percentage expansions of the surface area, ΔS (%) with respect to the neutral state with N electrons, are given.

Sheet	N		N-1			N+1		
	d_{B-B}	ID	d_{B-B}	ID	ΔS	d_{B-B}	ID	ΔS
α	1.71	-	1.700	-	0.50	1.690	-	-0.38
$\alpha - AA$	1.70	3.66	1.695	3.62	0.26	1.695	3.62	-0.02
$\alpha - AB$	1.71	3.63	1.700	3.62	0.14	1.65-1.76	1.87-3.34	-0.27
η	1.73	-	1.71	-	0.42	1.68	-	-0.51
$\eta - AA$	1.65-1.73	2.95-3.40	1.66-1.74	2.95-3.35	0.17	1.65-1.76	3.32-3.42	-0.01
$\eta - AB$	1.66-1.79	3.30-3.42	1.66-1.75	3.28-3.48	0.07	1.66-1.76	3.31-3.48	-0.21

the α sheet is buckled, as reported in a previous study65 (see Figure 2.1). As a result, the B-B bond distances are uneven in the α polymorph and shortened by 0.06-0.10 $\mathring{A}$ compared to those in the α_1 sheet. Similarly, the presence of twin hexagons in η-sheet gives the hollow hexagonal ring unequal B-B bonds (1.67-1.76 $\mathring{A}$) in comparison with α_1, where the hollow hexagons show equalisation of the six B-B bonds (1.70 $\mathring{A}$) (see Table 2.1). Electronic band structure calculations show that all three sheets are metallic. Note that, as in a previous report,45 the α sheet exhibits a non-zero DOS at the Fermi level, while its lower energy sigma antibonding-like states in the valence band remain empty (see Figure 2.4 in a later section). The above mentioned results and their corroborations with previous studies validate the model and methods used in this chapter. [50,51,53]

Further, inter-layer interactions are accounted for with dispersion (Grimme D2)-corrected DFT methods. This has been validated by computing the bilayer electronic structure. In all cases (α, α_1 and η), the AB-stacked configuration gains higher stability. Comparatively, the AB stacking of α, α_1 and η are stabilized by 26.56, 0.85 and 8.96 meV per atom with shorter inter-layer distances by 0.010, 0.001 and 0.040 $\mathring{A}$ than the respective AA configurations (see Figure 2.1). From the distance variation and difference in energetics for the various stacking patterns, it is quite evident that α_1 BSs can almost be equally stabilized in both (AA

and AB) patterns, exhibiting a lower inter-layer interaction energy (IL-IE) than the other two morphologies (α and η, see Table 2.1). In both (AA and AB) stacking patterns, α has the highest inter-layer interaction energy, greater than that of the α_1 (for AA/AB; 154.15/155.00 meV per atom) and η configurations (for AA/AB; 148.00/156.96 meV per atom). This is due to the formation of inter-layer covalent-like bonds at $\alpha 1.90$ $\mathring{A}$ distances in bilayer-α sheets.[50] This indicates that the α morphology does not prefer to stay as 2D layered sheets, rather it prefers clustering. The above-mentioned details rule out the possibility of α sheets as an active electrode material for Li storage as well as the reversible lithiation/delithiation process. Between η and α_1, α_1-AA and α_1-AB possess a 10 meV per atom lower inter-layer interaction energy and longer inter-layer distance by 0.30 $\mathring{A}$ than those of η-AA and η-AB respectively. The lower inter-layer interaction energy and slightly increased inter-layer spacing in α_1 might facilitate its intercalation capacity for other adsorbents which is needed for LIBs. However, both α and α_1 sheets are considered for further studies in this chapter.

2.3.2 Electrochemical Properties

A requirement for electrode materials is the ability towards the acceptance/removal of an electron without too much perturbation from its original neutral ground state geometry. The single positive and negative charge state structures of α_1 and η are optimized, and computed electronic and structural parameters are compared with the respective neutral state geometries (see Table 2.1). From the computed adiabatic ionization potential (AIP) and electron affinity (AEA) values of the monolayer in Table 2.2, we find that α_1 and η monolayers have a higher tendency to accept an electron than towards the removal of an electron. In other words, both sheets have a higher work function with larger AIP values. Furthermore, the presence of an extra electron (N + 1 electrons, in Table 2.1) delocalized over the

Table 2.2: Computed adiabatic ionization potential (AIP), electron affinity (AEA) in meV per atom, lithiation (LE) and delithiation energy (DLE) per atom (eV per atom) for the α_1 and η monolayers, and AA and AB bilayer configurations.

		Monolayer					Bilayer			
Sheets	N_{atom}	AIP	AEA	LE	DLE		AIP	AEA	LE	DLE
α	56	79	34	-0.22	-0.79	AA	21	8	-2.01	0.59
						AB	14	10	-1.51	0.58
η	48	82	50	-0.44	-0.72	AA	19	20	-1.82	1.77
						AB	21	11	-1.76	1.03

sheet makes the Fermi energy value lower than its respective neutral sheet Fermi energy. The change in electron density (due to positive and negative charged states) does not affect the planarity of the monolayer α_1 and η sheets, while a small variation of the B-B distance is observed due to the redistribution of electrons in the plane (see Table 2.1). The computed hollow hexagon B-B distances slightly increase (0.005-0.010 $\mathring{A}$) upon the removal of an electron, whereas the decrease in B-B distances (0.010-0.030 $\mathring{A}$) is due to the addition of an extra electron for both sheets. Compared to α_1, the η sheet undergoes a slightly larger structural distortion during redox processes (see Table 2.1). Irrespective of the configuration (α_1, η), the bilayers show their reluctance to accept an electron, which is apparent from the lower AEA values than their respective monolayers (see Table 2.2). This is due to the fact that the inter-layer interaction favors the stacked geometry which prevents structural distortion as well as electronic redistribution due to the addition of an external electron. This is revealed from the lower electron affinity values in the case of the bilayers with respect to the monolayers (see Table 2.2) because AEA is a reflection of the energetic stability gained by the system upon charging with an extra electron, which has a strong dependence on the presence of layers in comparison with the monolayer. However, the removal of an electron leads to a volume change (e.g. 0.2% expansion for $\alpha_1 - AA^+$) to higher extent in comparison with the volume shrinkage of 0.02% for ($\alpha_1 - AA^-$) associated with the

addition of an electron (see ΔS in Table 2.1). This illustrates the higher structural integrity of α_1 sheets in the presence of additional negative charge. Now let us compare two morphologies of two polymorphs (α_1 and η) with different stacking patterns. For α_1, the AA stacking pattern exists in a planar geometry in all three charge states (+1, -1 and 0), with AIP and AEA values of 21 and 8 meV per atom respectively, while α_1-AB buckles after the addition of an electron due to the strong electrostatic interaction between the two layers. This rigorous structural change is reflected in the structural parameters (AB inter-layer distance: 1.87-3.34 $\mathring{A}$ in negative α_1-AB and 3.62 $\mathring{A}$ in neutral α_1-AB) as well as in the electronic band structure, where the Fermi level is shifted enormously. These results indicate that the AB stacking might not be appropriate as an anode material, although it is more stable (0.85 meV per atom) than AA stacking. Conversely, η sheets retain their planarity in both (AA and AB) stacked forms. However, η-AA sheets require a lower amount of energy (19 meV per atom) to release an electron in comparison with the stability gained due to the addition of an electron (20 meV per atom). This may not facilitate them to act as an anode material in the aspect of charging. Meanwhile, η-AB stacking possesses a smaller EA value and larger IP value, as in α_1-AA. These results clearly show that α_1-AA and η-AB could serve as anode materials. Hence, these sheets are studied for their Li adsorption and desorption capabilities (Figure 2.2).

2.3.3 Adsorption/Desorption of Lithium

The minimal structural distortion due to the lithiation/delithiation processes and also the reversibility within a reasonable energy window are the major criteria for good electrode materials. The effect of inter-layer interactions towards the lithiation/delithiation and Li diffusion is equally important for the reversible processes to happen in rechargeable LIBs.[54] In this chapter, the effect of inter-layer

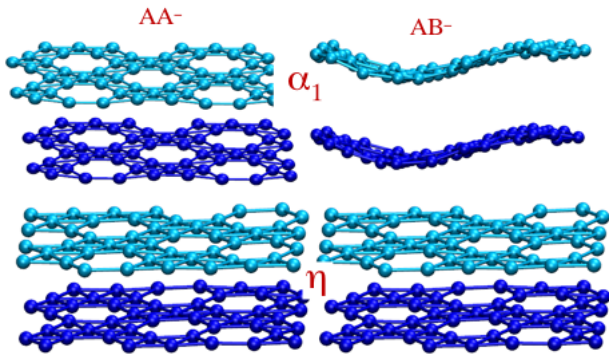

Figure 2.2: Optimized geometries of the negatively charged α_1-AA, α_1-AB, η-AA and η-AB bilayer configurations. The buckled nature of negatively charged α_1-AB is apparent from the figure.

interactions have been explored by considering monolayer and bilayer BSs for the adsorption/desorption and diffusion processes. The four possible adsorption sites (H, B, T_1, T_2) have been considered (see Figure 2.3).

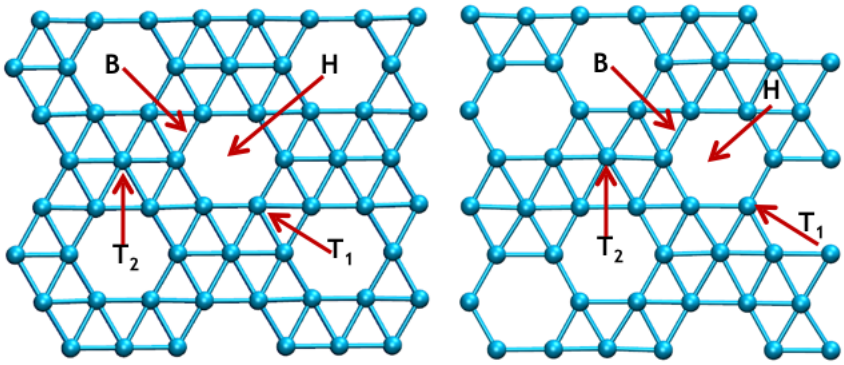

Figure 2.3: Various possible lithium adsorption sites (B, H, T_1 and T_2) for α_1 (left) and η (right) monolayers, indicated using red arrows.

The energetics for lithiation and the partial atomic charge of Li have been analyzed in these aspects. In the BSs, the electron density is lower at the 'H' site than at the B or T sites. In the H site, the ad-atom (Li) is stabilized at a 1.66 $\mathring{A}$ adsorbent-adsorbate distance and the 'H' site is energetically more preferable than the other respective sites (B or T). Further, this has become apparent from the maximum charge transfer from Li to the BS at the 'H' site, which is due to more electrostatic interactions (see Figure 2.3 and Table 2.3). Compared to

Table 2.3: Relative energies (eV) of various possible lithium adsorption sites in the α_1 and η monolayers with the partial Mulliken charge of the lithium atom (e).

Polymorph	Relative energies (eV)				Charge on Li (e)			
	H	T1	T2	B	H	T1	T2	B
α_1	0.00	1.33	1.44	2.24	0.54	0.48	0.44	0.32
η	0.00	1.06	1.54	1.73	0.51	0.51	0.45	0.37

the other sites, Li at the 'H' site does not induce noticeable distortions in B-B atom/bond hybridization/re-hybridization. Moreover, the 'H' site is favored due to having a larger ligation environment as adsorbed Li, present on the top of hexagonal ring, forms ionic-like bonding with six B atoms of the 'H' site rather than direct covalent-like bonding with one particular B atom. The computed adsorption energies (1.62-2.47 eV) and sheet-to-Li distances (1.50-1.76 $\mathring{A}$) are (see Table 2.4) in good agreement with previous reports on different polymorph BSs (1.62-1.89 eV adsorption energy, distances of 1.54-1.63 $\mathring{A}$).[55] Differences between

Table 2.4: Relative adsorption energy ($E_{max} - E$), distance of adsorbed Li on the surface (D_S) in $\mathring{A}$, partial positive charges on surface adsorbed Li (q_S) are given. Coverage is described in terms of the percentage coverage on 'H' sites for monolayer α_1. E_{max} is the highest adsorption energy per Li; E is the adsorption energy per Li for various extent of lithiation.

n_{Li}	**%Coverage**	$E_{max} - E$ **(eV)**	$D_S(\mathring{A})$	$q_S(e)$
1	12.5	0.20	1.66	0.53
2	25.0	0.00	1.69	0.52
3	37.5	0.03	1.73	0.50
4	50.0	0.04	1.66	0.47
5	62.5	0.04	1.49,1.62(4:1)	0.44
6	75 .0	0.07	1.60	0.43
7	87.5	0.11	1.76	0.42
8	100.0	0.18	1.69	0.37

the energy and distance parameters are due to changes in the morphologies of the polymorphs. η-binary BSs possess higher adsorption energy than α_1 by 0.65 eV. The ratio of adsorption energy to bulk cohesive energy ($\Delta E/E_c$) becomes

very high in α_1 (0.993 eV) and η (1.463 eV), while the bulk cohesive energy of Li is 1.63 eV. The above mentioned findings clearly suggest that Li atoms are able to form 2D layers on the BS surface, as proposed in graphene. However, the higher Li adsorption energy on η sheets raises the question of reversibility in the lithiation/delithiation process as well as the range of the open circuit voltage (OCV), which is addressed in a later section of this chapter.

The bonding features of adsorbed Li and the BSs have been further elucidated by electronic band structure calculations which show that, for 100% occupancy of 'H' sites, the Fermi energy (E_F) lies 0.82 and 1 eV above E_F for pure α_1 (3.96 eV) and η (4.01 eV) sheets respectively, because of the electron transfer from Li to the BS. The degeneracy of the Li spin-up and spin-down 2s states and the splitting and partial occupancy of the Li 2s state is shown in Figure 2.4. Hence, the concept of charge transfer and partial occupancy of the Li 2s orbital helps us to prove the bonding nature to be predominantly ionic. Furthermore, detailed analysis of the density of states (DOS) of α_1 and η sheets in the lithiated and delithiated forms reveals a sharp distinction in the electronic nature of the two BSs (α_1 and η). Lithiation reduces the DOS near the Fermi level for lithiated α_1-BS due to an interaction between the $2p_z$ orbital of B in the BS and a Li-2s orbital. However, in η sheets, the lithium adsorption reorganises the DOS, mostly at the valence states in lithiated BSs, which is apparent from the DOS and pDOS plots (see Figure 2.4).

In pure η sheets, the in-plane antibonding-like orbital possess zero DOS while the p_z orbital of B has non-zero DOS. In fact, upon lithiation, both exhibit non-zero values and Li 2s interacts with the in-plane (2s, $2p_x$, $2p_y$ of B) atomic orbitals, which is the reason for the larger binding energy of Li with the η sheets. Moreover, the charge transfer between Li and BSs and their ionic nature has been verified by computing partial charges using Mulliken population analyses, which are given in Table 2.3. The ionic nature of the adsorbed Li atoms on the BSs is apparent from the +0.5 e partial charge on Li for 12.5% coverage of the total 'H' sites (see

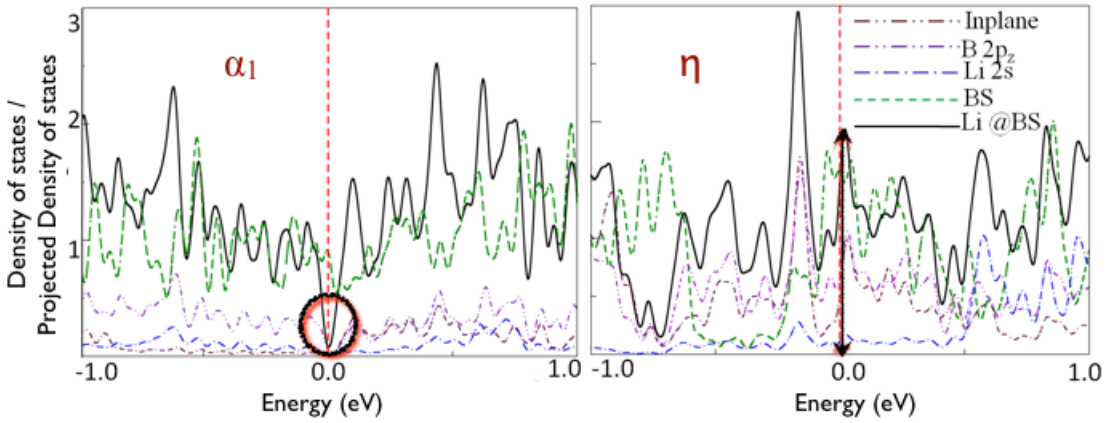

Figure 2.4: Computed density of states and projected density of states of lithiated and delithiated (a) α_1 and (b) η monolayers. All E_F values are rescaled to zero.

Table 2.4 and 2.5) . This value is in quantitative agreement with the extent of elec-

Table 2.5: Relative adsorption energy ($E_{max} - E$), inter-layer distance (ID), average distance of Li intercalated between sheets (D_I), distance of adsorbed Li on the surface (D_S) in bilayer-α_1, and Mulliken charge on intercalated Li (q_I) and on surface adsorbed Li (q_S) are given. The coverage is described in terms of the percentage coverage on 'H' sites

n_{Li}	%Coverage	$E_{max} - E$ (eV)	$ID(Å)$	$D_l(Å)$	$q_I(e)$	$D_S(Å)$	$q_S(e)$
1	12.5	0.142	3.62	1.81	0.49	1.70	0.61
2	25	0.068	3.51	1.75	0.45	1.69	0.59
3	37.5	0.000	3.42	1.71	0.42	1.65	0.57
4	50	0.015	3.28	1.64	0.39	1.65	0.54
5	62.5	0.009	3.32	1.66	0.38	1.63	0.47
6	75	0.051	3.32	1.66	0.38	1.60	0.47
7	87.5	0.058	3.33	1.67	0.37	1.59	0.45
8	100	0.041	3.34	1.67	0.36	1.43	0.43

tron transfer from Li to graphene. Moreover, the participation of the 2p orbitals of the B atoms (as revealed in pDOS analysis for lithiated sheets in Figure 2.4) leads to a subtle interplay between London dispersion and Coulomb interactions, which regulates the lithiation/delithiation energy. We first shed some light on the relation between the electrostatic and dispersion interactions in this model study. The dispersion energy per lithium adsorption becomes more negative than that of the first lithium (at the lowest concentration). These values vary as a function of

the extent of lithiation. Fluctuation occurs between -0.48 and -0.50 eV/Li, which can also be correlated to the OCV.

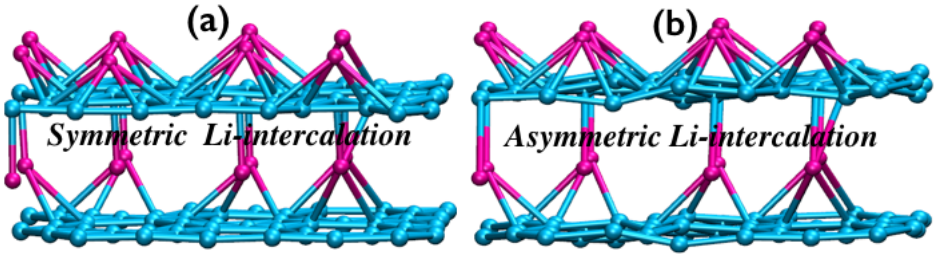

Figure 2.5: Optimized lithium saturated bilayer for (a) α_1-AA and (b) η-AB. Note that in η-AB the rippled nature and asymmetric Li adsorption between the layers is apparent.

In bilayers, Li can stay on top of the 'H' site at the surface or inbetween the stacked layers. Further, two types of intercalation are possible depending upon the bilayer configurations (AA or AB). In the AA configuration, Li is stacked in between the hollow hexagons, while in the AB configuration, it is stacked between one hollow site and one T site. Irrespective of the bilayer configurations, adsorption at the surface follows the same trend and almost the same amount of energy as the monolayer. The lithium intercalation between layers significantly changes the adsorption energy, compared to surface adsorption. In α_1-AA, Li is intercalated at the centre of both BS layers with an equal contribution from both layers, and possesses a larger interaction energy by 0.70 eV than by surface adsorption. However, in the η-AB configuration, Li becomes intercalated at a closer distance to the hollow hexagons (1.63 $\mathring{A}$), and remains far (2.16 $\mathring{A}$) from the layer where Li faces less favored T/B sites. This causes asymmetrical Li intercalation and more structural perturbation upon lithiation(see Figure 2.5), suggesting that η-AB sheets might not be appropriate for reversible Li adsorption and desorption processes in LIBs. Hence, we studied the diffusion barrier and storage capacity of bilayer α_1-AA BS polymorphs.

2.3.4 Function of Background Electron in Lithium Adsorption and Desorption

Li adsorption/desorption calculations were performed with BSs as the anode and $LiBH_4$ ($Li^+BH_4^-$) as an electrolyte. The electrochemical lithiation/delithiation process occurs in the presence of background charge, depending upon the voltage applied to the electrode. In order to model this, we considered the processes as follows: (a) Li is adsorbed on negatively charged BSs, with an additional background electron to mimic a uniform potential, and (b) it is desorbed during the discharging process, where sheets exist in the neutral charge state. The details are given in the following equations, and the respective lithiation/delithiation energies (LE/DLE) are calculated as follows.

$$[Li@BS]^+ + BH_4^- = BS + LiBH_4; DLE = (E_{BS} + E_{LiBH_4}) - (E_{[Li@BS]^+} + E_{BH_4^-}) \tag{2.3}$$

$$BS^- + LiBH_4 = [Li@BS] + BH_4^-; LE = (E_{Li@BS} + E_{BH_4^-}) - (E^-_{BS} + E_{LiBH_4}) \tag{2.4}$$

The calculated LE and DLE values are shown in Table 2.2, which indicate that in the monolayer, adsorption as well as desorption would be spontaneous for both α_1 and η BSs under thermodynamically favorable conditions. The presence of inter-layer interactions increases the LE and DLE, in comparison to the monolayer. This indicates that the lithiation at the inter-layer spacing is spontaneous, however the delithiation process requires more energy. Experimentally, this means a larger open circuit voltage (OCV) is required to remove the Li from the intercalated layer. Hence, we have computed the diffusion barrier to understand the energy requirement for Li diffusion in two charged states: neutral (N electron) and charged (N+1/N-1 electron).

2.3.5 Lithium Diffusion Barrier

Li diffusion determines the rate of the reversible lithiation/delithiation process, which was studied by following various charge state models of the α_1 monolayer and the α_1-AA bilayer. Moreover, various diffusion pathways between high-symmetry favored sites ('H') were considered in order to understand the diffusion mechanism. The diffusion paths between the highly favored 'H' sites are only considered (see Figure 2.6), because the energy differences (Table 2.3) between the less and most favored sites are significantly high. Various possible diffusion paths parallel to the

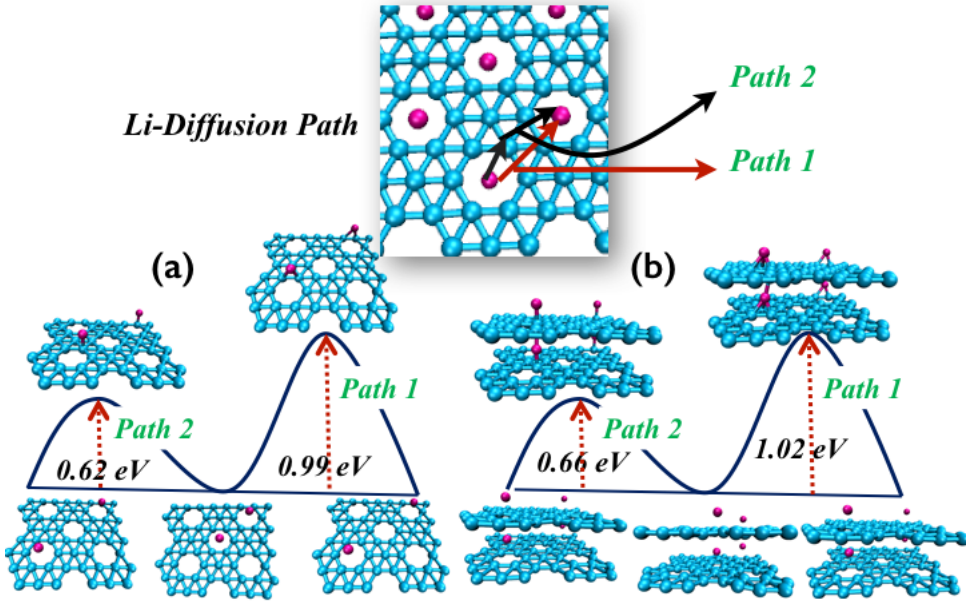

Figure 2.6: Diffusion barrier during the lithiation/delithiation process for (a) monolayer α_1 and (b) bilayer α_1-AA. The respective diffusion barriers are given in eV. In (b), the average diffusion barrier for the surface and intercalated lithium are given.

BS plane (including path 1: via B-B bonds, path 2: via the top of the B atom) are considered. Among these, path 2 possesses a lower energy barrier, 0.62 eV, as shown in Figure 2.6. By increasing the lithium concentration, the diffusion barrier gradually decreases, for 12%: 0.62 eV, 25%: 0.61 eV, 37.5%: 0.59 eV and 50%: 0.59 eV. This indicates that lithium diffusion at lower concentrations entails more energy than the higher extent of lithiation.

The inter-layer diffusion effects are studied by considering the α_1-AA bilayer configuration. Our computations show that intercalated Li diffusion occurs with higher energy than the surface adsorbed Li. Similar to the monolayer, the increase in concentration decreases the diffusion barrier. Further, we studied the diffusion barrier by first considering intercalated lithium and then on the surface, where 0.66 eV per lithium ion is obtained as the average diffusion barrier.

2.3.6 Adsorption and Diffusion of Lithium at 300 K Through *ab initio* Molecular Dynamic Simulation

The diffusion barrier can easily be influenced by thermal effects, hence AIMD studies were carried out. At first, the most favored Li adsorption 'H'-site was confirmed by generating a trajectory starting from various initial higher energy adsorption sites (B, T_1 and T_2). Irrespective of the initial configurations, Li reached the highly favored 'H'-site within 1.0 ps (Figure 2.7).

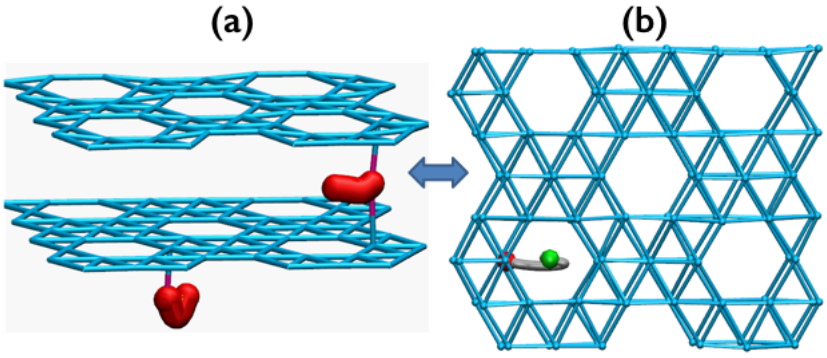

Figure 2.7: Trajectories during the diffusion of intercalated as well as surface-adsorbed Li in the α_1-AA bilayer from higher energy 'T' sites to 'H' sites. The red ('T') and green ('H') in (b) indicate the respective start and end points; (a) shows the side view of the trajectory and (b) represents the top view of the trajectory.

The difference in the adsorption energies for the 'H' and 'T' sites are still huge (0.76 eV) at T = 300 K, as observed in 0 K, hence the diffusion barriers have been studied for the migration of Li between the 'H'-sites at T = 300 K. Moreover,

it has already been shown from our DFT studies that lithium diffusion at lower Li concentrations is an energetically expensive process. Hence, 12.5% coverage of the 'H' site due to lithiation is considered at 300 K. This shows that Li diffusion on monolayer and bilayer α_1 features 0.35 eV and 0.39 eV energy barriers at 300 K, which are respectively smaller than the barriers at 0 K. The above mentioned results show that α_1 sheets can act as an anode material with a reasonable diffusion barrier for Li migration. Further, it is in a similar working energy range of the Li diffusion barrier as found in case of standard graphene-electrode. Note that the diffusion barrier could be tuned further in the presence of electrolyte and solvent environments.

2.3.7 Lithium Saturation

As mentioned above, lithiation occurs at the 'H' site in the thermodynamically most favoured way. In an electrode reaction, the voltage is influenced by the sequential adsorption/desorption of lithium from the electrode until it reaches the saturation point. Lithium saturation depends upon the surface area of the electrode. The α_1 sheet, considered in this study with a 1.63 nm^2 surface area, possesses eight 'H'-sites. The adsorption energies and distances of the adsorbed Li from the sheet are computed by varying the adsorbed lithium concentration (see Table 2.4 and 2.5). The computed negative AE values show that systems can easily uptake 8 lithium atoms in a thermodynamically favorable process. Further, there are insignificant structural changes as observed during the lithiation process, which is apparent from the average structural perturbation of $\sim$ 9% volume expansion at a 50% coverage of H sites in α_1-AA. A further increase in the concentration of lithium ($>$ 8 Li atoms) causes rippling in the planar geometry, while the lithiation occurs at other less favourable sites such as B, T_1 and T_2 (see Figure 2.3). Electronic redistribution upon lithiation at 'H' sites is shown in Figure 2.8. Lithium

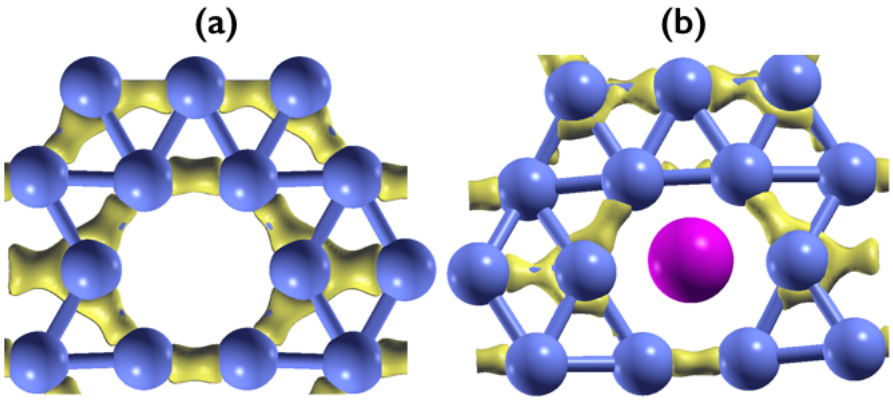

Figure 2.8: Electron density (isocontour = 0.06 e $\mathring{A}^{-3}$) distribution for bare negatively charged α_1-BS (a) and lithiated α_1-BS (b) unit cells.

adsorption on the 'H' sites redistributes electron density, which causes partial delocalization in comparison to extended delocalization (Figure 2.8), which is present in the pristine sheet. In fact, Figure 2.8 clearly reveals the absence of strong covalent Li-B bond while lithiation occurs at most favourable 'H' sites, which is also corroborative with the DOS plot shown in Figure 2.4. Further details of structural and electronic features ensure that the reversible lithiation/delithiation process involves only 'H' sites, where the structural integrity is retained throughout. Finally, the effect of the inter-layer interaction on the saturation is studied by increasing the number of layers up to four. As the number of layers increases, the distance between neighbouring layers remain almost the same. Accordingly, by increasing the number of layers, BSs are capable of forming stable three dimensional layered structures from 2D sheets as the precursor. First, lithium adsorption induces further lithiation and as a result, at higher Li concentration, BS becomes stabilised (see Figure 2.9). Moreover, upon lithiation on the 'H' sites, no drastic change occurs to the electronic nature of the BS matrix, and as a result it still exists as a metallic sheet. For the saturation lithium-adsorbed BS, the theoretical capacity

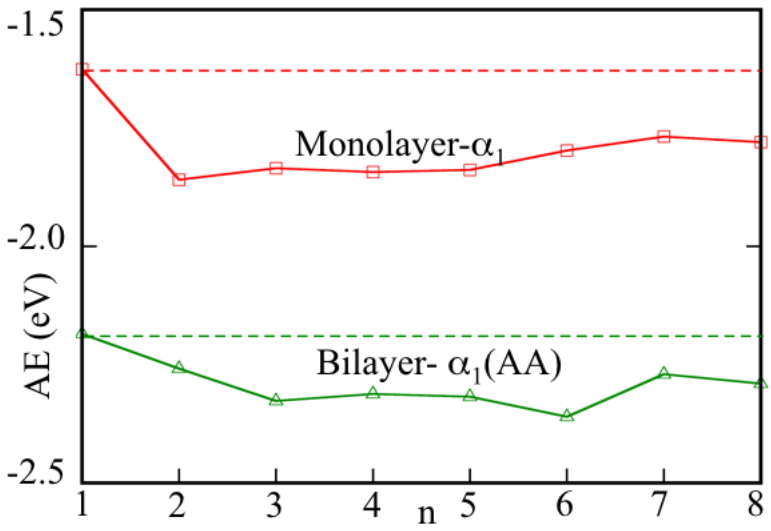

Figure 2.9: Adsorption energy (AE) plotted with respect to the number of Li atoms (n) for the lithium-adsorbed monolayer (α_1) and bilayer (α_1-AA) geometries.

is calculated using the equation:

$$Capacity = \left(\frac{n \times F}{3600 \times M}\right) \tag{2.5}$$

where, n is the number of electrons involved in the electrochemical process, F = 96500 mA h and M is the mass of the BSs in kg. The capacity value is calculated as 383 $mAhg^{-1}$ for α_1, which is larger than the conventional graphitic electrode capacity of $mAhg^{-1}$ and falls in the gravimetric capacity range for an acceptable new battery electrode material. Compactness in the lithiated multilayer shows more stability of the adsorbed Li in comparison with isolated monolayer adsorption.

2.4 Conclusions

ab initio DFT and MD based computational investigation on α, α_1 and $\eta_{4/28}$ Boron sheet (mono and bilayers) reveals the retention of their metallic nature in various state of charge while modelled as anode in Li-ion battery. Among the three sheets,

bilayer-α_1 and $\eta_{4/28}$ form perfect stacking and maintain the planarity of individual layers. In contrast, bilayer α forms a cluster-like arrangement. Extensive studies on various charge-state indicate that α_1, α_1-AA, $\eta_{4/28}$ and $\eta_{4/28}$-AB polymorphs have appropriate AIP and AEA values, making them suitable as electrode for easy charge/discharge. The computed inter-layer interaction energies and lithium adsorption studies show the reversible lithium adsorption capability of α_1 and α_1-AA sheets. Highly symmetric 'H' site on the α_1 and α_1-AA sheets is an energetically favourable site at both 0 and 298 K. The first lithium addition is the key process, which facilitates further lithiation to the system. In the bilayer, intercalated lithium becomes more stable by equnal interactions with two layers compared with the surface-adsorbed lithium. Li diffusion barrier studies on the α_1 sheets at lower concentration demonstrates that the migration occurs from one 'H' site to another via the top of a boron atom with 0.66 and 0.39 eV energy barriers at 0 and 298 K respectively. In the bilayer, the intercalated and surface adsorbed Li follows the same diffusion pathway, while the former has a larger diffusion barrier (0.71 eV) than the latter (0.45 eV). In addition, the effects of lithium concentration on the diffusion barrier are studied by increasing the adsorbed Li concentration up to 50% coverage ('H' sites). Increase in Li-concentration leads to the decrement of the diffusion barrier initially, and gradually reaches a saturation point to 0.59 eV at 0 K. The 1.63 nm^2 surface area of the α_1 sheet requires eight lithium atoms to be saturated by maintaining its structural integrity. We also demonstrate that 'H' sites are only appropriate for lithiation, while lithiation at other sites collapses the structural integrity. Consequently, the calculated value of the theoretical capacity is limited to 383 $mAhg^{-1}$ at the saturation point, which is higher than that of the conventional graphitic electrode. Structural stability of the anode host at the lithium saturation point has been further confirmed by increasing the number of layers to four. All of these studies corroborate with the appropriateness of α_1-AA as anode in LIBs.

References

[1] A. . K. Padhi, K. Nanjundaswamy, and J. Goodenough, Journal of the Electrochemical Society **144**, 1188 (1997).

[2] B. Scrosati, Electrochimica Acta **45**, 2461 (2000).

[3] Y.-H. Huang and J. B. Goodenough, Chemistry of Materials **20**, 7237 (2008).

[4] L.-X. Yuan, Z.-H. Wang, W.-X. Zhang, X.-L. Hu, J.-T. Chen, Y.-H. Huang, and J. B. Goodenough, Energy & Environmental Science **4**, 269 (2011).

[5] C. Sun, S. Rajasekhara, J. B. Goodenough, and F. Zhou, Journal of the American Chemical Society **133**, 2132 (2011).

[6] J. R. Owen, Chemical Society Reviews **26**, 259 (1997).

[7] L. Ji, Z. Lin, M. Alcoutlabi, and X. Zhang, Energy & Environmental Science **4**, 2682 (2011).

[8] M. Winter, J. O. Besenhard, M. E. Spahr, and P. Novak, Advanced Materials **10**, 725 (1998).

[9] M. Wakihara, Materials Science and Engineering: R: Reports **33**, 109 (2001).

[10] J. B. Goodenough and Y. Kim, Chemistry of Materials **22**, 587 (2009).

[11] K. Tang, X. Mu, P. A. van Aken, Y. Yu, and J. Maier, Advanced Energy Materials **3**, 49 (2013).

[12] K. Mizushima, P. Jones, P. Wiseman, and J. Goodenough, Materials Research Bulletin **15**, 783 (1980).

[13] S.-Y. Chung, J. T. Bloking, and Y.-M. Chiang, Nature Materials **1**, 123 (2002).

[14] A. S. Arico, P. Bruce, B. Scrosati, J.-M. Tarascon, and W. Van Schalkwijk, Nature Materials **4**, 366 (2005).

[15] N. Bernstein, M. Johannes, and K. Hoang, Physical Review Letters **109**, 205702 (2012).

[16] Y. Kiya, J. C. Henderson, G. R. Hutchison, and H. D. Abruña, Journal of Materials Chemistry **17**, 4366 (2007).

[17] P. G. Bruce, B. Scrosati, and J.-M. Tarascon, Angewandte Chemie International Edition **47**, 2930 (2008).

[18] J.-M. Tarascon and M. Armand, Nature **414**, 359 (2001).

[19] B. Scrosati and J. Garche, Journal of Power Sources **195**, 2419 (2010).

[20] J. Li, C. Daniel, and D. Wood, Journal of Power Sources **196**, 2452 (2011).

[21] W. Li, J. R. Dahn, D. S. Wainwright, et al., Science-AAAS-Weekly Paper Edition-including Guide to Scientific Information **264**, 1115 (1994).

[22] D. Ciuparu, R. F. Klie, Y. Zhu, and L. Pfefferle, The Journal of Physical Chemistry B **108**, 3967 (2004).

[23] F. Liu, C. Shen, Z. Su, X. Ding, S. Deng, J. Chen, N. Xu, and H. Gao, Journal of Materials Chemistry **20**, 2197 (2010).

[24] H. Tang and S. Ismail-Beigi, Physical Review Letters **99**, 115501 (2007).

[25] V. Bezugly, J. Kunstmann, B. Grundkotter-Stock, T. Frauenheim, T. Niehaus, and G. Cuniberti, ACS nano **5**, 4997 (2011).

[26] V. Bezugly, J. Kunstmann, B. Grundkotter-Stock, T. Frauenheim, T. Niehaus, and G. Cuniberti, ACS Nano **5**, 4997 (2011).

[27] J. Miller, Physics Today **60**, 20 (2007).

[28] H. Tang and S. Ismail-Beigi, Physical Review B **82**, 115412 (2010).

[29] C. Ozdogan, S. Mukhopadhyay, W. Hayami, Z. Guvenc, R. Pandey, and I. Boustani, The Journal of Physical Chemistry C **114**, 4362 (2010).

[30] X. Yang, Y. Ding, and J. Ni, Physical Review B **77**, 041402 (2008).

[31] J. P. Perdew, K. Burke, and M. Ernzerhof, Physical Review Letters **77**, 3865 (1996).

[32] J. VandeVondele, M. Krack, F. Mohamed, M. Parrinello, T. Chassaing, and J. Hutter, Computer Physics Communications **167**, 103 (2005).

[33] G. Santarossa, M. Iannuzzi, A. Vargas, and A. Baiker, Chemical Physics and Physical Chemistry **9**, 401 (2008).

[34] A. Vargas, G. Santarossa, M. Iannuzzi, and A. Baiker, The Journal of Physical Chemistry C **112**, 10200 (2008).

[35] C. Hartwigsen, S. Gœdecker, and J. Hutter, Physical Review B **58**, 3641 (1998).

[36] S. Goedecker, M. Teter, and J. Hutter, Physical Review B **54**, 1703 (1996).

[37] M. Krack, Theoretical Chemistry Accounts **114**, 145 (2005).

[38] S. Grimme, Journal of Computational Chemistry **27**, 1787 (2006).

[39] C. Broyden, Mathematics of Computation **24**, 365 (1970).

[40] J. Nocedal, Mathematics of Computation **35**, 773 (1980).

[41] D. C. Liu and J. Nocedal, SIAM Journal on Scientific and Statistical Computing **10**, 1 (1989).

[42] D. F. Shanno and P. C. Kettler, Mathematics of Computation **24**, 657 (1970).

[43] D. Goldfarb, Mathematics of Computation **24**, 23 (1970).

[44] A. Heyden, A. T. Bell, and F. J. Keil, The Journal of Chemical Physics **123**, 224101 (2005).

[45] J. Kästner and P. Sherwood, The Journal of Chemical Physics **128**, 014106 (2008).

[46] J. VandeVondele and J. Hutter, The Journal of Chemical Physics **118**, 4365 (2003).

[47] I.-F. W. Kuo, C. J. Mundy, M. J. McGrath, J. I. Siepmann, J. VandeVondele, M. Sprik, J. Hutter, B. Chen, M. L. Klein, F. Mohamed, et al., The Journal of Physical Chemistry B **108**, 12990 (2004).

[48] S. Kurth, J. P. Perdew, and P. Blaha, International Journal of Quantum Chemistry **75**, 889 (1999).

[49] J. M. Soler, E. Artacho, J. D. Gale, A. García, J. Junquera, P. Ordejón, and D. Sánchez-Portal, Journal of Physics: Condensed Matter **14**, 2745 (2002).

[50] X. Wu, J. Dai, Y. Zhao, Z. Zhuo, J. Yang, and X. C. Zeng, ACS Nano **6**, 7443 (2012).

[51] X. Wu, J. Dai, Y. Zhao, Z. Zhuo, J. Yang, and X. C. Zeng, ACS Nano **7**, 880 (2013).

[52] P. Ganesh, P. Kent, and D.-e. Jiang, The Journal of Physical Chemistry C **116**, 24476 (2012).

[53] H. Lu, Y. Mu, and S.-D. Li, ACS Nano **7**, 879 (2013).

[54] F. Yao, F. Gunes, H. Q. Ta, S. M. Lee, S. J. Chae, K. Y. Sheem, C. S. Cojocaru, S. S. Xie, and Y. H. Lee, Journal of the American Chemical Society **134**, 8646 (2012).

[55] Y. S. Wang, F. Wang, M. Li, B. Xu, Q. Sun, and Y. Jia, Applied Surface Science **258**, 8874 (2012).

3

Borocarbonitride as Anode in Sodium-ion Battery/Capacitor*

3.1 Introduction

Smooth integration of renewable energy resources into the grid, thus improving the grid reliability and utilization, demands large-scale energy storage systems with long-life, high efficiency, high safety and most importantly low cost.[1,2] As discussed in chapter 1, electrochemical approach represents one of the most promising means to store electricity in large-scale due to the flexibility, high energy conversion efficiency and simplicity of the device-designing.[2–4] Lithium-ion batteries (LIB) exhibit the highest energy density among all practical rechargeable batteries and play an essential role as an efficient power source for portable electronics.[5–7] In the near future, large-scale batteries would be more popular for electric vehicles.[8] Two major issues associated with large-scale lithium-ion based electronic devices are the limited resources of Li-metal and the safety-issues due to its high reactivity. On the other hand, sodium belongs to the same group as lithium and is relatively

*Work reported in this chapter is published in: Swastika Banerjee, Siam Khanthang Neihsial, and Swapan K. Pati, J. Mater. Chem. A, **4**, 15, 5517-5527 (2016)

abundant, which in combination with the standard redox potential, $E_{red}^{Na^+/Na}$ = -2.71 eV (close to $E_{red}^{Li^+/Li}$ = -3.04 eV; $E_{red}^{Mg^{2+}/Mg}$ = -2.37 eV) appears to be the most advantageous for battery applications after lithium.[9] The lower adsorption potential and weaker solvation of Na-ions are beneficial for higher voltage and power efficiency, in sodium-ion batteries (SIB). However, only a limited number of practical applications are found for SIB due to lack of layered materials[10–12] as an electrode to form SIB set-up. Sodium, being 55% larger than lithium, intercalates into graphite with huge structural exfoliation.[13,14] Over the last years, anodic performance has been improved through non-graphitised structures, which act as a buffer for the volume change during ion insertion/extraction.[15,16] However, the initial capacities for disordered carbon electrodes achieved up to 300 $mAhg^{-1}$ only and were associated with a major drawback of poor cyclability.[17,18] Recently, nano-structuring, e.g., hollow carbon nano-spheres[19] and carbon nano-fibres,[20] have been found to be effective due to the shortening of the transport length of active ions.[21] Based on these findings, we focus on low dimensional (two-dimensional (2D) or quasi 2D) materials rather than their perfectly stacked bulk counterparts. In contrast to pure carbon, we are interested in borocarbonitride ($B_xC_yN_z$) sheets as an anode because (1) boron- or nitrogen-substituted graphene sheets exhibit high lithium ion adsorption energies[22,23] as the B-substitution produces a low-lying LUMO, which leads to stronger binding of Li and easier transfer of electrons from Li to the sheet,[24] (2) N-substitution facilitates electron transport through the sheet[23] and (3) maximisation of the C-C and B-N bonds leads to an energetically favoured ternary system ($B_xC_yN_z$) with domain segregation into the C-rich and BN-rich domains.[25] These nano-sheets exhibit typical ambipolar semiconducting behavior[26] and also appear to be promising for electro-catalysis[27] and easy charge/discharge of a battery electrode with high capacity retention capability[28] ($\sim 100mAhg^{-1}$ at rate as high as $2Ag^{-1}$ for 5000 cycles). However, we lack

the microscopic understanding of the shape-effect of B_xN_z domains (see Figure 3.1) on the electrochemical performance. In fact, controlling the geometric configura-

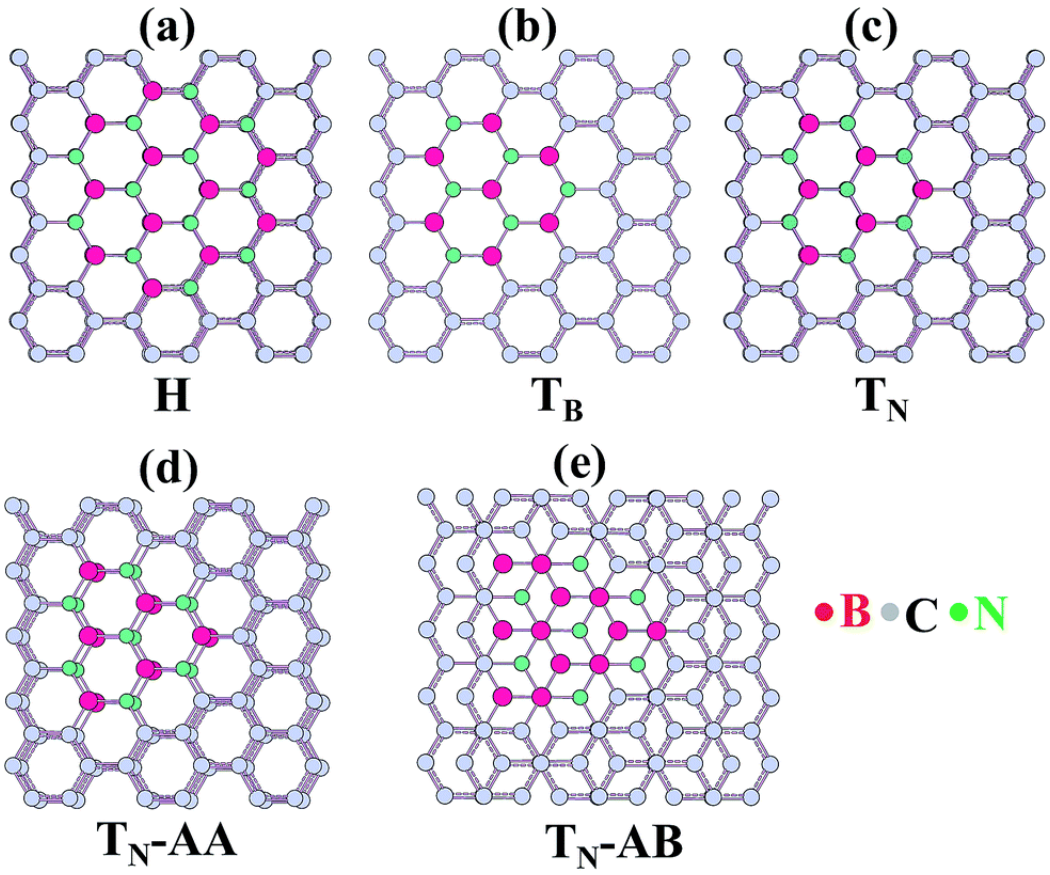

Figure 3.1: Different shapes of BN nanodomains embedded on a carbon matrix: (a) $H - B_xN_x$, (b) $T_B - B_xN_z$ and (c) $T_N - B_xN_z$. H, T_B and T_N are $B_xC_yN_z$ with $x : y : z = 1 : 3 : 1, 7 : 47 : 6$ and $6 : 47 : 7$, respectively. The colour notation is the following, B: pink; C: grey; N: green. (d), (e) show two different stacking patterns in the case of a bilayer.

tion of nanoscopic system has been found to be a promising approach for improved performance, which can lead to stable interfaces between the electrolyte, electrode and active ions.[29] Likewise, the shape of the edge structure of the B_xN_z domains could be a potential scheme used to control the carrier-type, concentration of the charge-carriers and conduction of ions as well as carriers. However, the microscopic understanding of the electrochemical properties of borocarbonitride as an anode is yet to be fully understood. From recent experimental advances, it has been ob-

served that BN domains preferably adopt a triangular shape to minimize the total interface length with a minimum number of B-C and N-C bonds.[30,31] Coarsening of these small domains leads to further hexagonal-BN domains.[31] Accordingly, $B_xC_yN_z$-nano-hybrids with trigonal (T) and hexagonal (H) BN-domains are the thermodynamically stable surface structures.[32,33] Hence, we consider the smallest possible BN domains (T and H) with the minimum number of B-C and N-C bonds to minimise the interfacial energy cost (Figure 3.1). The concentration of the BN-domain is also an important factor to determine the electrochemical properties of a borocarbonitride nano-hybrid. BN-domain polarise the carbon matrix and leads to modification in two aspects: (i) the open circuit voltage and (ii) the ease of charging/discharging. We focus on the C-rich borocarbonitride, as it is found to be superior for electrochemical performance, according to recent experimental studies.[27,34] Despite the abundance of literature on the advances in the chemistry used to produce borocarbonitrides and their applications, there are many unanswered queries: (1) Is borocarbonitride suitable as anode while Na and Mg act as active ions? (2) Whether the shape of the B_xN_z-domain can tune the interface structure and the electrochemical performance after alkali-ion storage? (3) What is the role of polar-covalent nature to control its electrochemical performance in batteries and capacitors?

Besides these concerns, there is another aspect which is the capacitive performance. Compared with the diffusion-controlled process such as Na-ion insertion and conversion in conventional Na-ion storage battery materials, capacitive charge storage has the additional advantage of rendering high charging rate and therefore high power. Particularly, pseudocapacitance results in underpotential deposition, faradaic charge-transfer reactions at the surface or near-surface redox reactions.[35–37] Till date, pseudocapacitive contributions have been realised in some insertion and conversion materials with high-rate performance in Li-ion battery (LIB) and SIB.[35,38,39] However, it has not yet been implemented practically

where the challenge is to realise high-capacity materials that can also exhibit fast kinetics.

In this chapter, we answer all the above mentioned questions.[40] We consider two types of regular-shaped BN nanodomains in the C-matrix: (i) hexagonal (H: $B_{12}N_{12}$) and (ii) triangular (T_N : $B_6N_7; T_B$: B_7N_6), as shown in Figure 3.1. First, we investigate how the shape of the B_xN_z patches in borocarbonitride can tune polarity, charge localization and electronic conductivity, and thus, control the charge/discharge process. We find that although $B_xC_yN_z$ is a perfectly planar sheet, B_xN_z-domains can give rise to high anisotropy in the spatial distribution on the surface topology, which in turn dictates in-plane anisotropy for electronic transport.[41] B_xN_z-domains can also tune the interface structure after alkali-ion storage, which would be of practical interest in rechargeable batteries and capacitors. Second, the shape effect of the B_xN_z-edge structure, hetero-atomic effects, charge-imbalance (due to $x \neq z$ in B_xN_z-domain), as well as inter-layer interactions, have been studied to understand the storage and diffusion of active ions. Third, we carried out a comparative analysis for different alkali/alkaline-earth metals (M: Li, Na and Mg) and clarify whether $B_xC_yN_z$ is appropriate as an anode for each of these ions. Finally, we rationalize the superiority of the combination of Na as active ion and $T_N - B_xC_yN_z$ as an anode for both battery and capacitive performance. In addition, the experimental ease in synthesising domain-segregated $B_xC_yN_z$ nano-hybrids holds good promise for next-generation energy (Li and Na) storage applications through shape engineering of the BN domains.

3.2 Computational Details

DFT-based calculations have been performed using the projected augmented wave (PAW) formalism[42] with the inclusion of DFT-D2 dispersion correction,[43] as implemented in the Quantum ESPRESSO program.[44] The electronic exchange-

correlation energy is approximated with a generalized gradient approximation (GGA) as parametrized by Perdew-Burke-Ernzerhof (PBE).[45,46] Choice of the functional is made such that the physical results obtained are not sensitive to these choices and the pseudopotentials are verified as available with Quantum ESPRESSO. Kohn-Sham wave functions are expanded in a plane-wave basis set, which has been truncated with an energy cut-off of 40 Ry and a charge-density cut-off of 320 Ry. Integrations over the Brillouin Zone (BZ) are sampled with a uniform (10 x 10 x 1) k-grid considering 56 special k-points. The geometry optimizations were performed using the Broyden-Fetcher-Goldfarb-Shanno (BFGS) algorithm. The convergence threshold was set at 10^{-3} Ry bohr^{-1} for force. We have checked that these conditions give good convergence of the total energy within 10^{-4} Ry per atom. The vertical (adiabatic) electron affinity [VEA(AEA)] and vertical (adiabatic) ionization potential [VIP(AIP)] have been calculated using Equation 3.1–3.4.

$$VIP = E_{total}(N) - E_{total}(N-1)^* \tag{3.1}$$

$$VEA = E_{total}(N) - E_{total}(N+1)^* \tag{3.2}$$

$$AIP = E_{total}(N) - E_{total}(N-1) \tag{3.3}$$

$$AEA = E_{total}(N) - E_{total}(N+1) \tag{3.4}$$

where, $E_{total}(N)$ represents the total energy of system with N number of electrons present within the supercell. '*' in the superscript represents the neutral geometry with one extra background electron for $N+1$ within the parenthesis and one electron deficient case for $N-1$ within the parenthesis. To estimate the energetics for the redox reaction of Li^+ at the electrode, we considered BH_4^- as the counter anion. This is to maintain the charge neutrality. Stability after intercalation and

the feasibility of the desorption processes (at x = 0.1) are quantified by the LE and DLE, respectively (see Equation 3.5 and 3.6).

$$Charging : LE = (E_{Li@Sheet} + E_{BH_4^-}) - (E^-_{Sheet} + E_{LiBH_4)} \quad (3.5)$$

$$Discharging : DLE = (E_{Sheet} + E_{LiBH_4}) - (E_{[Li@Sheet]^+} + E_{BH_4^-}) \quad (3.6)$$

E species (total energy of the respective species) is computed after consideration of the zero-point energy (ZPE) correction term. $LiBH_4$ is considered as a model electrolyte. The experimental crystal structure for the orthorhombic phase of $LiBH_4$ (as found at ambient conditions)[47] has been considered as a starting configuration. Then, we optimised the geometry, which is followed by the calculations of the phonon eigenmodes by solving the eigenvalue problem for the dynamical matrix, calculated by the force-constant method.[48] The atomic displacement is set at 0.02 $\mathring{A}$. The contribution of the Γ-phonon modes is only taken into account as considered earlier.[49] The vibrational density of states (VDOS) of $LiBH_4$ (Figure 3.2). Finally, the estimated ZPE-correction term for bulk $LiBH_4$ is found to be 188 meV per atom, which corroborates well with previous findings (178 meV per atom).[49] Therefore, BH_4^- does not form crystals, we obtained the ZPE-correction term from vibrational degrees of freedom using molecular calculations. We used the fcc supercell with a lattice constant a = 15 $\mathring{A}$. The extra negative charge is compensated by the uniform background charge. To attain a wide range of concentration of adsorbed Li and the interaction of Li atoms with the matrix, we adopted a 60 atom super-cell structure of BCN (similar to a 6 x 5 graphene super-cell). Few among these configurations are shown in Figure 3.18. Lower concentrations of BN (10%) have also been considered after adopting a bigger super cell (8 x 8) with

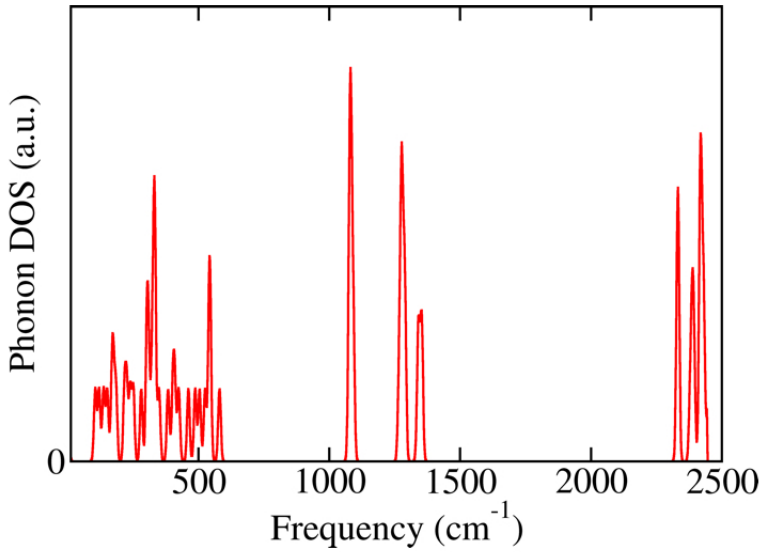

Figure 3.2: Phonon density of states for orthorhombic $LiBH_4$. The contribution of the optical Gamma-phonon modes is taken into account. Gaussian broadening with a width of 25 cm^{-1} has been used.

128 atoms. The interlayer interaction energy is calculated using equation 3.7.

$$ILE = \frac{E(bilayer) - 2E(monolayer)}{n_{atom}} \tag{3.7}$$

where E(bilayer) and E(monolayer) are the total energies of the bilayer and monolayer, respectively. n_{atom} is the number of atoms (n_{atom} = 60 for monolayer and 120 for bilayer). Structural optimization of alkali-metal clusters has been carried out at the M06-2X level of theory[50] using the Gaussian 09 program.[51] 6-311+G (d, p) basis set are assigned with the metal atoms (Li, Na and Mg). Frequency calculations have been conducted for all optimized geometries to ensure the structures at local minima on their respective potential energy surfaces. The correlation consistent cc-pVTZ and aug-cc-pVTZ basis sets were also used as implemented in Gaussian 09 for further verification.[52] The cohesive energy (CE) for all the complexes were computed with the method outlined in a study on thermochemistry, available in the Gaussian 09 online manual.[53] Equation 3.8 is the more general

form and the product (P) and reactant (R) designations correspond to the metal-cluster and individual atom, respectively.

$$CE(P,298K) = \Delta H(P,0K) + [(H(P,298K) - H(P,0K)) - \sum H(R,298K) - H(R,0K)] \quad (3.8)$$

The bulk cohesive energy (E_c) of the pure elements (in eV), Li: 1.63, Na: 1.11, Mg: 1.51 were adopted from literature.[54]

3.3 Results and Discussion

3.3.1 Electronic Structure of Pristine $B_xC_yN_z$ with Different Shapes of B_xN_z-patches (T and H)

H-sheet is completely charge-balanced due to $n_B = n_N$, whereas T-sheet can either be a nitrogen-rich (T_N: $n_N > n_B$) or boron-rich (T_B: $n_B > n_N$) system (Figure 3.1). The electronic density of states (DOS) is calculated for both H and T to understand the nature of the chemical bonding. H is a semiconductor with a direct band-gap of 1.47 eV (Figure 3.3), where as, for non-stoichiometric hybrids (T), the charge imbalance results in an odd number of valence electrons. As a result, T appears to be metallic in the presence of the mid-gap state, which agrees well with previous results.[32] T_N and T_B are the inherent electron- and hole doped system, respectively, which is reflected in the characteristic DOS near the Fermi energy. Although the N-lone pair can be expected to exhibit non-bonding character, we find a dissimilar feature after analyzing the projected density of states (Figure 3.3a-c). Both the valence band maximum (VBM) and conduction band minimum (CBM) has contribution predominantly from the p_z orbital of the carbon atoms. For T_B, the discontinuity in the low-energy conduction states ($\sim$1 eV) can prohibit the spontaneity in electronic conduction. In contrast, T_N shows superiority in electron transport due to continuous conduction states and can be used as an electrode for easier electron-insertion or electron-withdrawal. As shown in

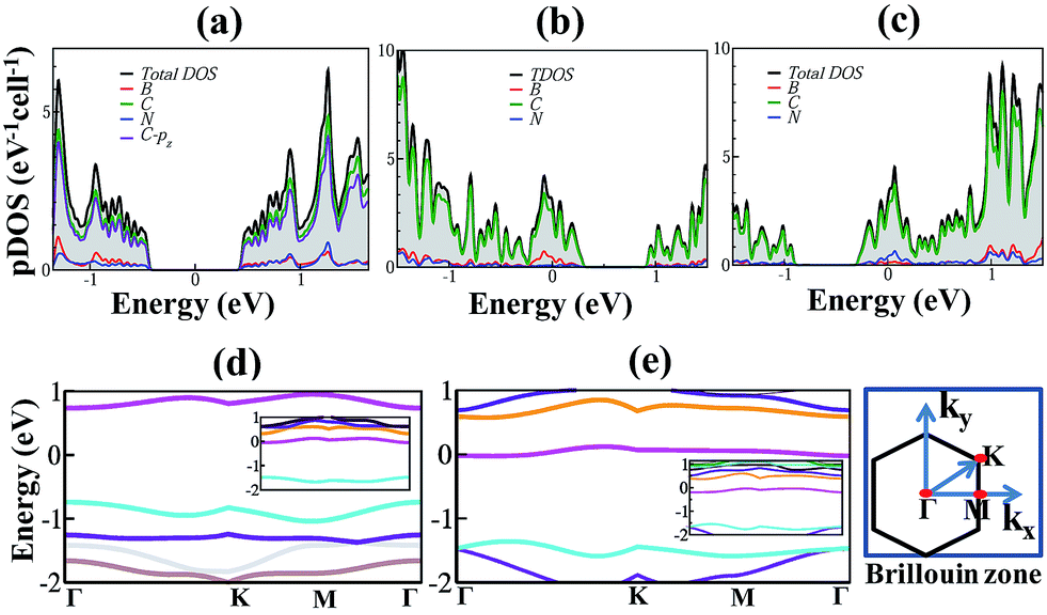

Figure 3.3: The total density of states (DOS) and projected density of states (pDOS) for pristine H, T_B and T_N sheets (a-c). The Fermi energy (E_F) has been rescaled at zero. The band dispersion (path: $\Gamma - K - M - \Gamma$) in pristine as well as lithiated state of the H (d) and T_N (e) sheets. The inset figures correspond to the Li-adsorbed state. $\Gamma = (0, 0, 0), K = (0, 0.5, 0), M = (0.5, 0.5, 0)$.

Figure 3.3, the carbon-$2p_z$ orbital is the major contributor to the DOS near the E_F for both H and T. For the metal-ion adsorbed state, both the VBM and VBM-1 have contribution from the C and N atoms of the sheet, whereas CBM is contributed by the M atoms (Figure 3.4). Thus, T-sheet interacts with ad-atoms (Li, Na, Mg) mostly via the carbon-$2p_z$ orbital, which is also found for H-sheet. It is also found that B-orbitals are low-lying and less perturbed in the presence of the ad-atom. This might help to attain the voltage as found in a graphene electrode, but the inherent polar covalence in the structure can result in dissimilar electrochemical performance. These fundamentals motivated us to investigate the potential of borocarbonitride, T_N, in particular, as an anode for alkali-ion batteries and capacitors.

Effect of the background electron on charging/discharging the sheet:

To understand the shape-effect of the B_xN_z domain on the charging/discharging

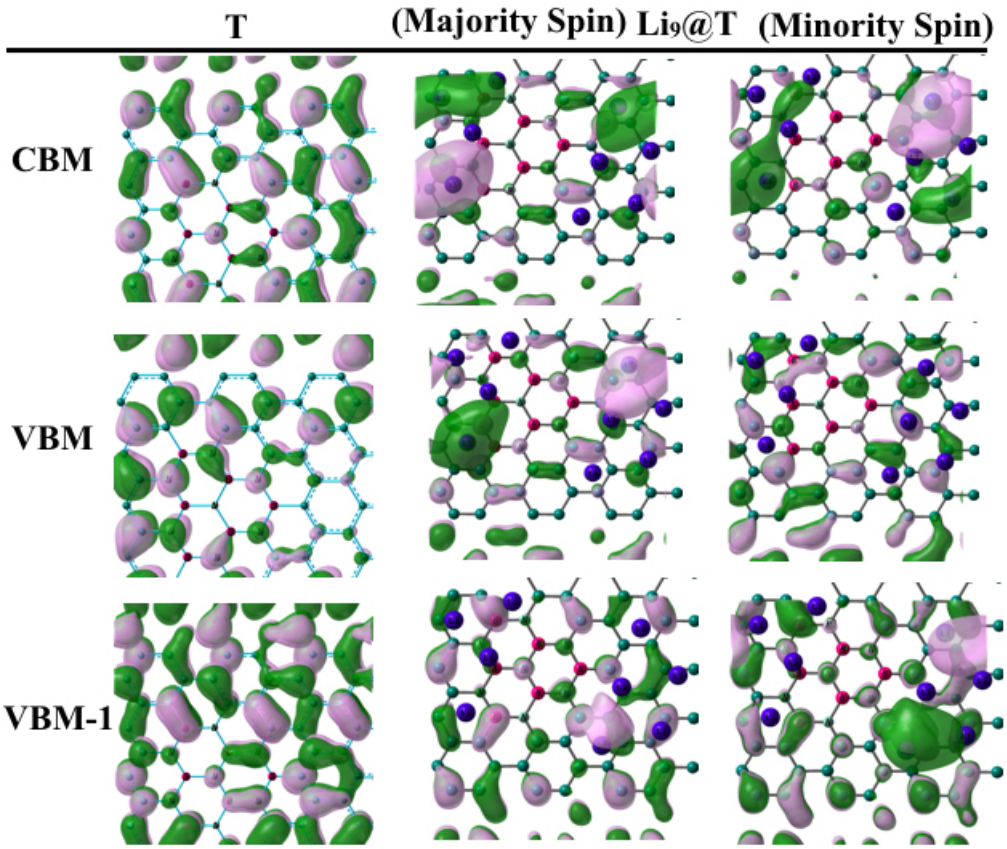

Figure 3.4: Real space wave function plot corresponding to the valence band maxima (VBM), VBM-1 and conduction band minima (CBM) states for fully charged state while T_N has been considered as the anode. Strong bonding in Li cluster is evident from prevalence of electron density. Iso value used for these plots is 0.02 and density 0.05 e $Bohr^{-3}$.

performance, we analyzed the redox-properties (Table 3.1). Charging/discharging in a rechargeable battery or supercapacitor is influenced by the effect of background charges at different bias. According to the definition (Equation 3.1 - 3.4), the vertical (adiabatic) electron affinity [V(A)EA] and vertical (adiabatic) ionization potential [V(A)IP] dictate the thermodynamic feasibility of charging the sheet after injection of the electrons and the energy cost for the reverse process.

During charging, the anode has a negative potential and accommodates partially positive Li. Thereby, the AEA provides us a reference frame for comparing the electrochemical performance of an anode and it is desirable to find AEA as

Table 3.1: Computed VIP (AIP) and VEA (AEA) in eV for monolayer $B_xC_yN_z$. Lithiation and de-lithiation energy (LE and DLE) in eV per Li atom have been provided for Li-intercalation into the stable AA configuration.

Sheet	**VIP (AIP)**	**VEA (AEA)**	**LE**	**DLE**
H	4.46 (4.86)	2.24 (2.25)	-2.46	-1.63
T_N	3.82 (3.50)	2.34 (2.34)	-2.22	-1.41
T_B	4.88 (4.56)	3.32 (3.70)	-	-

positive. Lowering of the magnitude of the AEA can result in less perturbation while charging the sheet with extra electrons. Hence, we find H and T_N to be more appropriate than T_B due to the suitable AEA and significantly high AIP preventing self-oxidation of the anode. The difference between VEA and AEA is the measure of electronic relaxation energy (E_λ) during the charging of the anode with an extra electron. Indeed, reversibility in the charge/discharge process necessitates the anode to be a perfect electron reservoir with less structural perturbation upon electron injection. Therefore, H and T_N are efficient as an electrode due to the lower value of E_λ. Added advantage due to the metallic nature of T_N, makes the electron transfer and transport process effective for the T_N-anode. Together with electron transfer/transport, Li storage/release in the anode (graphene-like layered matrix) occurs by the reversible process where the lithiation energy (LE) and delithiation energy (DLE) are the measures of the electrochemical potential of the Li^+/Li redox reaction during charging and discharging, respectively (see computational method section). Both the LE and DLE are negative (Table 3.1), which reveals the thermodynamic feasibility of the charging and discharging process irrespective of the shape of the B_xN_z domain. Indeed, our results corroborate fairly well with the available experimental findings and predicts the quantitative estimation of the OCV in LIB.[28,41] The plateaus in the cyclic voltammogram at around 1.20 V and 2.50 V in the charge cycle are due to the lithiation/de-lithiation process from the $B_xC_yN_z$ layers.[28,41] It compares fairly well with our results (1.41 and 2.46 eV), as shown in Table 3.1. Hence, the GGA + D2 functional can be

successfully used to find the OCV for alkali/alkaline-earth metal (M) ion storage on a borocarbonitride matrix. The higher value of the LE compared to DLE highlights the spontaneous Li^+ ion adsorption after electrolytic dissociation, when the $B_xC_yN_z$-electrode has been kept at a negative potential. This also points out the potential of such nanohybrids as an electrode in capacitors. However, the large value of LE and DLE for the H-anode may reduce the reversibility in the ion storage/release process during cycling of a rechargeable battery. In this context, T_N appears to be superior to H because of an intermediate value for the LE and DLE, resulting in at least a 0.3 eV higher voltage of the battery. Geometrical relaxation after charging/discharging the sheet with an electron is also found to be very low (see Table 3.2) for both the H and T_N.

Table 3.2: The percentage expansion of the surface area, ΔS (%) with respect to the neutral state (N = number of electrons) and computed average inter-layer distances (ID) in $\mathring{A}$ for the stable stacking pattern (AA and AB) of bilayer H and T_N. The $N+1$ and $N-1$ electronic state dictate an electron-rich and electron-deficient background, respectively.

Sheet	$N_{electron}$					
	N-1		**N**		**N+1**	
	ID	**ΔS**	**ID**	**ILE**	**1D**	ΔS
H	-	0.09	–	–	–	0.22
H-AA	3.19-3.69	-0.12	3.38-3.61	-23.99	3.26-3.55	-0.05
H-AB	3.23-3.42	0.03	3.26-3.51	-27.06	3.28-3.52	0.07
T_N	–	0.09	–	–	–	0.26
T-AA	3.40-3.55	-0.07	3.22-3.32	-27.62	3.35-3.51	0.12
T-AB	3.23-3.42	0.001	3.23-3.42	-30.25	3.22-3.40	0.001

In particular, after electron injection to the sheet, there are almost no changes in the surface area (S) of each layer as well as in the interlayer distance (ID). We also find that the interlayer interaction energy (ILE), which is defined as the extent of cohesive energy between layers, is comparable to the graphene layers (see Table 3.2).[55] The ILE for both the AA and AB stacking patterns are similar, which proves the feasibility of both the stacking patterns irrespective of the shapes of embedded B_xN_z domain. Hence, sliding of one layer over another, thus attaining

the conformational space with a wide variety of stacking arrangements is possible at room temperature. The AB stacking pattern for T_N is the most appropriate for charging-discharging due to the robustness of the geometrical parameters (ID and S) upon perturbing influence of the background electron.

On the other hand, in the Li(Na)-intercalated state, the AA stacking pattern becomes more favored due to the simultaneous sharing of two hollow hexagons from the layers, above and below. In the following section, we discuss the effect of the insertion/de-insertion of alkali ions on the H and T_N monolayer surface as well as through intercalation to understand the energy density and power efficiency of the electrochemical set up with Li, Na and Mg as active ions.

3.3.2 Theoretical Voltage Profile and the Limit for Specific Capacity

The open-circuit-voltage (OCV) is widely used for characterizing the performance such as state-of-charge and state-of-health of LIB(SIB). In theory, the OCV curve can be obtained by calculating the average voltage over parts of the varying Li-composition domains.[56,57] The average voltage for $Li_x@S_6$ at different states of charging ($0.1 \leqslant x \leqslant 0.9$) of the battery is expressed by Equation 3.9, where E_{S_6}, $E_{Li_x@S_6}$ and E_Li are the energy of sheet (Figure 3.11), $Li_x@S_6$ and metallic Li, respectively. The average adsorption potential for a series of configurations of $Li_x@S_6$ with x = 0.1-0.9 are summarized in Figure 3.5.

$$OCV = \left(\frac{E_{Li_n@S_6} - (E_{S_6} + n_{Li} \times E_{Li})}{n_{Li} \times e} \right) \tag{3.9}$$

$$Capacity = \left(\frac{n \times F}{3600 \times M} \right) \tag{3.10}$$

where n is the number of electrons involved in the electrochemical process, F = 96500 mAh and M is the mass of the electrode in kg. This method of screening

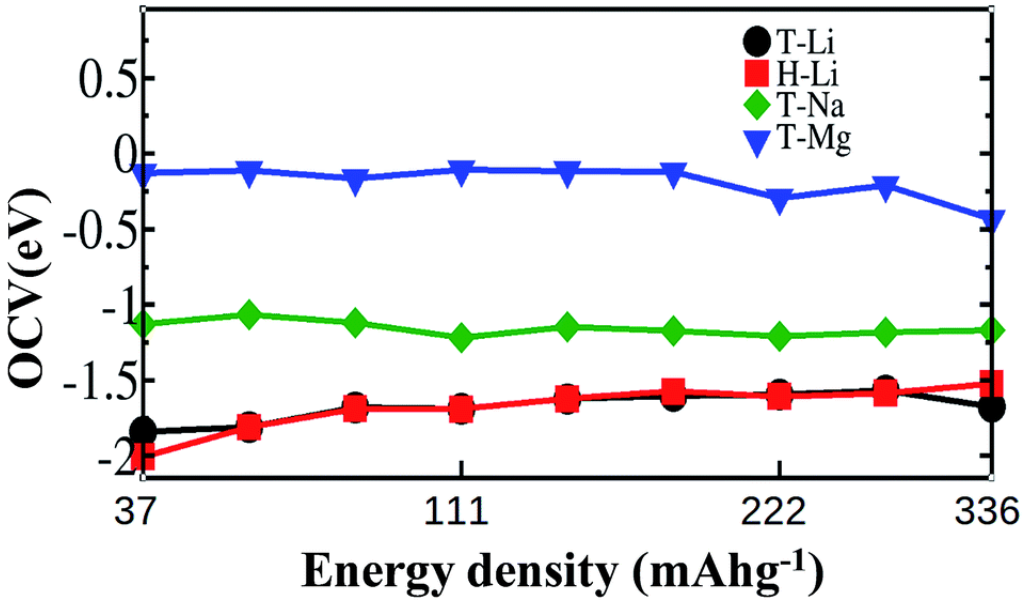

Figure 3.5: Computed OCV with respect to the specific capacity for Li, Na or Mg adsorbed atoms (x) on a monolayer (H and T) matrix.

a series of Li/S_6 ratios (x values) predicts the average Li-insertion potential to be always greater than 1.5 eV throughout the charge/discharge voltage profiles (Figure 3.5). The calculated OCV indicates that the Li-ion is still strongly bound on both the H and T sheets, although the adsorption energy is slightly lower for T at lower concentrations. At higher concentrations, there is an equalization of the open circuit voltage. The calculated adsorption energy of the Li atom on the H(T) monolayer is 2.00(1.75) eV, which is much higher than the same for Li adsorbed on monolayer graphene (1.04 eV)[58,59] and slightly lower than that of MoS_2 (2.12 eV).[60] Such strong Li adsorption indicates the increased stable capacity of the battery and possibility to be the anode material for LIBs with an open circuit voltage of 1.50-2.00 eV. Na can also exhibit an average OCV of $\sim$ 1.25 eV, whereas the same for Mg is thermodynamically disfavoured. This suggests that Li and Na are preferable as active ions in a rechargeable battery with $B_xC_yN_z$ as the anode, while Mg with a lower adsorption energy would result in an unwanted electrochemical reactions during the charging of the sheet.

For the betterment of our prediction on the OCV, we also estimated the contribution from the entropy term, TS, in the free energy G ($G = H - TS$). In this regard, we carried out an additional set of calculations based on ab initio molecular dynamics (AIMD) at 300 K. We found that the structural vibration leads to a TS value for the T_N-anode of 0.00025 eV per atom in the completely discharged state and reaches a value of 0.00045 eV per atom in the fully charged condition. Thus, the TS is negligibly small compared to the OCV computed through consideration of purely electronic degrees of freedom ($\sim$ 1.25 eV) for the sodium ion battery and $>$ 1.50 eV for the Lithium ion battery). The free energy calculation as derived from the AIMD study have been given in Figure 3.6.

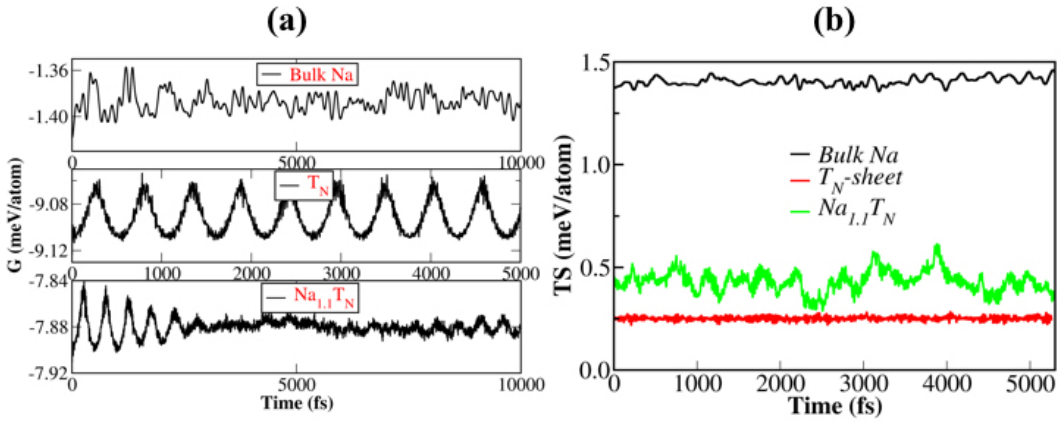

Figure 3.6: (a) Free Energy profile and (b) the energy term originated from entropy in thermally equilibrated T_N system versus time (at T = 300K). The fully charged state ($Na_{1.1}T_N$), pure sheet (T_N) and bulk Na have been compared.

As the average voltage of Na^+/Na is lower than that of Li^+/Li (difference: $\sim$ 0.5 eV), T_N can be considered as a promising anode for SIB, resulting in a higher cell voltage. Critical stoichiometries corresponding to the storage limit for the adsorbed active ions (on one side of the H(T) sheet) are $Na_{1.1}S_6$ and $Li_{0.9}S_6$ (Figure 3.7). Hence, sodiation results in more ion-storage capacity compared to lithiation. When the adsorption-concentration exceeds this critical stoichiometry ($Na_{1.1}S_6$ and $Li_{0.9}S_6$), extra ions form a secondary layer. The appearance of

such a secondary layer (Figure 3.7) of adsorbed Li/Na indicates that the electrode reaction cannot occur beyond a certain specific capacity with Li storage up to x = 0.9 and Na concentrations up to x = 1.1. This limits the specific capacity, which is 1.22 times higher for SIB than LIB. The estimated specific capacity (see equation 3.10) for the layered structure is 336(409) $mAhg^{-1}$ in case of LIB(SIB) and for the exfoliated layers it doubles to 672(810) $mAhg^{-1}$. This estimation compares well with the experimentally attainable specific capacity of LIB of up to 710 $mAhg^{-1}$ at a low current rate (0.05 Ag^{-1}).[61] Thus, the specific capacity of a SIB with borocarbonitride anode is larger than the conventional graphite electrode capacity of $\sim$ 360 $mAhg^{-1}$ for LIB and hence falls in the gravimetric capacity range for an acceptable new electrode material in the Na-ion battery.

Side view of Figure 3.7a, c appears like a chain with regular valleys of adsorbed Li(Na) atoms. In practice, it is an important issue to understand the storage pattern of such active ions on the anode-surface during the charging process of a battery and capacitor. For instance, the metal elements will have a two-dimensional (2D) or three-dimensional (3D) deposition pattern on electrode surface, which control the capacitive performance. The capacitance (C) of a double layer capacitor is inversely proportional to the distance of the ad-layer of active ions from the electrode surface (d) for two parallel plates of area 'A' separated by a distance (d). Although at low concentrations, the adsorbed Li-ion is found to be closer (at 2.26 $\mathring{A}$) to the T_N anode than a Na-ion (2.45 $\mathring{A}$); at high concentrations, the effective distance is much shorter in the case of a Na-ion (3.35 $\mathring{A}$) than a Li-ion (4.44 $\mathring{A}$). Therefore, adsorbed Na-ions with a smaller 'd' value result in better capacitive performance.

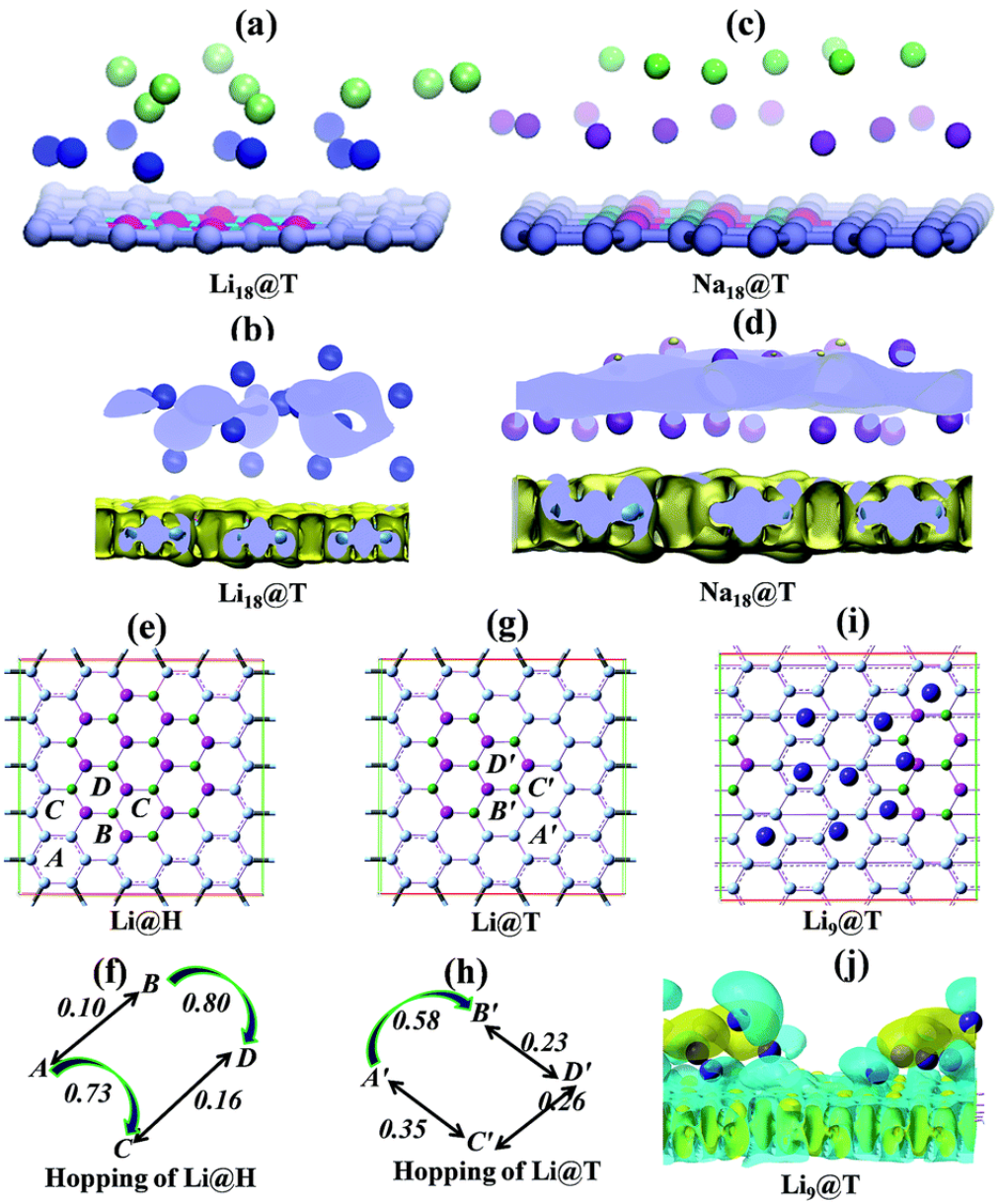

Figure 3.7: (a, c) The side view of the optimised geometry of the metal-layer adsorbed on the T_N-surface. The brightness and shadow on the Li/Na represent the front and back positions, respectively. (b, d) The charge density with an iso-surface value of 0.01 $e\mathring{A}^{-3}$. The yellow and blue regions indicate an increase and decrease in electron density, respectively. (e, g) The four possible adsorption sites of the 'm' type, denoted as A, B, C and D (A′, B′, C′ and D′) for Li adsorption on H(T) sheet. (f, h) The diffusion paths and corresponding energy barriers for various types of hopping of adsorbed Li (for low Li-concentrations; x = 0.1). (i) The relaxed structure of ad-atom adsorbed on the T_N surface at the storage limit (x = 0.9). The charge density distribution for the same is shown in the subplot (j), where the yellow and cyan regions indicate the negative and positive charge density, respectively.

To estimate the interfacial charge density after Li/Na-ion storage, we consider the net overlap density ($d_{net-overlap}$) after subtracting the superposition of the atomic density from the total charge density (Figure 3.7b and d). Subsequently, we applied Bader analysis and found highly positive charges (varying from +0.20 to +0.84) on adsorbed Na. Hence, the deposited Na atoms form two distinct layers with electron deficiency, i.e. storing the positive charge in the interlayer space (Figure 3.7d). On the other hand, Li atoms form clusters with significant bonding between the primary and secondary layers. A significant overlap among the adsorbed Li-ions themselves leads to a decrease in the ionicity, and prevents the storage of positive charge density to a certain extent. In addition, involvement of an increased number of active ions in the electrochemical reaction ($Na_{2.2}S_6$ vs. $Na_{1.8}S_6$) and high charge storage in the vicinity of the electrode surface leads to improved capacitive performance for Na-ions when compared to Li-ions. To further understand the effect of the state of charge on the electrochemical performance, we consider various possible adsorption-sites as well as varying the concentration of the adsorbed M-ions (M: Li, Na and Mg) on the monolayer T_N and H sheets (Figure 3.8).

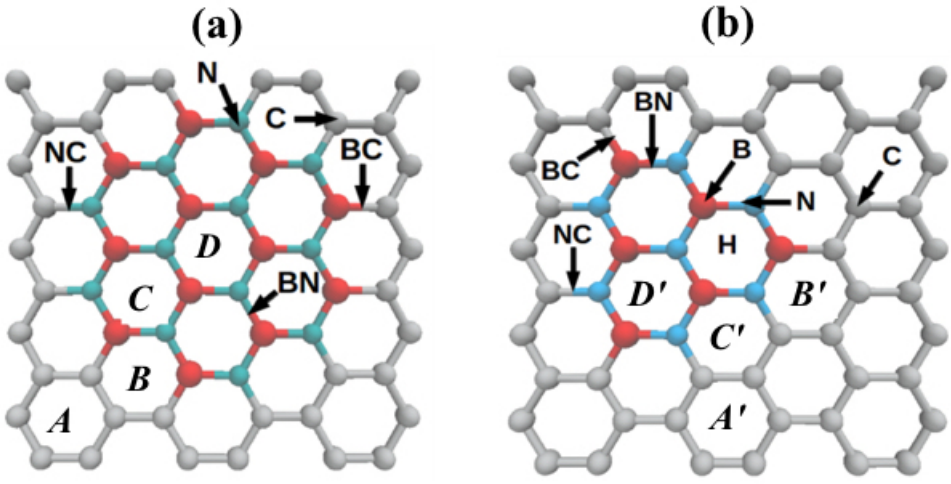

Figure 3.8: For 'm' type, there are four possible adsorption sites, which are denoted as A, B, C and D (A′, B′, C′ and D′) on H (T) surface. Other sites shown by the arrows are 't' site.

The hollow site (m) is placed above the centre of the hollow-hexagon and the top site (t) is situated directly above the B, C or N atom or specific bonds. There are four types of m site, which are shown as A (A′), B (B′), C (C′) and D (D′) for the H (T_N) surface topology (Figure 3.7e, g). By placing Li atoms at different sites and relaxing the structure, we calculated the adsorption energy (E_a) of Li on the monolayer $B_xC_yN_z$ sheet from the equation,

$$E_a = E_{Li@Sheet} - (E_{Sheet} + E_{Li}) \tag{3.11}$$

where E_{Sheet} is the energy of sheet without a Li atom, E_{Li} is the energy of an isolated Li atom and $E_{Li@Sheet}$ is the total energy of the Li-adsorbed system. We found that at low concentrations (x = 0.1), the 'm' site is favoured over the 't' site. The newly formed bonds between the adsorbed Li and the sheet are ∼2.25 $\mathring{A}$. Relative energy differences for Li-adsorption process on these sites have been given for low Li-concentration (x = 0.02) Table 3.3.

Table 3.3: The computed relative Li-adsorption energy (E_a) in eV for various 'm' sites on monolayer H (T_N) sheet. All the quantities are with respect to the value of E_a = -2.01 eV for the most stable site ('A') on the H-sheet

Sites	E_a
A (A′)	0.000 (0.149)
B (B′)	0.095 (0.734)
C (C′)	0.734 (0.503)
D (D′)	0.898 (0.244)

At the 'm' site, the Li atom in the middle of the hollow hexagonal site is coordinated by six atoms, whereas at 't' site, Li atom is strongly bonded to one/two atoms. Thus, the adsorption of the ad-atoms in the vicinity of the 't' site results in a decrease in the effective coordination number and a lower adsorption energy than the 'm' site. Among the various 'm' sites, A (A′) is the most stable where the ad-atom is equally coordinated to six C atoms in the hexagonal ring (Ta-

ble 3.3). Other possibilities with a fully B_xN_z-hexagon (D and D′) or partial B, N contributor in the hexagon (B, B′, C and C′) exhibit lower adsorption potential. Therefore, at a lower surface coverage, the adsorbed atoms disperse on the carbon matrix, which is simply the outcome of the preferential occupancy in the thermodynamically favored sites (A and A′). The relative energy differences between the most and least stable adsorption sites are 0.58 eV for the T_N sheet and 0.90 eV for the H-sheet. Thus, T (compared to H) shows more isotropic behavior for adsorption of Li-atoms, as the Li-orbital participates similarly for different m sites on the T-sheet (Figure 3.9c). This is because the surplus electron always occu-

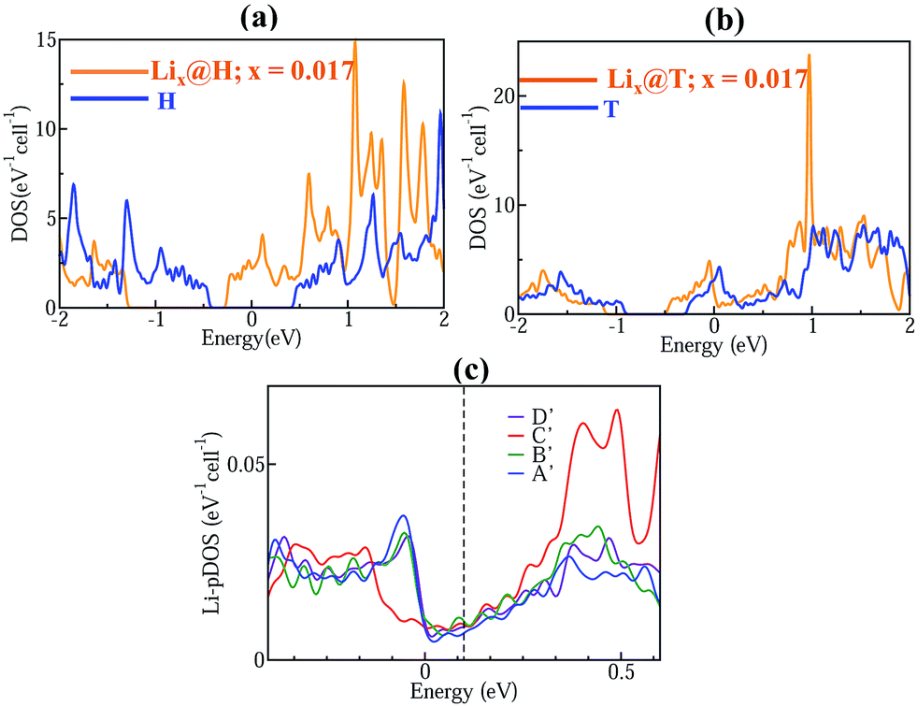

Figure 3.9: The density of states (DOS) for H and T sheets ((a) and (b)) in the pristine as well as lithiated states, respectively. (c) The projected DOS for Li while adsorbed on various 'm' sites of the T_N sheet.

pies the localized state near the Fermi-level. By means of the differential charge density analysis, we found significant electron transfers from the Li(Na) atom to the sheet (Figure 3.7b, d and j). According to the Bader charge analysis, Li(Na)

possesses 0.96(0.86)$|e|$ positive charge while stored on the surface of the T_N-anode, indicating certain ionic components in the newly formed Li(Na)-sheet bonds.

We estimated this diffusion barrier (at x = 0.1) under the assumption that the barrier height is the energy difference of the adsorption energies between the lowest and the next lowest adsorption energy site. Of course, it is necessary to do more accurate calculations to find the complete potential surface using, for example, the nudged elastic band method (NEB).[62] In addition, we verified our results with accurate calculations using the NEB method. As shown in Figure 3.7f and h, the diffusion barrier height strongly depends on the shape of the B_xN_z domains. The diffusion barrier (ΔE_{diff}) of the Li on T_N-sheet is lower than that of the H-sheet, leading to four times higher rate of diffusion for Li ions (by means of Arrhenius equation at 300 K) on the T_N-anode. We compared the ΔE_{diff} on T_N with the available results for graphene (0.28 eV),[63] which reveals that the diffusion energy barrier of the Li atom is (0.63 eV), twice of the ΔE_{diff} for a graphene surface (at x = 0.1). On the other hand, the diffusion energy barrier of Na atom is 0.15 eV. Thus, the rate of diffusion for a Na-ion is 50 times faster than the Li-ion on T_N and hence, it is a promising anode for faster ionic-diffusion in SIB. Irrespective of the adsorption sites on both H and T_N, the electrons are donated to the sheet after lithiation/sodiation, which results in the redistribution of electrons throughout the sheet (Figure 3.9a, b). Further renormalization of the injected electrons leads to population of the low-energy conduction states, which results in the enhancement of the metallic behavior for T_N and semiconductor-to-metal transition for H (Figure 3.9 and 3.10). We found that the characteristic features of the electronic states in both the H and T_N are well maintained after adsorption of the metal atoms (Li/Na), only with a shift in the Fermi level. Such a shift is comparatively smaller for T_N than H. The reason is that the bands for T_N with or without Li are more localized in nature than for H. Thus, electron transfer from the Li(Na) atom to the sheet during charging and the reverse process during discharging has

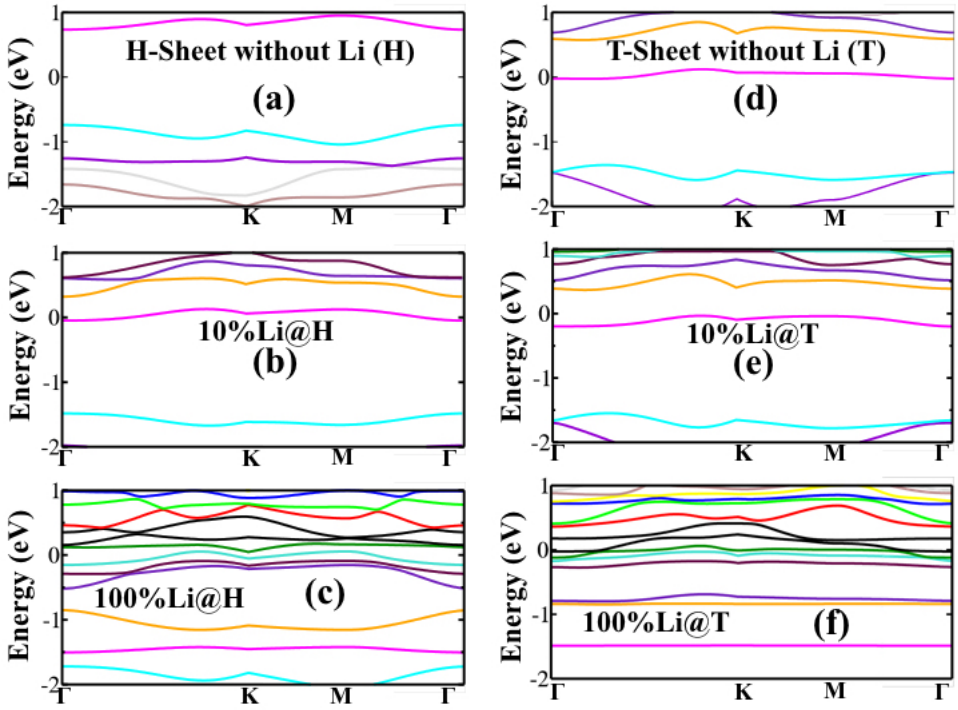

Figure 3.10: Band dispersion of (a) 'T' and (b) 'H' sheets, at different concentration of adsorbed Li. $\Gamma = (0, 0, 0), K = (0, 0.5, 0) and M = (0.5, 0.5, 0)$.

a local impact. The Fermi energy just shifts towards the higher energy states (Figure 3.9 and 3.10) upon ion-adsorption due to the occupation of surplus electrons injected into the sheet. This may result in higher columbic efficiency as well as reversibility in the electron transfer process between the active ion and the sheet, thus enhancing the power factor for the T_N-anode. The T_N-sheet interacts with M-ions through a donation/back-donation mechanism, where the nitrogen atom donates the electron, resulting in a greater population of the $2p_z$ orbital in the C atom. Such an electron-rich $2p_z$ orbital on the C atom promotes the adsorption of M-ions. The predominance of Li-pDOS in the conduction band indicates the completeness of the electron transfer from Li to the sheet irrespective of the various m sites (Figure 3.9c). The storage of active ions can lead to additional spin-polarization with full control over its spin components (Figure 3.11), which can find spintronic applications.

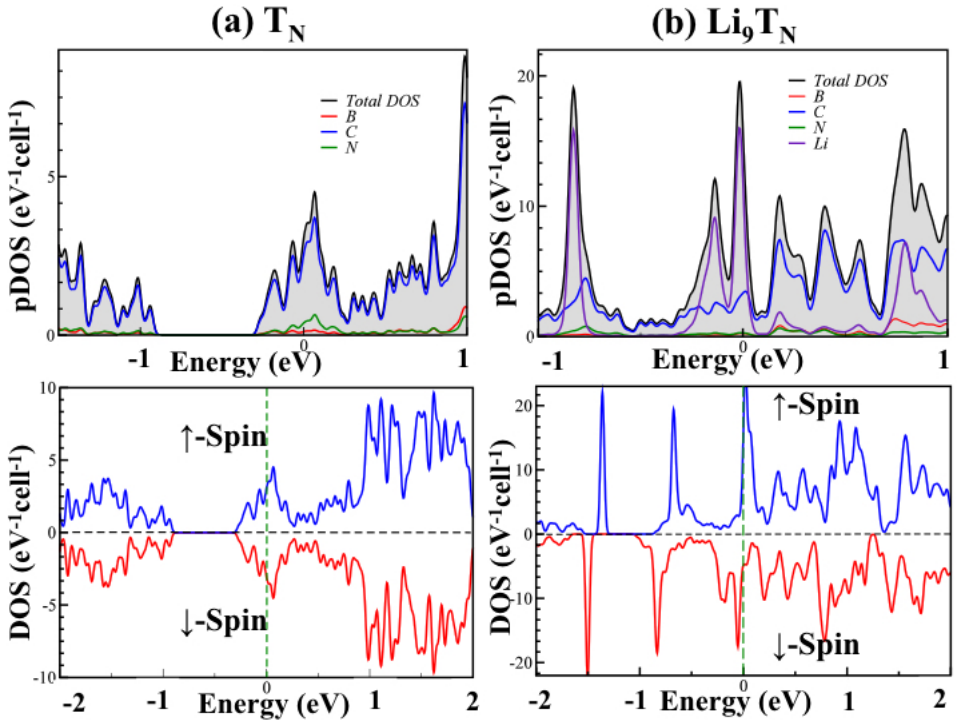

Figure 3.11: Total density of states (DOS) and projected density of states (pDOS) for pristine T_N-sheet as well as its lithiated state in (a) and (b) respectively.

Thus, there are four positive aspects for using the T_N-sheet as an anode: (i) spontaneous electron transport through the pristine sheet, (ii) enhancement of the electronic transport due to appearance of new conduction states after Li(Na)-ion storage and faster ionic-diffusion, (iii) completeness in the electron transfer process between the sheet and adsorbed Li(Na)-ion and (iv) an optimum adsorption potential for Li (Na)-ion within the range of 1.35-1.75 (1.05-1.25) eV, which can allow a significantly high operating voltage for a Li-ion (Na-ion) rechargeable battery. A similar study has been carried out after consideration of lower (10%) BN-concentrations in borocarbonitride (Figure 3.12). Wavefunction analysis reveals that the lower concentration of BN leads to the separation of polar BN-islands on the delocalised graphene sheet (Figure 3.13). Therefore, the OCV is found be in two different regimes: an OCV corresponding to the matrix as (i) graphene and (ii) BN-nanosheet.

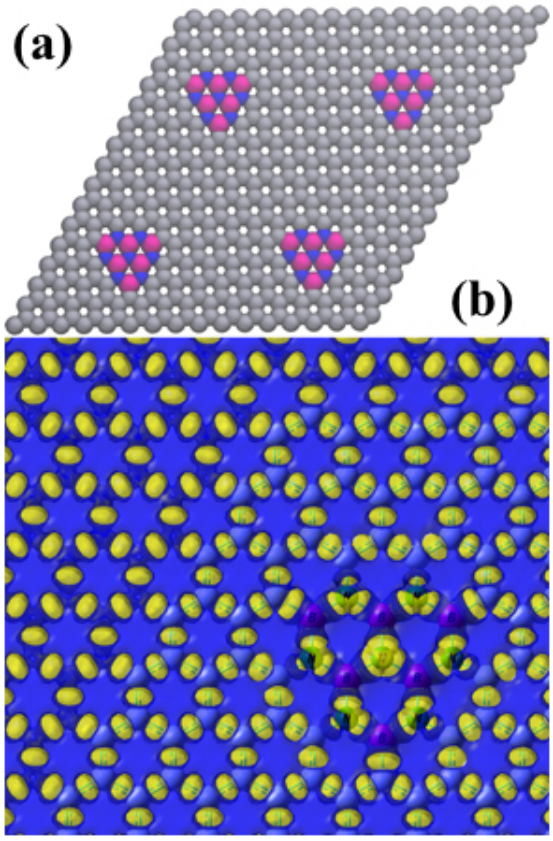

Figure 3.12: (a) Monolayer $B_xC_yN_z$: x = 6, y = 115 and z = 7, with overall 10% BN concentration with trigonal BN-domain. (b) Differential Charge density plot is shown with an iso-surface value of 0.02 and density of 0.01e $\mathring{A}^{-3}$. The yellow and blue regions indicate an increase and decrease in electron density, respectively.

On the other hand, <20% BN concentration (T) leads to interconnected polar BN-islands (Figure 3.13), which govern the easier charging/discharging and optimum OCV observed for the sodium ion battery. We find that the T sheet remains metallic with a mid-gap state (Figure 3.14), whereas there is an usual narrowing of the band gap in the H sheet due to higher carbon proportion at the 10% BN-concentration. The electronic transport through T-borocarbonitrides remains similar for both the BN-concentrations (10% and 21%). A higher BN-concentration (>25%) results in the localisation of charge, thus decreasing the electronic transport through the sheet due to the enhanced electron scattering by

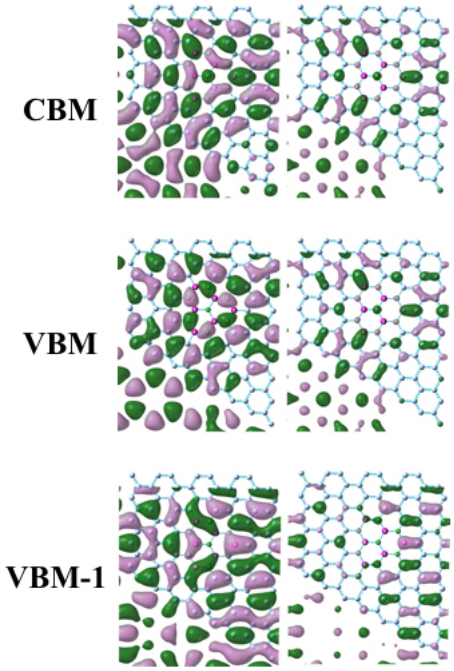

Figure 3.13: Real space wave function plot corresponding to the valence band maxima (VBM), VBM-1 and conduction band minima (CBM) states for borocarbonitride-monolayer with 10% BN concentration (with trigonal BN-domain). Two different iso-density plots have been shown. Iso value used for these plots is 0.02 and values of the density are 0.02 and 0.05 e $\mathring{A}^{-3}$, respectively from left to right column.

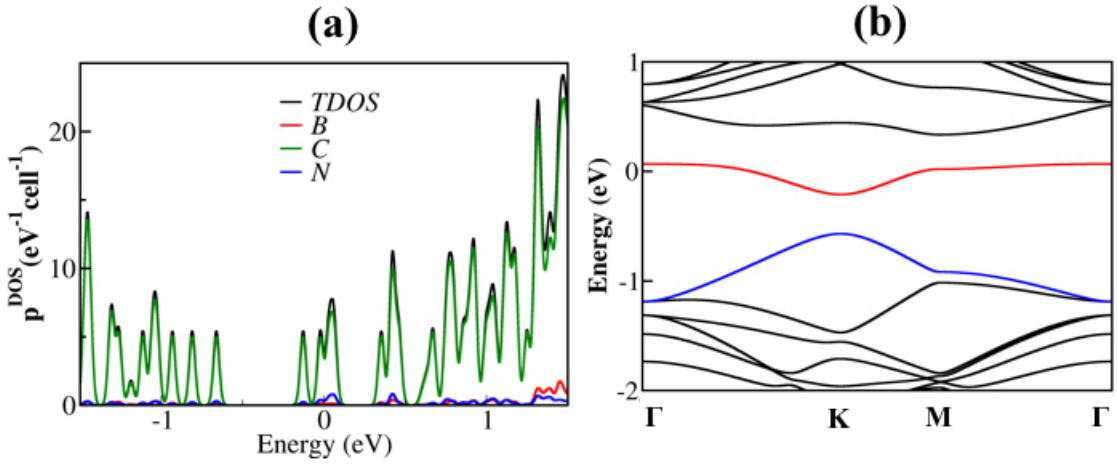

Figure 3.14: (a) Total density of states (TDOS) and projected density of states (pDOS) for BCN-sheet with 10% BN concentration (with trigonal BN-domain). Fermi energy (E_F) has been rescaled at zero. (b) Band dispersion pattern (path: $\Gamma - X - M - \Gamma$) is shown.

the BN clusters.[64,65] Hence, we propose that the ≈20% BN concentration (T) is optimum for the efficient electrochemical performance of the $B_xC_yN_z$-nanohybrid.

3.3.3 Intercalation of Li/Na into the T(H) Bi-layers

The average Li-insertion voltage for the intercalation of Li in layered T_N is found to be ∼2.50 V. This value is slightly larger than that of the monolayer (2.00 eV) as the Li atom binds strongly to both the layers at an equidistant arrangement (Figure 3.16). The range of voltage is qualitatively consistent with the experimental measurements too.[61] The absolute value of the adsorption energy of Li^+ ion is larger than the same for a Li atom. The interlayer space also exhibits a breathing motion (∼0.7 $\AA$) depending on the fact whether Li or Li^+ remains intercalated (Figure 3.16a and b and Figure 3.15). We find a 30% expansion in the interlayer

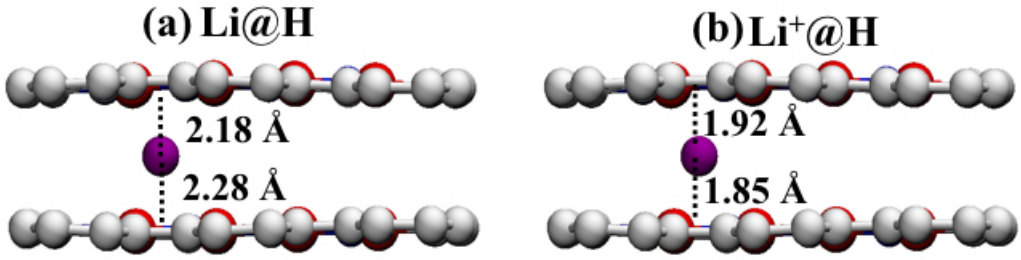

Figure 3.15: (a) Optimized stable configurations (side view) of lithium atom intercalated bilayer H sheet. (b) Optimized stable configurations (side view) of lithium ion intercalated bilayer H sheet.

distance revealing the exfoliation in the layered structure upon Na insertion. It clarifies the reason why fibre-like structures show good capacity retention ability.[66] On the other hand, the volume change is much lower (10%) for Li insertion in the layered anode. After intercalation of both the Li and Na, the bilayer becomes metallic in nature, which is similar to the monolayer (Figure 3.16c). The origin of such a transformation is the electron transfer from the adsorbed atom to the sheet. Bader and Lowdin population analyses were carried out to deter-

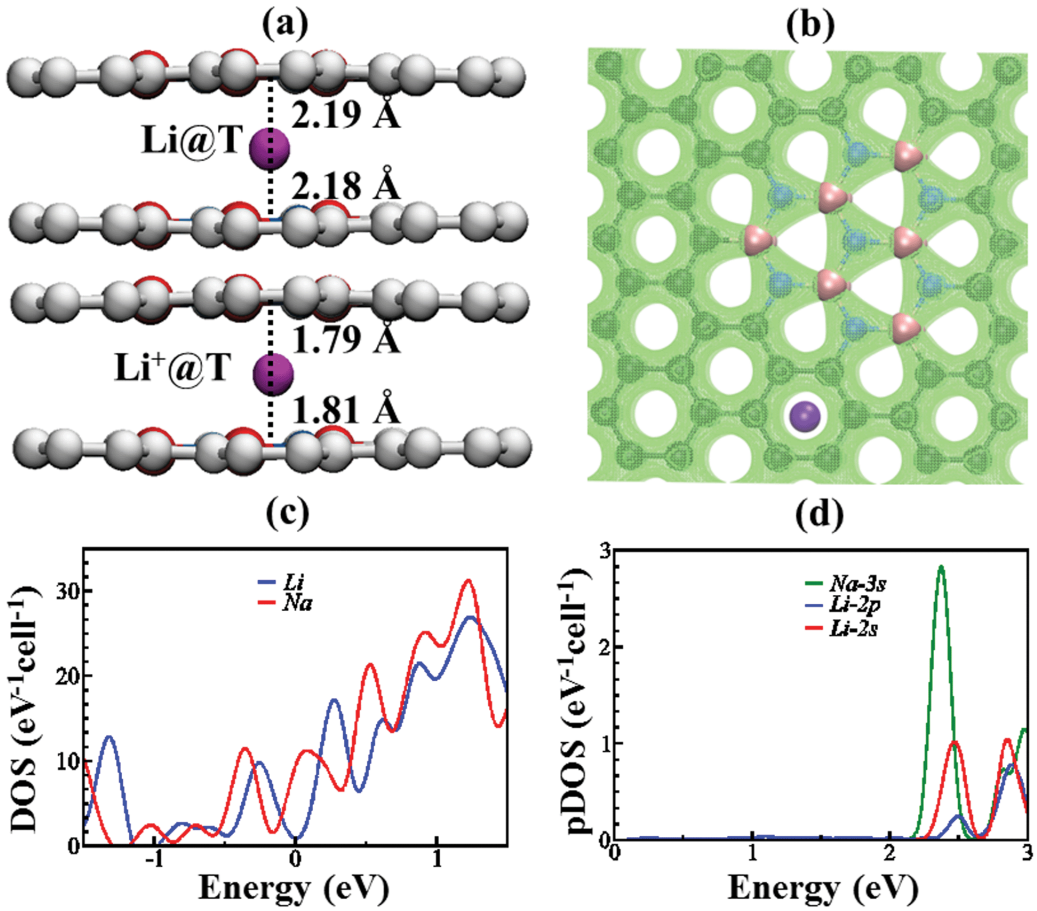

Figure 3.16: (a) The optimized stable configurations (side view) of the lithium intercalated bilayer T_N. (b) The top view showing intercalation at the middle of the hollow hexagonal site. A similar geometrical arrangement is also found for Na. (c) The total density of states (DOS) for the system with Li(Na) atoms intercalated into the T_N-anode. (d) The projected density of states (pDOS) of Li/Na. The Fermi energy has been rescaled at zero.

mine the partial charge on the M-ions and suggest complete electron transfer from the intercalated M to the electrode matrix [Li(Na): 0.96e(0.86e)]. The localized conduction state attributed to the 3 s orbital of Na suggests the electron-deficit nature of the Na and efficient anodic oxidation (Figure 3.16d). For Li, both the 2s and 2p states constitute the conduction band, which is broader than the Na-3s state. This suggests a more ionic nature for Na-binding to the anode and faster charging-discharging process. The presence of the nitrogen-excess B_xN_z-domain in borocarbonitride also facilitates an extraordinary electronic conduction. Thus,

the performance of the SIB with an T_N-anode can exceed the reversible capacity achieved so far with other carbonaceous electrodes as the anode.

3.3.4 Growth Morphology of Adsorbed Ions

In the preceding section, we argued on the superiority of the T_N sheet as an anode and Na-ion as the active ion for high energy density with appropriate OCV. In fact, in the fully charged state, the OCV can be affected by two factors: (i) Li-Li interactions between adjacent Li at the adsorbed state and (ii) Li-adsorption causes polarization to the sheet, which has great impact on the Li-adsorption affinity at high concentrations. Hence, it is worth studying how the power density of the electrochemical set-up is dependent on the growth morphology of the adsorbed ions. The growth morphology of the Li/Na ions on the electrode-surface is governed by the thermodynamic feasibility of clusterification and the diffusion kinetics of the adsorbed ions.[67] Nonetheless, the nature of the growth has been understood from the ratio of the adsorption energy (Ea) and bulk cohesive energy (E_c).[68] In this study, we used the experimental cohesive energy per atom of the bulk metal (E_c).[54] The value of Ea/E_c for Li(Na) varies from 1.23(1.01) to 0.92(1.12) for low to high concentrations of adsorbed Li(Na), which implies that the metal ad-atoms prefer a 2D growth mode on the substrate. On the other hand, the lower value of Ea/E_c (0.33) indicates the predominance of the interatomic interactions among the Mg ad-atoms, which favours the 3D island growth mode. Indeed, the cohesive energy (CE) of M-clusters at x = 0.9 were found to be considerate, $\sim$0.73($\sim$0.55) meV per atom for Li(Na), which is attributed to the significant bonding between atoms forming clusters (Figure 3.17). Such a high cohesive energy promoting the clusterification process can have two important outcomes: (i) an increase in the specific capacity and (ii) control over the ionic-diffusivity. Hence, we reconsidered the cohesive energy plus the adsorption energy and define R = $(E_a + E_c)/E_c$ to

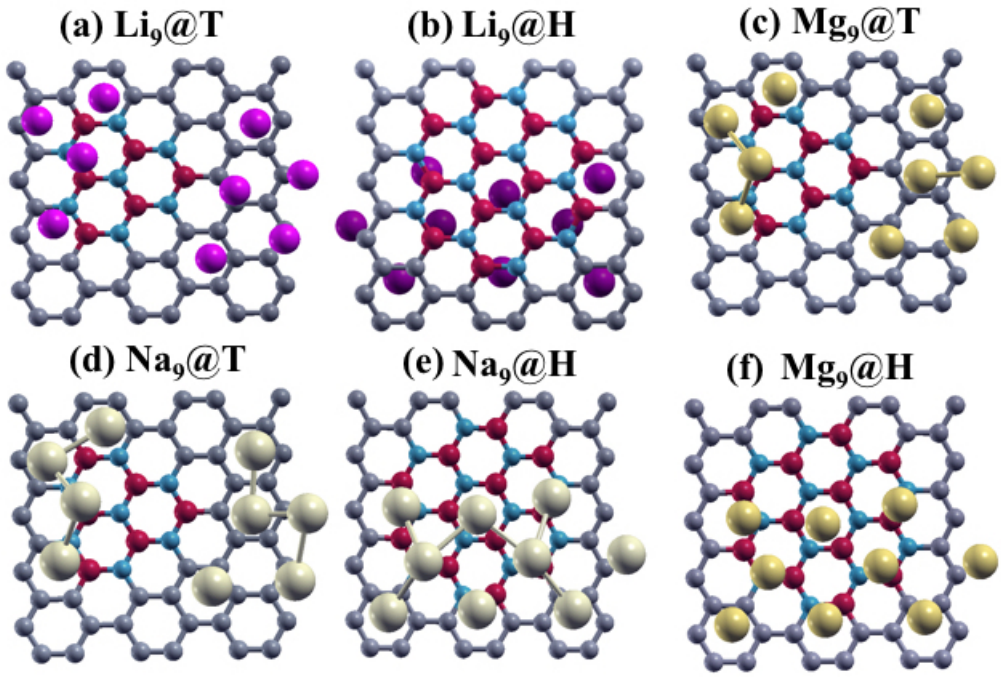

Figure 3.17: Optimized stable configurations of 9 atoms (Li, Na and Mg) adsorbed on the monolayer T_N and H sheets.

determine the growth process at higher concentrations. For Li and Na: R $>$ 1, whereas for Mg: R $<$ 1. Thus, the alkali metals (Li and Na) have R values larger than 1, suggesting the prevention from aggregation or segregation of the stored ions even at high concentrations. A dissimilar behavior was found for the alkaline earth metal Mg. Thus, the large R value observed for the Li and Na adsorption may bring a solution to the problem arising due to metal deposition in the conventional LiB/SIB systems. The thermal stability of the metal-island is a key factor to understand the growth mode. The difference of the bulk cohesive energy and adsorption energy ($E_c - E_a$) can express the thermal stability. Coarsening of the ad-atom island will take place easily for the small value of $E_c - E_a$ as found in the case of Li and Na. Therefore, Li and Na atoms in the adsorbed state can be easily detached from a small island and move to a bigger island. Noticeably, coarsening is always 2D in nature and independent of the shape of the B_xN_z domain

(Figure 3.17 and 3.18).

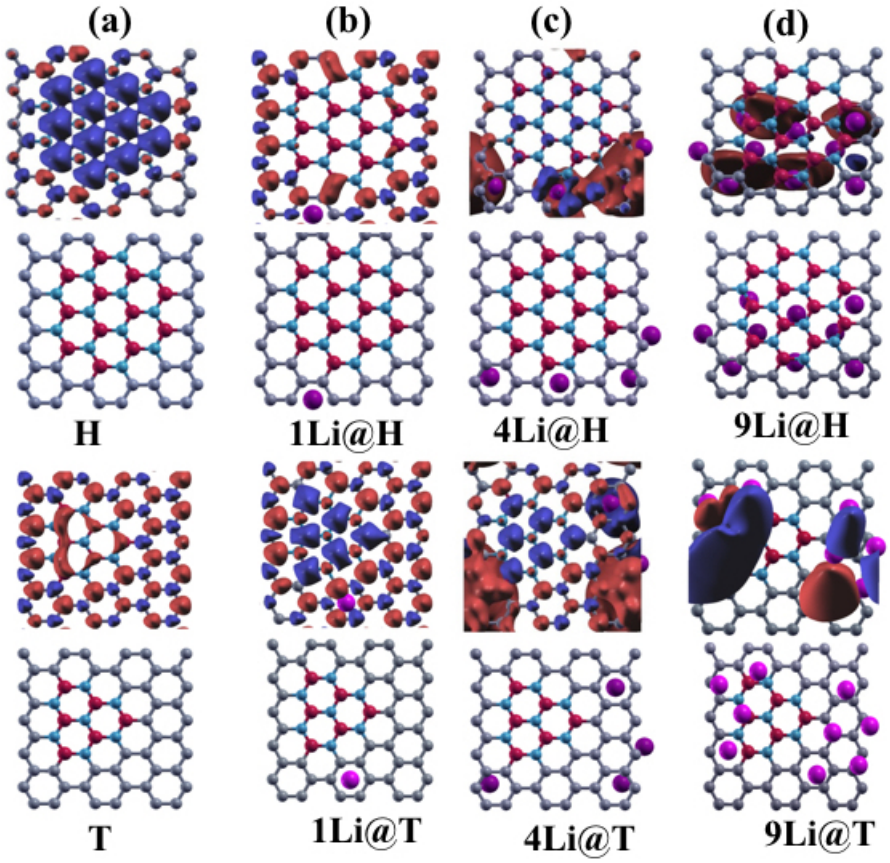

Figure 3.18: Optimized stable configurations of n Li atoms adsorbed on the monolayer H and T_N sheets: (a) n = 0, (b) n = 1, (c) n = 4, (d) n = 9. Charge density with an isosurface value of 0.01e $\mathring{A}^{-3}$ for borocarbonitride monolayer and the same with Li adsorbed at different concentration. The red and blue regions indicate an increase and decrease in electron density, respectively.

3.3.5 Li/Na-ion Diffusivity

The diffusion barrier is an important physical quantity in this regard. At higher concentrations, the formation of a 2D metallic layer further decreases the diffusion barrier through the collective movement of the adsorbed species. As the Li concentration increases, the difference in the adsorption energy for different Li distributions becomes smaller and vanishes quickly due to the formation of 2D

clusters (see Figure 3.7d) with significant CE. Considerate CE allows the placement of ad-atoms on the sheet for all possible sites, which is similar to the case of a metallic layer of Li intercalated into layers, as illustrated in Figure 3.7. This essentially can give rise to an intercalated layer of the 2D metallic sheet made up of M-ions. We also find that the Li and Na metal islands show high thermal stability against island coarsening and bulk formation. Li(Na) clusters with their 2D nature in the surface-adsorbed (Figure 3.19b, e) state is considered as the fully charged state. To this end, it is highly desirable to understand the nature of bonding and charging/discharging of M-clusters as the fully charged state involves the diffusivity of clusters rather than the simple isolated ions.

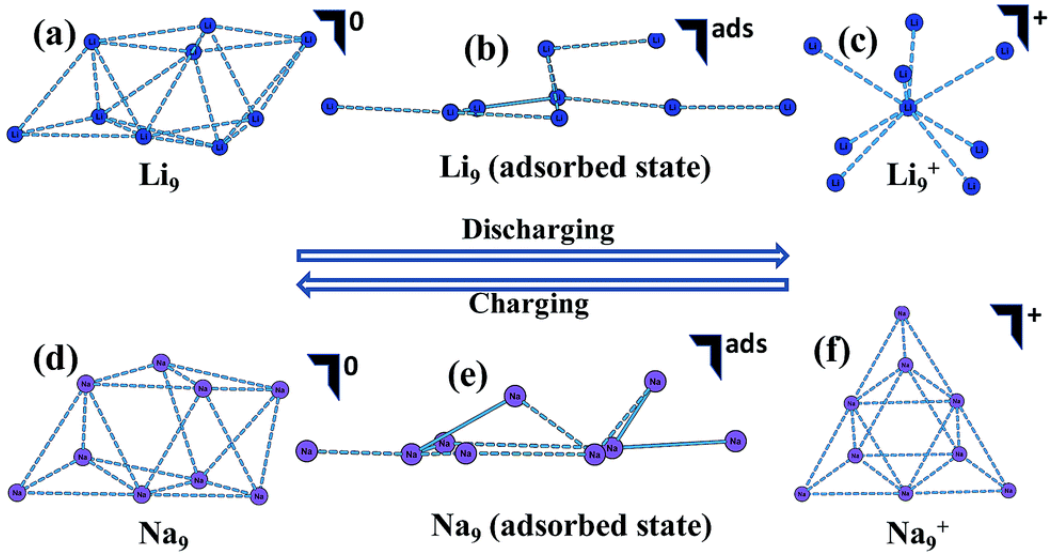

Figure 3.19: The relaxed geometry of isolated Li and Na clusters in their neutral state are shown in (a) and (d). (b, e) Li and Na ad-atom clusters in their charged state and (c, f) discharged state, while T_N has been considered as the anode. $M_9^+ + e^- + T_N \rightarrow M_9@T_N$ (charging); $M_9@T_N \rightarrow M_9^+ + e^- + T_N$ (discharging). Molecular orbital diagram for Li and Na clusters in their charged and neutral states (while T_N has been considered as the anode). The iso value used for these plots is 0.02 and the density is 0.01 e $Bohr^{-3}$.

At the maximum limit of specific capacity (336 $mAhg^{-1}$) corresponding to the $Li_{0.9}S_6$ composition, we find the Li-cluster with a maximum size limit of 9-atoms. Such a quasi-2D cluster can be considered as a potential active ion (Figure 3.19).

The size of the cluster is ~ 0.8 nm in its optimized neutral state (Figure 3.19a and d). In the adsorbed state, the cluster gets more flattened due to the significant surface affinity of the adsorbed atoms (Figure 3.19b and e). While charging with extra positive charge (M_9^+), the cluster becomes perfectly 3D (Figure 3.19c, f) revealing the disruption of the stable 2D layer in the charged state. Li_9^+ assumes a distorted body-centred cubic arrangement and Na_9^+ forms a 3D trigonal prismatic geometry. Such 2D to 3D transformation results in a decrease in the area of contact with the surface and facilitates the desorption of the stored M-ions during discharging. This effect is more prominent for the Na-cluster, which has a lower number of surface atoms (three) compared to Li_9^+ (eight). In addition, the larger size of Na leads to a decrease in the coordination number. The Na-Na bond distance increases when compared to the standard covalent bond (difference: ~ 0.8 $\mathring{A}$), while the Li-Li bond appears to be stronger than the single covalent bond. Therefore, we predict much easier desorption of the Na-ions during discharging owing to the weaker bonding among the Na atoms in the cluster-geometry. The molecular orbital diagram clearly predicts the occupancy and deficiency of the electrons on various atoms in the molecular clusters (Figure 3.20 and Table 3.4). The localised regions of electron density within the crystal voids are found and visualised by calculating the electron densities of the occupied states (H-1 and H, Figure 3.20) to detect the interstitial regions. In the Li_9^+ cluster, one Li residing on the centre possesses a highly positive (+0.98e) charge. Importantly, the surface atoms in the Li_9^+ cluster are neutral with one valence s-electron in each and form a diffused electronic cloud (see Figure 3.21 and Table 3.4).

In contrast, the Na atoms placed on the surface of the Na_9-cluster have a lower coordination number and possess a highly negative charge ($\sim$-1e). Five Na atoms situated in the core-region of the cluster have comparatively higher coordination numbers and acquire a highly positive ($\sim$+1e) charge on each atom. Such high surface-charge density in the Na_9^+ cluster plays two important roles:

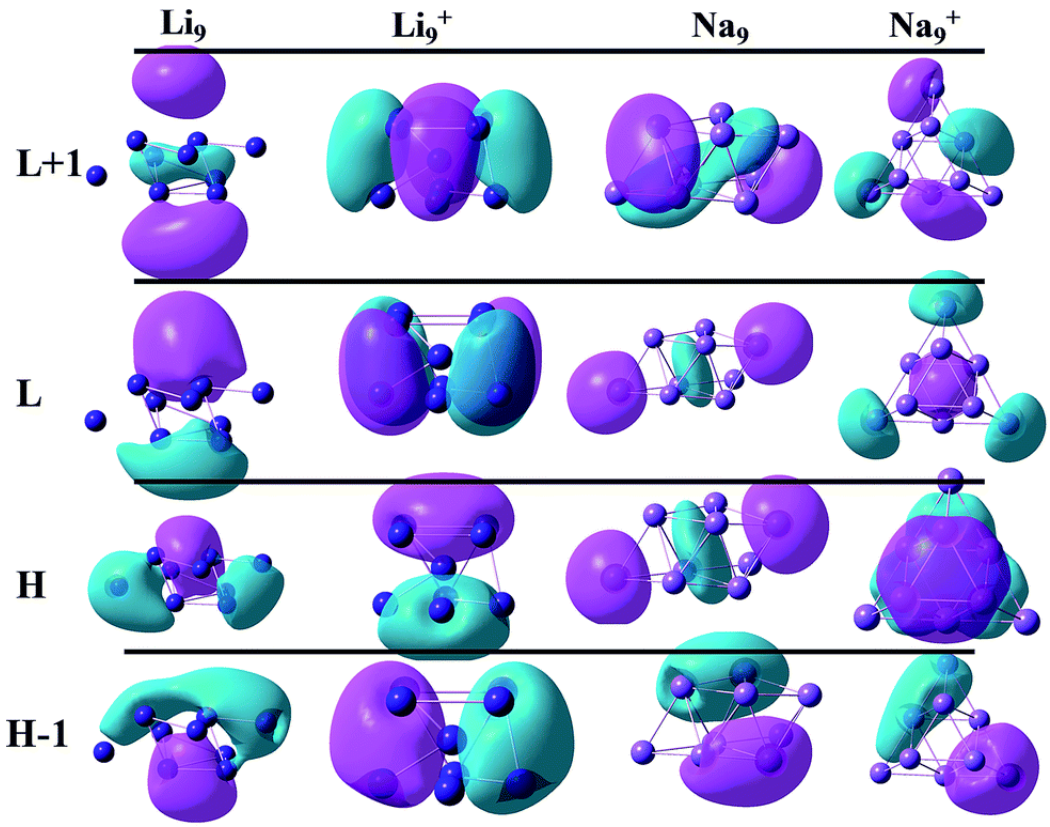

Figure 3.20: Molecular orbital diagram for Li and Na clusters in their neutral and charged states (while T_N has been considered as the anode). The iso value used for these plots is 0.02 and the density is 0.01 e $Bohr^{-3}$.

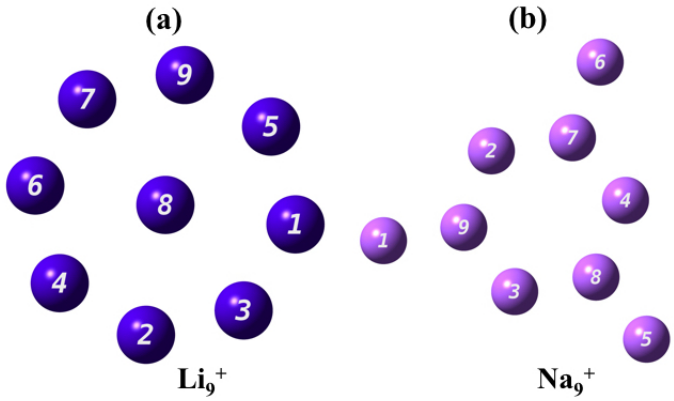

Figure 3.21: Stable configurations (2D view) of lithium and sodium cluster (positively charged). Atom numbers, N_M, are shown.

Table 3.4: Bader charge (e) on the Lithium and Sodium atoms in the Li and Na clusters as shown in Figure 3.19. Numbering of cluster atoms (N_M) are shown in Figure 3.21.

$\mathbf{N}_M$	**Li**	**Na**
1	0.01	-1.03
2	0.02	+0.98
3	0.02	+0.98
4	0.05	+0.98
5	-0.02	-1.03
6	-0.02	-1.03
7	+0.04	+0.98
8	+0.98	+0.98
9	-0.03	-0.74

(1) it prohibits the agglomeration process, which keeps the alkali ion cluster small in size and results in high diffusion and (2) the highly negative charge on the surface atom can facilitate the desorption process due to the repulsive interaction with the negatively charged electrode surface. This can result in a faster rate performance for charging/discharging the Na-ion cell. These characteristic features are applicable for both rechargeable batteries and supercapacitors.

3.4 Conclusions

In summary, we have studied the anodic properties of borocarbonitride ($B_xC_yN_z$) in M-ion batteries and capacitors (M: Li, Na and Mg). The $Na_{2.2}B_xC_yN_z$ exhibits a reversible capacity of 810 $mAhg^{-1}$ at an average storage voltage of 1.25 V which is far from the sodium plating voltage, making the battery potentially safer. We find (1) T_N-$B_xC_yN_z$ facilitates faster transport and transfer of electrons through the sheet. Thus, the T_N-anode serves the purpose of a superior electrode with high charge/discharge rate. (2) The Li(Na)-ion battery can exhibit an open circuit voltage of 1.50-2.00 eV (1.25 eV) with the T_N-anode. Therefore, the overall cell voltage for LIB and SIB can be applicable for practical purposes. (3) The

2D metallic layers made up of Li(Na) result in compact storage on the surface of the monolayer T_N and the estimated specific capacity is as high as 672(810) $mAhg^{-1}$. (4) Electronic conduction through the metallic state and fast Na-ion diffusion with the migration energy barrier as small as 0.15 eV can give rise to a high power efficiency for SIB. The estimated Na-diffusion (at 300 K) on T_N would be 102 times higher than that of a Li-ion on the T_N-anode. In the fully charged state, the formation of 2D clusters removes the discrimination among the various preferential sites, which effectively reduces the diffusion barrier further. Thus, irrespective of the charge state, the Na-ion cell can exhibit a higher power efficiency than the Li-ion cell. (5) During charging, the deposited Li(Na) atoms arrange to form clusters by sharing valence pairs. Such clusters store charges in the centre (surface) of the Li-cluster (Na-cluster). This reveals that sodium is a better choice than lithium in terms of (i) the coulombic efficiency for electron transfer and (ii) the facile adsorption/desorption process during cycling. Moreover, charging with extra positive charge results in the conversion of a stable 2D metallic layer to a 3D metal-cluster, which helps faster rate performance during the charge/discharge process. (6) The formation of a double-layer structure on the electrode surface with significant charge storage at the interstitial leads to superior performance of the Na-ion capacitor compared to its Li-ion analogue. Accordingly, we suggest an efficient design of the $B_xC_yN_z$ anode using a simple approach making the B_xN_z domain ($\sim$20% BN concentration) triangular and with an N-excess. We also justify the superiority of Na as the active ion for batteries and capacitors due to its better efficiency in the electron transfer process, ionic diffusion and smaller sized nano-cluster with high surface charge. The knowledge on how Li/Na is stored in the electrode material can also be used for various electrochemical set-ups. Tuning the B:C:N ratio in T_N may further improve the electrochemical performance. Thus, these findings open a new avenue in the search of better negative electrode materials for sodium-ion batteries. Understanding the interfacial properties and

screening of the appropriate electrolyte need special attention for future endeavour.

References

[1] Z. Yang, J. Zhang, M. C. Kintner-Meyer, X. Lu, D. Choi, J. P. Lemmon, and J. Liu, Chemical Reviews **111**, 3577 (2011).

[2] B. Dunn, H. Kamath, and J.-M. Tarascon, Science **334**, 928 (2011).

[3] C. D. Wessells, R. A. Huggins, and Y. Cui, Nature Communications **2**, 550 (2011).

[4] M. Pasta, C. D. Wessells, R. A. Huggins, and Y. Cui, Nature Communications **3**, 1149 (2012).

[5] J. B. Goodenough and K.-S. Park, Journal of the American Chemical Society **135**, 1167 (2013).

[6] A. . K. Padhi, K. Nanjundaswamy, and J. Goodenough, Journal of the Electrochemical Society **144**, 1188 (1997).

[7] J. B. Goodenough and Y. Kim, Chemistry of Materials **22**, 587 (2009).

[8] M. M. Thackeray, C. Wolverton, and E. D. Isaacs, Energy & Environmental Science **5**, 7854 (2012).

[9] N. Yabuuchi, M. Kajiyama, J. Iwatate, H. Nishikawa, S. Hitomi, R. Okuyama, R. Usui, Y. Yamada, and S. Komaba, Nature Materials **11**, 512 (2012).

[10] M. H. Han, E. Gonzalo, G. Singh, and T. Rojo, Energy & Environmental Science **8**, 81 (2015).

[11] S. Komaba, T. Nakayama, A. Ogata, T. Shimizu, C. Takei, S. Takada, A. Hokura, and I. Nakai, Ecs Transactions **16**, 43 (2009).

[12] D. Stevens and J. Dahn, Journal of The Electrochemical Society **147**, 1271 (2000).

[13] Y. Cao, L. Xiao, M. L. Sushko, W. Wang, B. Schwenzer, J. Xiao, Z. Nie, L. V. Saraf, Z. Yang, and J. Liu, Nano Letters **12**, 3783 (2012).

[14] Y. Mizutani, T. Abe, M. Inaba, and Z. Ogumi, Synthetic metals **125**, 153 (2001).

[15] R. Song, H. Song, X. Chen, Y. Cui, J. Zhou, and S. Zhang, Electrochimica Acta **127**, 186 (2014).

[16] F. Wang, R. Song, H. Song, X. Chen, J. Zhou, Z. Ma, M. Li, and Q. Lei, Carbon **81**, 314 (2015).

[17] S. Komaba, W. Murata, T. Ishikawa, N. Yabuuchi, T. Ozeki, T. Nakayama, A. Ogata, K. Gotoh, and K. Fujiwara, Advanced Functional Materials **21**, 3859 (2011).

[18] V. L. Chevrier and G. Ceder, Journal of The Electrochemical Society **158**, A1011 (2011).

[19] K. Tang, L. Fu, R. J. White, L. Yu, M.-M. Titirici, M. Antonietti, and J. Maier, Advanced Energy Materials **2**, 873 (2012).

[20] W. Luo, J. Schardt, C. Bommier, B. Wang, J. Razink, J. Simonsen, and X. Ji, Journal of Materials Chemistry A **1**, 10662 (2013).

[21] S. Wenzel, T. Hara, J. Janek, and P. Adelhelm, Energy & Environmental Science **4**, 3342 (2011).

[22] Z.-S. Wu, W. Ren, L. Xu, F. Li, and H.-M. Cheng, ACS nano **5**, 5463 (2011).

[23] N. Kurita, Carbon **38**, 65 (2000).

[24] S. Banerjee, G. Periyasamy, and S. K. Pati, Journal of Materials Chemistry A **2**, 3856 (2014).

[25] L. Ci, L. Song, C. Jin, D. Jariwala, D. Wu, Y. Li, A. Srivastava, Z. Wang, K. Storr, L. Balicas, et al., Nature materials **9**, 430 (2010).

[26] Y. Lin and J. W. Connell, Nanoscale **4**, 6908 (2012).

[27] M. Chhetri, S. Maitra, H. Chakraborty, U. V. Waghmare, and C. Rao, Energy & Environmental Science **9**, 95 (2016).

[28] W. Lei, S. Qin, D. Liu, D. Portehault, Z. Liu, and Y. Chen, Chemical communications **49**, 352 (2013).

[29] S. H. Lee, S.-H. Yu, J. E. Lee, A. Jin, D. J. Lee, N. Lee, H. Jo, K. Shin, T.-Y. Ahn, Y.-W. Kim, et al., Nano Letters **13**, 4249 (2013).

[30] Y. Liu, S. Bhowmick, and B. I. Yakobson, Nano Letters **11**, 3113 (2011).

[31] Y. Gong, G. Shi, Z. Zhang, W. Zhou, J. Jung, W. Gao, L. Ma, Y. Yang, S. Yang, G. You, et al., Nature Communications **5** (2014).

[32] A. K. Manna and S. K. Pati, The Journal of Physical Chemistry C **115**, 10842 (2011).

[33] C. Rao, K. Gopalakrishnan, and A. Govindaraj, Nano Today **9**, 324 (2014).

[34] K. Gopalakrishnan, K. Moses, A. Govindaraj, and C. Rao, Solid State Communications **175**, 43 (2013).

[35] V. Augustyn, P. Simon, and B. Dunn, Energy & Environmental Science **7**, 1597 (2014).

[36] V. Augustyn, J. Come, M. A. Lowe, J. W. Kim, P.-L. Taberna, S. H. Tolbert, H. D. Abruña, P. Simon, and B. Dunn, Nature Materials **12**, 518 (2013).

[37] P. Simon, Y. Gogotsi, and B. Dunn, Science **343**, 1210 (2014).

[38] C. Chen, Y. Wen, X. Hu, X. Ji, M. Yan, L. Mai, P. Hu, B. Shan, and Y. Huang, Nature Communications **6** (2015).

[39] P. Yu, C. Li, and X. Guo, The Journal of Physical Chemistry C **118**, 10616 (2014).

[40] S. Banerjee, S. Neihsial, and S. K. Pati, Journal of Materials Chemistry A **4**, 5517 (2016).

[41] S. Banerjee and S. K. Pati, Nanoscale **6**, 13430 (2014).

[42] P. E. Blöchl, Physical Review B **50**, 17953 (1994).

[43] S. Grimme, J. Antony, S. Ehrlich, and H. Krieg, The Journal of Chemical Physics **132**, 154104 (2010).

[44] P. Giannozzi, S. Baroni, N. Bonini, M. Calandra, R. Car, C. Cavazzoni, D. Ceresoli, G. L. Chiarotti, M. Cococcioni, I. Dabo, et al., Journal of Physics: Condensed Matter **21**, 395502 (2009).

[45] J. P. Perdew, K. Burke, and Y. Wang, Physical Review B **54**, 16533 (1996).

[46] B. Hammer, L. B. Hansen, and J. K. Nørskov, Physical Review B **59**, 7413 (1999).

[47] J.-P. Soulié, G. Renaudin, R. Černỳ, and K. Yvon, Journal of Alloys and Compounds **346**, 200 (2002).

[48] K. Kunc and R. M. Martin, Physical Review Letters **48**, 406 (1982).

[49] K. Miwa, N. Ohba, S.-i. Towata, Y. Nakamori, and S.-i. Orimo, Physical Review B **69**, 245120 (2004).

[50] Y. Zhao and D. G. Truhlar, Theoretical Chemistry Accounts **120**, 215 (2008).

[51] M. J. Frisch, G. Trucks, H. Schlegel, G. Scuseria, M. Robb, J. Cheeseman, G. Scalmani, V. Barone, B. Mennucci, G. Petersson, et al., Gaussian Inc., Wallingford, CT (2009).

[52] B. P. Prascher, D. E. Woon, K. A. Peterson, T. H. Dunning Jr, and A. K. Wilson, Theoretical Chemistry Accounts **128**, 69 (2011).

[53] J. W. Ochterski, Gaussian Inc pp. 1–19 (2000).

[54] C. Kittel, Tech. Rep., ISBN 978-0-471-41526-8 (2004).

[55] W. Wang, S. Dai, X. Li, J. Yang, D. J. Srolovitz, and Q. Zheng, Nature Communications **6** (2015).

[56] M. Aydinol, A. Kohan, G. Ceder, K. Cho, and J. Joannopoulos, Physical Review B **56**, 1354 (1997).

[57] R. E. Doe, K. A. Persson, Y. S. Meng, and G. Ceder, Chemistry of Materials **20**, 5274 (2008).

[58] C. Uthaisar, V. Barone, and J. E. Peralta, Journal of Applied Physics **106**, 113715 (2009).

[59] S. Komaba, K. Okushi, T. Ozeki, H. Yui, Y. Katayama, T. Miura, T. Saito, and H. Groult, Electrochemical and Solid-State Letters **12**, A107 (2009).

[60] Y. Li, D. Wu, Z. Zhou, C. R. Cabrera, and Z. Chen, The Journal of Physical Chemistry Letters **3**, 2221 (2012).

[61] S. Sen, K. Moses, A. J. Bhattacharyya, and C. Rao, Chemistry–An Asian Journal **9**, 100 (2014).

[62] G. Henkelman and H. Jónsson, The Journal of Chemical Physics **113**, 9978 (2000).

[63] L.-J. Zhou, Z. Hou, and L.-M. Wu, The Journal of Physical Chemistry C **116**, 21780 (2012).

[64] C.-K. Chang, S. Kataria, C.-C. Kuo, A. Ganguly, B.-Y. Wang, J.-Y. Hwang, K.-J. Huang, W.-H. Yang, S.-B. Wang, C.-H. Chuang, et al., Acs Nano **7**, 1333 (2013).

[65] Y. Gong, H. Fei, X. Zou, W. Zhou, S. Yang, G. Ye, Z. Liu, Z. Peng, J. Lou, R. Vajtai, et al., Chemistry of Materials **27**, 1181 (2015).

[66] L. Fu, K. Tang, K. Song, P. A. van Aken, Y. Yu, and J. Maier, Nanoscale **6**, 1384 (2014).

[67] H. Xiong, M. D. Slater, M. Balasubramanian, C. S. Johnson, and T. Rajh, The Journal of Physical Chemistry Letters **2**, 2560 (2011).

[68] X. Liu, C.-Z. Wang, M. Hupalo, W. Lu, M. C. Tringides, Y. Yao, and K.-M. Ho, Physical Chemistry Chemical Physics **14**, 9157 (2012).

4

Black Phosphorus as Anode in Magnesium-ion Battery: the Significance of Mg-P Bond Synergy*

4.1 Introduction

Magnesium-based batteries (MgB) represent the most demanding category of the upcoming battery technologies.[1,2] MgB is based on a metal that is light, cheap and environmentally friendly. Like lithium cells, these batteries are also 'rocking-chair' devices in which magnesium ions shuttle back and forth during the discharge and recharge cycles. The anode is generally commercial magnesium alloy and pure magnesium. Cathode is Mo_6S_8, which can intercalate magnesium reversibly. The polymer gel in which Mg-ions can exhibit high ionic diffusivity, act as electrolyte. Recently, integration of all these components forming MgBs[3,4] have

*Work reported in this chapter is published in: Swastika Banerjee and Swapan K Pati, Chem. Commun., **52**, 8381-8384 (2016).

attracted huge attention to address the energy needs of large scale device applications. Compared to Li/Na-ion batteries (LIBs/SIBs), the electrochemical capacity is enhanced by a factor of two in the presence of a bivalent Mg-ion, which leads to a concomitant increase in the energy density of the Mg-ion cells.[5] Additionally, abundant raw materials and high-safety characteristics make MgB technology more practical. However, current state-of-the-art rechargeable Mg batteries are far from reaching their promised potential.[6] Several serious limitations, such as the absence of a low-potential anode, improper electrolyte[7] and lack of a high voltage/capacity cathode,[8,9] remain to be resolved. Particularly, the negative-limited performance of MgB due to Mg-anode/electrolyte incompatibility is very common.[10,11] To overcome this problem, the metallic Mg-anode has been replaced with the insertion-type anode, such as $Bi_{0.55}Sb_{0.45}$, exhibiting low potential (0.4 V vs. bulk Mg).[12] However with this, specific capacity, as well as the cycling rate, is found to be poor (298 $mAhg^{-1}$ at a 1C rate). Recently, alloying/de-alloying reactions in Mg/Sn intermetallic phases promise the low working potential (0.15 V vs. bulk Mg) associated with high capacity (903 $mAhg^{-1}$).[13] However, the poor Columbic efficiency and substantial volume expansion (214%) limit the anodic performance. Indeed, two fundamental issues remain as key hurdles: (a) structural instability during the charging/discharging cycle, and (b) very slow diffusion of Mg^{2+} ions within the anode. Sluggish Mg^{2+}-diffusion arises from high polarizability of the bivalent cation,[8,11,14] which can be overcome by using a covalent anode-host. In this regard, chemistry of the electrode (anode)-ion reaction is very crucial.[15–18] On the other hand, achieving efficient cyclability requires the knowledge of the maximum limit for charging which needs a thorough understanding of different state-of-charge (SOC) of an anode. In this chapter, we highlight the anodic performance of elemental phosphorus (P) which provides a sufficiently covalent framework. The P-matrix can also store Li (Na)-ions up to Li_3P[19–22] (Na_3P)[23,24] compositions, resulting in a high capacity (2596 $mAhg^{-1}$). Herein,

we report on the thermodynamics and kinetic properties of Mg-ions within the P-matrix through first principles computations. Microscopic details on different SOC of the P-anode reveal that charging up to MgP composition circumvents the difficulties associated with the pulverization of the P-anode, which has been found to disrupt the LIBs/SIBs set-up at a high-charge-state.[20,22,24] Additionally, P-Mg interaction effectively reduces the polarizability of Mg^{2+}-ions, which is immensely useful in achieving fast Mg-diffusion kinetics. Thus, the combination of Mg-ions and the P-anode deserves attention for its practical applications as well as fundamental understanding of chemical bonding.

4.2 Computational Method

Electronic structure calculations are based on Density Functional Theory[25–27] (DFT-D2[28]) and Ab initio Molecular Dynamics (AIMD)[29,30] . For all DFT-based calculations, Electron-ion interactions and electron exchange-correlation interactions have been taken into account by Projector- augmented-wave (PAW) potentials,[31] and generalized gradient approximation (GGA),[32] respectively, as implemented in Vienna ab initio simulation package (VASP).[33,34] Plane wave cut-off of 600eVis used for all the calculations. The conjugate gradient algorithm is used to obtain the unstrained configuration. Atomic relaxation is performed until the change in total energy is less than 0.01 meV and all the forces on each atom are smaller than 0.01 eV/$\mathring{A}$. K- point samplings of 7 x 7 x 1 (monolayer phosphorene) and 7 x 7 x 7 (bulk black phosphorus) are used for the structure relaxation. Dense k-meshes of 15 x 15 x 1 (monolayer) and 15 x 15 x 15 (bulk) are used to find the total energy, density of states and electron density. For the monolayer phosphorene, a vacuum space of 20 $\mathring{A}$ is placed between adjacent layers to avoid mirror interactions. Bulk black phosphorus is denoted as P, throughout the manuscript. Regarding the size of the P-anode, we would like to mention clearly that bulk

form of black phosphorus is considered in this study, which is periodic along all three directions. To model different SOC, a series of Mg_qP compositions with varying q values are taken into account with 2 x 2 x 1 supercell with 32 P atoms. For 2D phosphorene, we have considered 2 x 2 x 1 supercell with 16 P atoms. To understand the nature of the chemical bonding in M_qP composites (M = Li, Na and Mg), we have looked for the nature of the orbital overlap. Differential charge density has been computed by subtracting the superposition of the atomic charge densities from the total charge density in the crystal framework. ab initio Molecular Dynamics Simulations (NVT; 300 K) are based on quantum density functional theory using the same protocol as used for structural optimization.The length and time scales achieved in this study are 10 ps and 1fs, respectively. Nose-Hoover type thermostat has been applied as temperature bath. To investigate the microstructure of crystalline materials, integrated radial pair distribution function has been calculated which allows local bonding analysis of multi-component mixtures. Representation of the Radial pair distribution function (RPDF) is based on a structural model using:

$$G(r) = \frac{1}{r}\sum_i \sum_j \frac{f(0)_i f(0)_j}{\langle f(0)\rangle^2}\delta(r - r_{ij}) - 4\pi r\rho_0 \tag{4.1}$$

The atomic RPDF is written as,

$$g(r) = 4\pi r[\rho(r) - \rho(0)] \tag{4.2}$$

where, $\rho(0)$ is average atomic number density, and $\rho(r)$ is the atomic pair-density within the radial distance, r. Here the $f(0)$s are the atomic form factors evaluated at Q = 0 and Q denotes the momentum transfer. The simplified form of the so-called partial radial distribution functions, $g_{ij}(r)$, (when more than one chemical

species are present) is:

$$g_{ij}(r) = \frac{dn_{ij}(r)}{4\pi r^2 dr \rho_i}; \rho_i = \frac{V}{N_i} \tag{4.3}$$

where N_i represents the number density of atomic species, 'i'. These functions give the density probability for an atom of the 'i' species to have a neighbor of the 'j' species at a given distance r.

To visualize the bonding feature upon M-ion incorporation in α-phase, we have calculated the charge density difference using the following equation:

$$\Delta\rho(r) = \rho_{P+M}(r) - \rho_P(r) - \rho_M(r) \tag{4.4}$$

where $\rho_{P+M}(r)$ represents the charge density of M incorporated P-matrix, $\rho_P(r)$ is the charge density of the P, and $\rho_M(r)$ is the charge density of isolated M atoms in the same position as in the total systems. For the case of Li atom embedded in the interlayer space of P-matrix, a net loss of electronic charge could be found above the Li. On the other hand, large gain in charge on P- atoms demonstrate the significant electronic transfer from Li atom to the neighbouring P atoms, which indicates the high ionic bonding of the embedded Li atom. These findings are consistent with the previous Bader analysis,[35] and also confirm the high ionic interaction between Li and P.

4.3 Results and Discussion

4.3.1 Structural Phases at Different State-of-charge of Black Phosphorus Anode

In this chapter, the P-anode is orthorhombic black phosphorus (bulk), which is the most stable phosphorus allotrope under ambient conditions.[36] During charging,

Mg-ions get loaded into the interlayer space of the P-matrix. We have considered a series of Mg_qP compositions with varying q values to model different SOC. We find three distinct structural phases (α, β and γ), depending on the extent of charging ($0 \leqslant q \leqslant 1$). At a low charge state ($0 \leqslant q \leqslant 0.25$), the perfect two-dimensional (2D) P-framework (similar to phosphorene) is retained, and Mg ions get inserted into the interlayer space resulting in the α-phase (see Figure 4.1a). Further charging ($0.25 \leqslant q \leqslant 0.50$) leads to the β-phase, where the 2D framework of a phosphorene-like structure gets transformed into the 1D P-P chain (see Figure 4.1b). At q = 1.0, the MgP complex (γ-phase) is formed, which exhibits a complete 3D-network consisting of Mg-P bonds (see Figure 4.1c) and P-P dimers. Such Mg-insertion processes can be expressed as,

$$P_8 + 2Mg^{2+} + 4e^- = Mg_{0.25}P\ (\alpha - phase) \tag{4.5}$$

$$P_{0.25}P + 2Mg^{2+} + 4e^- = Mg_{0.50}P\ (\beta - phase) \tag{4.6}$$

$$P_{0.50}P + 4Mg^{2+} + 8e^- = MgP\ (\gamma - phase) \tag{4.7}$$

We note that there is a steady increase in the volume with a gradual increase in Mg-storage ($\alpha \rightarrow \beta \rightarrow \gamma$) (see Figure 4.1d(i) and Table 4.1). This is reminiscent of Vegard's law, as applicable for a solid-solution. However, there is a significant difference in a local bonding feature of Mg-ions at different structural phases (α, β, γ), as summarized in Figure 4.1d(i) and Table 4.1.

In the α-phase, each Mg has the effective coordination number (C.N.) as 6, with four equatorial (2.70 $\mathring{A}$) and two axial (2.58 $\mathring{A}$) Mg-P bonds. Mg-Mg (3.62 $\mathring{A}$) interaction is much weaker compared to the Mg-P interaction. On the other hand, in β and γ phases, the C.N. for Mg drops to 5 and 4, respectively, with a concomitant increase in the Mg-Mg interaction. In the β-phase, Mg atoms form a hexagonal chair structure with Mg-Mg bonds (3.14 $\mathring{A}$) shorter than that of

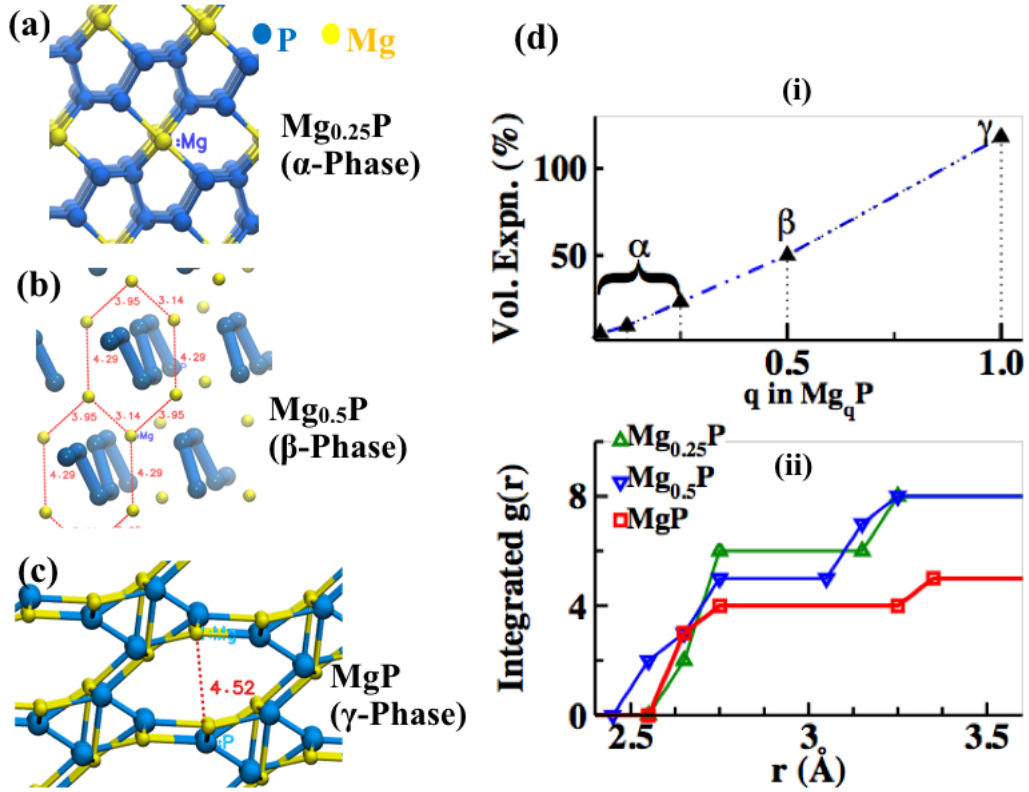

Figure 4.1: Optimised structures of Mg_qPs; for (a) q = 0.25; (b) q = 0.5 and (c) q = 1.0. In each case, 2 x 2 x 1 supercell is outlined, showing the Mg–P (cyan-yellow) and P–P (cyan) bonds. (d) (i) Volume expansion after a gradual increase in Mg content within the P-anode ($\alpha \rightarrow \beta \rightarrow \gamma$ phase). (ii) Integrated g(r) plots for Mg–P pairs (coordination number of Mg) for α, β and γ phases.

Mg-Mg van der Waals bond distance (3.46 $\mathring{A}$). Fusion of such hexagons results in the growth of the Mg-ad-layer (see Figure 4.1b). In the γ phase, Mg-Mg bonds become more stronger (2.92 $\mathring{A}$). However, there is no signature of strongly dimerized Mg systems which is confirmed by the bonding analysis where the cut-off distance up to 2.70 $\mathring{A}$ does not capture any Mg-Mg bond (see Figure 4.1c). Thus, in all the phases, Mg_qP behaves like a special class of solid solution, where Mg-agglomeration or even Mg-Mg covalent bond formation does not occur. Due to this, the charging process avoids Mg/P phase segregation, which essentially circumvents the pulverisation of the P-anode. This urges for quantification of the thermodynamic potential of Mg-storage to understand the electrode potential.

Table 4.1: Calculated lattice parameters (lattice vectors: a, b and c are in $\mathring{A}$ and corresponding angles are in degree (°) and volumes ($\mathring{A}^3$) of the conventional unit cell of bulk black phosphorus with varying concentrations of Mg-ions are given.

	a ($\mathring{A}$)	b ($\mathring{A}$)	c ($\mathring{A}$)	x (°)	y (°)	z (°)	V ($\mathring{A}^3$)
MgP	6.98	5.23	9.82	90.19	110.69	90.11	335.74
$Mg_{0.5}P$	4.21	6.71	11.45	69.19	68.40	51.12	230.86
$Mg_{0.25}P$	3.86	4.79	11.09	71.19	87.92	77.46	189.62
$Mg_{0.125}P$	3.25	4.71	11.55	72.30	90.07	89.98	168.30
$Mg_{0.06}P$	3.28	4.56	11.29	73.29	90.25	90.24	161.84
$Mg_{0.03}P$	3.26	4.51	11.38	72.65	90.00	90.00	160.83
$Mg_{0.02}P$	3.30	4.48	11.31	73.05	90.09	90.03	159.78
P_8	3.32	4.42	10.47	90.00	90.00	90.00	153.90

4.3.2 Electrochemical Properties

To estimate the thermodynamic potential (voltage) of Mg-ion insertion, E_b (V) at different states-of-charge, we apply Equation (4.8).

$$E_b(V) = \frac{E_{M_{q1}P} + (r \times E_M) - E_{M_{q2}P}}{r \times e} \tag{4.8}$$

where, r = q2 - q1 (q2 > q1) refers to the number of M-ion transferred, EM is the energy of an isolated (bulk) M atom, $E_{M_{q1}P}$ and $E_{M_{q2}P}$ are the total energies of $M_{q1}P$ and $M_{q2}P$, respectively. Positive E_b for Li, Na and Mg-ions over the range of $0 \leqslant q \leqslant 1$ (see Figure 4.2a) suggest the thermodynamic feasibility of the charging process and the stability of α, β and γ phases. A comparative analysis reveals that (1) E_b increases with an increase in 'q', suggesting the cooperative effect for gradual rise of Mg-content, which is absent in the case of Li and Na. (2) The storage potential of Mg-ions is optimum over a wide range of charging states, while it is too high for Li and too low for Na (see Figure 4.2a, b).

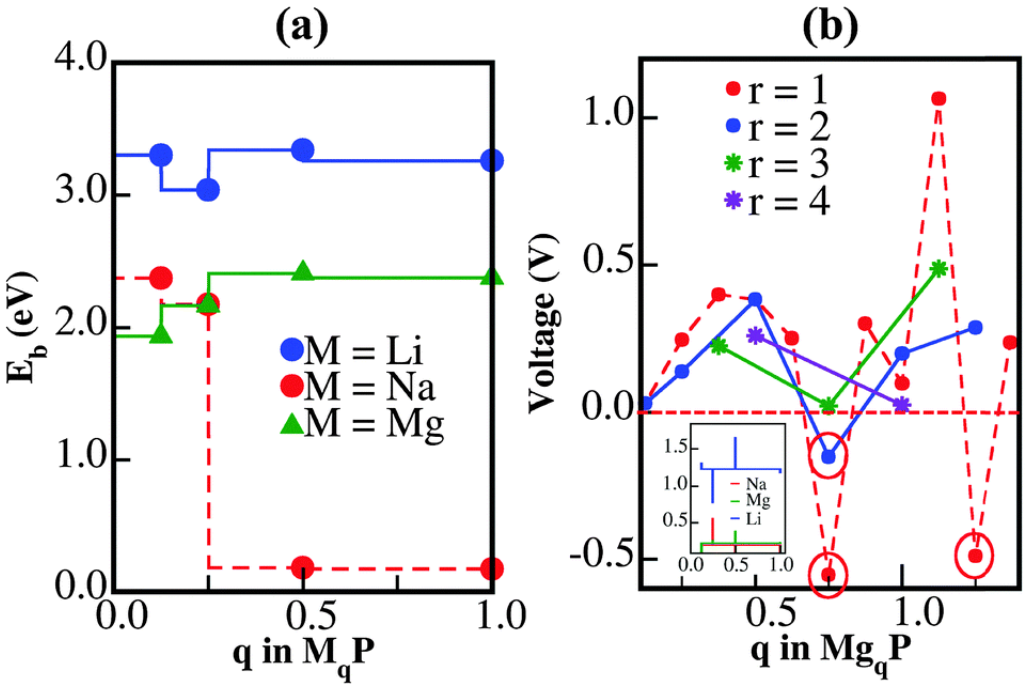

Figure 4.2: (a) Insertion potential of M-ions within the P-anode (E_b) vs. SOC (q). (b) Voltage (V) profile for the step-wise charging process for M = Mg. Zero is indicated by the red horizontal dotted line. Inset figure shows the V vs. q profiles for Li, Na and Mg, where the horizontal baselines indicate the average voltage (V_{avg}).

4.3.3 Mg-ion Diffusion

Besides the thermodynamics of Mg-ion storage, rate performance is also an important issue, which demands an in-depth understanding of Mg-ion diffusivity within the Mg_qP framework. We have carried out AIMD simulations at ambient temperature (300 K) for 10 ps with a step length of 1 fs, which is sufficient to capture the Mg-P bond reformation/reorientation mechanism in our systems.[37,38] Analyses of the Mg-trajectories indicate highly directional Mg-ion migration in all the three structural phases (α, β and γ), as shown in Figure 4.3a-c. However, each structural phase opens a unique diffusion-channel. In the α-phase, Mg-ion shuttles only along the z-direction (see Fig. 3a).

This essentially indicates that Mg-ion hopping in the α-phase is associated with a finite energy barrier (E_{diff}) which cannot be captured within the time

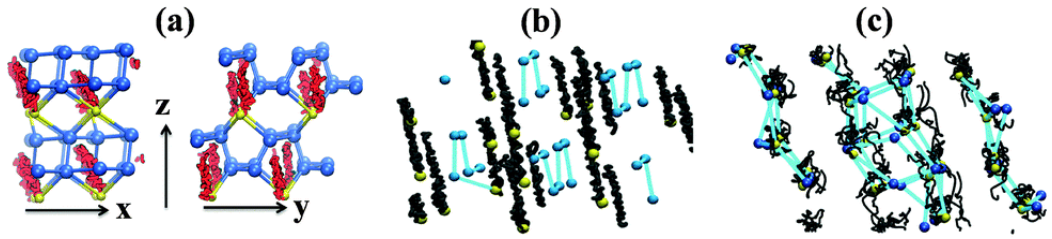

Figure 4.3: 2 x 2 x 1 supercell structure of (a) α-phase: Mg_8P_{32}, with in-plane (x, y) and out-of-plane (z) diffusion channels, (b) β-phase: $Mg_{16}P_{32}$, and (c) γ-phase: $Mg_{32}P_{32}$. Red and black wavy lines (a-c) show Mg-ion trajectory (10 ps) within the equilibrium structural framework.

scale of our simulation. On the other hand, in the β-phase, Mg-diffusion becomes barrier-less, which results in a spontaneous 2D transport of Mg-ions (see Figure 4.3b). The simulation time scale of 5 ps has also been able to capture the possible Mg-ion migration in the γ-phase through the cavity (diameter is 4.52 $\AA$; Figure 4.1c) within the cage-like framework (see Figure 4.3c). We find that reordering of the P-P dimers leads to the Mg-ion disorder in the solid MgP alloy which results in fast Mg-ion migration in the γ-phase. Thus, the preceding discussion proves spontaneous Mg-ion diffusion at higher charge states (β and γ phases), whereas, a finite diffusion barrier (E_{diff}) at a low charge state (α-phase) acts as the rate limiting factor. Here, we estimate the E_{diff} and rate of diffusion along different transport channels in the α-phase, using the Climbing Image Nudged Elastic Band (CI-NEB) method.[39,40] We find that the most favorable diffusion channel for interlayer Mg-diffusion is x (E_{diff} (x) is the least, Fig. 4a).

Compared to Li (Na)-ions, Mg-ions exhibit 7 (81) times higher rate of diffusion (see Figure 4.4b), as evaluated using the Arrhenius equation (at T = 300 K), where diffusion constant (D) is defined as:

$$D = A\ exp\{\frac{-E_{diff}}{K_B T}\} \tag{4.9}$$

This result is in sharp contrast to the commonly observed sluggish diffusion of highly polarizable Mg-ions. Mg-diffusion becomes more facile on the surface (E_{diff}

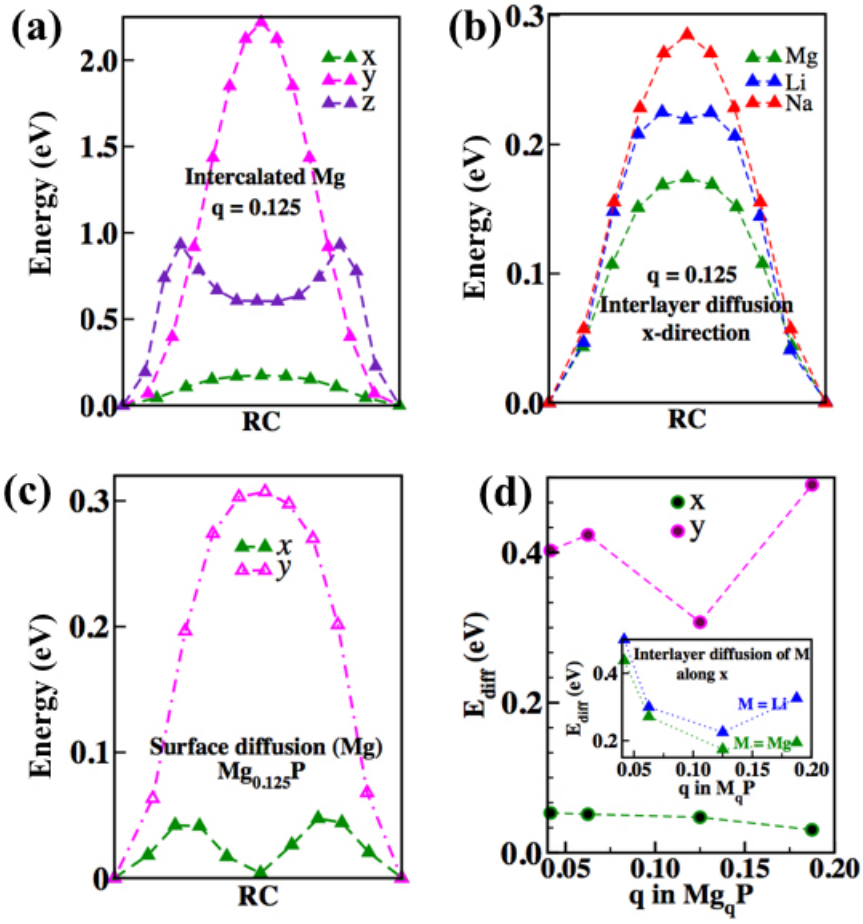

Figure 4.4: Energy profiles for interlayer diffusion in the α-phase: (a) Mg-diffusion along x, y and z-directions, (b) Li, Na, Mg-diffusion along the x-direction, (c) Mg diffusion along x and y directions on the phosphorene surface. (d) $E_{diff}s$ for surface-diffusion of Mg-ion. Inset figure shows $E_{diff}s$ for M(Li and Mg) ion diffusion at interlayer.

(x) = 0.05; E_{diff} (y) = 0.31 eV, see Figure 4.4c and d) compared to interlayer space (E_{diff} (x) = 0.17; E_{diff} (y) = 2.22 eV). We also note that diffusion along the x-channel is 4.9 x 10^2 (9.4 x 10^5) times faster than along the y-channel, on the P-surface (within interlayer space). So, interlayer diffusion of Mg-ions appears to be solely one-dimensional due to the additional interactions with the adjacent layer. On the other hand, surface-diffusion is quasi-one dimensional. Comparison of the rate of Mg-diffusion on the phosphorene surface with Li-diffusion on the conventional LIB-anode (MoS_2 and graphene) reveals that the former is 4.4 x

10^3 (7.6 x 10^4) times faster than the Li-diffusion on the MoS_2 [41] (graphene) [42] surface. Hence, an extremely high rate performance is expected for phosphorus-based anodes in Mg-batteries.

4.3.4 Why is Mg Diffusion Faster than Li/Na Diffusion ?

To understand the reason behind exceptionally fast Mg-diffusion kinetics, we have studied the stereo-electronic factors involved in Mg-P bonding at the rate-limiting α-phase. It is found that, while hopping, M-ions arrive at the transition state configuration (TR) from their stable binding site (BS) and the octahedral coordination environment (see Figure 4.5a) gets distorted.

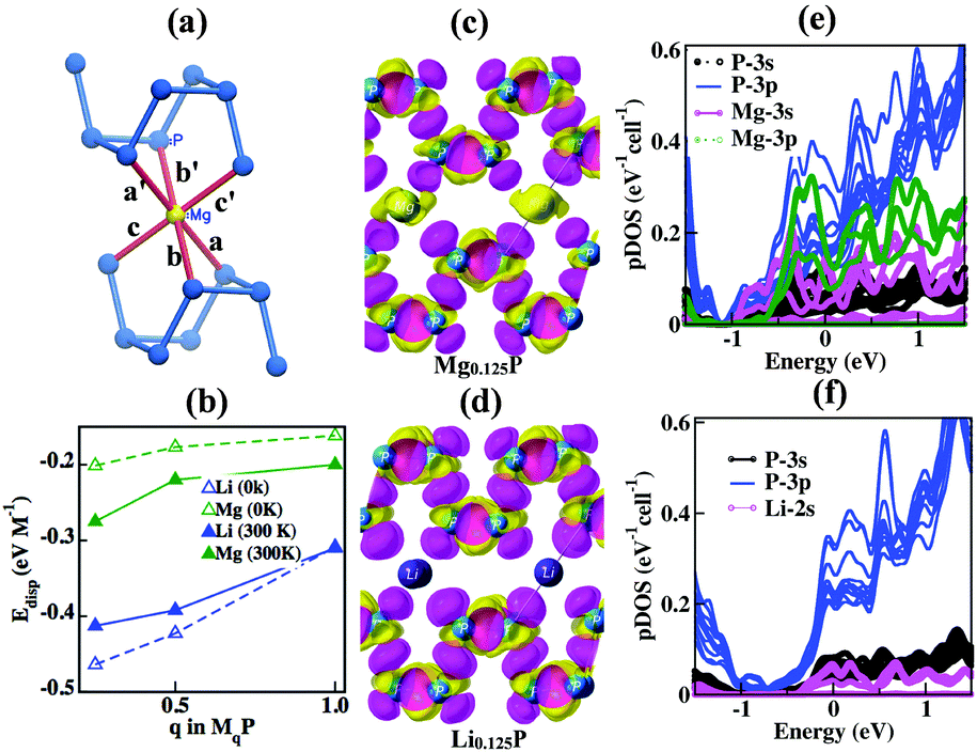

Figure 4.5: (a) Octahedral coordination number of Mg-ions at the α-phase, (b) the dispersive interaction per M-ions at α ($M_{0.125}P$), β ($M_{0.50}P$) and γ ($M_{1.0}P$) phases. Differential charge density for $M_{0.125}P$ (M = Li/Mg) while intercalated M is at the transition state during diffusion along the x-channel (side view): (c) M = Li and (d) M = Mg. The loss of electrons is indicated in yellow and the gain of electrons is indicated in pink. The projected density of states (pDOS) of $M_{0.125}P$ (TR): (e) M = Li and (f) M = Mg.

We have estimate the percentage elongation or shrinkage of M-P bonds at TR on BS, for determination of the steric-instability (see Table 4.2).

Table 4.2: M(Li / Mg)-P bond distances (r in $\mathring{A}$) at stable adsorption site (BS) as well as at the transition state configuration (TR) during hopping. The percentage elongation or shrinkage of M-P bonds at TR on BS (dr/r 100 %) determines of the steric-instability at TR.

M in $M_{0.25}P$	a($\mathring{A}$)	a$'$($\mathring{A}$)	b($\mathring{A}$)	b'($\mathring{A}$)	c($\mathring{A}$)	c'($\mathring{A}$)
Mg(TR)	2.87	2.87	2.87	2.87	2.46	2.46
Mg(BS)	2.72	2.72	2.72	2.71	2.59	2.59
dr/r x 100 %,	5.52	5.89	5.89	6.28	-4.64	-4.64
Li(TR)	2.83	2.83	2.83	2.83	2.39	2.39
Li(BS)	2.65	2.65	2.65	2.65	2.55	2.56
dr/r x 100 %	6.79	6.79	6.79	6.79	-6.27	-6.27

Notably, (i) steric-instability for Mg (TR) is lesser compared to that of Li (TR), which essentially reduces the E_{diff} for Mg-diffusion. (ii) Bonding analysis reveals that two axial Mg-P bonds (c, c$'$) get shortened from 2.59 $\mathring{A}$ (at BS) to 2.46 $\mathring{A}$ (at TR) which is close to the Mg-P single covalent bond distance of 2.36 $\mathring{A}$. On the other hand, equatorial bonds become elongated, which results in a delicate balance through decreasing the repulsion between valence electron pairs of the axial and equatorial bonds. Indeed, Mg-P bonds exhibit weaker non-local interaction and stronger covalency, which is evident from the lesser dispersion energy for Mg-storage compared to the Li-storage ($E_{disp(Mg_qP)}$): ($E_{disp(Li_qP)}$) = 0.42-0.67; see Figure 4.5b). Lesser number of Mg-P pairs contributes to the dispersive interaction (N_{Mg_qP}) compared to the Li-P pairs (N_{Li_qP}) (Table 4.3) and results in weaker $E_{disp(Mg_qP)}$, which further proves the less diffused electronic cloud surrounding Mg-P bonds.

We also note that random thermal motion of Li-ions at 300 K reduces the dispersive interaction which implies the electrostatic component of the van der Waals force. But, a Mg-ion behaves oppositely, proving the predominance of the covalency. Indeed, the electron density plot with an iso-value of 0.02 e $\mathring{A}^{-3}$ captures significant net orbital overlap for Mg-P bonds (see Figure 4.5c), while

Table 4.3: The dispersive interaction energy per M (Li/Mg)-ions in α (q = 0.25), β (q = 0.50) and γ (q = 1.00) phases. The ratio between the number of Li-P and Mg-P pairs contributing to the dispersive interaction (N_{Li_qP}:N_{Mg_qP} at different structural phases are given.

q	$E_{disp(Li_qP)}$:($E_{disp(Mg_qP)}$ 0K (300K)	N_{Li_qP}:N_{Mg_qP}
0.25	2.30 (1.50)	1.11 :1
0.50	2.39 (1.78)	1.13 :1
1.00	1.91 (1.55)	1.21 :1

the same for Li-P bonds show minimal orbital overlap (see Figure 4.5d). pDOS analysis also corroborates with the same feature, where Mg-pDOS contributes to the valence band over a broad energy window of 1 eV near the Fermi level (see Figure 4.5e) and participates in bonding overlap. In contrast, Li transfers the valence electron to the P-matrix and becomes positively charged which is clear from the contribution of Li-pDOS in the conduction band (5f). The reason behind such a distinct feature of Mg-P bonding is s-p mixing, which is specific only for Mg. The 3p state of P and 3s-3p mixed states of Mg leads to significantly covalent Mg-P bonds (see Figure 4.5e).

For both the Li and Mg storage in α-phase, s and p states of phosphorus form separate s and p-bands (see Figure 4.6a, c). However, the electronic states of Li and Mg ions (within P- matrix) exhibit different features. 3s-3p orbital mixing (see Figure 4.6d) is found for Mg-ion, which participates in bonding with $3p$ states of P-matrix, whereas, Li-s orbital (see Figure 4.6b) alone participates in bonding. Strong covalent interactions between Mg-ions and the P-matrix are of immense importance to reduce the polarisability of Mg-ions, which in combination with lesser steric instability of the transition state results in superior Mg-diffusivity.

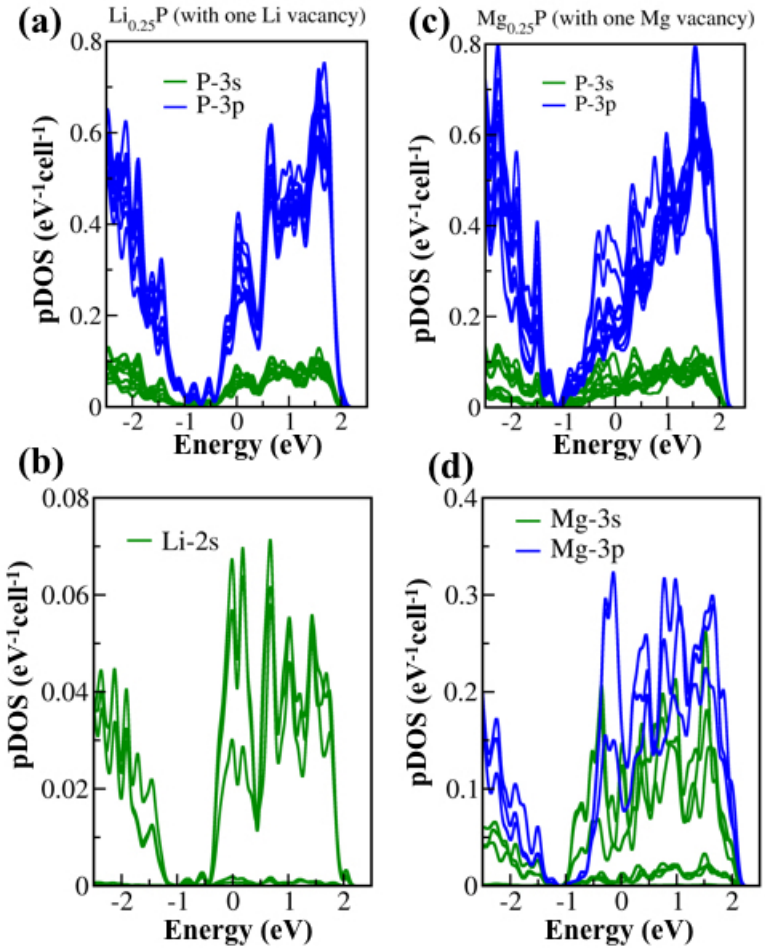

Figure 4.6: The projected density of states (PDOS) of M_qP (TR): (a, b) M = Li; (c, d) M = Mg.

4.4 Conclusions

In summary, this chapter discusses the storage potential and diffusion kinetics of the Mg-ions within black-phosphorus (P). Based on first principles analyses, we propose that P-matrix as anode, exhibits optimally low potential (0.15 V) and high specific capacity (1730 $mAhg^{-1}$). In contrast, strong Li-adsorption affinity of the phosphorus anode is mostly electrostatic in nature and results in much higher insertion-voltage compared to the Mg-storage. Mg_qP $(0 \leqslant q \leqslant 1)$ behaves like a special class of solid solution without any signature of Mg-metal deposition and

Mg/P phase segregation, which essentially avoids the pulverisation of the P-anode. However, three distinct structural phases (α, β, and γ) appear depending on the extent of charging which results in different Mg-diffusion behaviors at various states-of-charge. At a low charge state (α-phase), Mg-ion diffusion becomes 7.39 (3.64) times faster than Li-ion diffusion on the P-surface (bulk), which is in sharp contrast to the commonly observed slow diffusion of a highly polarizable Mg-ion. Notably, the α-phase is the rate-limiting step for Mg-ion diffusion. At a higher charge state (β, and γ phases), Mg-diffusion becomes barrier-less. We emphasise that it is the synergistic interaction between the 3p orbital of P and 3s-3p mixed states of Mg that leads to significant covalent Mg-P bonding, which in turn, reduces the polarisability of Mg ions. This results in high rate capability as well as the optimum anodic potential for the Mg-ion cell. On the basis of these findings, we conjecture that black phosphorus is a promising candidate as an anode in an Mg-ion cell. Future endeavour must be done to fully characterize the electrochemical set-up after integrating cathode and electrolyte with P-anode to optimize the battery's behaviour.

References

[1] T. D. Gregory, R. J. Hoffman, and R. C. Winterton, Journal of The Electrochemical Society **137**, 775 (1990).

[2] D. Aurbach, Z. Lu, A. Schechter, Y. Gofer, H. Gizbar, R. Turgeman, Y. Cohen, M. Moshkovich, and E. Levi, Nature **407**, 724 (2000).

[3] O. Chusid, Y. Gofer, H. Gizbar, Y. Vestfrid, E. Levi, D. Aurbach, and I. Riech, Advanced Materials **15**, 627 (2003).

[4] D. Aurbach, Z. Lu, A. Schechter, Y. Gofer, H. Gizbar, R. Turgeman, Y. Cohen, M. Moshkovich, and E. Levi, Nature **407**, 724 (2000).

[5] C. B. Bucur, T. Gregory, A. G. Oliver, and J. Muldoon, The Journal of Physical Chemistry Letters **6**, 3578 (2015).

[6] R. Mohtadi and F. Mizuno, Beilstein Journal of Nanotechnology **5**, 1291 (2014).

[7] J. Muldoon, C. B. Bucur, A. G. Oliver, T. Sugimoto, M. Matsui, H. S. Kim, G. D. Allred, J. Zajicek, and Y. Kotani, Energy & Environmental Science **5**, 5941 (2012).

[8] E. Levi, Y. Gofer, and D. Aurbach, Chemistry of Materials **22**, 860 (2009).

[9] E. Levi, E. Lancry, A. Mitelman, D. Aurbach, G. Ceder, D. Morgan, and O. Isnard, Chemistry of Materials **18**, 5492 (2006).

[10] H. Kim, G. Jeong, Y.-U. Kim, J.-H. Kim, C.-M. Park, and H.-J. Sohn, Chemical Society Reviews **42**, 9011 (2013).

[11] H. D. Yoo, I. Shterenberg, Y. Gofer, G. Gershinsky, N. Pour, and D. Aurbach, Energy & Environmental Science **6**, 2265 (2013).

[12] Y. Shao, M. Gu, X. Li, Z. Nie, P. Zuo, G. Li, T. Liu, J. Xiao, Y. Cheng, C. Wang, et al., Nano Letters **14**, 255 (2013).

[13] N. Singh, T. S. Arthur, C. Ling, M. Matsui, and F. Mizuno, Chemical Communications **49**, 149 (2013).

[14] D. Imamura, M. Miyayama, M. Hibino, and T. Kudo, Journal of the Electrochemical Society **150**, A753 (2003).

[15] X. Liu, Y. Du, X. Xu, X. Zhou, Z. Dai, and J. Bao, The Journal of Physical Chemistry C **120**, 3214 (2016).

[16] L. Hu, X. Zhu, Y. Du, Y. Li, X. Zhou, and J. Bao, Chemistry of Materials **27**, 8138 (2015).

[17] Y. Du, X. Zhu, L. Si, Y. Li, X. Zhou, and J. Bao, The Journal of Physical Chemistry C **119**, 15874 (2015).

[18] Y. Liu, L. Si, Y. Du, X. Zhou, Z. Dai, and J. Bao, The Journal of Physical Chemistry C **119**, 27316 (2015).

[19] X. Yu, J. Bates, G. Jellison, and F. Hart, Journal of the Electrochemical Society **144**, 524 (1997).

[20] C.-M. Park and H.-J. Sohn, Advanced Materials **19**, 2465 (2007).

[21] L. Wang, X. He, J. Li, W. Sun, J. Gao, J. Guo, and C. Jiang, Angewandte Chemie International Edition **51**, 9034 (2012).

[22] L.-Q. Sun, M.-J. Li, K. Sun, S.-H. Yu, R.-S. Wang, and H.-M. Xie, The Journal of Physical Chemistry C **116**, 14772 (2012).

[23] J. M. Sangster, Journal of Phase Equilibria and Diffusion **31**, 62 (2010).

[24] J. Qian, X. Wu, Y. Cao, X. Ai, and H. Yang, Angewandte Chemie **125**, 4731 (2013).

[25] J. P. Perdew, K. Burke, and M. Ernzerhof, Physical Review Letters **77**, 3865 (1996).

[26] P. E. Blöchl, Physical Review B **50**, 17953 (1994).

[27] G. Kresse and D. Joubert, Physical Review B **59**, 1758 (1999).

[28] S. Grimme, J. Antony, S. Ehrlich, and H. Krieg, The Journal of Chemical Physics **132**, 154104 (2010).

[29] G. Kresse and J. Furthmüller, Physical Review B **54**, 11169 (1996).

[30] Y. Shao, L. F. Molnar, Y. Jung, J. Kussmann, C. Ochsenfeld, S. T. Brown, A. T. Gilbert, L. V. Slipchenko, S. V. Levchenko, D. P. ONeill, et al., Physical Chemistry Chemical Physics **8**, 3172 (2006).

[31] P. E. Blöchl, Physical Review B **50**, 17953 (1994).

[32] J. P. Perdew, K. Burke, and M. Ernzerhof, Physical Review Letters **77**, 3865 (1996).

[33] G. Kresse and J. Furthmüller, Computational Materials Science **6**, 15 (1996).

[34] G. Kresse and D. Joubert, Physical Review B **59**, 1758 (1999).

[35] G.-C. Guo, D. Wang, X.-L. Wei, Q. Zhang, H. Liu, W.-M. Lau, and L.-M. Liu, The Journal of Physical Chemistry Letters **6**, 5002 (2015).

[36] Y. Katayama, T. Mizutani, W. Utsumi, O. Shimomura, M. Yamakata, and K.-i. Funakoshi, Nature **403**, 170 (2000).

[37] S. Nosé, The Journal of Chemical Physics **81**, 511 (1984).

[38] W. G. Hoover, Physical Review A **31**, 1695 (1985).

[39] G. Henkelman, B. P. Uberuaga, and H. Jónsson, The Journal of Chemical Physics **113**, 9901 (2000).

[40] G. Henkelman and H. Jónsson, The Journal of Chemical Physics **113**, 9978 (2000).

[41] Y. Li, D. Wu, Z. Zhou, C. R. Cabrera, and Z. Chen, The Journal of Physical Chemistry Letters **3**, 2221 (2012).

[42] C. Uthaisar and V. Barone, Nano Letters **10**, 2838 (2010).

5

Ternary Borocarbonitrides: Effect of BN and C Domains on Charge-transport*

5.1 Introduction

Semiconducting electronic material fulfils two functions, (i) light absorption, and (ii) charge carrier transport. Sensing light and electron field emissions are properties associated with the optical and electronic band gap in semiconductors. On the other hand, the power factor of electronic devices depends both on carrier transport properties and on current conversion efficiency. The popular electronic material, graphene (in single layer), shows very high carrier mobility ($\sim$1.5 x 10^4 $cm^2V^{-1}s^{-1}$ at room temperature), due to the presence of massless Dirac fermions.[1] However, in spite of this large carrier mobility, its gapless semimetallic nature limits its performance as a versatile electronic material. This has given impetus to the search for graphene-analogues which would be able to compensate the shortcomings of

*Work reported in this chapter is published in: Swastika Banerjee and Swapan K Pati, (Communication) Nanoscale, **6**, 13430-13434 (2014)

graphene.[2,3] Interestingly, a hexagonal-BN sheet exhibits large optical phonon modes and a large electronic band gap (∼5.97 eV), but poor intrinsic carrier mobility due to the charge traps on the B and N atoms.[4,5] Moderate carrier mobility coupled with a suitable electronic band gap has recently been attempted by optimising a combination of carbon (responsible for electrical conductivity) and B and N concentration (acting as redox centres).[6–8] In practice, borocarbonitrides with the combination of sensible carrier mobility ($10^2 - 10^3$ $cm^2V^{-1}s^{-1}$) and a finite band gap are used in electron field-emission, electrocatalysis,[9] supercapacitors[10,11] and other modern electronic devices.[12,13] On the other hand, p- or n-type conduction polarity has been controlled through electrochemical doping, surface adsorption, chemical functionalization and lattice symmetry breaking. For back-gate field-effect transistors, B doping in graphene has been found to exhibit p-type behaviour and lower electron mobility (350-550 $cm^2V^{-1}s^{-1}$) than the N-doped analogue (450-650 $cm^2V^{-1}s^{-1}$).[14,15] However, there are practical difficulties associated with poor mobility and in preserving the doping state in an ambient environment.[16] This has pointed us towards understanding how surface structure and the interface affect carrier mobility in borocarbonitride nano-hybrids.

In the present chapter, we debate whether topological modification in borocarbonitrides is a promising approach for addressing these issues, since the properties controlled by surface topology are arguably more robust to external polarization and electrochemical oxidation/reduction than doping with electron(s) and/or hole(s). In fact, sustainable electrochemical performance (100 $mAhg^{-1}$ at 2 Ag^{-1} for 5000 cycles with a capacity retention of 93%) of $B_{2.5}CN_{2.5}$ has been demonstrated by Lei et al.[12] This confirms the stability of the material, even at high current levels, and reflects its high intrinsic carrier mobility. We shall discuss the carrier transport characteristics and the topological criticality of monolayer and bilayer $B_{2.5}CN_{2.5}$ (see Figure 5.1).The subject of the present investigation is not only of fundamental academic interest but also be of significant technical relevance

to modern electronic devices and energy storage.

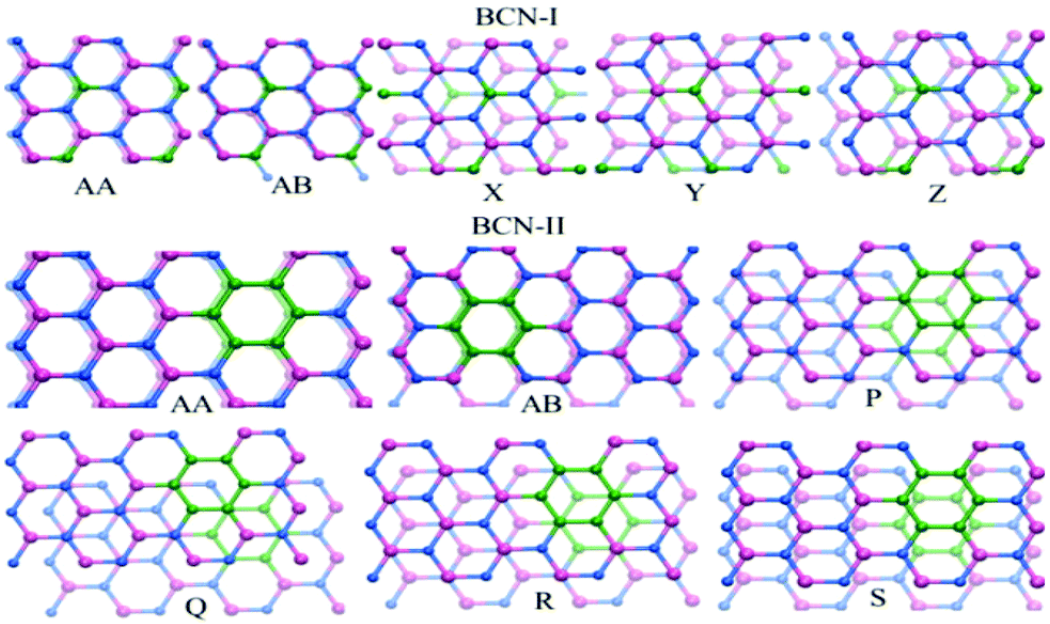

Figure 5.1: View of the various stacking patterns of bilayer $B_{2.5}CN_{2.5}$; BCN-I: AA, AB, X, Y, Z; and BCN-II: AA, AB, P, Q, R, S. The pink spheres represent B atoms and the green and blue spheres C and N, respectively.

5.2 Computational Methodology

5.2.1 First Principles Simulation Details

In the DFT calculations, we have used projector augmented wave (PAW) method [17] for representation of ionic core and valence electrons. The exchange-correlation energy of electron is described by the Perdew-Burke-Ernzerhof functional (PBE). [18] We use an energy cutoff of 500 eV for the plane wave basis set expansion. The Brillouin zone was represented by Monkhorst-Pack 30 x 30 x 1 k-point mesh. Large enough supercell has been considered to ensure that the vacuum space is 20 $\mathring{A}$ assuring sufficient vacuum along non-periodic direction. Structural optimisations are done with PBE functional with the inclusion of DFT-D2 dispersion correction [19]

as implemented in Vienna ab initio simulation package (VASP).[20–22].

5.2.2 Boltzmann Transport Formalism

The band energy, ε_i, and group velocity, ν_β , obtained from first principles calculations, are used for computing carrier-mobility (μ) based on the Boltzmann transport formalism within the Deformation Potential (DP) theory.[23] Mobility ($\mu_\beta^{e(h)}$) for electron (e) and hole (h) is defined as,

$$\mu_\beta^{e(h)} = \frac{e}{k_B T} \frac{\sum\limits_{i \epsilon CB(VB)} \int \tau_\beta(i,\vec{k}) {\nu_\beta}^2 b(\vec{k}) d\vec{k}}{\sum\limits_{i \epsilon CB(VB)} \int b(\vec{k}) d\vec{k}} \tag{5.1}$$

where,

$$b(\vec{k}) = exp[\mp \frac{\varepsilon_i(\vec{k})}{k_B T}] \tag{5.2}$$

Minus (plus) sign in the exponent stands for electron (hole). β denotes the direction of the external electric field. The summation runs over all the k^{th} state of the all the i^{th} band in the Brillouin zone (BZ). The summation of the band was carried out using valence band (VB) for holes and conduction band (CB) for electrons. We find the relaxation time, $\tau_\beta(i,k)$, using the collision term in the BTE[24],

$$\frac{1}{\tau_\beta(i,\vec{k})} = k_B T \frac{4\pi^2 \left(E_\beta^c\right)^2}{h C_\beta} \sum_{k' \epsilon BZ} \left[1 - \frac{\nu_\beta(\vec{k'})}{\nu_\beta(\vec{k})} \delta[\varepsilon_i(\vec{k'}) - \varepsilon_i(\vec{k})] \right] \tag{5.3}$$

Elastic constant (C_β) and deformation potential constant (E_β^c; c: electron or hole) have been derived from first principles calculations. E_β^c is defined as,

$$E_\beta^c = \frac{\Delta E_{band}}{\Delta l / l_0} \tag{5.4}$$

where ΔE_{band} is energy shift at the band-edge position with respect to the lattice dilation $\Delta l/l_0$ along the transport direction (β). The change in total energy ($E - E_0$), is given by,

$$2(E - E_0) = C_\beta S_0 \left(\Delta l/l_0\right)^2 \tag{5.5}$$

where, E_0 and S_0 are the energy and the surface area of the unit cell without any strain. The value of C_β is obtained from the curvature of the parabola.

All the transport parameters discussed above are obtained from first principles analysis. *ab initio* molecular dynamics simulations (NVT, 300 K)[25,26] have been carried out using GPW formalism and GTH pseudo-potential[27] with Perdew-Burke-Ernzerhof (PBE)[18] exchange correlation functional have been used for AIMD simulation, adopting the CP2K set of programs.[21,22,28,29]

5.3 Results and Discussion

5.3.1 Surface Structures and Stacking Patterns in $B_xC_yN_z$-sheets

DFT-optimized lattice vectors are 8.72 (x); 7.56 (y) for BCN-I-AB unit cell and 13.05(x); 7.54(y) for BCN-II-AB unit cell (see Figure 5.2). An understanding of the surface electronic structure and basic transport mechanism has been used to provide an efficient design for electronic devices and electrochemical applications. Apart from this particular composition, we have also considered two recently highlighted carbon-rich compositions, BCN and BC_4N (Figure 5.2),[30,31] and have applied the principle discussed in the present chapter. The composition of $B_{2.5}CN_{2.5}$ itself allows the possible surface structures shown in the Figure 5.1 and Figure 5.3.

Apart from the structure and composition, stacking pattern in the layered

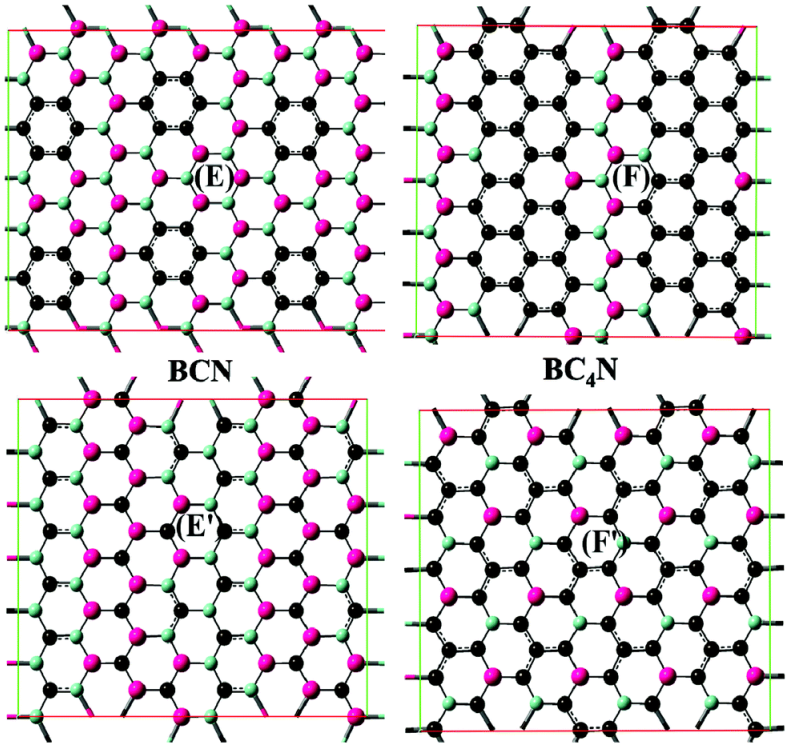

Figure 5.2: E and F are equally separated localized C-domains in BCN and BC_4N, respectively, and E′ and F′ represent random B, C and N distributions in BCN and BC_4N.

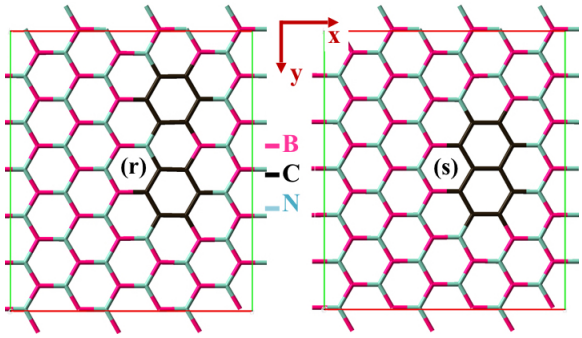

Figure 5.3: Unequal separations (three and five atoms) between localized C-domains (r) and long bridging chain (seven atoms) between two localized C-domains (s).

material is one of our concerns for device applications. Structural analysis therefore becomes relevant in addressing the importance of various stacking patterns and in providing the preliminary information for our further investigations into carrier transport characteristics. It has been confirmed that the surface topology of model

BCN-I (interlayer distance (ID) = 0.33 nm) is in complete agreement with the experimental X-ray measurements. The B, C and N atoms are positioned in a random manner with each hexagonal ring containing only one C atom (see BCN-I). We also suggest another model having surface structures with a localized C-domain, in good agreement with previous theoretical studies and the experimental evidence (BCN-II and Figure 5.3r, s)[10,13] (ID $\approx$ 0.40 nm).

5.3.2 Stability

Based on the relative energy (RE; the energy of any stacking pattern with respect to the most stable stacking arrangement) and the cohesive energy (CE; the estimate of the stability gained due to bilayer formation), we are able to determine the most stable stacking pattern for BCN-I and BCN-II (Table 5.1). The difference

Table 5.1: Relative energy (RE), cohesive energy (CE) in meV/atom and interlayer distance (ID) in $\mathring{A}$ of various stacking patterns of bilayer BCN-I and BCN-II.

Sheet	**RE**	**ID**	**CE**
BCN-I-AA	19.39	3.66	-17.26
BCN-I-AB	0.00	3.46	-36.65
BCN-I-X	5.11	3.63	-31.54
BCN-I-Y	6.78	3.50	-29.87
BCN-I-Z	8.84	3.63	-27.81
BCN-II-AA	14.29	3.70	-19.19
BCN-II-AB	3.07	3.55	-30.41
BCN-II-P	0.00	3.62	-33.48
BCN-II-Q	1.86	3.43	-31.63
BCN-II-R	2.10	3.45	-31.39
BCN-II-S	4.99	3.42	-28.50

in stability is much small for different stacking patterns in either of the surface topologies (see Table 5.1 and Figure 5.4) at both low (0 K) and room temperature (300 K). This confirms that these stacking arrangements are highly feasible under ambient conditions. In addition, a graph of dispersion energy (DE) vs.

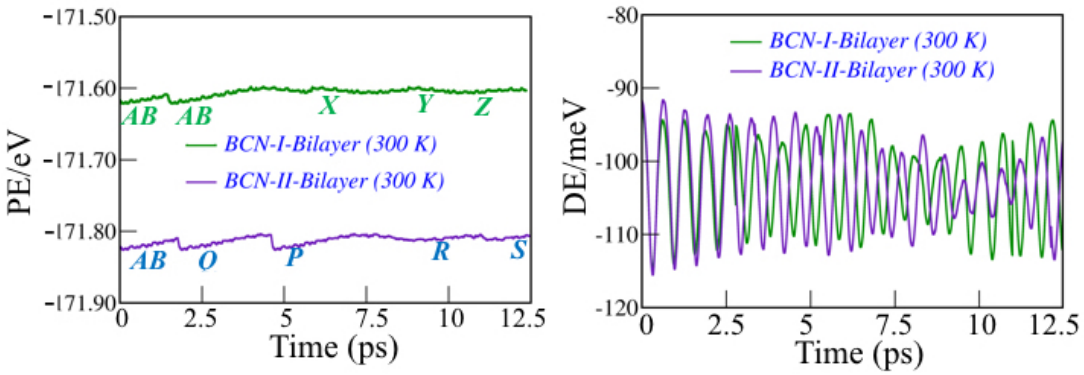

Figure 5.4: Potential energy (PE) vs. time (left), and dispersion energy (DE) vs. time (right) for bilayer BCN-I and BCN-II with PBE-D2 functional.

time helps to establish the relationship of dispersive force and structural integrity, indicating favourable stacking patterns and equilibrium separation distances between two layers in various stacking arrangements. By comparative analysis of two different sheets, BCN-II-AB has been found to be energetically more stable than BCN-I-AB, the difference being ∼0.21 eV per atom.

5.3.3 Charge Transport Property

We used the structural analysis and sampled the energetically stable bilayer stacking patterns (BCN-I-AB and BCN-II-AB) to study the transport characteristics. In the study, charge-carrier mobility ($\mu_{\beta}^{e(h)}$) was evaluated on the basis of Boltzmann transport formalism within the deformation potential (DP) theory (see Equation 5.1).[32,33] We note that the acoustic phonon mechanism and deformation potential theory could also explain the charge transport behaviour in graphene nanoribbons.[34] In the Boltzmann method, the relaxation time is calculated by the collision term (see Equation 5.3).[35]

We find that for bilayer BCN-I, the intrinsic electron mobility (Table 5.2) extends to an order of 10^6 $cm^2V^{-1}s^{-1}$ along the y-direction, in which two consecutive C atoms are non-collinear and are separated by one B-N bond. On the other hand,

bilayer BCN-II exhibits a reversal of conduction polarity, showing high hole mobility ($\sim 10^6\ cm^2V^{-1}s^{-1}$) along the y-direction, in which two hexagonal C-domains are periodically separated by an odd number of B/N atoms (3 B, N atom), formed either by an extra electron or an extra hole.

Table 5.2: Deformation potential E_β (eV), elastic constant C_β (Jm^{-2}), carrier mobility μ ($10^4 cm^2V^{-1}s^{-1}$), and the averaged value of scattering relaxation time τ (ps) at 300 K for electrons and holes, denoted as, $Carriertype_{direction}$ ($e(h)_{x/y}$), in monolayer and bilayer $B_{2.5}CN_{2.5}$ with different surface topologies (A = BCN-I, B = BCN-II).

Sheet	$e(h)_{x/y}$	**Monolayer**				**Bilayer**			
		E^c_β	C_β	μ	τ	E^c_β	C_β	μ	τ
A	e_x	3.74	297.88	0.82	1.16	2.42	598.28	7.28	10.62
	h_x	1.76	297.88	3.27	5.34	1.76	598.28	11.8	19.15
	e_y	0.44	285.57	56.75	80.40	0.44	575.69	212.04	309.12
	h_y	2.86	285.57	1.39	2.78	1.32	575.69	20.22	32.76
B	e_x	3.96	302.14	0.13	0.79	3.30	618.98	0.33	1.81
	h_x	0.66	302.14	8.65	49.29	1.76	618.98	1.59	6.86
	e_y	3.74	302.39	0.15	0.89	3.30	616.23	0.32	1.80
	h_y	1.54	302.39	1.59	9.06	0.22	616.23	101.08	436.91

5.3.4 Electronic Structure and Microscopic Reason

Band structure calculation relates BCN-I to a narrow band gap semiconductor ($\sim$0.45 eV at the Γ-point), whereas BCN-II is a wide band gap semiconductor ($\sim$2.80 eV at the Γ-point) (see Figure 5.5). For Both BCN-I and BCN-II, AA stacking pattern shows least band gap whereas AB stacking or other turbulent stacking patterns are energetically more stable with little more opening of band-gap. Tune-ability of band structure and lifting of the degeneracy in conduction and valence band is also found through change in the stacking pattern in case of BCN-II type. Irrespective of the stacking is, electronic band gap for BCN-II is pretty larger in comparison with BCN-I. Band dispersion in BCN-I arises from the contributions of B, N and C to the valence band and conduction band (see Figure 5.5 and 5.7). On the other hand, localized C domain (BCN-II) introduces sharp lo-

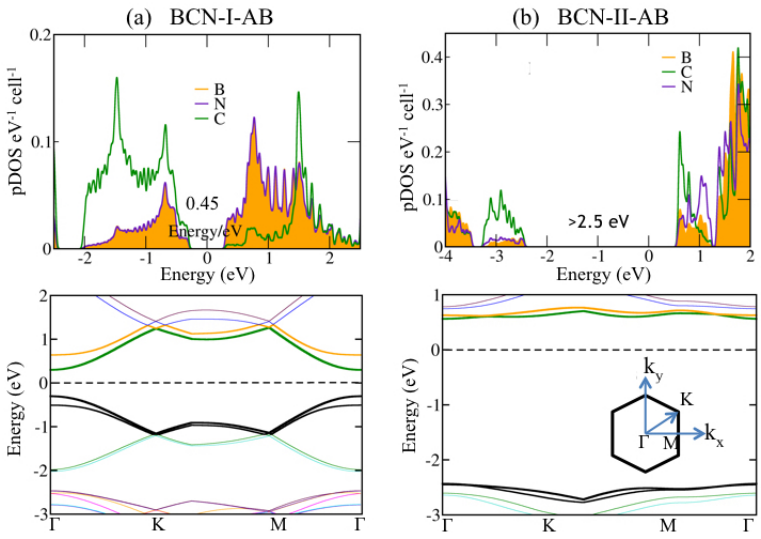

Figure 5.5: Band structure and projected density of states for bilayer borocarbonitride ($B_{2.5}CN_{2.5}$) sheets in stable packing pattern, obtained from DFT calculations. Both exhibit direct band gap. Inset: the first Brillouin zone of the primitive cell, with three high symmetry points, Γ, K and M.

calized peak in DOS contributed by carbon $2p_z$ orbitals, as shown in Figure 5.6. Hence the conduction bands are more flattened in BCN-II, which results in higher electronic effective mass whereas, C-valence $2p_z$ orbital (see Figure 5.7) contribute to the broad peak near Valence Band Maximum (VBM). Electronic structural calculations show that in the case of BCN-I the conduction band minimum (CBM) is delocalized due to the diffuse nature of the N $2p_z$ orbitals (Figure 5.5 and 5.6), and shows fewer nodes along the y-direction. This leads to weak coupling between the electrons and the acoustic phonons, reducing effective scattering and increasing the electron mobility of BCN-I. On the other hand, in the CBM of BCN-II carbon hexagons and BN-domains combine anti-symmetrically (an anti-bonding feature), while the valence bond maximum (VBM) consists of symmetrical bonding features, with the appearance of kink states at N sites, acting as a connector between two diffused electronic islands. It is noteworthy that the kink states always appear on N sites in VBM when localized C-domains form (Figure 5.6, I (B, C and D) and II (B)).

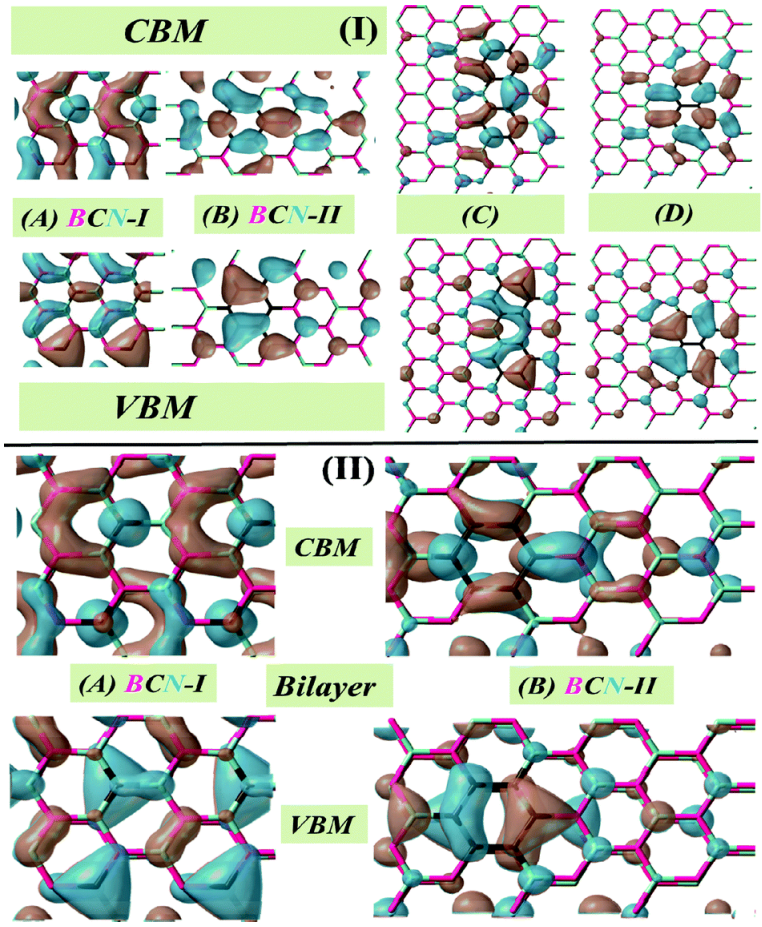

Figure 5.6: Γ-point VBM and CBM for model surface topologies; (I) monolayer, and (II) bilayer. I(A) CBM consists of more extended islands than VBM; the number of nodes in VBM is equal in either direction. I(B), (C) and (D) VBM shows a more delocalized character than CBM along the y-direction, and kink states appear on the N atom. I(C) and (D) plots are for the surface structures described in Figure 5.3, r and s, respectively.

A further aspect is that, irrespective of the surface topology, the carrier mobility increases in the bilayer structure (compared to the monolayer, see Table 5.2) for both electron and hole. To understand the effect of the layers, we analysed each of the terms in Equation 5.1 contributing to mobility and found that the relaxation time (τ) value changed significantly from monolayer to bilayer. This underlines the importance of subsurface scattering (Equation 5.3). The significant contribution of the $2p_z$ orbitals of C, B and N (perpendicular to the transport plane) to both CBM and VBM (Figure 5.7) gives a change in the value of E^c_β (eV) in the layered

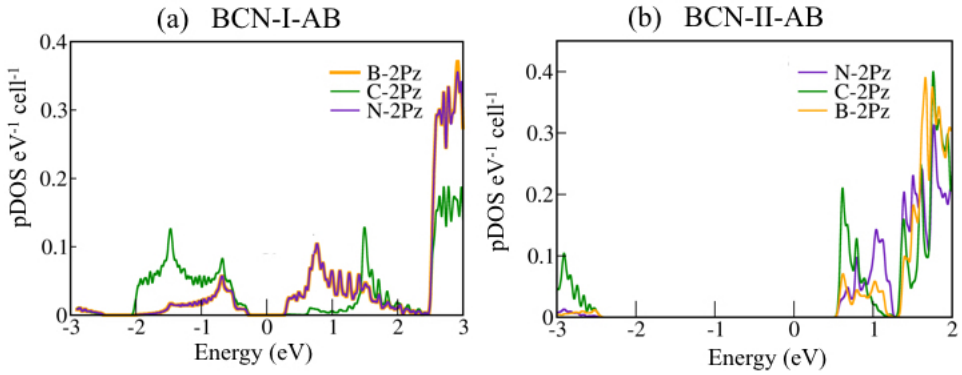

Figure 5.7: Projected density of states (pDOS) for out-of-plane valence orbitals in bilayer boro-carbonitride ($B_{2.5}CN_{2.5}$) sheets (BCN-I in the left and BCN-II in the right) in their stable stacking pattern are obtained from DFT calculations.

structure. The modulation in carrier transport property in the layered structure is thus due to electronic structural changes, leading to phonon softening. This corroborates previous observations on anomalous phonon softening in the case of bilayer graphene.[36]

5.3.5 Transport Property and Composition Dependence

We also studied the composition dependency of the intrinsic carrier mobilities. Unlike BN predominant compositions ($B_{2.5}CN_{2.5}$), C-rich compositions (BCN and BC_4N) with truly random surface structure (Figure 5.2, E′ and F′) drive the material to be metallic, which corroborates earlier studies.[30,31] On the other hand, the stable surface with localised C-domains is semiconducting in nature (Figure 5.2, E and F). Extremely high hole mobility ($\sim 10^6\ cm^2V^{-1}s^{-1}$), but comparatively poor e-mobility of BCN ($\sim 10^4\ cm^2V^{-1}s^{-1}$) is found (Figure 5.8 and Table 5.3), using the same rationale as discussed earlier. BC_4N exhibits both electron and hole mobility of the order of $\sim 10^5\ cm^2V^{-1}s^{-1}$, attributed to the equalization of both hole and electronic relaxation times (see Table 5.3). Hence, extended C-domains (see Figure 5.8) lead to the equalization of intrinsic hole and electron mobility (compensates electron mobility at the cost of hole mobility.

Table 5.3: Deformation potential E_β (eV), elastic constant C_β (Jm^{-2}), carrier mobility μ (x$10^4 cm^2V^{-1}s^{-1}$)), and the averaged value of scattering relaxation time τ (ps) at 300 K for electrons and holes in monolayer 'r', 's' ($B_{2.5}CN_{2.5}$) (shown in Figure 5.3) and E, F surface topologies (shown in Figure 5.2)

Sheet	**Carrier type**	**Transport parameters**			
		E^c_β	C_β	μ	τ
r	e_x	3.52	304.18	0.07	0.51
	h_x	0.66	304.18	5.07	18.54
	e_y	3.96	301.77	0.05	0.40
	h_y	1.76	301.77	0.71	2.59
s	e_x	2.20	308.20	0.16	9.01
	h_x	2.20	308.20	0.22	9.29
	e_y	4.62	302.61	0.04	2.01
	h_y	0.44	302.61	5.41	150.00
E	e_x	2.64	308.20	3.09	3.51
	h_x	2.64	308.20	3.06	2.44
	e_y	3.52	308.56	1.75	1.98
	h_y	0.22	308.56	441.42	352.23
F	e_x	1.32	345.66	31.15	33.52
	h_x	3.08	345.66	5.70	6.16
	e_y	3.96	336.06	3.37	3.62
	h_y	1.10	336.06	43.61	46.93

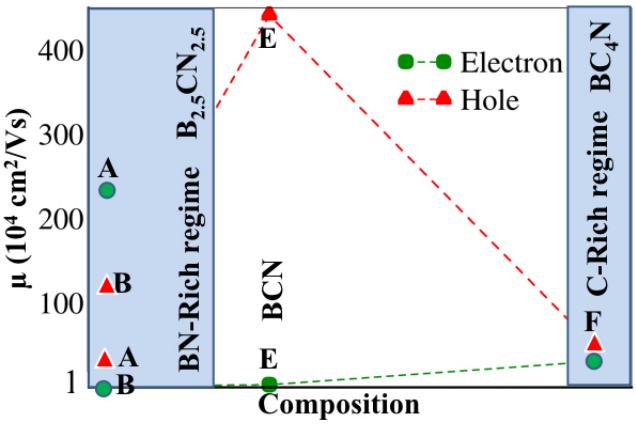

Figure 5.8: Carrier mobility (μ) for electrons and holes in borocarbonitrides ($B_xC_yN_z$) exhibiting different stoichiometric proportions of B, C and N. The different surface topologies are A: BCN-I, B: BCN-II, E: BCN, and F: BC_4N.

Thus, (1) electron-hole anisotropy maximises when B:C:N = 1:1:1; (2) BN-rich

$B_xC_yN_z$ result in two semiconducting phases (A: BCN-I B: BCN-II type). Here is A, the truly mixed C atoms in BN matrix which gives rise to higher e-mobility, whereas, B, the separated BN C-domain results in higher hole mobility; and (3) at C-rich domain transport response is isotropic.

5.4 Conclusions

In conclusion, we wish to stress that BN-rich borocarbonitrides ($B_{2.5}CN_{2.5}$) are semiconducting in nature, irrespective of surface topology, and the random mixing of B, N and C (BCN-I) is energetically less stable than the structure with localized domains (BCN-II). Thus, the topological feature of BCN-I can be defined as a topological defect in the stable surface of type BCN-II. Such topological defects give rise to extremely high electronic mobility, in this case a higher performance by a factor of 10^3 compared with the most stable topological feature. Secondly, electronic confinement becomes dominant and transport channels have a directional behaviour. In addition, for a particular composition the electronic bandgap can be varied within a wide range of energy spectrum (0.45 to 2.8 eV), by tuning the surface topology. Thirdly, reversal of the conduction polarity[32] has also been found to follow the change in surface topology. The leading carrier transport in transistors can be changed from electrons (for BCN-I) to holes (for BCN-II), with high mobility value ($\mu = 10^6\ cm^2V^{-1}s^{-1}$). Large electron mobility can be achieved for surface structures with random (truly mixed) C atoms in a BN matrix (model BCN-I). On the other hand, hole mobility becomes extremely high and more robust when localized C-domains (see BCN-II model structure) are both closest and also equidistant (periodically situated). These principles turn out to be not only specific to $B_{2.5}CN_{2.5}$, but can also be extended to borocarbonitrides in different stoichiometric proportions. This can lead to optimization of the atomically engineered surface topology to tailor low-dimensional carrier transport

mobility, and is fundamental to the design of a smart material for modern day electronic (transport) and energy storage devices.

References

[1] K. Novoselov, A. K. Geim, S. Morozov, D. Jiang, M. Katsnelson, I. Grigorieva, S. Dubonos, and A. Firsov, nature **438**, 197 (2005).

[2] M. Y. Han, B. Özyilmaz, Y. Zhang, and P. Kim, Physical review letters **98**, 206805 (2007).

[3] S. Banerjee, G. Periyasamy, and S. K. Pati, Journal of Materials Chemistry A **2**, 3856 (2014).

[4] K. Watanabe, T. Taniguchi, and H. Kanda, Nature materials **3**, 404 (2004).

[5] G. Giovannetti, P. A. Khomyakov, G. Brocks, P. J. Kelly, and J. van den Brink, Physical Review B **76**, 073103 (2007).

[6] S. Dutta, A. K. Manna, and S. K. Pati, Physical review letters **102**, 096601 (2009).

[7] D. Wei, Y. Liu, Y. Wang, H. Zhang, L. Huang, and G. Yu, Nano letters **9**, 1752 (2009).

[8] C. R. Dean, A. F. Young, I. Meric, C. Lee, L. Wang, S. Sorgenfrei, K. Watanabe, T. Taniguchi, P. Kim, K. Shepard, et al., Nature nanotechnology **5**, 722 (2010).

[9] L. Qu, Y. Liu, J.-B. Baek, and L. Dai, ACS nano **4**, 1321 (2010).

[10] K. Moses, K. Pramoda, S. N. Shirodkar, A. K. Mishra, U. V. Waghmare, A. Sundaresan, C. Rao, et al., Journal of Materials Chemistry A **1**, 5806 (2013).

[11] K. Gopalakrishnan, K. Moses, A. Govindaraj, and C. Rao, Solid State Communications **175**, 43 (2013).

[12] W. Lei, S. Qin, D. Liu, D. Portehault, Z. Liu, and Y. Chen, Chemical communications **49**, 352 (2013).

[13] S. Sen, K. Moses, A. J. Bhattacharyya, and C. Rao, Chemistry–An Asian Journal **9**, 100 (2014).

[14] H. Wang, Y. Zhou, D. Wu, L. Liao, S. Zhao, H. Peng, and Z. Liu, Small **9**, 1316 (2013).

[15] T. Wu, H. Shen, L. Sun, B. Cheng, B. Liu, and J. Shen, New Journal of Chemistry **36**, 1385 (2012).

[16] J. H. Bong, O. Sul, A. Yoon, S.-Y. Choi, and B. J. Cho, Nanoscale **6**, 8503 (2014).

[17] G. Kresse and D. Joubert, Physical Review B **59**, 1758 (1999).

[18] J. P. Perdew, K. Burke, and M. Ernzerhof, Physical review letters **77**, 3865 (1996).

[19] S. Grimme, Journal of computational chemistry **27**, 1787 (2006).

[20] G. Kresse and J. Furthmüller, Physical review B **54**, 11169 (1996).

[21] G. Kresse and J. Hafner, Physical Review B **47**, 558 (1993).

[22] G. Kresse and J. Hafner, Physical Review B **49**, 14251 (1994).

[23] J. Bardeen and W. Shockley, Physical Review **80**, 72 (1950).

[24] J. M. Ziman, *Principles of the Theory of Solids* (Cambridge university press, 1972).

[25] J. VandeVondele, M. Krack, F. Mohamed, M. Parrinello, T. Chassaing, and J. Hutter, Computer Physics Communications **167**, 103 (2005).

[26] J. Hutter, M. Iannuzzi, F. Schiffmann, and J. VandeVondele, Wiley Interdisciplinary Reviews: Computational Molecular Science **4**, 15 (2014).

[27] M. Elstner, D. Porezag, G. Jungnickel, J. Elsner, M. Haugk, T. Frauenheim, S. Suhai, and G. Seifert, Physical Review B **58**, 7260 (1998).

[28] J. VandeVondele, M. Krack, F. Mohamed, M. Parrinello, T. Chassaing, and J. Hutter, Computer Physics Communications **167**, 103 (2005).

[29] J. Hutter, M. Iannuzzi, F. Schiffmann, and J. VandeVondele, Wiley Interdisciplinary Reviews: Computational Molecular Science **4**, 15 (2014).

[30] K. Raidongia, D. Jagadeesan, M. Upadhyay-Kahaly, U. Waghmare, S. K. Pati, M. Eswaramoorthy, and C. Rao, Journal of Materials Chemistry **18**, 83 (2008).

[31] K. Moses, S. N. Shirodkar, U. Waghmare, and C. Rao, Materials Research Express **1**, 025603 (2014).

[32] J. Bardeen and W. Shockley, Physical Review **80**, 72 (1950).

[33] Y. Cheng, R. Silbey, D. A. da Silva Filho, J. P. Calbert, J. Cornil, and J.-L. Brédas, The Journal of chemical physics **118**, 3764 (2003).

[34] M.-Q. Long, L. Tang, D. Wang, L. Wang, and Z. Shuai, Journal of the American Chemical Society **131**, 17728 (2009).

[35] J. M. Ziman, *Principles of the Theory of Solids* (Cambridge university press, 1972).

[36] J. Yan, E. A. Henriksen, P. Kim, and A. Pinczuk, Physical review letters **101**, 136804 (2008).

6

Elemental Black Phosphorene: Effect of Puckered Structure on Transport*

6.1 Introduction

Graphene, the famous one-atom-thick layer of carbon, has attracted huge attention of materials scientists due to its electrical properties, which allow almost free flow of electrons across its surface. But the material lacks band gap, which restricts its widespread application. In fact, gap-state is useful as switch of the electron flow to be on and off. Recently, a new elemental 2D-sheet (phosphorene) has been proposed as a promising candidate that could combine both the aspects: (1) an atom-thick layer of the elemental phosphorus (2) an intrinsic band gap. Moreover, out-of-plane atomic arrangement in phosphorene sheets differentiates them from other 2D electronic materials, like graphene, borocarbonitrides, h-boronitrides, etc. Symmetric buckling of six-membered rings is found in

*Work reported in this chapter is published in: Swastika Banerjee and Swapan K Pati, Phys. Chem. Chem. Phys. **18**, 16345-16352 (2016)

P-allotrope (blue phosphorene)[1] and silicene.[2] In contrast to blue-P, black phosphorus exhibits asymmetric buckling along two in-plane directions. This results in anisotropy in the electronic and optical responses of black-phosphorus.[3,4] Recently, two dimensional (2D) black phosphorene and 3D black phosphorus (BP) have drawn huge attention as promising materials for nano-electronics[5,6] due to their high carrier (electron/hole) mobilities (10^3 to 10^5 $cm^2V^{-1}s^{-1}$).[7,8] Especially, strong in-plane anisotropy[9–11] makes phosphorene distinct from other isotropic materials like graphene and MoS_2. Nano-structuring results in the further enhancement of anisotropy,[12] leading to a higher on-off ratio of a BP transistor[13] and better performance for thermoelectrics.[14] But, nanostructures often exhibit lower mobility.[13] Recent advances in the application of strain have overcome this limitation to a certain extent.[10] Strain also results in direct-indirect band-gap switching and multi-valley participation in transport.[15–17] Bilayer phosphorene under compressive strain perpendicular to its surface exhibits higher (2 orders of magnitude) room temperature electron mobility than for ground state phosphorenes.[23] Besides in-plane anisotropy, it has been found that anisotropic response in carrier relaxation dynamics leads to the minimization of electron-hole recombination, which is required for solar cell applications[18] of phosphorene. A recent experimental study reveals that bulk BP has anisotropic particle-hole excitation.[19] However, understanding of the origin of transport-anisotropy is critical for its application in advanced transport devices. Previous endeavors based on empirical tight-binding[20,21] as well as ab initio density functional theory (DFT)[11,15,22,23] have shown that the anisotropic effective mass results in carrier anisotropy. But, the complexity arises because of the nearly-linear dispersive bands which put a question mark on 'effective mass' (m^*) evaluation

$$m^* = \hbar^2(\frac{d^2E}{dk^2})^{-1} \tag{6.1}$$

So, despite the abundance of band-structure and effective mass derived results,[24,25] fundamentals of transport still remain unanswered. For example, what is the origin of the effective mass anisotropy? What is the role of the carrier scattering process in dictating the anisotropic transport in phosphorene? How can we achieve both the in-plane as well as electron-hole anisotropy for a given system?

In this chapter, we present a numerical scheme based on the Boltzmann transport equation (BTE) and determine the relevant quantities needed to answer the above questions. First-principles simulations have been employed to obtain the electronic structural details and the relevant parameters for evaluation of the transport integrals. All of the studied systems including the 2D monolayer, quasi-2D few-layers as well as bulk black-phosphorus exhibit a nearly direct band gap.[26,27] However, the nature of the band gap state is strongly dependent on the number of the layers. Trilayer black phosphorus (TBP) is unique due to its structure and fundamental symmetry criteria which results in a special case for charge-carrier anisotropy. Information on the scattering process involving purely the carrier states helps to understand the layer-dependent optical responses, particularly, the sudden drop in photoluminescence efficiency[28] as observed from trilayer onwards. We also discuss two descriptors for the assessment of transport anisotropy and layer-dependent relaxation dynamics of the charge-carriers in phosphorene-like complex systems. The remainder of this chapter is organized as follows: first, we introduce the theoretical methods which are followed by discussion on the layer-dependent criticality of electronic structure in black phosphorus, based on the band structure derived parameters. Next, we present a detail description on the evaluation of relevant parameters and the transport characteristics in TBP. This is followed by a thorough analysis of the carrier scattering process to understand the origin of transport-anisotropy. Finally we summarize our findings.

6.2 Computational Methodology

6.2.1 First Principles Simulation Details

Structural optimizations are carried out with Perdew-Burke-Ernzerhof (PBE)[29] functional and Projector Augmented-Wave (PAW)[30,31] method with the inclusion of DFT-D2 dispersion correction as implemented in Vienna Ab initio Simulation Package (VASP).[32–34] Energy cutoff of 540 eV is used for the plane wave basis set expansion. Band structure details have been obtained with the PBE functional in the SIESTA[35] and the Heyd-Scuseria-Ernzerhof (HSE)06[36,37] functional as implemented in VASP. Reciprocal space has been meshed using the Monkhorst-Pack method with fine k-grid (70 x 70 x 1) for the PBE and 11 x 9 x 1 for HSE06 functional. Fine grid (70 x 70 x 1) has been used to attain the better accuracy for the numerical integrations.

6.2.2 Boltzmann Transport Formalism

Transport parameters, such as, elastic constant (C_β) and deformation potential constant (E^c_β; c: electron or hole) have been derived from first principles calculations (see section 5.2.2 in Chapter 5). Using C_β and E^c_β, thermally averaged carrier-acoustic phonon scattering probability, $\langle|M_i(k,k')|^2\rangle$, can be defined as,

$$\left\langle|M_i(k,k')|^2\right\rangle = k_B T \frac{4\pi^2 \left(E^c_\beta\right)^2}{hC_\beta} \tag{6.2}$$

We define the parameter S^c_β as,

$$S^c_\beta = \left[\left\langle|M_i(k,k')|^2\right\rangle\right]^{-1} \tag{6.3}$$

Indeed, mobility, μ_β^c is proportional to the parameter S_β^c (see Equation 6.7),

$$\mu_\beta^c \propto S_\beta^c \tag{6.4}$$

To account for the scattering process among the electron (hole) carrier states, we estimate the probability of transition from one state to another through the collision term in BTE,

$$F(\vec{k}) = \sum_{k'\epsilon BZ} \left[\left(1 - \frac{\nu_\beta(\vec{k'})}{\nu_\beta(\vec{k})} \right) \delta[\varepsilon_i(\vec{k'}) - \varepsilon_i(\vec{k})] \right] \tag{6.5}$$

where, the δ-function accounts for elastic scattering. $F(\vec{k})$ determines the number of carrier states (N_c) participating in charge-transport and the corresponding relaxation time, $\tau_\beta(i, \vec{k})$. The number of carrier states (N_c) is governed by the correlation factor, $F(\vec{k})$, which in turn dictates the rate of carrier relaxation (k_{relax}) within the CB and VB ($\tau(\vec{k}) \propto 1/F(\vec{k})$); (see Equation 6.5 and 6.6). where, the relaxation time, $\tau_\beta(i, k)$, can be defined using the collision term in the BTE[38] as,

$$\frac{1}{\tau_\beta(i, \vec{k})} = k_B T \frac{4\pi^2 \left(E_\beta^c\right)^2}{hC_\beta} \sum_{k'\epsilon BZ} \left[1 - \frac{\nu_\beta(\vec{k'})}{\nu_\beta(\vec{k})} \delta[\varepsilon_i(\vec{k'}) - \varepsilon_i(\vec{k})] \right] \tag{6.6}$$

Accordingly, $F(\vec{k})$ dictates the mobility for electrons and holes along a specific direction. Thus, through the computation of $F(\vec{k})$, we are able to analyze the carrier scattering process which avoids the parametric dependence and assumptions associated with DP theory. The band energy, ε_i, and group velocity, ν_β are obtained from first principles calculations which are used for computing carrier-mobility (μ) based on the Boltzmann transport formalism within the Deformation Potential (DP) theory which has been detailed in previous chapter (chapter 5).

Mobility ($\mu_\beta^{e(h)}$) for electron (e) and hole (h) is defined as,

$$\mu_\beta^{e(h)} = \frac{e}{k_B T} \frac{\sum\limits_{i \epsilon CB(VB)} \int \tau_\beta(i, \vec{k}) {\nu_\beta}^2 b(\vec{k}) d\vec{k}}{\sum\limits_{i \epsilon CB(VB)} \int b(\vec{k}) d\vec{k}} \tag{6.7}$$

where,

$$b(\vec{k}) = exp[\mp \frac{\varepsilon_i(\vec{k})}{k_B T}] \tag{6.8}$$

Minus (plus) sign in the exponent stands for electron (hole).

6.3 Results and Discussion

6.3.1 Layer-dependent Criticality in the Electronic Structure of Black Phosphorus

Black phosphorus (BP) possesses an orthorhombic crystal structure (see Figure 6.1a). In the bulk state, it behaves like a van der Waals solid with significant interlayer interaction (81 meV per atom). This is due to a higher charge distribution in the interlayer spacing[39] compared to other van der Waals solids. The structure of TBP has been shown in Figure 6.1a.

Irrespective of the number of layers, phosphorene is always semiconducting with a wide range of optical and electronic band gaps.[7] Monolayer and bilayer phosphorene exhibit the gap state strictly at the Γ point. From 3-layers onwards, the valence band maximum (VBM) and conduction band minimum (CBM) begin to deviate from the high-symmetry (Γ) point. The band dispersion pattern for TBP is shown in Figure 6.1b (see Figure 6.2 showing the high symmetry points).

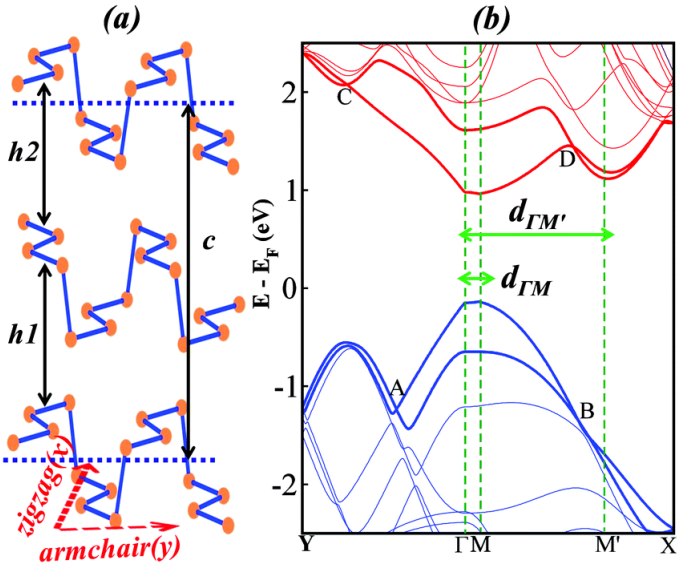

Figure 6.1: (a) Optimized structure of TBP (α-phosphorus, ABA stacking). 'c' is defined as the distance between the mid-line of a layer and the mid-line of another layer of the same phase in the ABA stacking pattern. h1 (h2) is the interlayer distance. (b) HSE06-predicted band-structure of TBP; A, B, C and D are the band-crossing points. M and M' are the 1st and 2nd minima at the conduction band. Offsets of M and M' from the Γ point have been denoted as $d_{\Gamma M}$ and $d_{\Gamma M'}$, respectively. Wigner-Seitz cell with high symmetry k-point is shown in Figure 6.2

The deviation for the 1st CBM, M, from the Γ point which is denoted as $d_{\Gamma M}$ (see Figure 6.1a) reaches the maximum at the bulk limit, as shown in Figure 6.3a. On the other hand, the deviation of the 2nd CBM (M′),$d_{\Gamma M'}$, is robust with respect to the variation in the number of layers (see Figure 6.3b). We also find that the energy difference between M and M′ in conduction band minima ($E_{MM'}$) increases linearly with the increase in number of layers from trilayer onwards (see

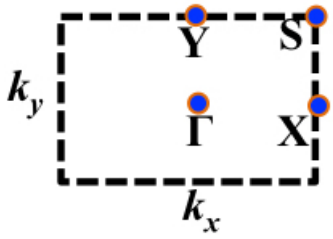

Figure 6.2: Wigner-Seitz cell with high symmetry k-points is shown for TBP (α-P), the optimised structure is shown in Figure 6.1a

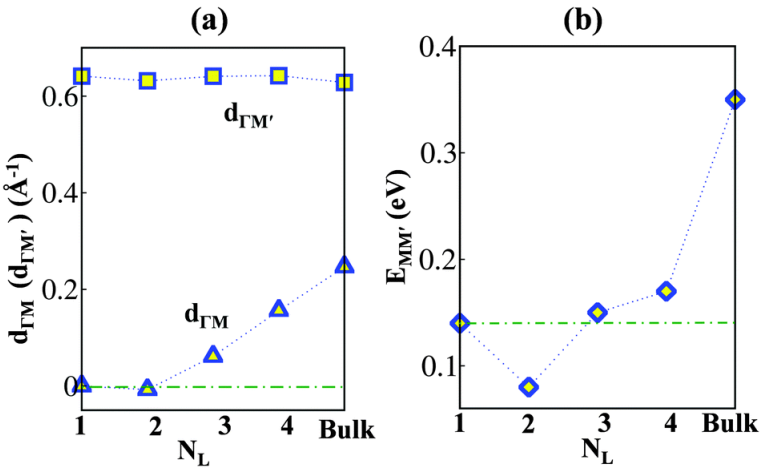

Figure 6.3: (a) $d_{\Gamma M}$ and $d_{\Gamma M'}$ versus number of layers (N_L), and (b) $E_{MM'}$ versus N_L.

Figure 6.3b). Notably, lesser the value of $|E_{MM'}|$, higher is the feasibility of multi-valley participation for electron transport. These band structure-derived features reveal that, tri-layer black phosphorus (TBP) appears to be interesting as both $d_{\Gamma M}$ and $E_{MM'}$ versus N_L alter their slope from negative to positive for $N_L \geq 3$. Moreover, TBP is unique due to its structure and fundamental symmetry criteria. First of all, it exhibits the ABA stacking pattern (Figure 6.1a) and belongs to the C_1 point group, thus, does not possess any spatial symmetry. This structural asymmetry breaks the electron-hole symmetry creating the possibility for bipolar conduction. Secondly, nanostructures can sustain more strain than bulk, thus, favoring strain-engineering.[40] Hence, TBP draws our attention for detailed analysis of its transport characteristics.

6.3.2 Carrier Transport Properties in TBP

For TBP, we find that the band gap (E_g) is 1.03 eV, where the gap-state is flat and slightly offset along the $\Gamma - X$ direction (see Figure 6.1b). We also note that the band-dispersion pattern indicates some hidden complexity. Near the gap state, the bands do not follow a parabolic dispersion pattern, rather it appears to be some-

what closer to a linear dispersion, that too only along the $\Gamma - X$ line for small k-values. However, in general, linear fitting is unsuitable for both the electron and hole effective mass calculations at the band-minima. Along the $\Gamma - Y$ line, we find perfect parabolic dispersion for small k-values. But, for several points in the band structure, the quadratic fitting is impossible. Hence, effective mass approximation is quite error prone. So, in this chapter, we use anisotropic relaxation time approximation (see Equation 6.6) for evaluation of the transport integrals which avoids the limitations associated with the effective mass approximation. Both the PBE and HSE06 functionals give consistent results for the nature of the wave function in the gap state and direct-indirect gap switching after application of strain. But, the variation of the shift in the band-edge due to applied strain cannot be predicted correctly by the PBE functional which is crucial to determine the deformation potential constant (E^c_β). Based on GGA approximation considered in PBE, the energy shift at the band edge position due to the application of strain reveals that, the slope of the linear fit defining E^c_β needs three different regimes as shown in Figure 6.4.

To understand the origin of such behaviour, we perform the wave function analysis (see Figure 6.5) at the Γ (high symmetry point) and M (band-gap state) points. At either of these points, both the VBM and CBM consist of extended islands. We also find that the p_z orbital is the major contributor to the VBM and CBM as well. Such diffused nature of the electronic wavefunctions lead to predominant electron-ion interaction over the electron-electron interaction in the exchange term (H). Accordingly, we confirm that improper account for the electron-ion interaction and the electron-electron interaction in the exchange term within PBE gives rise to such discrepancy. Indeed, the hybrid functional HSE06 with 35% Hartee exchange gives the E_g at 1.03 eV which corroborates well with the previous experimental result of 0.98 eV.[28] Additionally, this also provides a linear relationship (see Figure 6.6a and b) for the E_{band} versus strain.

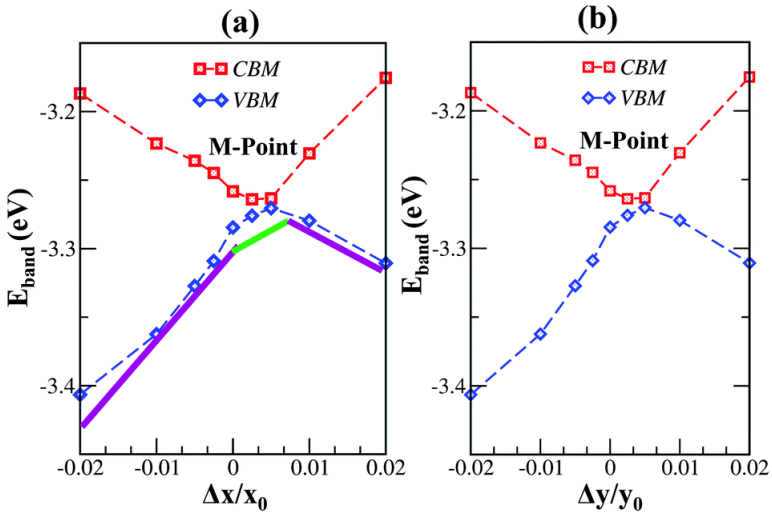

Figure 6.4: The band edge positions (E_{band}) of the valence band maximum (VBM) and the conduction band minimum (CBM) with respect to the lattice dilation $\Delta l/l_0$ along different in-plane directions for TBP. Band structures of TBP have been calculated at the PBE level of theory. E_{band} versus strain at the M point along the (a) zigzag direction, and (b) armchair direction.

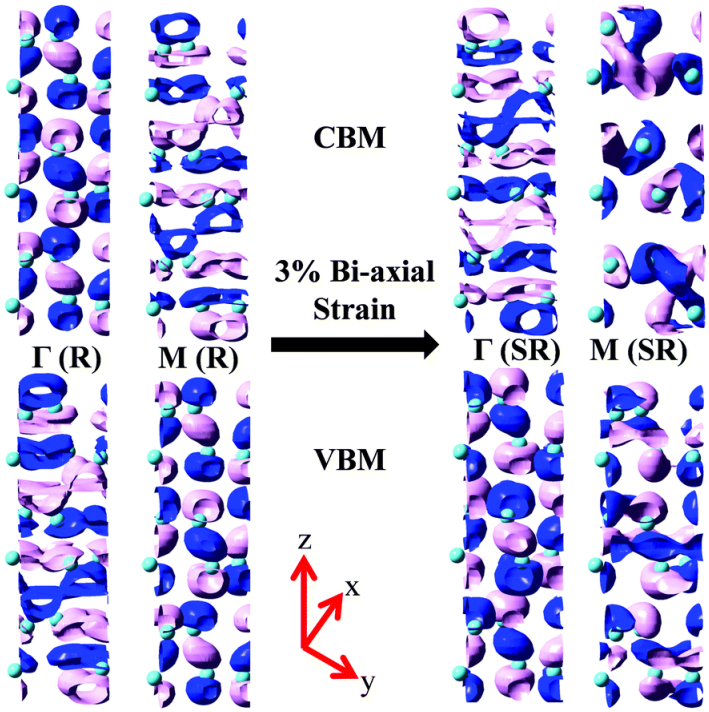

Figure 6.5: VBM and CBM wave functions at the Γ and M-point for TBP, before (left) and after (right) the application of strain. The isosurfaces for the wavefunction plots correspond to a value of 0.07 e $\AA^{-3}$ (left) and 0.06 e $\AA^{-3}$ (right).

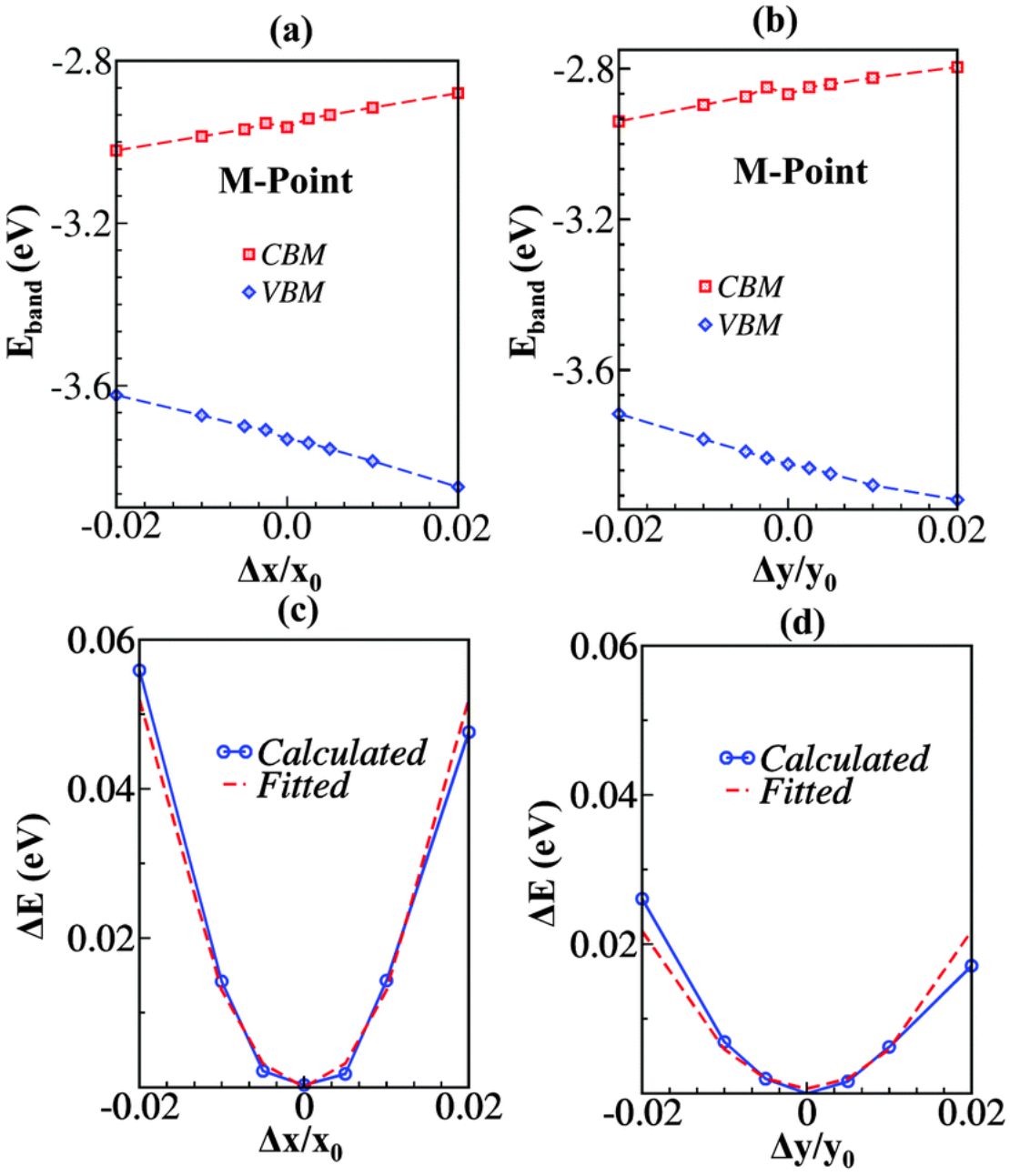

Figure 6.6: HSE06 computed E_{band} versus strain at the M point along the (a) zigzag (x) and (b) armchair (y) directions. (c) Increase in the total energy (ΔE) of the unit cell versus lattice deformation along the x direction and the same along the y direction is shown in (d). Dotted lines are the parabolic fittings, which give the elastic constant (C_β).

This linear relationship for E_{band} versus strain can be explained based on the analysis of nature (bonding or anti-bonding) of the electronic states. The amount of shift at the band-edge due to strain can be written as,

$$E_{Bonding} = 2E_0 + \frac{e^2}{R} + \frac{K+H}{1+S_O^2} \tag{6.9}$$

$$E_{Antibonding} = 2E_0 + \frac{e^2}{R} + \frac{K-H}{1-S_O^2} \tag{6.10}$$

where, E_0 is the energy for an isolated atom, K is the classical Coulomb energy, H is the exchange term and S_O is the overlap integral of the orbitals between different atomic sites. Application of positive (tensile) strain would result in an increased value for H which leads to an increase in $E_{Bonding}$ and a decrease in $E_{Antibonding}$. Since, S_0 will be negligibly small compared to K and H, behaviour of the bonding/antibonding state is dominated by the H term. In practice, the maximum (minimum) energy k-point belonging to the VBM (CBM) is considered as bonding (antibonding) in nature, generally. This is because, the minimum point at the CBM is the next higher energy state after the maximum point at the VBM. But, the complexity arises if there is a significant overlap along the out-of-plane direction whereas we focus on the number of nodes along in-plane directions to determine the bonding/antibonding characters. In a few layer phosphorene also, we find significant overlap interaction between two layers in the out-of-plane direction (see Figure 6.5). At the M point, VBM is anti-bonding (with a higher number of nodes) and CBM is bonding in nature (from a view along the xy plane). In fact, the VBM gets stabilized due to additional out-of-plane overlap interaction. So, the bonding or antibonding nature is an outcome of the interplay between both the in-plane and out-of-plane overlap which apply for every k-point constituting

a particular band. The reversal of the nature of the wave-functions for the VBM (CBM) at the M point leads to a gradual decrease (increase) in the eigenvalues with the increase in tensile strain. Thus, after examining the bonding (antibonding) character of the CBM (VBM), the linear relationship in the band-edge shift versus strain as shown in Figure 6.6a and b, is established. The deformation potential constant (E^c_β) is obtained from the slope of these linear plots, and is given in Table 6.1.

Table 6.1: Carrier types (P), where, $e(h)_{x/y}$ denotes the electron(hole) transport direction along x/y. E^c_β (eV) and $C_\beta(Jm^{-2})$ are the deformation potential and 2D elastic modulus. Effective mass (m^*) in TBP with 2% biaxial strain, $S = S^c_\beta/S^h_y$ values (see Equation 6.3 and 6.4) are given. Mobilities ($\mu_{effective}$) for intrinsic (0%); 4% uniaxial (y) strain; 2% biaxial tensile strain (x, y) have been calculated using Equation 6.7 at T = 300 K.

P	E^c_β	C_β	m*	S	$\mu_{effective}(10^3 cm^2V^{-1}s^{-1})$		
					0%	4%(y)	2%(x,y)
e_x	3.52	288.49	0.01	9.24	49.77	59.83	373.02
e_y	3.54	84.50	0.25	2.68	0.12	0.09	0.11
h_x	5.66	288.49	0.04	1.05	9.28	0.18	0.13
h_y	5.79	84.50	0.17	1.00	0.01	0.03	0.03

We note that, for TBP, E^c_β is sensitive only to the carrier type and not the directions which is unlike the case for the monolayer or the bulk.[7] This is due to the stacking-induced inter-layer overlap which equalises the number of the nodes along zigzag and armchair directions for the CBM (see Figure 6.5), resulting in equal electron-(acoustic) phonon scattering along different in-plane directions ($E^e_x \approx E^e_y$). This is also true for hole-(acoustic) phonon scattering ($E^h_x \approx E^h_y$). Irrespective of the directions, $E^h_{x/y}$ is $\sim$1.6 times higher than $E^e_{x/y}$. This gives rise to a unique feature with lesser electron-phonon (acoustic) coupling than hole-phonon (acoustic) coupling, which implies a faster excited-state decay process for electrons through quasi-equilibrium states. The 2D elastic constant (C_β) is obtained from the curvature of the parabolas (Figure 6.6c and d) and is given in Table 6.1. The lower value of C_y reveals that uniaxial strain along the armchair

(y) direction is easier. In particular, the tensile strain is more effective than the compressive strain for direct-indirect gap switching efficiency. In contrast to the uniaxial (y) strain (4%), we find the threshold value of biaxial tensile strain (TS) as direct-indirect gap switching is lower (3%). The conduction band dispersion for different values of TS has been shown in Figure 6.7. The critical strength of

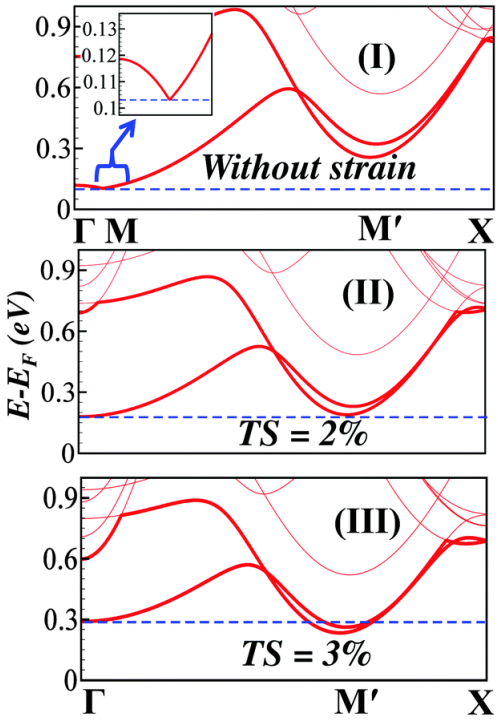

Figure 6.7: Dispersion of the conduction band: (I) before, and after the application of biaxial tensile strain (TS): (II) 2% and (III) 3%. All calculations are done with a dense grid at the PBE level of theory. The inset shows a zoomed in area.

TS (2%) results in $E_{MM'} \approx 0$ (see Figure 6.7 II), which facilitates multi-valley participation for electron transport. Moreover, since the biaxial strain does not need predetermination of the edge structure, it is more practical to use in devices. Hence, we put a special emphasis on the application of biaxial tensile strain over the uniaxial strain to control electron (hole) mobility. In response to the in-plane biaxial (tensile) strain, individual layers get stretched due to modulation of the out-of plane dihedral angle. As a result, the interlayer distances, (h1(h2) in Fig-

ure 6.1), get modulated due to the flattening of the ridged layers. But the mid-line of each layer remains at the same position, thus, the c-axis remains unchanged. For relaxed geometry (see Figure 6.1a), interlayer distances are found to be 3.08 $\mathring{A}$ (h1 = h2 = 3.08 $\mathring{A}$). Then again, h1 = h2 = 3.12 $\mathring{A}$ is found in the presence of 2% biaxial tensile strain which has also been found in previous studies.[16,22] Such mechanical responses give rise to modulation of band-structure e.g. crossing or avoidance (Landau quasi-degeneracy) after application of strain, which in turn can completely change the richness in transport parameters as reported in Table 6.1 and Figure 6.8.

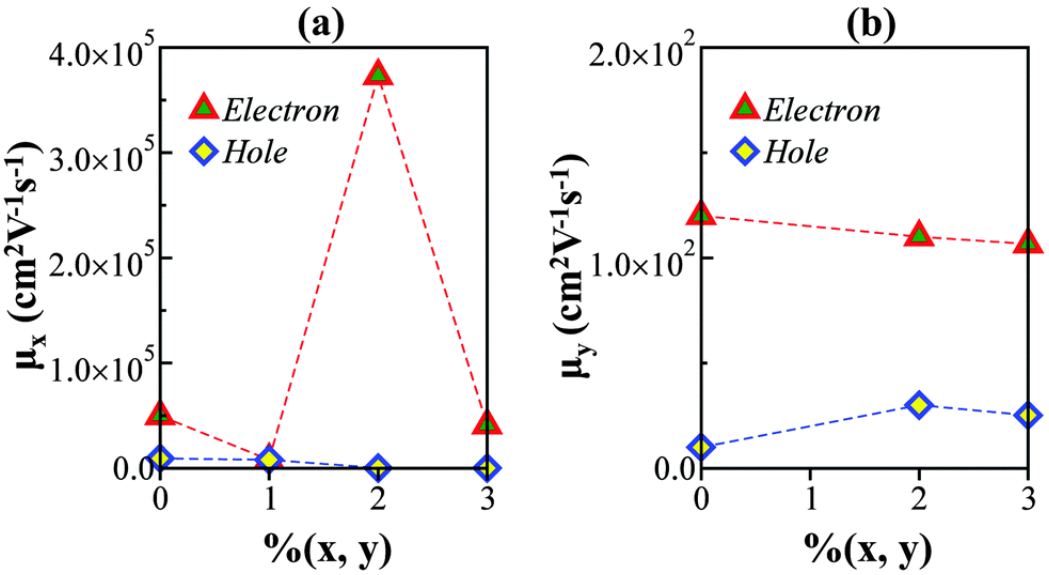

Figure 6.8: Carrier mobility along the (a) x and (b) y direction, for relaxed (0%x, y) as well as biaxially strained (%x, y) TBP. Note that, carrier mobility along the y direction is 10^3 fold lesser than the same along the x-direction.

After a systematic analysis of Figure 6.8 and the tabulated quantities in Table 6.1, we find that (a) both the carriers (e and h) exhibit higher mobility ($\sim 10^4$ $cm^2V^{-1}s^{-1}$) along the zigzag (x) direction compared to the armchair (y) direction, thus showing intrinsic directional anisotropy in transport behavior. (b) Strain favors one polarity (electronic transport) over the other, resulting in electron-hole anisotropy. The critical value of 2% biaxial tensile strain (TS) exhibits maximum

anisotropy (see Figure 6.8a). (c) TS_y is found to be even more influential than TS_x to regulate the mobility along the x-direction (see Figure 6.8b) which reveals that, although uniaxial input strain is vectorial, the output stress is tensorial. Hence anisotropic external perturbation can give rise to isotropic response.

6.3.3 Analysis of the Carrier Scattering Process

To determine the origin of such transport behavior, we need to find whether the anisotropy is associated with carrier-phonon scattering or carrier-carrier scattering. In view of the above, thermally averaged carrier-acoustic phonon scattering probability, $|M_i(k,k')|^2$, is evaluated based on two parameters, E^c_β and C_β (see computational details). E^c_β carries information on the carrier-type (c) as well as transport-direction (β). Thus, $M_i(k,k')$ can result in the discrimination of the electron-hole and/or transport direction. But, we find that E^c_β for TBP is sensitive only to the carrier type and not the directions. Hence, directional anisotropy cannot be attributed solely to the deformation potential, although it gives rise to slight carrier anisotropy. On the other hand, $C_{\beta(x,y)}$ depends only on the in-plane directions ($C_x > C_y$). Here, we define the parameter S (S^c_β; see Equation 6.3) which combines both the effects of E^c_β and $C\beta(x,y)$, determining the contribution of carrier-acoustic phonon scattering towards mobility. However, $S(h_x) : S(h_y)$, (see Table 6.1) cannot account for the directional anisotropy for hole mobility. Although, $S(e_x) : S(e_y) = 3.45 : 1$ accounts for a little directional anisotropy for electrons, it cannot explain the strain-induced amplification of mobility. Indeed, the $\mu_{effective(electron)}$(x): $\mu_{effective(hole)}$(x) ratio is found to be 5.36, which further increases to the order of 10^3 after application of biaxial strain. This remains unanswered from the S parameter. Since, the deformation potential constant and stretching modulus could not account for such large anisotropy in carrier transport,[24] we look at other descriptors, namely, $F(\vec{k})$, N_c and τ(k) (see Equation 6.5

and 6.6) to find whether the carrier-carrier scattering can explain the same.

To account for the scattering which involves the electron (hole) carrier states, we estimate the probability of transition from one state to another ($F(\vec{k})$, see eqn (6)). The band dispersion pattern which is often shown without using fundamental symmetry principles might be incorrect to determine $F(\vec{k})$. So, we employ the group theory to identify the symmetry of the discrete lattice/wave-functions and the band crossing at A, B, C and D (see Figure 6.1b). We find that electron mobility is very sensitive to the crossing between two lowest energy CBs. After consideration of only the CBM, electron mobilities for intrinsic (0%), 4% uniaxial (y) strain and 2% biaxial (x, y) strain are found to be 4.99 x 10^4, 6.36 x 10^4 and 40.44 x 10^4 ($cm^2V^{-1}s^{-1}$), respectively. These are significantly different from the quantities shown in Table 6.1 for electron mobility along the x-direction. On the other hand, such variation is negligibly small while only the VBM is considered as a representative for the whole VB. So, the effect of band crossing is insignificant to control the hole-mobility. Hence, we conjecture that, in the case of TBP, inter-band scattering play a significant role only in transport for electrons and not for holes.

From the τ(i,k) versus k plot, we find that the number of carrier states (N_c), their distribution pattern and the corresponding relaxation time (see Figure 6.9) vary while altering the carrier type or shifting the transport-direction. For electrons, the dynamics of collision systems covers a broad range of k-space along the $\Gamma - X$ band line but is restrained along $\Gamma - Y$ (see Figure 6.9b and d), revealing the directional anisotropy in electron scattering. More number of carrier states associated with high relaxation time along the zigzag direction essentially attributes to $\mu_{effective(electron)}(x) > \mu_{effective(electron)}$(y). This also explains the origin of the anisotropy in the excited state decay dynamics,[41] as found in very recent polarization-resolved transient reflection measurements. Interestingly, application of strain has dissimilar impact along different in-plane directions. From

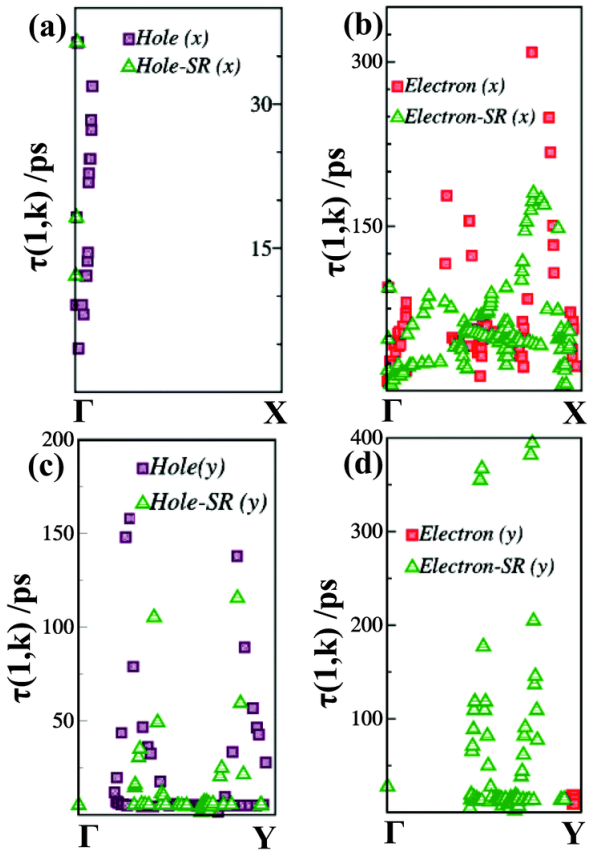

Figure 6.9: Relaxation time versus carrier-state along the $\Gamma - X$ band line is shown for (a) holes and (b) electrons in TBP. Similar plots along the $\Gamma - Y$ band line are shown for (c) holes and (d) electrons. 'SR' denotes the application 2% biaxial tensile strain (TS). The number of points corresponds to the number of carrier states (N_c) giving rise to the transport behavior dominated by the scattering relaxation time (τ).

Figure 6.9a and b, it is clear that, N_c for electrons does not change significantly due to strain (along the $\Gamma - X$ line). Thus, the recombination along the faster transport channel (x) is robust in the presence of strain, which also corroborates with previous findings.[34] But, along $\Gamma - Y$, available final states for electron scattering increases significantly (see Figure 6.9d) and new scattering states possess a higher relaxation time. Strain also induces perfect parabolic dispersion for the VBM and the CBM. This allows us to calculate the effective mass (m^*) for the strained structure and we find lower electronic effective mass (see Table 6.1) along x than along y. All these factors in combination with v_x and τ(k) keep the

electron mobility significantly high along the x-direction. But, hole-mobility gets reduced along x after application of strain (as shown in Table 6.1) which results in strain-induced carrier anisotropy ($\mu_{effective(electron)}(x/y) > \mu_{effective(hole)}(x/y)$). In fact, we find a very small overlapping region of carrier states (at small k-values along the $\Gamma - X$ line) which causes lowering of hole-scattering (see Figure 6.9a). Additionally, larger group velocity at these small k-values gives rise to high hole mobility. Along the y-direction, N_c dominates at higher k-values associated with lesser group velocity, which in turn gives rise to lesser hole mobility. Thus, similar to electrons, holes also exhibit directional anisotropy in the scattering process leading to $\mu_{effective(hole)}(x) > \mu_{effective(hole)}(y)$. Application of strain leads to a fewer carrier states compared to its unstrained state (see Figure 6.9a). Hence, a lesser number of carrier states effectively reduces the term present in the numerator of Equation 6.7, which contains relaxation time and group velocity as well. This leads to a decrease in hole-mobility along the $\Gamma - X$ direction. Despite the fact that strain induces new electron-scattering states along $\Gamma - Y$ with higher $\tau(\vec{k})$, $\mu_e(y)$ does not increase (see Table 6.1). This is due to lowering of $\nu_y(\vec{k})$ in the presence of strain. Consequently, strain induces a much higher ratio for $\mu_{effective(electron)}(x/y) : \mu_{effective(hole)}$(x/y). At the same time, it is noteworthy that, the x-direction is the dominating channel for charge-transport, as carrier mobility is much higher along this direction compared to the y-direction (see Table 6.1 and Figure 6.8) irrespective of whether the external strain is being applied or not. Thus, analysis of the carrier-scattering process proves that multiple correlations which involve both the group velocity and relaxation time of the carrier states dictate the transport behavior in TBP. To understand the layer-dependent alteration in the carrier-scattering process, we have re-examined the distribution of the carrier states and the corresponding relaxation time for TBP, as shown in Figure 6.9. Similar plots have been set for the monolayer and for the bulk (see Figure 6.10). Two factors remain crucial, (1) the number of carrier states (N_c) which govern the

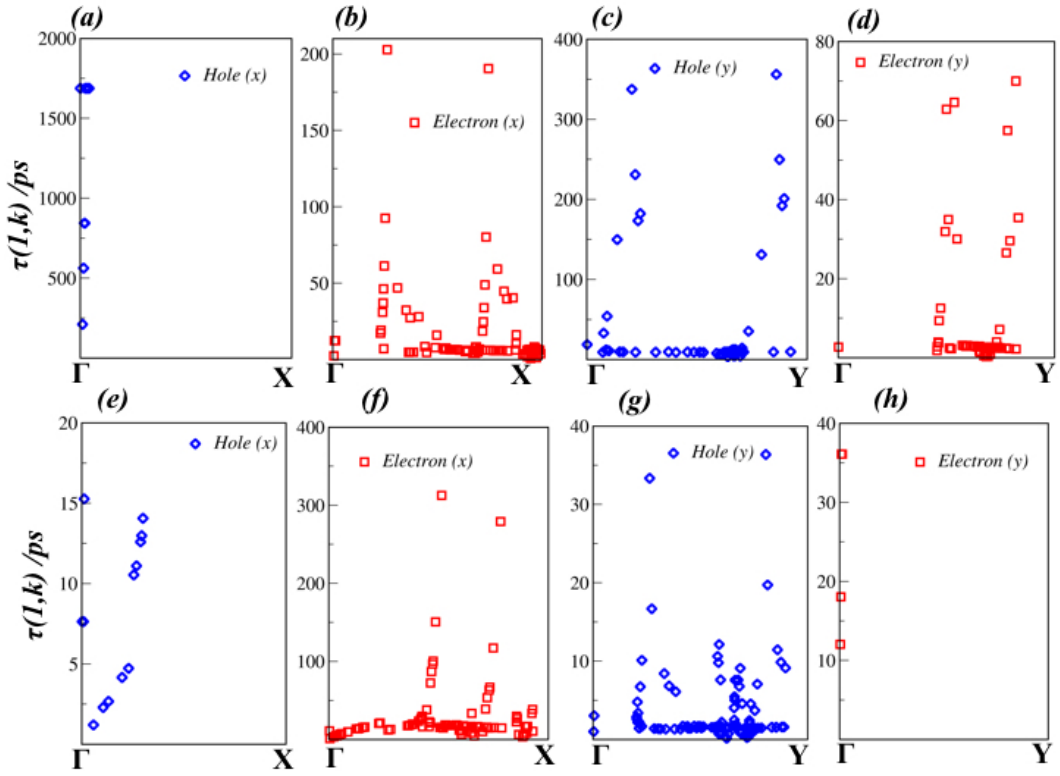

Figure 6.10: (a), (b), (c) and (b) represent the plot of relaxation time (as in eq. 2) vs. corresponding carrier-states (in k-space) along different transport direction and carriers for monolayer. (e), (f), (g) and (h) are the same for bulk (black) phosphorous.

scattering relaxation time (τ), and (2) their distribution patterns, whether they are localized or have equal probability throughout the transport direction ($\Gamma - X$ or $\Gamma - Y$). After a comparative analysis of two extremes i.e. monolayer and bulk, we find that both the N_c and their distribution patterns are different, resulting in the layer-dependent relaxation dynamics of electrons and holes. Especially, the carrier states near the Γ-point control the relaxation process for the charge carriers. This feature, however, depends crucially on the number of phosphorene layers. From tri-layer (TBP) onwards, more number of scattering states for electrons and holes show up within the conduction and valence bands, respectively (Figure 6.9 and Figure 6.10). Appearance of these states in the vicinity of the Γ-point (see Figure 6.9) along the $\Gamma - X$ band line is due to the Dirac-shaped

dispersion in the conduction (valence) band extrema (see the inset in Figure 6.7 I). The emergence of new states enhance the scattering of charge carriers within the CB (VB), leading to higher rates for relaxation (k_{relax}) for the electron (hole) in trilayer phosphorene and thereafter k_{relax} remains high even up to bulk phosphorus (see Figure 6.9 and Figure 6.10). Notably, the rate of electronic relaxation (k_{relax}) determines the photoluminescence (PL) quantum efficiency (η) which can be expressed as $k_{rad}/(k_{rad} + k_{relax})$, where k_{rad} is the rate of radiative recombination. As the number of layers increases from the monolayer to the trilayer and bulk, k_{rad} remains unaffected due to the maintenance of the direct band-gap nature. But more number of scattering states enhance the relaxation rates (k_{relax}) for electrons (holes) within the CB (VB), leading to a lower quantum efficiency in the trilayer onwards in comparison with that in the monolayer. This theoretical understanding on PL physics explains the experimental results too.[28] So, $F(\vec{k})$ appears to be a good descriptor to understand the transport anisotropy as well as electron-hole recombination process. Comparative analysis on the carrier mobility between monolayer phosphorene and TBP reveals that a much higher hole mobility (see Table 6.2) is found for the monolayer, whereas, TBP exhibits equal mobility

Table 6.2: Carrier types (P), where, $e(h)_{x/y}$ denote electron(hole) transport direction along x/y. Mobilities ($\mu_{effective}$) for monolayer have been calculated using Equation 6.7 at T = 300 K.

P	$\mu_{effective}$
e_x	0.28
e_y	0.01
h_x	0.57
h_y	12.49

for both the electron and the hole. Thus, our results clearly show the ambipolar behaviour for TBP, corroborating the experimental field effect mobility[5,6] for a few layer phosphorene (ambipolar), in contrast to monolayer phosphorene which acts as a p-type material.[13]

6.4 Conclusions

In summary, we have studied the charge-transport properties of a few layered black phosphorus based on Boltzmann transport formalism and density functional theory based first principles results. We find two important descriptors (S and $F(\vec{k})$) to analyze the electron (hole) scattering process in black phosphorus which confirmed collective multiple correlations in determining the recombination and relaxation dynamics of the carriers. The emergence of off-Γ scattering states caused by interfaces leads to a sharp drop in the photoluminescence efficiency for the number of layers ≥ 3. We propose that, trilayer black phosphorus (TBP) is unique in its electronic and spatial properties that differ from both the lower and the higher number of layers. Two important transport characteristics of TBP are: (i) both the electron and the hole exhibit high mobility with directional (zigzag) preference due to the higher relaxation time and group velocity of participating carrier states along the zigzag direction. (ii) In-plane tensile strain (biaxial) produces electron-hole anisotropy $[\mu_{electron} : \mu_{hole}] = 10^3 : 1$ with a maximum response at 2%. Criticality arises from the carrier scattering process, which is immensely dependent on strain induced multi-valley participation. The systematic scheme described in this chapter helps to understand the fundamentals of anisotropy associated with the carrier scattering process for any such complex quasi-2D materials which indeed has significant potential to design and optimize advanced transport (logical) devices. Importantly, phosphorene's success in electronics greatly depend on finding efficient ways to produce precise number of layers.

References

[1] C. Chowdhury, S. Jahiruddin, and A. Datta, The Journal of Physical Chemistry Letters **7**, 1288 (2016).

[2] D. Jose and A. Datta, Accounts of Chemical Research **47**, 593 (2013).

[3] M. Born and K. Huang, *Dynamical theory of crystal lattices* (Oxford university press, 1998).

[4] J.-W. Jiang, Nanotechnology **26**, 315706 (2015).

[5] M. Buscema, D. J. Groenendijk, S. I. Blanter, G. A. Steele, H. S. van der Zant, and A. Castellanos-Gomez, Nano Letters **14**, 3347 (2014).

[6] L. Li, Y. Yu, G. J. Ye, Q. Ge, X. Ou, H. Wu, D. Feng, X. H. Chen, and Y. Zhang, Nature Nanotechnology **9**, 372 (2014).

[7] J. Qiao, X. Kong, Z.-X. Hu, F. Yang, and W. Ji, Nature Communications **5** (2014).

[8] J. Guan, Z. Zhu, and D. Tománek, Physical Review Letters **113**, 046804 (2014).

[9] J. Xiao, M. Long, X. Zhang, J. Ouyang, H. Xu, and Y. Gao, Scientific Reports **5** (2015).

[10] Y. Cai, Q. Ke, G. Zhang, Y. P. Feng, V. B. Shenoy, and Y.-W. Zhang, Advanced Functional Materials **25**, 2230 (2015).

[11] R. Fei and L. Yang, Nano Letters **14**, 2884 (2014).

[12] S. Banerjee and S. K. Pati, Nanoscale **6**, 13430 (2014).

[13] H. Liu, A. T. Neal, Z. Zhu, Z. Luo, X. Xu, D. Tománek, and P. D. Ye, ACS Nano **8**, 4033 (2014).

[14] R. Fei, A. Faghaninia, R. Soklaski, J.-A. Yan, C. Lo, and L. Yang, Nano Letters **14**, 6393 (2014).

[15] H. Lv, W. Lu, D. Shao, and Y. Sun, Physical Review B **90**, 085433 (2014).

[16] X. Peng, Q. Wei, and A. Copple, Physical Review B **90**, 085402 (2014).

[17] A. Rodin, A. Carvalho, and A. C. Neto, Physical Review Letters **112**, 176801 (2014).

[18] J. Dai and X. C. Zeng, The Journal of Physical Chemistry Letters **5**, 1289 (2014).

[19] R. Schuster, J. Trinckauf, C. Habenicht, M. Knupfer, and B. Büchner, Physical Review Letters **115**, 026404 (2015).

[20] P. Li and I. Appelbaum, Physical Review B **90**, 115439 (2014).

[21] A. N. Rudenko and M. I. Katsnelson, Physical Review B **89**, 201408 (2014).

[22] M. Elahi, K. Khaliji, S. M. Tabatabaei, M. Pourfath, and R. Asgari, Physical Review B **91**, 115412 (2015).

[23] H. Morgan Stewart, S. A. Shevlin, C. R. A. Catlow, and Z. X. Guo, Nano Letters **15**, 2006 (2015).

[24] B. Liao, J. Zhou, B. Qiu, M. S. Dresselhaus, and G. Chen, Physical Review B **91**, 235419 (2015).

[25] D. Kamburov, H. Shapourian, M. Shayegan, L. Pfeiffer, K. West, K. Baldwin, and R. Winkler, Physical Review B **85**, 121305 (2012).

[26] V. Tran, R. Soklaski, Y. Liang, and L. Yang, Physical Review B **89**, 235319 (2014).

[27] V. Tran and L. Yang, Physical Review B **89**, 245407 (2014).

[28] S. Zhang, J. Yang, R. Xu, F. Wang, W. Li, M. Ghufran, Y.-W. Zhang, Z. Yu, G. Zhang, Q. Qin, et al., ACS Nano **8**, 9590 (2014).

[29] J. P. Perdew, K. Burke, and M. Ernzerhof, Physical Review Letters **77**, 3865 (1996).

[30] P. E. Blöchl, Physical Review B **50**, 17953 (1994).

[31] G. Kresse and D. Joubert, Physical Review B **59**, 1758 (1999).

[32] G. Kresse and J. Hafner, Physical Review B **47**, 558 (1993).

[33] G. Kresse and J. Hafner, Physical Review B **49**, 14251 (1994).

[34] G. Kresse and J. Furthmüller, Physical Review B **54**, 11169 (1996).

[35] E. Artacho, E. Anglada, O. Diéguez, J. D. Gale, A. García, J. Junquera, R. M. Martin, P. Ordejón, J. M. Pruneda, D. Sánchez-Portal, et al., Journal of Physics: Condensed Matter **20**, 064208 (2008).

[36] J. Heyd, G. E. Scuseria, and M. Ernzerhof, The Journal of Chemical Physics **118**, 8207 (2003).

[37] J. Heyd, G. E. Scuseria, and M. Ernzerhof, The Journal of Chemical Physics **124**, 219906 (2006).

[38] J. M. Ziman, *Principles of the Theory of Solids* (Cambridge university press, 1972).

[39] L. Shulenburger, A. D. Baczewski, Z. Zhu, J. Guan, and D. Tomanek, Nano Letters **15**, 8170 (2015).

[40] Q. Wei and X. Peng, Applied Physics Letters **104**, 251915 (2014).

[41] S. Ge, C. Li, Z. Zhang, C. Zhang, Y. Zhang, J. Qiu, Q. Wang, J. Liu, S. Jia, J. Feng, et al., Nano Letters **15**, 4650 (2015).

7

Stereo-control & Formation mechanism of Bisphenol A metabolites*

7.1 Introduction

Wide-spread exposure of Bis-phenol A (BPA) plays the adverse role as a micro-pollutant. Despite this fact, BPA-compounds are still in use as the key component of many commercial products made up of polycarbonate plastics and epoxy resins,[1–4] used in commercial products like coatings and liners of food containers,[5,6]. Thus, BPA-pollution becomes a part of our daily life. According to the survey executed by the National Toxicology Program (NTP), there exists "some concern for effects on the brain, behaviour, and prostate gland in foetuses, infants, and children at current human exposure to BPA". In fact, Tetrabromobisphenol A (TBBPA) is the most widely used brominated flame retardant (BFR). It is an excellent molecule that reduces the flammability of plastics and textile applications, for example, electronics, clothes, and furniture. This compound also

*Work reported in this chapter is published in: Swastika Banerjee, Ganga Periyasamy and Swapan K Pati, J. Phys. Chem. B, **118**, 31, 9258-9262 (2014)

degrades to Bisphenol A (BPA) and to an ether derivative of TBBPA (TBBPA-dimethyl-ether). These (TBBPA and its derivatives convert to BPA in the cycle of events) act as a potential source of pollutants in the environment.[7–9] In fact, the toxicity of BPA is often linked with the fact that its cage structure is very similar to that of dioxin compounds. This feature highlights the fact that stereocontrol is important to control the toxicity. According to earlier studies,[5,10–13] BPA acts as a transcriptional activator of human estrogen receptor ($ER\alpha$, $ER\beta$) and involves major health risks. It accumulates in nature without decomposition, causing neurotoxicity and reproductive damage in living organisms.[14–16] Low levels of BPA are detected in 90% of human urine samples, indicating the widespread exposure to BPA. Surprisingly, a predominant metabolite of BPA, called BPA monoglucuronide, is an inactive estrogen.[17] Hence, BPA-compounds and their potential health issues demand our understanding of the underlying mechanism behind its toxicity. When glucuronidation is unable to work as a detoxification pathway of BPA, metabolic activation occurs,[18] thereby producing two constitutional (structural) isomers with molecular formula ($C_{18}H_{20}O_2$), M-1 and M-2, as shown in Figure 7.2 . Importantly, recent endeavors[19,20] emphasize the fact that neither BPA nor M-1 but M-2 is the potential environmental estrogen because of its activity at nM concentration. The appropriate spacing of two terminal phenolic moieties and a middle aliphatic spacer group triggers M-2 to act as a potential disruptor toward the estrogen receptors ($ER\alpha$ and $ER\beta$).[21] However, the possibilities of controlling the selective formation and the detrimental action of toxic metabolite (M-2) are not well-known. Hence, computational studies have been employed to understand the electronic structural factors influencing the mechanistic pathway and the conformational features of biologically active M-2. In this context, previous studies on external-perturbation-induced conformational regulation of biological systems,[22] modulation of neuronal ion channels,[19,23,24] and protein targeting[25] are insightful. In this chapter, we present a thorough investigation of

the switching of the relative stability of BPA metabolites (isomers: M-1 and M-2) and the control over the conformation of the toxic metabolite (M-2) by external perturbation.

7.2 Computational Details

We suggest the mechanistic pathway for BPA metabolic activation, based on experimental findings as described in previous study(15) and our electronic structure calculations. The geometries of the reactants, intermediates, transition states, and products according to Schemes 1 and 2 are optimized using B3LYP as well as M06-2X functionals[26–33] with the 6-311+G (d, p) basis set.[34] Three different implicit solvent models of different dielectric constants (low (ε = 1), intermediate (ε = 46), and high (ε = 88)) have also been considered. Gaussian 09 programs are used for the density functional theory (DFT) calculations.[35–37] ^{1}H NMR peaks for M-2 have been calculated. There is excellent agreement between experimental and computational ^{1}H NMR peaks (see Table 7.1). The solvation effect in aqua phase (dielectric constant (ε) = 88) as well as DMSO solvent (ε = 46) was taken into account by the conductor-like polarizable continuum model[38,39] study. The computed ^{1}H NMR peaks obtained for M-2 (according to gas phase calculation) using Gaussian 09 package[40,41] with B3LYP hybrid functional and 6-311+G(d,p) basis set are well corroborative with the experimental (the solvent medium with ε = 4) findings which are given in Table 7.1.

These results validate our methods and show the appropriateness of the level of theory used for this study (see computational details). The same level of theory has been used to build a model interaction to understand the formation mechanism of M-1 and M-2 from various precursor radicals. The structure maximum energy structure for further calculations, which are specific for obtaining the structure of saddle points (OPT = TS keyword; followed by Transit-guided Quasi- Newton

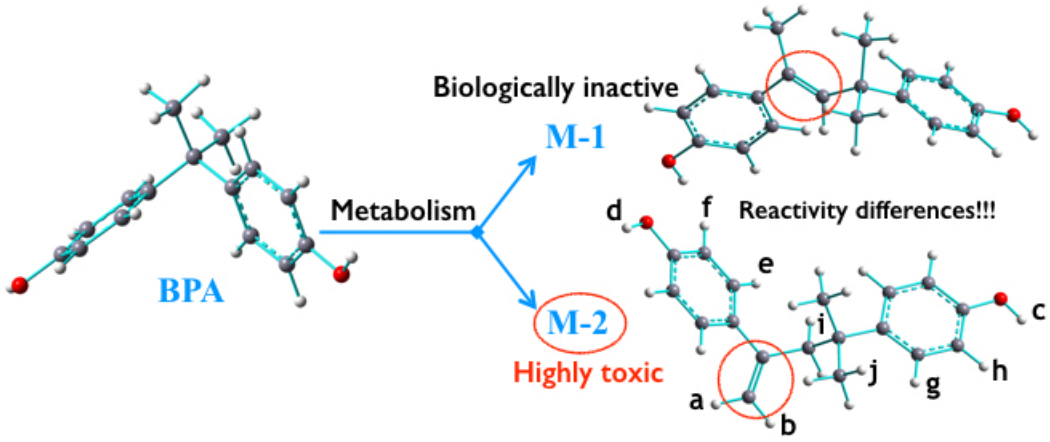

Figure 7.1: Molecular structure of (Bisphenol A; BPA) and consequential formation of 4-methyl-2,4-bis(p-hydroxyphenyl)pent-2-ene (M-1) and 4-methyl-2,4-bis(4-hydroxyphenyl)pent-1-ene (M-2). Note the assignment of particular H-atoms in M-2 (used in Table 7.1).

Table 7.1: Experimentally observed and computed ^1H NMR (ppm) for the assigned H atoms (see Figure 7.1) have been provided.

Proton	**Exp. ref:** [18]	**Theoretical**
a	5.07	5.13
b	5.29	5.29
c	4.64	3.67
d	4.71	3.70
e	7.25	7.34
f	6.68	6.52
g	7.13	7.12
h	7.10	6.45
i	2.74	2.51
j	1.50	1.55

method (QST3) procedure).[42–44] Finally, we have used the QST2 method, which does not need the information of a guessed structure of the transition state. All these trials give the same transition state energy and geometrical parameters, obtained by the intrinsic reaction coordinate analysis. Transition states and energy minima are verified by frequency calculations. Various appropriate conformations have been considered. Intrinsic reaction coordinate[45,46] (IRC) calculations were performed to confirm that the transition states (TS (M-1/M-2)) are connected with their corresponding reactant and product states.

Natural bonding orbital analysis (NBO) gives insights into the nature of the chemical bonding. Bond order has been characterized using Wiberg bond index matrix in the NAO (Natural Atomic Orbital) basis. All thermo chemical quantities have been calculated using Gaussian 09. Electronic energy with zero-point energy correction(E), enthalpy (H), free energy (G) are calculated considering T = 298 K and vibrational partition function depending on the frequencies (using the minima and saddle point structures). We explore effects of an applied field confining to the realm of perturbation theory which is away from the regime of high field. The applied uniform static electric field gradually increases from zero in steps of 0.0005 a.u.. Hence, we perform density functional theory computations with highly diffused and polarisable B3LYP/6-311++G (2d, 2p) basis set.

7.3 Results and Discussion

7.3.1 Mechanistic Pathways of BPA-metabolism

We analyse the electronic structural properties of the reactants, intermediates, transition states, and products to find the kinetically favoured path for BPA-metabolism and the possibility of the thermodynamic stereo-control. Our calculations also corroborate with previous experimental findings, such as, an ex-

cellent agreement between experimental and computational ^{1}H NMR peaks (see Table 7.1).[18] which agree with the fact that the recombination of radical precursors to form M-1 and M-2 complexes is thermodynamically more favourable than the recombination of ionic fragments.

In this chapter, two possible schemes (Schemes 7.2 and 7.3) are developed to understand the metabolic activation of BPA. These two schemes are well sup-

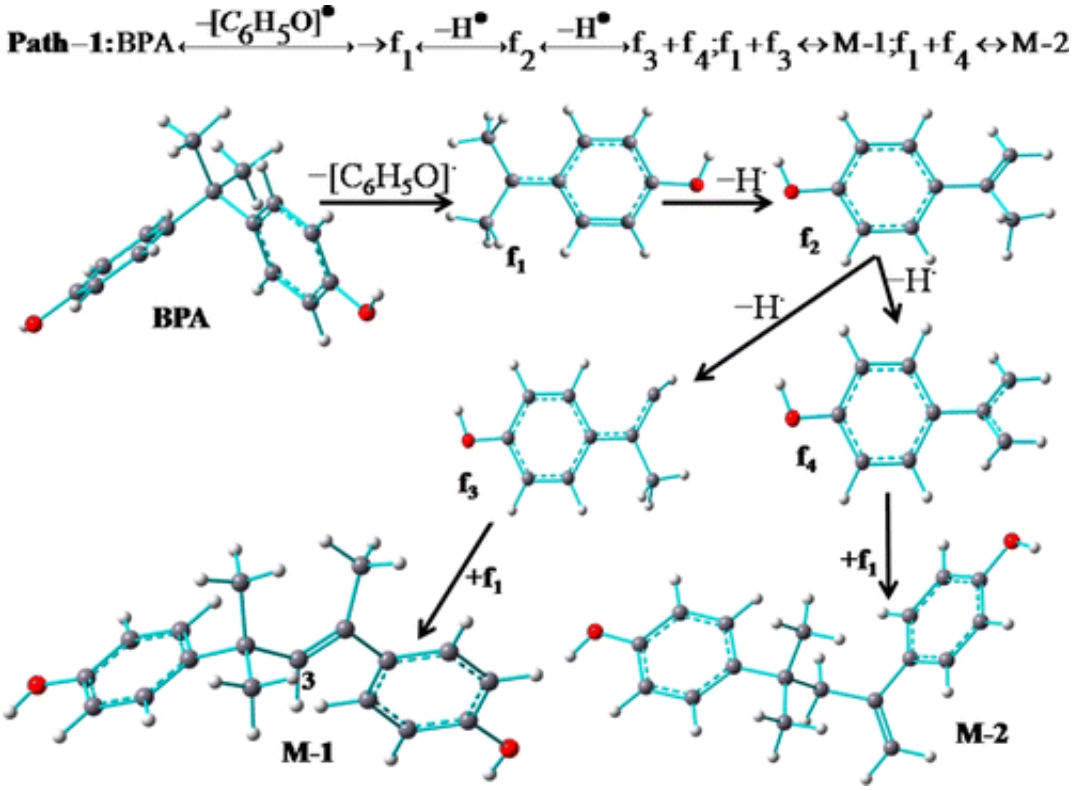

Figure 7.2: Possible mechanistic pathway for the formation of M-1 and M-2 from BPA.

ported by the LC/MS analysis of BPA metabolites (M-1 and M-2).[18] Our initial calculations have been carried out with the hybrid functional (B3LYP) and triple-ζ basis set including polarization as well as the diffusive nature of the atomic orbitals. This method is well verified, and the size of the basis set is good enough to study the energetics of such small purely organic molecules. In fact, using this functional, we find a negative free energy of formation for M-1 and M-2. As the

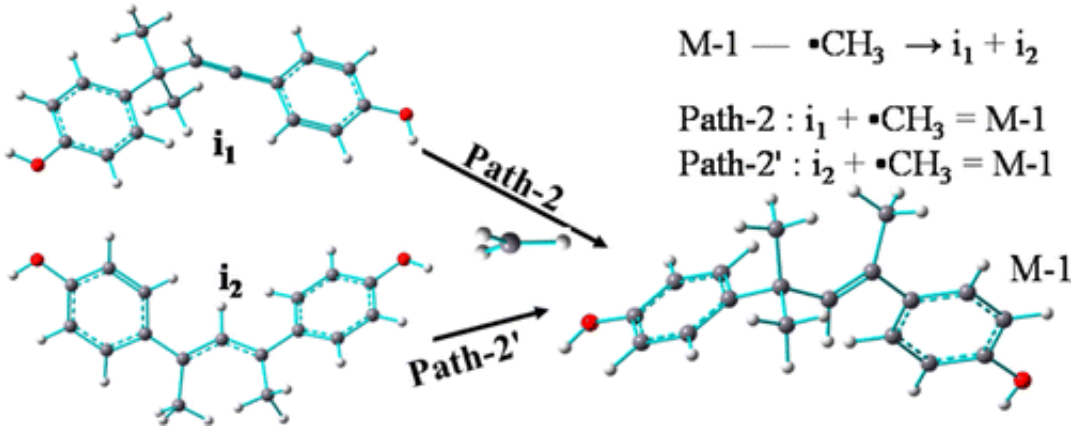

Figure 7.3: M-1 formation involving another set of precursor radicals as evidenced from mass-spectrometry.

metabolic activation happens under physiological conditions, we have provided the result that corresponds to the water solvent media.

The overall reaction is the following: 2 mol of BPA produced 2 mol of phenol and 1 mol of M-1/M-2. A negative free energy shows that formation of M-1 and M-2 is thermodynamically favorable; ΔG : -31.1 (M-1); -27.2 (M-2) kcal mol^{-1} (in water medium).

According to scheme 7.2, BPA degrades into two radical fragments, f_1 and phenolic radical. Rearrangement of f_1 is followed by the elimination of acidic $H^{\cdot}$ (f_2). Further elimination of H radical gives rise to f_3 and f_4 radicals, which remain in the medium along with the residuals f_1 and f_2. These fragment radicals are chemically stable with a larger HOMO-LUMO gap (see Table 7.2), resulting in a finite lifetime. This facilitates the occurrence of sequential steps (Figure 7.2). Extensive calculations prove that the combinations of f_3 and f_4 radicals with f_2 are the rate-determining steps for formation of M-1 and M-2, respectively. However, spectroscopic evidence[18] for the sustainability of i_1 and i_2 (molecular weight = 252) radicals from mass spectrometric analysis points toward the presence of another set of radical fragments as reactants for path-2 and path-2′ (see Figure 7.3). Here, i_1 and i_2 are interconvertible through intramolecular methyl group transfer.

Table 7.2: Effect of dielectric constant (ε) of solvent environment on the HOMO-LUMO energy gap (H-L) for various precursor radicals described in Figure 7.2 for M-1 and M-2 formation. ε = 1(gas-phase), ε = 46.7(DMSO) and ε = 88(Water).

Species	**H-L (eV)**		
	$\varepsilon = 1$	$\varepsilon = 46.7$	$\varepsilon = 88$
BPA	5.41	5.43	5.43
f_1	4.27	4.28	4.28
f_2	5.08	5.20	5.20
f_3	2.18	4.42	3.99
f_4	4.32	4.30	4.30
M-1	5.12	5.08	5.10
M-2	5.15	5.39	5.14

Thus, three different sets of precursor radicals (see path-1, path-2, and path-2′) participate in M-1 formation, whereas for M-2, only one set of radical precursors is involved (see path-1). Hence, the activation (enthalpy and free energy) barrier for the formation of M-1 and M-2 is essential to predict the most favorable pathway among the possibilities. Because this metabolic process happens in physiological conditions, we have included different dielectric media to mimic the solvent environment to assess the thermodynamic stability and kinetic feasibility.

We note that there are some recent theoretical advances and experimental evidence showing the poor performance of B3LYP in predicting reaction barriers.[47] The meta-hybrid-GGA functional M06-2X overcomes this problem associated with B3LYP to an appreciable extent. Hence, we have reconsidered our computational findings with M06-2X for predicting the reaction enthalpy as well as free-energy barriers, including the rate constants and entropic contribution toward the reaction kinetics (see Tables 7.3 and 7.4).

Interestingly, we find that the transition-state geometry does not differ for both functionals, showing its robustness. We also infer that both path-1 and path-2 (k is 7.318 s^{-1} at ε = 46 for path-1 and 1.211 s^{-1} at ε = 88 for path-2) are favored for M-1 formation (see Table 7.4), whereas M-2 formation appears to be preferred

Table 7.3: Computed activation barrier for various pathways in terms of the enthalpy ($\Delta H^{\#}$) and free energy ($\Delta G^{\#}$), in kcal mol^{-1}. Values shown in the table have been computed at B3LYP/6-311+G(d,p), and the values within the parentheses are the quantities obtained with M06-2X/6-311+G(d,p).

Path	**Complex formed**	$\Delta H^{\#}; \Delta G^{\#}$		
		$\varepsilon = 1$	$\varepsilon = 46.7$	$\varepsilon = 88$
Path-1	**M-1**	37.6 (4.8); 50.2 (17.8)	11.5 (16.1); 27.6(18.3)	11.5 (16.1); 27.5 (17.3)
	M-2	27.4(16.7); 40.2(28.5)	28.1 (17.9); 41.5(30.1)	28.1 (17.9); 41.5(30.1)
Path-2	**M-1**	21.6 (9.7); 33.0(20.7)	13.3(4.5); 20.2(14. 9)	15.9(10.1); 10.3(20.6)
Path-2'	**M-1**	65.5; 81.8	67.6; 82.5	67.8; 80.5

Table 7.4: Entropy change associated with the formation of transition states in different paths ($\Delta S^{\#}$ in cal mol^{-1}) and the reaction rate constant k in s^{-1} at T = 298 K.

Path	**Complex formed**	$\Delta S^{\#}; k$		
		$\varepsilon = 1$	$\varepsilon = 46.7$	$\varepsilon = 88$
Path-1	**M-1**	-45.0; 0.557	-7.9; 0.216	-4.3; 1.211
	M-2	-41.1; 7.456 x 10^{-7}	-42.3; 0.527 x 10^{-9}	-42.3; 0.518 x 10^{-9}
Path-2	**M-1**	-38.1; 0.004	-36.0; 7.318	-36.1; 0.005

via path-1 with a rate constant of k = 7.456 x 10^{-7} s^{-1} in a medium with low dielectric constant. Interestingly, the increase in the dielectric constant (ε) of the medium boosts the selective formation of less toxic M-1 (see Tables 7.3 and 7.4).

7.3.2 Factors Leading to Selective Formation of Less Toxic Metabolite From BPA

The significant difference in reaction activation free energy and enthalpy barriers shown in Table 7.3 reveals the striking role of entropy changes during reaction. In fact, the entropy decreases substantially due to the formation of a transition state after the combination of radical precursors (see Table 7.4). The entropic effect is comparatively less important in the case of M-1 formation via path-1 in a medium with a high dielectric constant. Moreover, the formation of M-1 and

M-2 involves a polar transition state (see Figure 7.4), which is reflected in the pronounced sensitivity of the transition-state energy barrier (see Table 7.3) and rate constant (see Table 7.4) to the different polar environments.

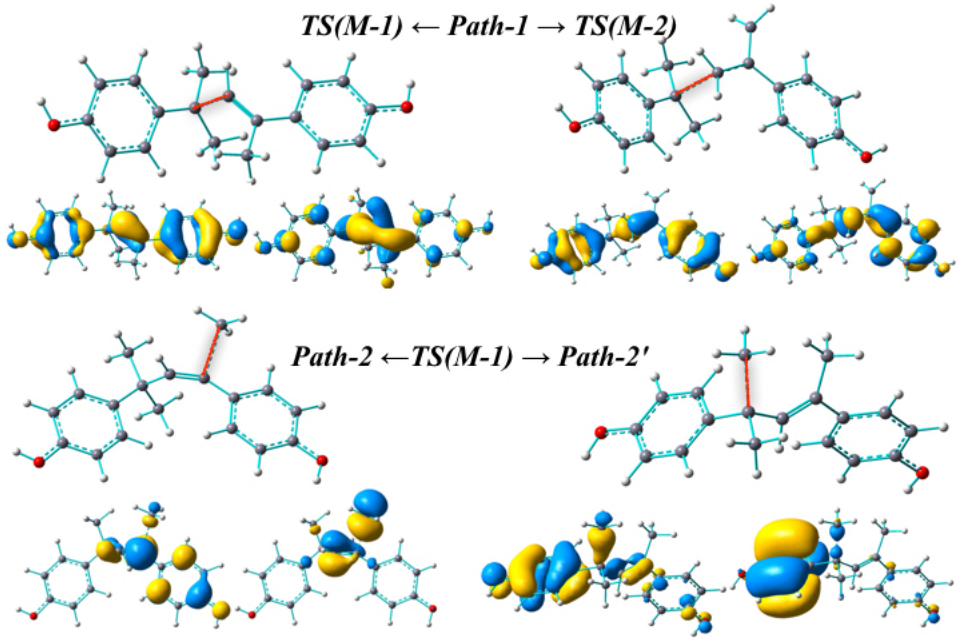

Figure 7.4: B3LYP/6-311+G (d,P)/PCM optimized transition-state geometries of the rate-determining steps for M-1 and M-2 formation. Transition orbitals are also shown.

Although the fundamental conclusions on favored paths and control over the reaction rates based on B3LYP calculations are very corroborative with the findings using the M06-2X functional, there is a difference in quantitative values for the activation energy barrier. While both set of results agree well with each other, predicting the possibility for path-2 toward the formation of M-1, the computed activation energy barriers using M06-2X appear to be lower in comparison with B3LYP. This is due to the increase in the relative stability of the transition state with the consideration of a highly nonlocal functional with a double amount of nonlocal exchange (in M06-2X). The difference in the reaction energy barrier is expected because proper consideration of the treatment of the orbital transition (π-π^*) and asynchronicity associated with the activation have been treated differ-

ently for two different density functionals.[47]

7.3.3 Relative Thermodynamic Stability of Isomeric Metabolites (M-1 and M-2)

Relative stability of BPA metabolites (M-1 and M-2) has been studied at different solvent polarities (see Table 7.5). However, the relative stability change is in the energy range of thermal processes at room temperature.This reveals equal stability of M-1/M-2 in various implicit solvent considerations. Therefore, polarizable

Table 7.5: Effect of dielectric constant (ε) of solvent environment on the relative stability, ΔE, ΔH and ΔG in kcal mol^{-1} are the difference in energy of M-2 and M-1.

$\varepsilon = 1(gas-phase)$			$\varepsilon = 46.6(DMSO)$			$\varepsilon = 88(Water)$		
ΔE	ΔH	ΔG	ΔE	ΔH	ΔG	ΔE	ΔH	ΔG
-0.6	-0.9	-0.1	1.4	0.9	0.3	-0.9	-1.1	-0.4

continuum solvation is unable to selectively stabilize one over another. Hence, the responses of M-1 and M-2 are studied in the presence of static electrical polarization to investigate the possibility of electrical polarization as a switch to control their relative stability. To study the response of M-1 and M-2 to external uniform static electric fields, we perform density functional theory computations with a highly diffused and polarizable basis set. We have considered fields in the range of 0.00-0.01 a.u. (to avoid numerically very large field strengths; 0.01 a.u. of the electric field = 0.5142 V/$\mathring{A}$). Figure 7.5 reveals that the stability of M-1 and M-2 can be swapped by controlling the static electric polarization in media. M-1 becomes preferential below a threshold value of $\sim$0.005 a.u.. We believe that this is an appropriate direction for alteration of the relative stability of M-1 and M-2. In order to understand this different response of M-1 and M-2 to an external electric field, we focus on their inherent polarization (see the electrostatic potential map in Figure 7.6), which is significantly different for M-1 and M-2. In fact, M-1 and

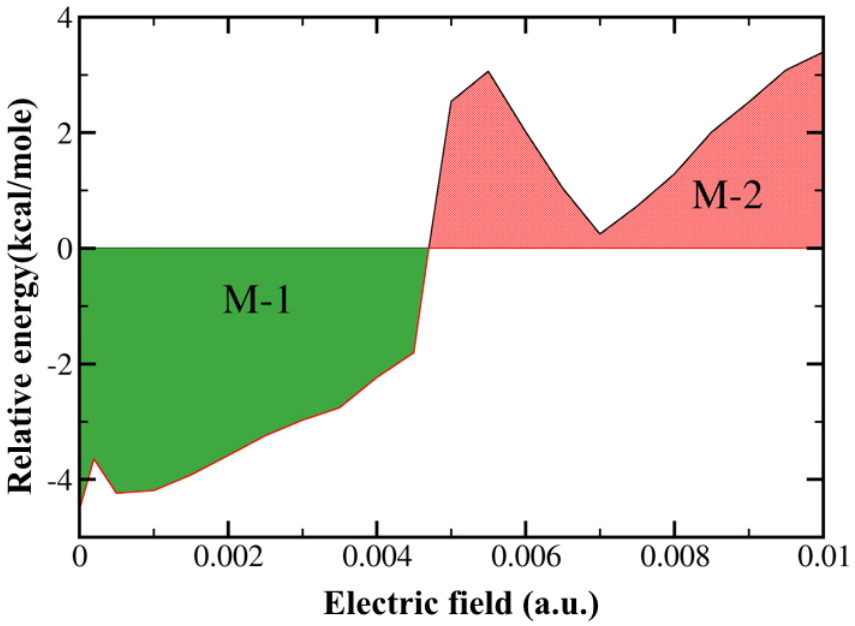

Figure 7.5: Relative energy (difference in electronic energy of M-1 and M-2) is shown under the influence of uniform static electric field.

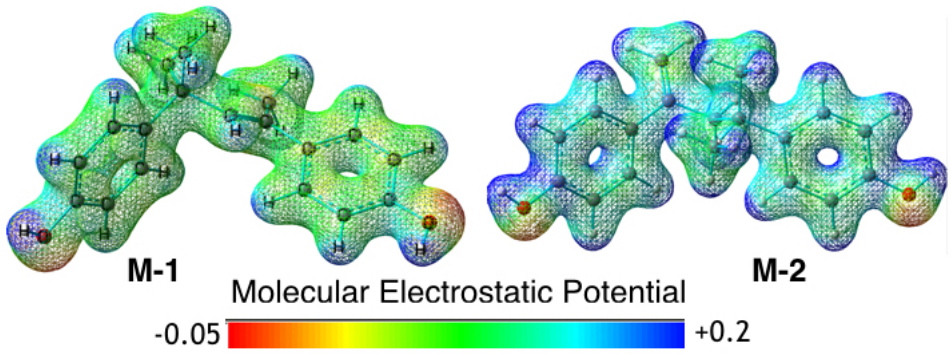

Figure 7.6: Molecular electrostatic potential mapped on the total electron density. An isocontour value of 0.02 e bohr^{-3} has been used for mapping. The blue and red regions indicate electrophilic sites and nucleophilic sites respectively.

M-2 possess different π delocalization patterns; hence, the electric field polarizes them differently and brings out the discrepancy in electronic redistribution and stabilization. Therefore, static electric polarization controlling the relative stability of M-1 over M-2 and vice versa can be used as a "switch", which occurs at a very small field strength ($\sim$0.005 a.u. $\approx$ 0.26 V/$\mathring{A}$).

7.3.4 Stereo-control of Toxic Metabolite (M-2) Through External Electric Field

An optimum conformational feature (terminal O-H bond orientation, molecular length) of M-2 is a crucial factor for its receptor binding. Hence, we focus on the possible stereocontrol of a toxic metabolite (M-2). Detailed conformational analyses reveal that M-2 exhibits two possible orientations of the terminal O-H (short length conformer: SLC and extended length conformer: ELC, shown in Figure 7.7 I). They are energetically equal but have strikingly different molecular lengths (dif-

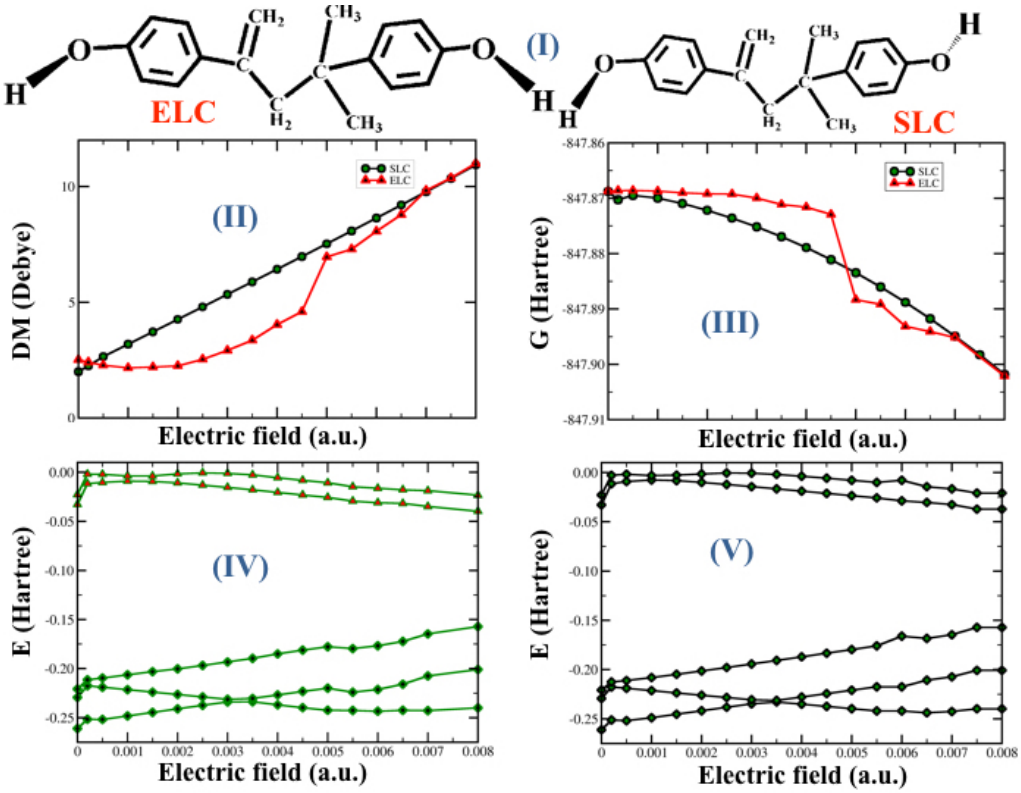

Figure 7.7: (I) Two conformers of M-2 (ELC and SLC); (II) their different responses in the electric dipole moment; (III) free energy responses; (IV) energetics of electronic states (from bottom to top starting from HOMO-2 up to LUMO+1) of the ELC; and (V) for SLC under the influence of uniform static electric polarization.

ference: $\sim$1 $\mathring{A}$) and dipole moments (difference: $\sim$0.51 D). The interaction of an overall electrically neutral polar species (net dipole moment = μ) with an imposed

electric field F comes through a dipole interaction given by -μF. This interaction favors alignment of individual bond dipoles along the field direction and promotes electronic redistribution. Figure 7.7 II shows that the dipole moment increases smoothly with an increase in external perturbation with a constant slope for SLC but not for ELC. An abrupt increase in the dipole moment of ELC ($\sim$0.005 a.u.) is followed by equalization in dipole moments and the free energy with SLC, after 0.007 a.u. (see Figure 7.7 II and III). At a critical electric field value (0.003 a.u.), their HOMO-LUMO gap remains large, but the gap between HOMO-1 and HOMO-2 tends to zero (see Figure 7.7 IV). Moreover, NBO analysis discloses that individual bond orders are not affected (at $<$ 0.01 a.u.), ensuring that the lower electric field strength does not cause fragmentation/structural breakdown but confers conformational switching with (a) changes in the effective length of the molecule and (b) dihedral angle changes in the linker aliphatic group. Thus, selective stabilization of one (between ELC and SLC) is found to be possible through regulation of static electric polarization. This might be considered as a powerful tool to control the simultaneous binding of two terminal phenolic groups to the receptor utilizing an effective alteration of the overall length of M-2. On the other hand, closing of the frontier molecular energy levels (HOMO and LUMO), leading to destabilization and fragmentation, occurs at a high enough field strength (see Figure 7.8 and 7.9).

Hence, redistribution of electron density culminates into a catastrophic structural breakdown beyond a specific threshold field strength (0.018 a.u.). Electronic structural changes are found to be accompanied by an abrupt increase in the electric dipole moment, showing a transition point (0.018 a.u.). Thus, uniform static electric polarization becomes a powerful tool for conformational switching and structural evolution of M-2, depending on the choice of strength of external polarizations.

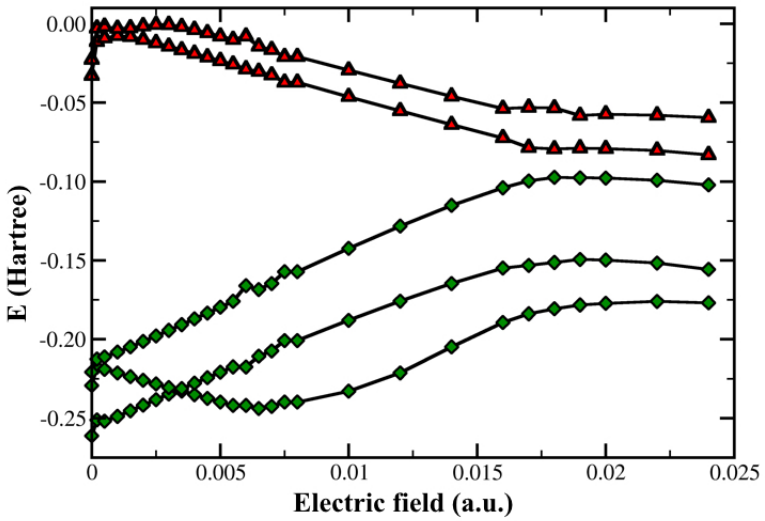

Figure 7.8: Variation in energetics of electronic states (HOMO-2, HOMO-1, HOMO, LUMO, LUMO+1 from down to up) with increase in electric field strength for ELC are shown. Only, ELC has been considered for clarity in figure as both the conformers (ELC and SLC) follow the similar response pattern in the energetics of electronic states.

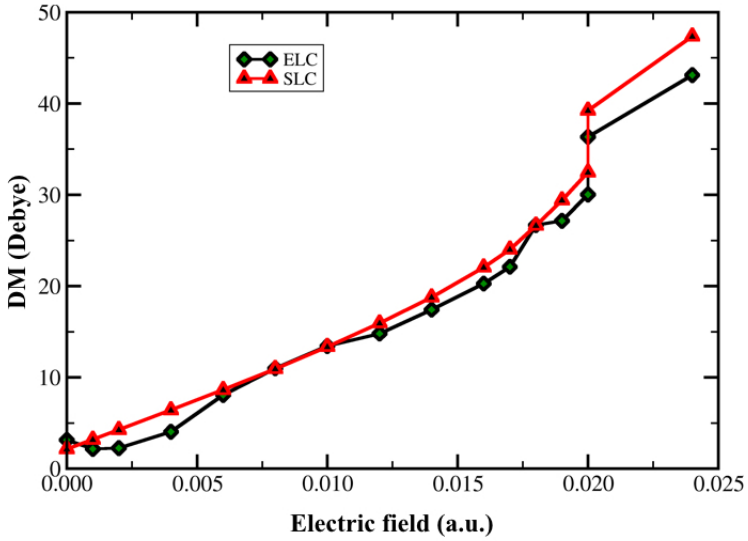

Figure 7.9: Different responses in electric dipole moment of two conformers of M-2 (ELC and SLC) with increase in electric field strength.

7.4 Conclusion

In summary, DFT calculations along with corroborative experimental findings[18] elucidate that the solvent polarity and nature of radical intermediates determines different reaction pathways of metabolic activation. Harmful metabolite (M-2) formation decreases with an increase in the dielectric constant (ε) of the environment (solvent). Sensitivity toward static polarization offers experimental possibilities to achieve reversible switching between a biologically active (M-2) and an inactive state (M-1). Hence, the critical value of the field strength is found to be $\sim$0.005 a.u. We also point toward the conformational change of M-2, which in turn can affect binding to the receptor.

References

[1] H. L. Wang, L. Toppare, and J. E. Fernandez, Macromolecules **23**, 1053 (1990).

[2] A. Dondoni, C. Ghiglione, A. Marra, and M. Scoponi, Chemical Communications pp. 673–674 (1997).

[3] D. Das, J.-F. Lee, and S. Cheng, Chemical Communications pp. 2178–2179 (2001).

[4] Z. Liu, X. Zhang, S. Poyraz, S. P. Surwade, and S. K. Manohar, Journal of the American Chemical Society **132**, 13158 (2010).

[5] A. V. Krishnan, P. Stathis, S. F. Permuth, L. Tokes, and D. Feldman, Endocrinology **132**, 2279 (1993).

[6] K. C. Dowling and J. Thomas, Macromolecules **23**, 1059 (1990).

[7] M. Alaee, P. Arias, A. Sjödin, and Å. Bergman, Environment International **29**, 683 (2003).

[8] H. J. Geyer, K.-W. Schramm, P. O. Darnerud, M. Aune, E. A. Feicht, K. W. Fried, B. Henkelmann, D. Lenoir, P. Schmid, and T. A. McDonald, Organohalogen Compounds **66**, 3867 (2004).

[9] T. Hamers, J. H. Kamstra, E. Sonneveld, A. J. Murk, M. H. Kester, P. L. Andersson, J. Legler, and A. Brouwer, Toxicological Sciences **92**, 157 (2006).

[10] A. Tabata, S. Kashiwada, Y. Ohnishi, H. Ishikawa, N. Miyamoto, M. Itoh, and Y. Magara, Water Science and Technology **43**, 109 (2001).

[11] P. Eriksson, E. Jakobsson, and A. Fredriksson, Organohalogen Compounds **35**, 375 (1998).

[12] C. A. Staples, P. B. Dome, G. M. Klecka, S. T. Oblock, and L. R. Harris, Chemosphere **36**, 2149 (1998).

[13] X. Shen, L. Zhu, N. Wang, L. Ye, and H. Tang, Chemical Communications **48**, 788 (2012).

[14] A. Atkinson and D. Roy, Environmental and Molecular Mutagenesis **26**, 60 (1995).

[15] D. Roy, M. Palangat, C.-W. Chen, R. D. Thomas, J. Colerangle, A. Atkinson, and Z.-J. Yan, Journal of Toxicology and Environmental Health Part A **50**, 1 (1997).

[16] N. Ben-Jonathan and R. Steinmetz, Trends in Endocrinology & Metabolism **9**, 124 (1998).

[17] J. B. Matthews, K. Twomey, and T. R. Zacharewski, Chemical Research in Toxicology **14**, 149 (2001).

[18] S. Yoshihara, T. Mizutare, M. Makishima, N. Suzuki, N. Fujimoto, K. Igarashi, and S. Ohta, Toxicological Sciences **78**, 50 (2004).

[19] X. Mu, C. V. Rider, G. S. Hwang, H. Hoy, and G. A. LeBlanc, Environmental Toxicology and Chemistry **24**, 146 (2005).

[20] M. E. Baker and C. Chandsawangbhuwana, PloS One **7**, e46078 (2012).

[21] K. Pettersson and J.-Å. Gustafsson, Annual Review of Physiology **63**, 165 (2001).

[22] J. M. Hall, D. P. McDonnell, and K. S. Korach, Molecular Endocrinology **16**, 469 (2002).

[23] M. Stierl, P. Stumpf, D. Udwari, R. Gueta, R. Hagedorn, A. Losi, W. Gärtner, L. Petereit, M. Efetova, M. Schwarzel, et al., Journal of Biological Chemistry **286**, 1181 (2011).

[24] G. Mayer and A. Heckel, Angewandte Chemie International Edition **45**, 4900 (2006).

[25] P. Walter and A. E. Johnson, Annual Review of Cell Biology **10**, 87 (1994).

[26] M. Ernzerhof and G. E. Scuseria, The Journal of Chemical Physics **110**, 5029 (1999).

[27] T. Yanai, D. P. Tew, and N. C. Handy, Chemical Physics Letters **393**, 51 (2004).

[28] D. Bilc, R. Orlando, R. Shaltaf, G.-M. Rignanese, J. Íñiguez, and P. Ghosez, Physical Review B **77**, 165107 (2008).

[29] M. Frisch, G. Trucks, H. B. Schlegel, G. Scuseria, M. Robb, J. Cheeseman, G. Scalmani, V. Barone, B. Mennucci, G. Petersson, et al., Inc., Wallingford, CT **200** (2009).

[30] Y. Zhao, N. E. Schultz, and D. G. Truhlar, Journal of Chemical Theory and Computation **2**, 364 (2006).

[31] Y. Zhao and D. G. Truhlar, The Journal of Physical Chemistry A **110**, 13126 (2006).

[32] Y. Zhao and D. G. Truhlar, The Journal of Chemical Physics **125**, 194101 (2006).

[33] Y. Zhao and D. G. Truhlar, Theoretical Chemistry Accounts **120**, 215 (2008).

[34] M. P. Andersson and P. Uvdal, The Journal of Physical Chemistry A **109**, 2937 (2005).

[35] W. Kohn, A. D. Becke, and R. G. Parr, The Journal of Physical Chemistry **100**, 12974 (1996).

[36] A. D. Becke, The Journal of Chemical Physics **98**, 5648 (1993).

[37] A. G. Baboul, L. A. Curtiss, P. C. Redfern, K. Raghavachari, et al., The Journal of Chemical Physics **110**, 7650 (1999).

[38] M. Cossi, V. Barone, R. Cammi, and J. Tomasi, Chemical Physics Letters **255**, 327 (1996).

[39] E. Cances, B. Mennucci, and J. Tomasi, The Journal of Chemical Physics **107**, 3032 (1997).

[40] F. Blanco, I. Alkorta, and J. Elguero, Magnetic Resonance in Chemistry **45**, 797 (2007).

[41] S. Wolff and T. Ziegler, The Journal of Chemical Physics **109**, 895 (1998).

[42] C. Peng and H. Bernhard Schlegel, Israel Journal of Chemistry **33**, 449 (1993).

[43] P. Y. Ayala and H. B. Schlegel, The Journal of Chemical Physics **107**, 375 (1997).

[44] M. M. Midland, The Journal of Organic Chemistry **63**, 914 (1998).

[45] K. Fukui, The Journal of Physical Chemistry **74**, 4161 (1970).

[46] C. Gonzalez and H. B. Schlegel, Journal of Physical Chemistry **94**, 5523 (1990).

[47] M. Linder and T. Brinck, Physical Chemistry Chemical Physics **15**, 5108 (2013).

8

Surface Mediated Isolation and Detection of BPA Derivatives*

8.1 Introduction

Micro-pollutants, classified as endocrine disrupting chemicals (EDCs)[1] cause severe human health risk, for example, disorder in reproductive,[2] immune,[3] hormonal,[4] and nervous systems.[5] Bisphenol A and its derivatives belong to this category of EDCs, which are commonly found in surface water, drinking water, and the commercial plastic products used in our day-to-day life. Over the last decade, there have been several efforts towards detection of these environmental pollutants.[6] There is also a deep concern for the removal of these contaminants from water.[7,8] As a matter of fact, traditional processes such as coagulation and flocculation are ineffective in this regard.[9,10] Treatment with the chemical oxidants is also limited due to the possibility of formation of even more toxic oxidation products.[11] There are a few studies using reverse osmosis and nanofiltration as tools.[12] However, these techniques are economically unfeasible. In reality, both the water and wastewater treatment plants are not properly designed to re-

*Work reported in this chapter is published in: Swastika Banerjee and Swapan K. Pati, ACS Applied Materials & Interfaces, **7**, 43, 23893-23901 (2015)

move micropollutants. In this scenario, a new technology is needed that would be abundant, efficient, and feasible. A composite of activated carbon fiber and $Ce^{3+}-TiO_2$ treatment has been accepted as an efficient strategy for the removal of hydrophobic micro-pollutants.[13,14] However, this approach is reserved for drinking water treatment. Moreover, recyclability of this material needs regenerative oxidation of absorbed BPA, creating inconvenience for practical applications. Thus, absorption-desorption kinetics is crucial to design a functional component with better synergy in terms of reusability of the material. Apart from the strategy for physical separation, detectable response upon EDC adsorption is an important factor for recognition of such micropollutants. Very recently, Huang et al. have shown that oxidation product of BPA could effectively quench the fluorescence of graphene quantum dots (GQDs).[15] The quenching of photoluminescence intensity of GQDs can give the quantitative estimate of concentration of BPA. But there is irreversibility in the process, as the redox process driving the quenching cannot be recyclable. We seek two-dimensional (2D) layered materials (in contrast to QDs) with high surface area for efficient surface-adsorption.

Discussions in this chapter is divided into two parts. In first part consisting of four subsections, we discuss how the EDCs can be detected and singled out with the help of the matrix. In the second part, we focus on the effect of perturbing influences. In particular, we study the photoinduced changes in electronic structure and optical-absorption property of EDCs in their adsorbed state on 2D matrices. The reason behind the photo-stability[16,17] of such organic molecules has also been discussed. We ask the question whether the molecular electronic states and vibration modes can be tuned using suitable matrix, which in turn would influence the optical response and, hence, possibly photodissociation of adsorbed molecules.

We have selected BPA as model micropollutant because of its widespread exposure.[18] Additionally, these molecules are difficult to biodegrade.[19] BPA undergoes metabolism where two metabolites, namely, 4-methyl-2,4-bis(p-hydroxyphenyl)

pent-2-ene (M-1) and 4-methyl-2,4-bis (4-hydroxyphenyl) pent-1-ene (M-2), form (see Figure 8.1). The toxicity of M-2 is even higher than the parent BPA molecule.[20]

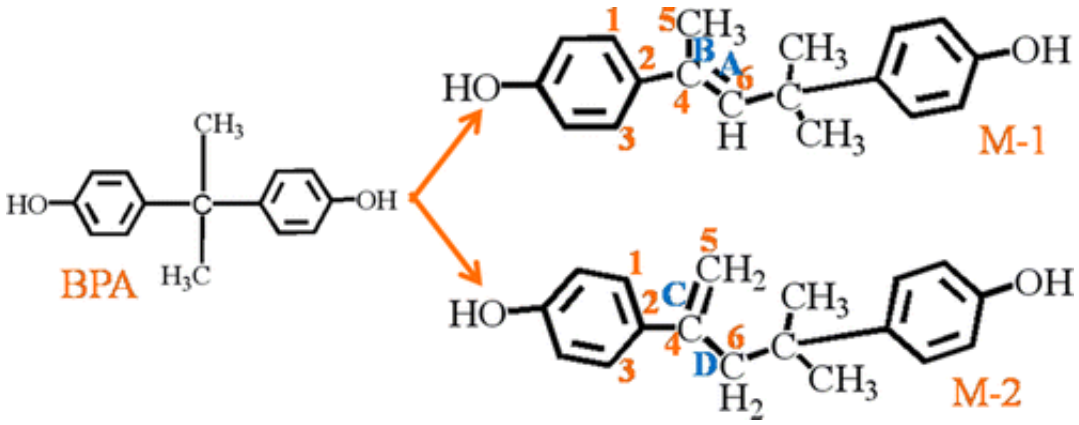

Figure 8.1: Molecular structures of BPA and its metabolites (M-1 and M-2) are shown. Bonds, dihedrals (DH) are assigned as A: 4-6 (M-1); B: 4-5 (M-1), C: 4-5 (M-2); D: 4-6 (M-2), DH-1:3-2-4-6 (M-1); DH-2:1-2-4-5 (M-2) (presented in Table 8.3).

So, rapid, simple, and economically feasible removal of contaminated BPA and its derivatives in water deserves urgent attention. There are some endeavors in this regard based on photochemical,[21] electrochemical,[22] and other advanced oxidation[23,24] processes.

Here, we propose a new surface-mediated interaction mechanism of EDCs with two types of matrices consisting of (1) few layers of pure graphene and (2) metal dichalcogenide (2H-MoS_2). We also quantified the interactions present in molecular self-assembly as well as molecular solvation. We select graphitic material as membrane due to its extended π delocalization. For evaluation of the adsorption capacity, we maintain a particular adsorbent concentration of $\approx$180 mg/g for BPA-adsorption on monolayer graphene. This critical concentration corresponds to the experimental value in previously reported literature[25] at 172 mg/g, which was among the highest values obtained in case of graphene, compared to other carbonaceous adsorbents. Considering the Brunauer-Emmett-Teller surface area of the adsorbents, the high affinity of graphene to BPA was even more obvious.

Therefore, graphene is an excellent BPA absorbent in wastewater treatment. Recently, graphene-TiO_2 composite was studied for the removal and mineralization of a few pollutants.[26,27] However, MoS_2 is promising because of its low friction properties as well as robustness against dilute acids and aerial oxygen.[28] In fact MoS_2 is widely used as a solid lubricant.[29] We considered 2H-MoS_2, which is the most stable form among all the polymorphs of MoS_2.[30] In addition, being p-type material, it helps the electron-donating species to stick on the surface.[31,32] Thus, graphene and MoS_2 represent two different classes of surfaces, which were scrutinized to obtain insight into the rigidity of the bonding between substrates and the EDCs as guest molecules.

8.2 Computational Details

First-principles calculations are based on both the density functional theory (DFT) and ab initio molecular dynamics (AIMD) methods. DFT calculations for periodic systems were performed using the GPW formalism with Perdew-Burke-Ernzerhof (PBE) functional in the Quickstep module of the CP2K set of program.[33] We use GTH (Goedecker, Teter, and Hutter)[34] pseudopotential, and the valence electrons are handled using triple-ζ valence (TZV) basis set. The van der Waals (vdW) corrections (DFT-D2 and D3) as prescribed by Grimme[35,36] were employed for noncovalent interactions. It is noteworthy that D3 correction becomes very crucial to capture the strong adsorption feature, particularly for EDC-adsorption on graphene surface. A realistic model for the specific surface adsorption of BPA, M-1, and M-2 at dilute concentration was achieved by adopting a large super cell (8 x 8) matrix (192 atoms for MoS_2; 384 atoms for bilayer graphene) compared to small adsorbed molecule (the intermolecular distances between two adsorbed molecules were kept more than 10 $\mathring{A}$ away, mimicking very dilute situation). Geometry optimizations were performed using the Broyden-Fletcher-Goldfarb-Shanno (BFGS)

minimization algorithm,[37,38] with the convergence threshold of 1 x 10^{-4} Hartree for energy and 1 x 10^{-4} Hartree/Bohr for force. All the pseudopotential calculations are performed with the plane-wave cutoff of 40 Ry. The charge density cutoff was set at 480 Ry. Adsorbent/adsorbate potential energy surface directs the dynamics of adsorbed molecule. We also perform a set of calculations for monolayer graphene and MoS_2 through Quantum espresso suite of programs.[39] To maintain the concentration of ∼180 mg/g for BPA adsorption on monolayer graphene, we consider (6 x 6) supercell matrix with 141 atoms, which is applied for MoS_2 surface too. We employ the PBE functional and augmented-wave method[40] along with consideration of scalar relativistic effects for d-electrons of molybdenum. Plane-wave basis was truncated with energy cutoffs of 40 Ry in representation of wave functions, and density cutoff was fixed as 320 Ry. k-meshes (5 x5 x 1) are used to sample Brillouin zone integration for structural optimization. We find that the CP2K results agree well with the findings through Quantum espresso. All the adsorption energy values shown in the Figure 8.3 in main text (for monolayer, 6 x 6 supercell), were calculated with Quantum Espresso. For bilayer as well as at the dilute limit of adsorption (with significantly larger number of atoms, 8 x 8 supercell), we employ CP2K-based calculations. Since the modelling of real microfaceting requires the consideration of the thermal motion as well as various conformations of the adsorbed molecule on the surface, we perform AIMD simulations coupled with DFT calculations. Characterization of the dynamical physisorption on MoS_2 surface was investigated with AIMD simulation[41] at 300 K and 1 atm pressure using same package with the same level of theory. Simulations were run at 300 K using Nose-Hoover thermostat. The time step of 0.5 fs was used to integrate the equations of motion. The 5 ps trajectory was generated for analysis. For AIMD study, we freeze the matrix due to negligible geometrical perturbation in surface after molecular adsorption. Mulliken population analysis was done to assess the sharing of charges between the guest molecule and the

host matrix. Relative stabilization (RE) of M-1/M-2 on different matrices was characterized using the following equation.

$$RE = E_{M-1@Matrix} - E_{M-2@Matrix} \tag{8.1}$$

We calculate the adsorption energy (AE) of guest molecules on matrix (either graphene or MoS_2) using the following equation.

$$AE = E_{M-1/M-2@Matrix} - E_{M-1/M-2} - E_{Matrix} \tag{8.2}$$

where, E stands for total energy (with dispersion correction) for the respective species mentioned in the subscript, and $E_{M-1/M-2@Matrix}$ is the energy of the combined species of M-1 or M-2 with matrix.

Spectral feature is highly dependent on a variety of possible inter-molecular interactions such as ionic, cation-π, π-π, quadrupole-quadrupole and hydrogen bonding (H-bonding) interactions. For investigating non-covalent interactions of the molecules in presence explicit water solvent or implicit polarization continuum model, we performed quantum mechanical calculations with dispersion corrected functional. Moreover, quantitative description of non-covalent interactions is highly sensitive to the choice of level of theory and computational method. We have done the spectral analysis from five different methods. Time-dependent density functional theory (TDDFT) calculations, as implemented in Gaussian 09,[42] were performed with Hartree-Fock (HF),[43] DFT with hybrid functional (B3LYP)[44,45] at B3LYP/6-311+G(d,p) level, and DFT with dispersion correction (DFT-D)[46] method at $\omega b97xd$/6-311+G(d,p) level. For validation of the methodology and the appropriateness of the level of theory, we compared our results with the observed (see ref[47]) wavelengths and relative intensities of 4,4′-methylene bisphenol (see Figure 8.2). Absorption wavelengths and spectral features pre-

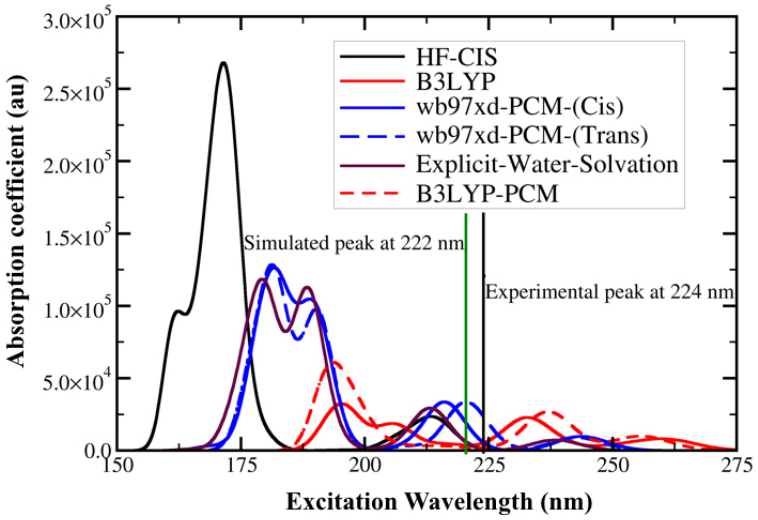

Figure 8.2: Absorption spectra of 4, 4' -methylene bisphenol have been computed with six different methods. Black vertical line represents the position (224 nm) of the characteristic peak (experimentally observed). Green line shows the simulated peak at 222 nm calculated using TDDFT/$\omega b97xd$/6-311+g(d, p)/pcm (water medium).

dicted with $\omega b97xd$ functional and 6-311+G(d, p) as the basis set in presence of implicit solvent model ($\varepsilon = 80$) agree satisfactorily with experimental findings on 4, 4′-methylene bisphenol.[47] The same level of theory has been used for all TDDFT calculations.

The TDDFT calculations, which is impossible for periodic system, were performed only for molecule at their surface-adsorbed state, since the electron transfer between surface and adsorbate molecules (BPA, M-1, and M-2) remain very weak. Thus, the geometrical changes due to dispersive interaction would give rise to changes in optical properties without the change in electron count in the molecule. Thus, it is well-accepted to consider the geometrical changes in the molecule upon surface adsorption. Hence, we performed the TD-DFT calculations on the molecule after removing the surface. Minimum-energy structures are verified by frequency calculations. Nature of the chemical bonding is discussed on the basis of natural bonding orbital analysis (NBO). Natural transition orbital analysis was performed for orbital interpretation of electronic excitation. Hence,

orbital transformation helps to provide a description of occupied natural transition orbital paired with a single unoccupied orbital. One specific transition is weighted with the appropriate eigenvalue (l).

8.3 Result and Discussion

8.3.1 Surface-Mediated Interaction of Bisphenol A, M-1, and M-2

Molecular adsorption of all the three BPA compounds (see Figure 8.3) on graphene surface occurs very strongly (AE $\approx$ 60 kcal mol^{-1}). According to our ab initio

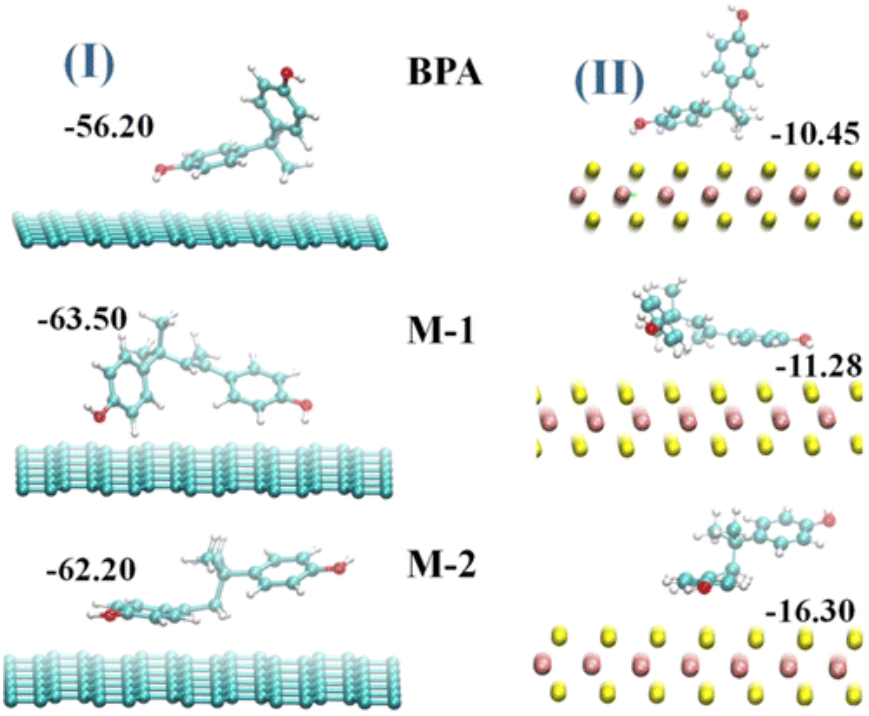

Figure 8.3: Equilibrium adsorption configurations with corresponding AE (kcal mol^{-1}) values for BPA (upper), M-1 (middle), and M-2 (lower) on bilayer matrices; (I) graphene, (II) MoS_2. Spheres of color white: H, cyan: C, red: O, yellow: S and pink: Mo atoms.

results, based on both the static calculation through DFT and considering the

conformational dynamics through AIMD, we find the flattening of the molecule resulting in strong molecular adsorptions on the defect-free graphene surface. This result is in contrast with the adsorption on activated carbon. In fact, enthalpy of adsorption of phenol also shows weaker surface affinity and there is dependence on the pore diameter of carbon nanotube, which changes from -23.9 to -18.1 kcal/mol with increasing pore diameter from 9.4 to 18.8 $\mathring{A}$.[48] So, BPA shows a strong adsorption at pristine graphene surface, whereas the functionalized graphene surface shows lesser adsorption affinity. For BPA, the adsorption energy (depending on adsorption site and molecular orientation) is in the similar range as found for the phenol on Ni(111) surface (0.64-0.91 eV).[49] In both the cases, the carbon ring lies parallel to the surface at an equilibrium distance of $\approx$2.0 $\mathring{A}$. The presence of surface functional group such as hydroxyl, carbonyl, or carboxylic acid in the oxidized graphene restricts the possibility for direct attachment of the BPA with graphene surface. Instead, there is favorability for adhesion of molecule on the surface through H-bonding interaction as evidenced in previous experimental study.[25] We emphasize the fact that the clean graphene surface triggers exceptionally strong adhesion and assists removal of the BPA. However, carbonaceous materials, such as, activated carbon, carbon nanotubes, porous carbon, and graphene oxide have large specific surface areas with abundant pore size distributions, but all of them have lesser strength for surface-adhesion. Between two conventional models for adsorption kinetics (pseudo-first-order and pseudo-second-order), the pseudo-second-order kinetic model fits the adsorption of BPA on graphene.[25] Importantly, the pseudo-second-order model includes all the steps of adsorption including external film diffusion, adsorption, and internal particle diffusion. The magnitude (>1) of Freundlich constant supports favorable adsorption. These experimental findings[25] compare fairly well with the outcome from our molecular dynamics study. Our ab initio results support highly negative standard free-energy change. Negative standard entropy change reflects the decreased

randomness at the solid-liquid interface during the adsorption of BPA on graphene for the spontaneous adsorption process. Interestingly, irreversibility is associated with the strong surface affinity that supports complete removal of the BPA from environment, while pristine graphene plays the role of surface. Decisively, strong π-π stacking and C-H/O-H π interactions leads to such irreversible surface adsorption, which is evidenced from the analysis on IR stretching frequency as will be discussed later.

EDCs consist of two terminal -OH groups as well as two aromatic rings bridged via an aliphatic spacer group. Only, the chemical nature of the aliphatic spacer group varies from one to another (BPA, M-1, and M-2; see Figure 8.1). Different spacer aliphatic groups for isomeric molecules (M-1/M-2) and BPA have almost equal contribution to dispersive interactions with graphene. This rules out the possibility of selective isolation of M-1 and M-2. Hence, we conjecture that the graphene layer would find application in removing the EDCs completely.

8.3.2 EDC-Detection

Mulliken electronic charge transferred from molecule to the graphene sheet is 0.03 E upon adsorption of BPA on bilayer graphene. Nature of the wave function for the conduction band minima (CBM) and valence band maxima (VBM) at the Γ-point supports the partial electron transfer from adsorbed molecule to the sheet (see Figure 8.4). Since it is difficult to do rigorous calculations to predict optical transition in a periodic system; we looked at CBM and VBM wave functions carefully. They indeed show opposite parity with the functional we used. So, the transition dipole moment would be nonzero between these two states. We find the optical band gap (1.25 eV) at the Γ point upon strong adsorption of BPA on bilayer graphene, arising from the coupling of electronic states to the asymmetric stretch mode. This is to say that the optical absorption would appear in near-infrared

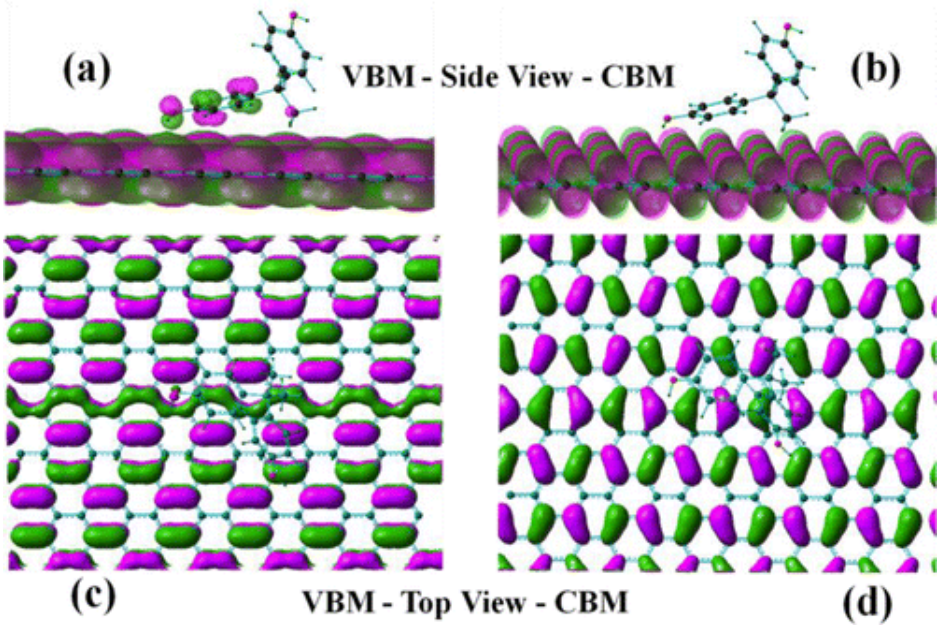

Figure 8.4: Γ-point frontier orbitals (VBM and CBM) for model surface topologies. (a and b) Side view of VBM and CBM for BPA@bilayer-graphene, respectively; (c, d) top view of the same. Isocontour value used for orbital plots is 0.02 E bohr^{-3}.

(NIR) regime. Mobile π-electrons, induced due to strong adsorbent-surface affinity and weak electronic charge transfer from molecule to matrix, lead to a strong NIR absorption as both the states remain in the same k-point value. Thus, the response can be detectable.

To confirm the adsorption mechanism further, we performed the IR studies on the molecular structure as it was in its adsorbed state over graphene and MoS_2 (see Table 8.1). Such analysis, in fact, helped in identifying the presence of different interaction patterns between BPA and graphene.[25] Emergence of peaks at 2800-3000 and 400-1800 cm^{-1} are in accordance with the peaks from the Fourier transform IR spectrum of BPA as found experimentally, indicating that BPA molecules were adsorbed on the surface of graphene. These new peaks originate from (i) aromatic C-H bonds (ii) skeletal vibrational modes as well as π-aromatic ring vibration in the low-energy regime. Furthermore, the stretching frequency of the O-H group in BPA gets shifted from 3700 to 3500 cm^{-1}, which can be ascribed

Table 8.1: Shift in vibrational frequencies (in cm^{-1}) for specific modes (in BPA) upon surface adsorption, computed using $\omega b97xd$/6-311+G (d, p) have been given.

Modes	**@Graphene**	**@MoS2**
O-H (Stretching)	-200	-220,-200
O-H (Bending)	+28	+28
Aromatic C=C	-30	-23
Aromatic C-H	-40	-50
Aliphatic C-H	-55	-50

to hydrogen bonding between hydroxyl groups in BPA and π-electronic cloud on the surface. The peak at 1640 cm^{-1} is associated with the skeletal vibration of aromatic C-C bonds, which also blue-shifts by 30 cm^{-1} and gets widened after adsorption, confirming the π-π interaction[50] between the benzene rings of BPA and the graphene planes. Such blue-shift in frequency is less (23 cm^{-1}) while BPA is adsorbed on MoS_2 surface. After comparative analysis between two different surfaces and their adsorption affinity, it is clear that π-π interaction between the benzene rings of BPA and the graphene planes force strong adhesion as evident in the significantly higher shifting of the vibrational frequency of aromatic C-C bonds. Because of the added forces from the interaction between BPA and graphene layers, two significant changes can be expected to happen compared to pristine graphene. These are: (1) splitting of the 2D peak and (2) shift in the G-mode, i.e alterations in Raman spectra which originates due to the tuning of in-plane vibration after surface adsorption.

8.3.3 Carbonaceous Surface versus Inorganic Metal Chalcogenide (MoS_2) Surface

In contrast to the carbonaceous surface, EDCs get adsorbed on the inorganic metal chalcogenide (MoS_2) surface through the attachment of only one terminal phenolic moiety (see Figure 8.3). Other tail of the adsorbed molecule remains far from

the surface. This confers significantly less adsorption energy (ΔE = 10-17 kcal mol^{-1}). We also performed a set of calculations and found that adsorption of BPA on 1T-MoS_2 is thermodynamically disfavorable with highly positive ΔG value. The other analogue of MoS_2, MoSe2, also shows similar feature like 1T-MoS_2. Hence BPA-adsorption is specific for 2H-MoS_2 especially. Notably, structural relaxations associated with locally modified charges on adsorbed molecule results in conformational dynamics (see Figure 8.5) which has been elaborated in later part. Adsorption energy for M-1 (-16.30 kcal/mol) is the highest among all three (BPA: -10.45 and M-2: -11.28 kcal/mol, see Figure 8.3). Thus, at the optimized conformation of adsorbed state, we find M-1 becomes more stable (RE = -5.10 kcal/mol) than M-2, on MoS_2 surface. Note that, isomeric M-1/M-2 are equally stable in both the cases: isolated states (as described previously in Chapter 7)[51] and the surface-adsorbed state (on graphene surface). In addition, adsorption energy of water on MoS_2 surface varies (3.65-4.33 kcal/mol) depending on various possible adsorption sites. Now, the selection for adsorption on the surface appears to be in the order of M-1 > M-2 $\approx$ BPA $\gg$ H_2O. For the desorption process, the trend gets reversed (H_2O > M-2 $\approx$ BPA > M-1). Thus, MoS_2 surface serves the purpose of a stationary adsorbing medium analogous to the chromatographic technique and leads to a facile surface-induced isolation of EDCs. So, we can infer that graphene surface is efficient due to the strong affinity but at the cost of irreversibility, whereas MoS_2 surface is facile in terms of relatively more reversible nature of adsorption as well as selective isolation.

8.3.4 Selective Isolation of EDCs

There are two kinds of adsorbent-adsorbate interactions. One main interaction is the π-π interaction between the benzene rings of BPA and the surface planes. The other is the hydrogen bonding between the oxygen-containing groups as well

as C-H group (aromatic and / or aliphatic) contained in BPA and respective surfaces. Importantly, structural changes in the adsorbed molecule can give rise to alteration of bond strengths and, thus, IR stretching frequencies of the specific modes participating in the interaction. To determine the selectivity/separation of solvated EDCs, we considered water as solvent media for water-soluble EDCs. Hence, we focus on the subtle interplay among the possible interactions such as surface-molecule, surface-solvent, solvent-molecule, and the intermolecular self-assembly. Adsorption energy of water on MoS_2 surface is in the range of 4-5 kcal/mol. This value is negligibly small compared to surface affinity of EDCs on MoS_2 Surface ($\sim$15 kcal/mol). It also corroborates with the report on the weak interaction of water with defect-free MoS_2 surface.[52–54] Less interaction energy discards the possibility of competitive surface coverage by water that might cause limitations for accessibility of the desired molecule on the surface. In the context of molecular solvation, we find strong hydration energy for the EDCs. Typical H-bonding interactions are present between phenolic O-H and water. There is existence of H-bond varying within a range of 1.7-2.0 $\mathring{A}$. Water molecules can act either as a bridge (H-bond distance: 1.63 and 2.10 $\mathring{A}$) between two molecules or being associated with a single molecule by forming H-bond at $\sim$1.82 $\mathring{A}$. Quantification of the adsorption energy of solvated dimer (along with 14 solvent molecules) turns out to be -31.45, -23.57, and 22.29 kcal/mol for M-1, M-2, and BPA, respectively. We find that M-1 shows more surface adsorption affinity (7.88 kcal/mol) than M-2 in its solvated state too. In fact, through solvated dimer (along with 14 solvent molecules), we consider intermolecular (e.g., M-1M-1), solvent-molecule, as well as solvent-solvent interactions. Considering the whole system on the surface, there appear two more interaction modes: surface-solvent and surface–molecule, which can possibly affect the surface adsorption of the molecule in their solvated state. Also, we found the adsorption energy of a single unsolvated M-1 molecule to be $\sim$16 kcal/mol. Hence, dimer in the solvated state exhibits the surface affinity

almost twice the value of the same for an isolated molecule. Basically, it proves that, the molecular solvation and surface adsorption are not competitive. Rather, there is a cooperative interplay between two types of interactions.

In addition, surface affinity for solvent (∼4 kcal/mol) and for EDCs (∼15 kcal/mol irrespective of the state of solvation) confirms that the surface affinity of EDCs does not get affected while they are in solvated or in assembled state. However, adsorption affinity of water on the surface is much less and cannot compete with the EDCs (4-5 kcal/mol). As we want the extraction of EDCs from their water-contaminated state, we examine whether the solvation of the EDCs will hamper their sorption property on the surface. The surface-adsorption affinity (>22 kcal/mol) for all the solvated EDC dimers (BPA, M-1, and M-2) was found to be also high; we conclude that the surface adsorption does not get affected, while the EDCs are solvated. However, the solvation energy of BPA, M-1, and M-2 lies in the range from -3.5 to -3.8 kcal per water molecule. Therefore, solvation energy does not overcome of the strength of surface affinity of EDCs. Although relative affinity difference is in the order of water adsorption energy, we should point out that it is the absolute strength of the surface affinity for EDCs that eventually matter. Moreover, energetics reveal that the solvated complex gets more strongly bound to the surface when the water comes and solvates the EDCs. Thus, there is no possibility to wash out the EDCs from surface by water, which further supports the MoS_2 surface to act as an ideal matrix to extract the EDCs. Although the effective area of contact between the EDCs and surface is less due to their nonlinear chain framework, the adsorption energy is in the order of electron-volt (see Figure 8.3). This needs a detailed understanding of the existence of effective surface-mediated mechanisms and charge transfer. We find the adsorption of BPA, M-1, and M-2 on both of these model surfaces (graphene and MoS_2) are dominated by the vdW interactions. Through consideration of conformational dynamics of adsorbed EDCs at 300 K, we find that RE can fluctuate in the range

from -3 to -7 kcal/mol (see Figure 8.5). Dynamical behavior of the adsorbent

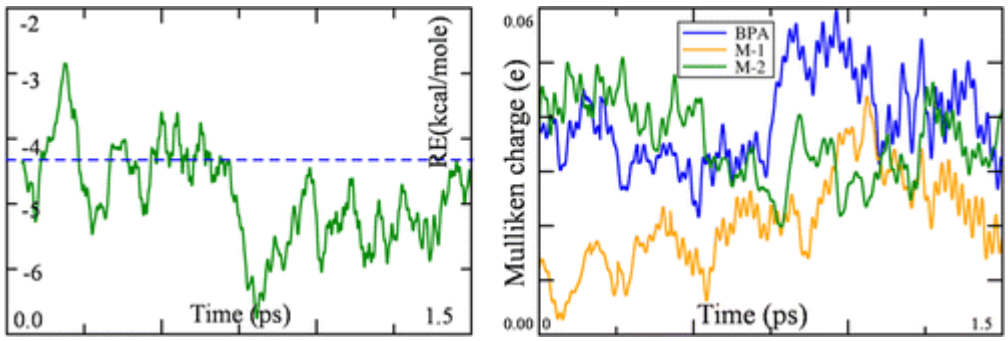

Figure 8.5: RE versus time (left) and charge fluctuation (right) due to electronic charge transferred from molecule to the p-type surface MoS_2 triggered by conformational dynamics.

regulates the electrostatic interaction, as a result of which electron transfer from EDC to the surface may vary from 0.003 to 0.06. In particular, collective behavior results in small electron transfer (∼0.03e), and a molecule diffuses laterally along the surface maximizing the interaction between polar H in molecule and S atoms on MoS_2 matrix.

Thus, conformational dynamics triggers the interplay between electrostatic and dispersive interactions in physisorbed EDCs. To understand the adsorbent-adsorbate interfacial interaction, zeta potential is a physical parameter quantifying the surface electrical potential of the solid particle and the stability of liquid dispersions. We find that the partial electron transfer from BPA to the sheet (∼0.03 e/BPA) results in excellent stability of graphene dispersions that originate from the mutual electrostatic repulsion among graphene sheets. This indicates the graphene sheets are negatively charged. In fact, the zeta potential of graphene measured in aqueous solutions of BPA were observed to be negative,[25] which reached -46 mV for pH 10.0 implying sufficient mutual repulsion[55] and ensured the stability of the dispersion. As shown in Figure 8.3, OH is more likely to stick with bending mode where H takes part in interaction. Importantly, OH groups are not prone to be dissociated as revealed from frequencies of the OH stretching modes (from the MD

trajectories). We can account these surface-mediated interactions for broadening and shifting of the stretching mode of hydrogen-bonded hydroxyl groups. Accordingly, dispersive interaction is attributed to the interaction of lone pair of surface-S with π-aromatic-ring, aromatic H atoms, polar O-H bonds, and π-cloud at spacer group. S ions also provide weak Lewis acidic (electron-acceptor) nature to the MoS_2 surface for BPA, M-1, and M-2 adsorption. These types of interactions can vary due to a subtle difference in π-cloud orientation in spacer group, which actually arises between M-1 and M-2. Thus, a difference in interaction energy is found for two isomers providing a way of isolation through surface-mediated couplings. Thus, loading the specific substances and then releasing them on the MoS_2 matrix can occur through diffusion-controlled mechanisms, without erosion of the matrix.

8.3.5 Optical Responses of Bisphenol A and Its Metabolites (M-1 and M-2)

Computed absorption spectra (see Figure 8.6) reveal predominant UV absorption for EDCs. Absorption maxima get slightly shifted ($\Delta\lambda_{ex} \approx$ 2 nm) by changing the dielectric constant of solvent media, that is, the nature of solvent molecule's coordination mode (see Table 8.2). So, probing the solvent dielectric media and structural identification of EDCs are insensible through direct investigation of the absorption spectra in different solvent media.

To understand the aspect of photodegradability of such EDCs, we focus on their photoresponse and subsequent chemical changes. We search for two major aspects upon illumination: whether (i) irreversible change in molecular shape happens or not; (ii) any site or bond becomes prone to the radical reaction or fragmentation. The natural transition orbital (NTO) shows the orbital involved in optical transition (see Figure 8.7).

Two lowest-energy intense absorptions appear to be π to π^*. For the lowest-

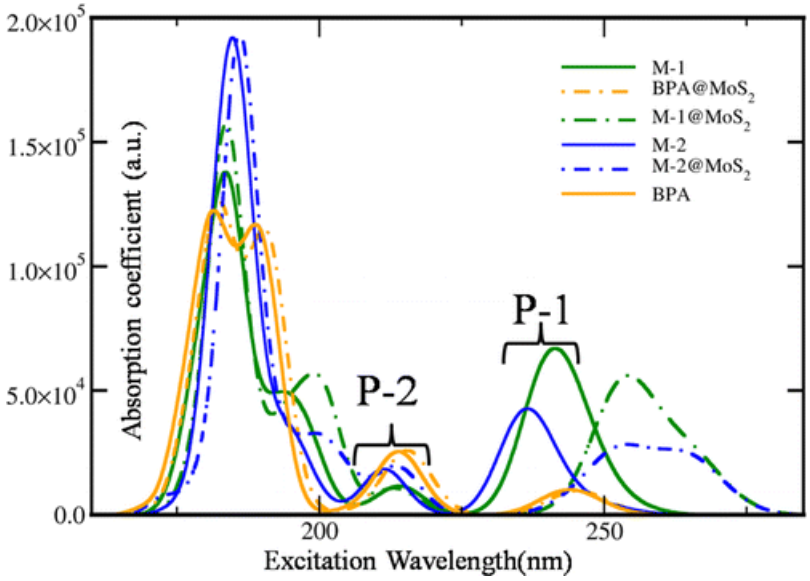

Figure 8.6: Computed absorption spectra of isolated molecules: BPA, M-1, and M-2 (represented by solid lines) and at the matrix-adsorbed state (dotted lines) using TD-DFT. Two lowest absorption maxima (λ_{ex}) values (P-1 and P-2) are given in Table 8.2.

energy excitation, the final state turns out to be an antibonding orbital, the predominant contribution to which comes from C-C in the spacer group as well as aromatic ring. So, optical transition reduces the bond orders of the C-C in both the terminal aromatic rings and middle spacer part, which is common for π-delocalized systems. Interestingly, the second-lowest optical transitions are also shown to be aromatic-H assisted π-to-π^* transition. Rotation of the aromatic ring about C-

Table 8.2: Prominent absorption peaks (low energy) for M-1 and M-2, computed using TDDFT/$\omega b97xd$/6-311+G(d, p). Different dielectric constant of the medium (implicit solvent model), such as, gas-phase ($\varepsilon = 1$), DMSO ($\varepsilon = 46.7$), Water ($\varepsilon = 88$) as well as explicit solvent model (four H_2O molecules are coordinated to terminal O-H bonds) show different spectral features.

Solvent environment	**Absorption wavelegth (nm)**		
	BPA	**M-1**	**M-2**
$\varepsilon = 1$	214, 242, 245	216, 244, 248, 256	212, 230, 244, 249
$\varepsilon = 46.7$	215, 243, 246	216, 246, 248, 256	213, 234, 244, 250
$\varepsilon = 88$	214, 242, 245	214, 240, 245, 253	211, 236, 242, 250
H_2O	212, 237, 240	211, 234, 240, 248	208, 233, 237, 246

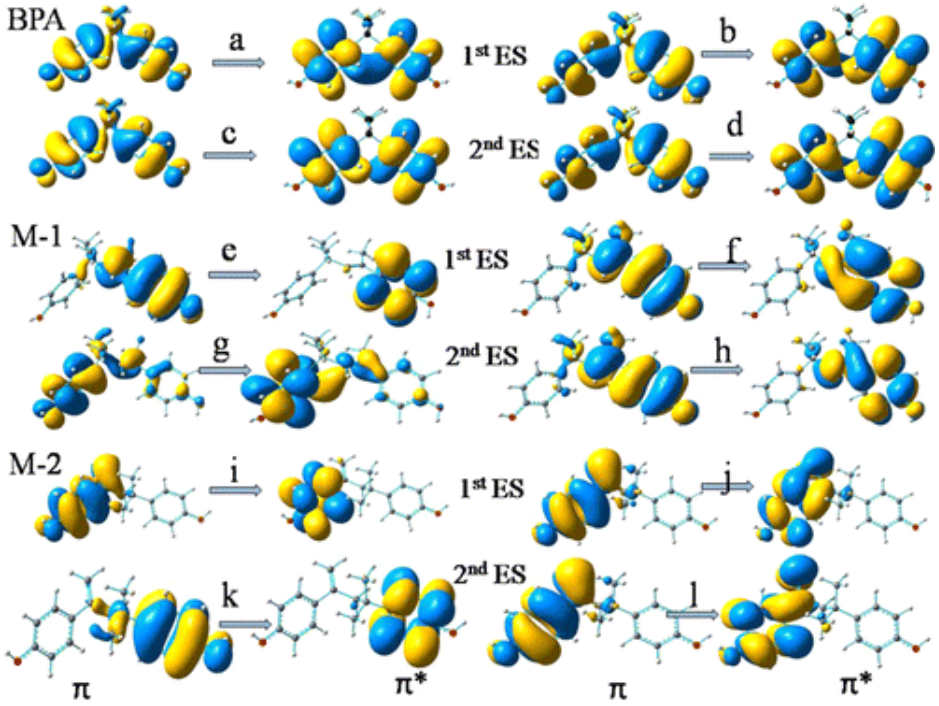

Figure 8.7: Dominant natural transition orbital pairs for the first two excited singlet states (ES) of BPA, M-1/M-2, and BPA/M-1/M-2@MoS_2 are given. Initial state is on the left; the final state is on the right. Associated eigenvalues are (a) 0.61, (b) 0.59, (c) 0.49, (d) 0.51, (e) 0.86, (f) 0.92, (g) 0.75, (h) 0.90 (i) 0.84, (j) 0.94, (k) 0.84, (l) 0.87.

C (C4-C5 and C4-C6 for M-1 and M-2, respectively) bond is found to separate the charges in atoms to minimize the electron-electron repulsion. In case of M-1 and M-2, internal electron transfer occurs, where π-electrons get transferred from middle aliphatic moiety to terminal aromatic groups. Optimum bond distances lengthen by 0.07 $\mathring{A}$ for first (λ_{ex} = 249 nm; 244 nm found as shoulder in Figure 8.5) two lowest excitation, whereas lengthening of 0.05 $\mathring{A}$ occurs with the third excitation (λ_{ex} = 230 nm). Moreover, from NBO analysis we confirm that the bond length alterations (see Table 8.3) upon illumination become significant for M-1 and M-2 but not for BPA. So, spacer aliphatic moiety (absent in BPA) plays an important role in photochemistry of bisphenol compounds. Importantly, partial equalization of consecutive single and double bonds occurs in M-1 and M-2 through electronic redistribution. The middle spacer group in between two

Table 8.3: Bond orders ("Wiberg bond index") of specific bonds (A, B, C, D) for M-1 and M-2 (as shown in Figure 8.1) in ground state (GS) and optically excited (1st and 2nd) states (ES).

State	Bond order & Dihedrals					
	M-1			M-2		
	A	B	DH-1	C	D	DH-2
GS	1.828	1.025	40.63	2.120	1.012	-42.11
ES-1	1.715	1.034	9.72	1.766	1.019	-7.35
ES-2	1.713	1.027	13.29	1.316	1.011	-6.40

terminal phenyl groups tends to align in different plane (see the dihedral angle changes in Table 8.3). M-1 exhibits the more geometric rearrangements than M-2. Basically, π-electron in aliphatic spacer group contributes to such changes, and because of its absence BPA exhibits the less structural distortion (less electronic redistribution throughout the molecular framework due to optical transition). Thus, optical excitation creates concomitant shape rearrangements to different extents for different EDCs. However, such geometrical changes upon photoexcitation are reversible. This was confirmed by our AIMD study. We find that, within ∼500 fs, the photoexcited state conformation of M-1 relaxed back to the ground-state configuration. Thus, the photo-decomposition due to the irreversible shape changes in the EDCs (BPA, M-1, and M-2) becomes impossible. However, in the surface-absorbed state, terminal aromatic ring becomes electron-rich and susceptible to electrophilic attack (e.g., by $OH^{\cdot}$; see nature of the orbital in Figure 8.8D,E). This would give rise to the decomposition of aromatic ring and, hence, might facilitate photo-decomposition. So, a possibility for surface-assisted photodegradation was found, which is in accordance with our molecular orbital analysis.

Thus, the preceding discussion reveals that BPA metabolites (M-1and M-2) are photoresponsive, but in the UV absorption region. However, shifting of absorption spectral range from UV to visible is desirable for efficient solar-energy absorption. We find that EDCs can also absorb much lower wavelength ($\Delta\lambda \approx +50$ nm) solar radiation (see Figure 8.6) after surface adsorption. This is attributed to the

extended delocalization through terminal aromatic and aliphatic moiety in spacer group. Hence, we propose the utilization of coating with graphene and MoS_2 on photocatalytic surfaces, such as, TiO_2. Because of the specific surface adsorptions of M-1 and M-2 (on graphene, MoS_2), red shifting of low-energy absorption peaks (see Figure 8.6) occurs. Higher-energy (lower λ) peaks do not get affected much in presence of the matrix. But, low-energy excitation peaks get broadened and split into two (see Figure 8.6) due to coupling between the surface and adsorbed molecule. Indeed, the spectral shift is attributed to the perturbing influence of the matrix on π-electronic cloud in transition orbital (see Figure 8.7). As a result, surface induces conformational changes and subsequent electronic redistribution of the π-electronic cloud in the spacer group of adsorbed molecule in its excited state. Particularly interesting is the π-electronic cloud in spacer group, which dictates different extent of stabilization to each of the states involved in transition. In fact, this has great importance in case of surface-induced spectral shifting. This understanding decisively brings out the possibilities for alteration of absorption-spectral region of EDCs through appropriate choice of matrices.

8.3.6 Effect of Various Perturbing Influences on the Molecular States

We look for the basic difference in the impact of electric polarization and optical pulses on EDCs. In presence of electric polarization, M-1 and M-2 undergo a conformational change without major changes in bond order (at low electric field strength < 0.26 V/$\mathring{A}$).[51] Switchable stereocontrol of M-2 associated with O-H bond reorientation was elaborated previously in chapter 7.[51] However, the threshold value of uniform electric field to induce bond order alteration, was found to be 0.93 V/$\mathring{A}$. This static electric field strength creates redistribution of electron density and intramolecular charge transfer. In contrast, when exposed to specific

wavelengths of light (see Table 8.3), optical field distorts the ground-state (GS) optimized geometry by elongating C=C and shortening the C-C bond, hence, resulting in a structural transformation (see Table 8.4 and Figure 8.8) to arrive at the other degenerate ground state.

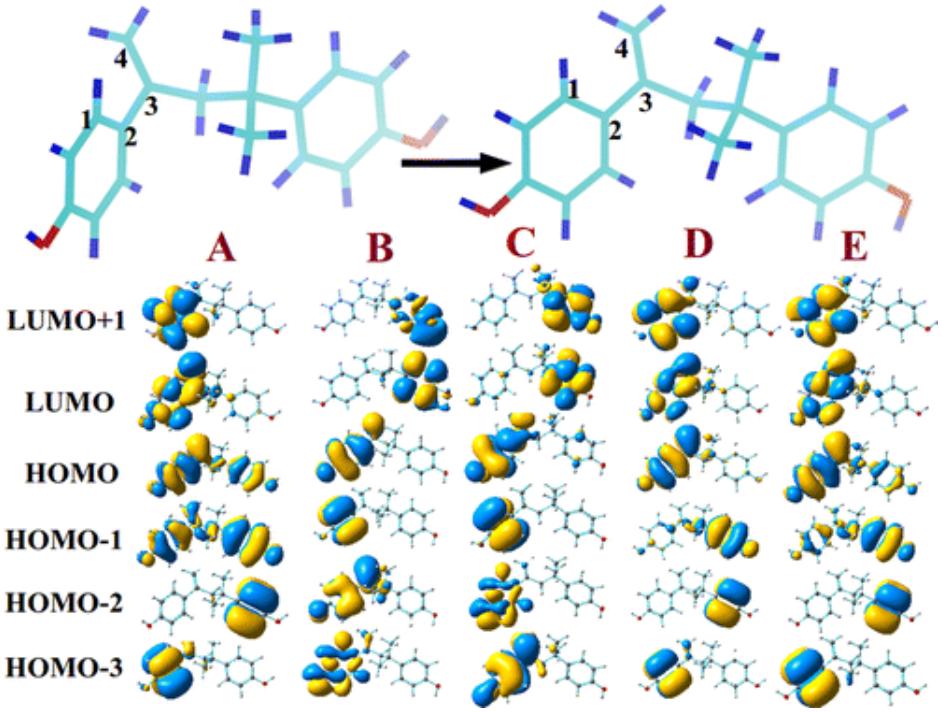

Figure 8.8: Molecular orbital representation of M-2 in the presence of various perturbing influences: (A) ground state; (B) directional static electric field (0.018 a.u.); (C) uniform static electric field (0.018 a.u.); (D) optically excited state (1st); (E) adsorbed (physisorption) on MoS_2 matrix.

Here, we discuss the influences of various perturbing influences to utilize them as a tool for removal and photodegradation of EDCs. The changes in electron delocalization pattern are also reflected in their structural parameters (see Table 8.4). Hence, the perturbing efficiency, reflected through several structural parameters, is dependent on the directional feature of the electric field. We find that there are clearly visible changes, including large shifts of charge density from one end of the molecule to the other due to both the optical and electric field-induced perturbation (see Figure 8.8). But, the estimation of the electric field strength

Table 8.4: A, B, C, D, E dictates optimized state in presence and absence of various external perturbing Influences as described in Figure 8.7. Within parentheses: A(G): gas-phase; A(W): water dielectric medium; B: directional static electric field (0.018 a.u.); C: uniform static electric field (0.018 a.u.); D: Optically excited state (1st); E(M): adsorbed on MoS_2 surface; E(Gr): adsorbed on graphene surface. Structural parameters are: molecular length (ML in $\mathring{A}$), C=C (A in $\mathring{A}$), C-C (B in $\mathring{A}$) and dihedral angles (DH-1, DH-2 in degree)

Structural parameters	**A(G)**	**A(W)**	**B**	**C**	**D**	**E(M)**	**E(Gr)**
M-1							
ML	11.49	11.46	12.14	12.15	11.27	11.77	12.03
A	1.35	1.35	1.37	1.36	1.41	1.35	1.35
B	1.51	1.51	1.52	1.52	1.52	1.52	1.52
DH-1	40.63	39.92	26.18	-33.06	9.72	28.59	30.26
M-2							
ML	13.07	13.17	12.69	12.22	13.25	13.11	12.73
A	1.34	1.34	1.35	1.37	1.41	1.35	1.35
B	1.52	1.52	1.53	1.55	1.43	1.51	1.52
DH-2	-42.11	-40.56	-26.80	34.58	-7.35	-20.16	9.06

required for such changes is quite high ($\sim$1.0 V/$\mathring{A}$). However, optimization of the optically excited state would give rise to similar structural perturbation, which can be achieved upon irradiation with UV radiation (250 nm), which is less abundant in solar spectrum. These drawbacks associated with electric field and optical excitation led us to search for other options. We find capturing of EDCs can easily be achieved by surface adsorption, but the electronic states (highest occupied molecular orbital (HOMO) and lowest unoccupied molecular orbital in particular) do not change drastically upon surface adsorption. Only a slight modification in the orbital representations reflects the changes in molecular electronic structure, which is governed by small conformational changes. Actually, there is no signature of catastrophic structural breakdown as evident from the structural parameters in Table 8.4. Thus, surface adsorption appears to be perfectly reversible in nature (for MoS_2 as substrate). Importantly, as we always look for reversibility to achieve a recyclable isolation process, the perturbation should not be very strong as found in case of graphene surface. Hence, MoS_2 surface proves its superiority.

We assessed the reactivity of the adsorbed species based on the electronic structural feature of the molecule in its isolated and surface-adsorbed states. To be more precise, we looked to see whether the orbital representation changes and whether the changes can give rise to reactivity in the adsorbed species. What we find is, irrespective of the state whether it is surface-adsorbed or isolated molecule, two terminal rings possess more electron density which indicates that the terminal aromatic rings will be prone to electrophilic attack. In presence of surface, the process can be facilitated due to easy exposure of the reactive sites to the electrophile. For isolated state, two terminal aromatic rings possess homogeneous electron density, whereas inhomogeneity occurs after surface adsorption. As a result, one terminal ring is found to have more electron density than the other. Moreover, relative reduction in the electron density for occupied states (HOMO-1 and HOMO) occurs at surface-adsorbed state. Thus, surface adsorption facilitates molecular accumulation on the surface and creates appropriate sites for both the electrophilic and nucleophilic attacks which may lead to structural fragmentation.

8.4 Conclusion

In summary, MoS_2 surface exhibits optimum surface-molecule affinity and hence is perfect for reversible extraction of EDCs from environment. Surface adsorption is dominated by dispersive interaction, which is sensitive to the nature of the spacer aliphatic group of EDCs. Thus, different EDCs, on the basis of varying spacer groups, can be isolated selectively. The charge transfer from EDCs to the surface is negligibly small and gets tuned (from 0.005 to 0.06 e) by conformational dynamics. However, graphene bilayer matrix results in very strong adsorption of EDCs with a detectable response at NIR regime. Associated results are important in designing graphene surface for complete removal and graphene-TiO_2 composite for degradation of bisphenol-based EDCs. The separation efficacy for

both the matrices (graphene and MoS_2) is not affected at the solvated state of the molecules. These microscopic details demonstrate the superiority of the membrane in cleaning water by affinity-based separation of such pollutants. In the context of the optical responses of EDCs, we find that dielectric constant of the medium alone cannot confer significant changes in spectral feature. Interestingly, while EDCs get adsorbed on carbonaceous substrate (bilayer graphene) or metal di-chalcogenide (MoS_2) as matrices, cause significant red-shifting ($\sim$40 nm) of absorption spectra covering a broad spectral range. Because of photo-excitation, internal electron transfer occurs from π-system to C-C antibond, thus, decreasing the bond order. Prominently, terminal phenyl rings of EDCs become prone to undergo radical reaction at surface-absorbed (on MoS_2) state. Thus, surface-assisted photodegradation of BPA metabolites seems to be appropriate due to the bond-dissociative internal electron-transfer mechanism, triggered by optical transition. We conjecture that surface-assisted degradation of the EDCs in the presence of external perturbation is very much plausible.

References

[1] J. M. Hall, D. P. McDonnell, and K. S. Korach, Molecular Endocrinology **16**, 469 (2002).

[2] A. Atkinson and D. Roy, Environmental and Molecular Mutagenesis **26**, 60 (1995).

[3] A. Casanova-Nakayama, M. Wenger, R. Burki, E. Eppler, A. Krasnov, and H. Segner, Marine Pollution Bulletin **63**, 412 (2011).

[4] N. Ben-Jonathan and R. Steinmetz, Trends in Endocrinology & Metabolism **9**, 124 (1998).

[5] P. Eriksson, E. Jakobsson, and A. Fredriksson, Organohalogen Compounds **35**, 375 (1998).

[6] M. Huerta-Fontela, M. T. Galceran, and F. Ventura, Water Research **45**, 1432 (2011).

[7] M. Klavarioti, D. Mantzavinos, and D. Kassinos, Environment International **35**, 402 (2009).

[8] A. Matilainen, M. Vepsäläinen, and M. Sillanpää, Advances in Colloid and Interface Science **159**, 189 (2010).

[9] N. Vieno, T. Tuhkanen, and L. Kronberg, Environmental Technology **27**, 183 (2006).

[10] S. Suarez, J. M. Lema, and F. Omil, Bioresource Technology **100**, 2138 (2009).

[11] C. D. Adams and S. J. Randtke, Environmental Science & Technology **26**, 2218 (1992).

[12] J. Radjenović, M. Petrović, F. Ventura, and D. Barceló, Water Research **42**, 3601 (2008).

[13] A. Matilainen, N. Vieno, and T. Tuhkanen, Environment International **32**, 324 (2006).

[14] L. Liu, G. Zheng, and F. Yang, Chemical Engineering Journal **156**, 553 (2010).

[15] H. Huang, Z. Feng, Y. Li, Z. Liu, L. Zhang, Y. Ma, and J. Tong, Analytical Methods **7**, 2928 (2015).

[16] K. Nomiyama, T. Tanizaki, T. Koga, K. Arizono, and R. Shinohara, Archives of Environmental Contamination and Toxicology **52**, 8 (2007).

[17] C. Guo, M. Ge, L. Liu, G. Gao, Y. Feng, and Y. Wang, Environmental Science & Technology **44**, 419 (2009).

[18] A. V. Krishnan, P. Stathis, S. F. Permuth, L. Tokes, and D. Feldman, Endocrinology **132**, 2279 (1993).

[19] C. A. Staples, P. B. Dome, G. M. Klecka, S. T. Oblock, and L. R. Harris, Chemosphere **36**, 2149 (1998).

[20] S. Yoshihara, T. Mizutare, M. Makishima, N. Suzuki, N. Fujimoto, K. Igarashi, and S. Ohta, Toxicological Sciences **78**, 50 (2004).

[21] Y. Ohko, I. Ando, C. Niwa, T. Tatsuma, T. Yamamura, T. Nakashima, Y. Kubota, and A. Fujishima, Environmental Science & Technology **35**, 2365 (2001).

[22] Y.-B. Xie and X.-Z. Li, Journal of Hazardous Materials **138**, 526 (2006).

[23] S. Horikoshi, M. Kajitani, and N. Serpone, Journal of Photochemistry and Photobiology A: Chemistry **188**, 1 (2007).

[24] S. Tanaka, Y. Nakata, H. Kuramitz, and M. Kawasaki, Chemistry Letters pp. 943–944 (1999).

[25] J. Xu, L. Wang, and Y. Zhu, Langmuir **28**, 8418 (2012).

[26] C. Liu, Y. Teng, R. Liu, S. Luo, Y. Tang, L. Chen, and Q. Cai, Carbon **49**, 5312 (2011).

[27] W.-S. Wang, D.-H. Wang, W.-G. Qu, L.-Q. Lu, and A.-W. Xu, The Journal of Physical Chemistry C **116**, 19893 (2012).

[28] N. Liu, P. Kim, J. H. Kim, J. H. Ye, S. Kim, and C. J. Lee, ACS Nano **8**, 6902 (2014).

[29] A. Savan, E. Pflüger, P. Voumard, A. Schröer, and M. Simmonds, Lubrication Science **12**, 185 (2000).

[30] M. Hershfinkel, L. Gheber, V. Volterra, J. Hutchison, L. Margulis, and R. Tenne, Journal of the American Chemical Society **116**, 1914 (1994).

[31] C. Rao, U. Maitra, and U. V. Waghmare, Chemical Physics Letters **609**, 172 (2014).

[32] C. Rao, K. Gopalakrishnan, and U. Maitra, ACS Applied Materials & Interfaces **7**, 7809 (2015).

[33] J. P. Perdew, K. Burke, and M. Ernzerhof, Physical Review Letters **77**, 3865 (1996).

[34] M. Elstner, D. Porezag, G. Jungnickel, J. Elsner, M. Haugk, T. Frauenheim, S. Suhai, and G. Seifert, Physical Review B **58**, 7260 (1998).

[35] S. Grimme, S. Ehrlich, and L. Goerigk, Journal of Computational Chemistry **32**, 1456 (2011).

[36] L. Goerigk and S. Grimme, Physical Chemistry Chemical Physics **13**, 6670 (2011).

[37] M. F. Møller, Neural Networks **6**, 525 (1993).

[38] J. D. Head and M. C. Zerner, Chemical Physics Letters **122**, 264 (1985).

[39] P. Giannozzi, S. Baroni, N. Bonini, M. Calandra, R. Car, C. Cavazzoni, D. Ceresoli, G. L. Chiarotti, M. Cococcioni, I. Dabo, et al., Journal of Physics: Condensed Matter **21**, 395502 (2009).

[40] P. E. Blöchl, Physical Review B **50**, 17953 (1994).

[41] J. Hutter, M. Iannuzzi, F. Schiffmann, and J. VandeVondele, Wiley Interdisciplinary Reviews: Computational Molecular Science **4**, 15 (2014).

[42] E. C. Barnes, G. A. Petersson, J. A. Montgomery Jr, M. J. Frisch, and J. M. Martin, Journal of Chemical Theory and Computation **5**, 2687 (2009).

[43] A. McLachlan and M. Ball, Reviews of Modern Physics **36**, 844 (1964).

[44] C. Lee, W. Yang, and R. G. Parr, Physical Review B **37**, 785 (1988).

[45] A. D. Becke, The Journal of Chemical Physics **98**, 5648 (1993).

[46] D. N. Laikov, Chemical Physics Letters **281**, 151 (1997).

[47] N. Watanabe, S. Horikoshi, H. Kawabe, Y. Sugie, J. Zhao, and H. Hidaka, Chemosphere **52**, 851 (2003).

[48] I. Efremenko and M. Sheintuch, Langmuir **22**, 3614 (2006).

[49] L. Delle Site, S. Leon, and K. Kremer, Journal of the American Chemical Society **126**, 2944 (2004).

[50] R. W. Coughlin and F. S. Ezra, Environmental Science & Technology **2**, 291 (1968).

[51] S. Banerjee, G. Periyasamy, and S. K. Pati, The Journal of Physical Chemistry B **118**, 9258 (2014).

[52] A. AC08788386, *Integrated ferroelectrics: an international journal* (Taylor & Francis, 1992).

[53] F. A. Frame and F. E. Osterloh, The Journal of Physical Chemistry C **114**, 10628 (2010).

[54] Y. Li, H. Wang, L. Xie, Y. Liang, G. Hong, and H. Dai, Journal of the American Chemical Society **133**, 7296 (2011).

[55] J. D. Jackson, *Classical electrodynamics* (Wiley, 1999).

9

Modelling BPA-based Molecular Architecture for Photochemical Energy Storage*

9.1 Introduction

2, 2′-bis(4-hydroxyphenyl) propane (Bisphenol A; BPA) is an unavoidable component of polycarbonate plastics[1] and epoxy resins,[2,3] which are widely used in many commercial products, such as, food and drink packaging, medical devices, compact discs, impact-resistant safety equipment, and water supply pipes. However, widespread human exposure to BPA eventually creates serious health hazards.[4–7] The origin of such adverse reactivity of BPA is their photo-stability,[8] resulting in their accumulation in nature without degradation.[9] Hence, the detailed understanding on photo-cycle which avoids spontaneous photo-degradation is of fundamental interest. In this chapter, we have described the microscopic mechanism of photo-cycle present in BPA class of compounds and subsequent

*Work reported in this chapter has been submitted: Swastika Banerjee and Swapan K. Pati, Modelling BPA-based Molecular Architecture for Photochemical Energy Storage (2016)

transformations. From a fundamental point of view, photo-stability in these systems indicates a self-sustaining mechanism upon excitation energy transfer. In this work, we take the advantage of the photostability of BPA-like architecture which avoids the photo-decomposition during its photo-cycle. This can give rise to stable photo-switchable molecular material(s), which is highly demanding for various applications[10] ranging from memory devices[11], photochromic displays[12] to optical switches and chemo-mechanical devices[13]. Notably, energy storage in photochromic molecules has drawn huge attention which has been detailed in chapter 1 (see section 1.3.3).

9.1.1 Principles of Energy Storage in Photochromic Molecules

The basic requirements of an active molecule for photochemical energy storage are the following: (1) wide fundamental gap which prevents the thermal generation of free charge carriers;[14,15] (2) no permanent charges, since the charges may create complex influence of field on charge transfer;[1] and (3) no photo-decomposition processes. We note that, all these three criteria are well satisfied by BPA-derivatives which exhibit weakly polar molecular surfaces and extreme photo stability. Apart from these basic requirements, electronic structural details are very crucial to justify the ultimate applicability. Mostly, donor-bridge-acceptor (D-B-A) molecules impart efficient light to energy conversion process through reversible photo-switchability.[16] The bridge fundamentally acts as a rectifier that promotes electron transfer (ET) from donor to acceptor but resist ET in the reverse direction, stabilising the charge transfer state.[17,18] Moreover, avoiding the radiative emission process leads to photo-induced ET state which is a bound state and maintains a finite energy difference with the ground state. Such processes can effectively result in the photochemical energy storage.[10]

9.1.2 System of our Interest

Herein, we introduce two BPA-metabolites, namely, 4-methyl-2,4-bis (p-hydroxyphenyl) pent-2-ene (M-1) and 4-methyl-2, 4-bis (4-hydroxyphenyl) pent-1-ene (M-2) as photo-stable molecular materials. We note that, BPA-derivatives represent a broad class of molecular systems consisting of two terminal phenol groups, with an aliphatic counterpart as a linker (see Figure 9.1a). Accordingly, M-1/M-2 possesses a D-B-A-like molecular architecture. However, their weakly polar molecular surface is unlike the conventional D-B-A molecules. Hence, we rename them as X-

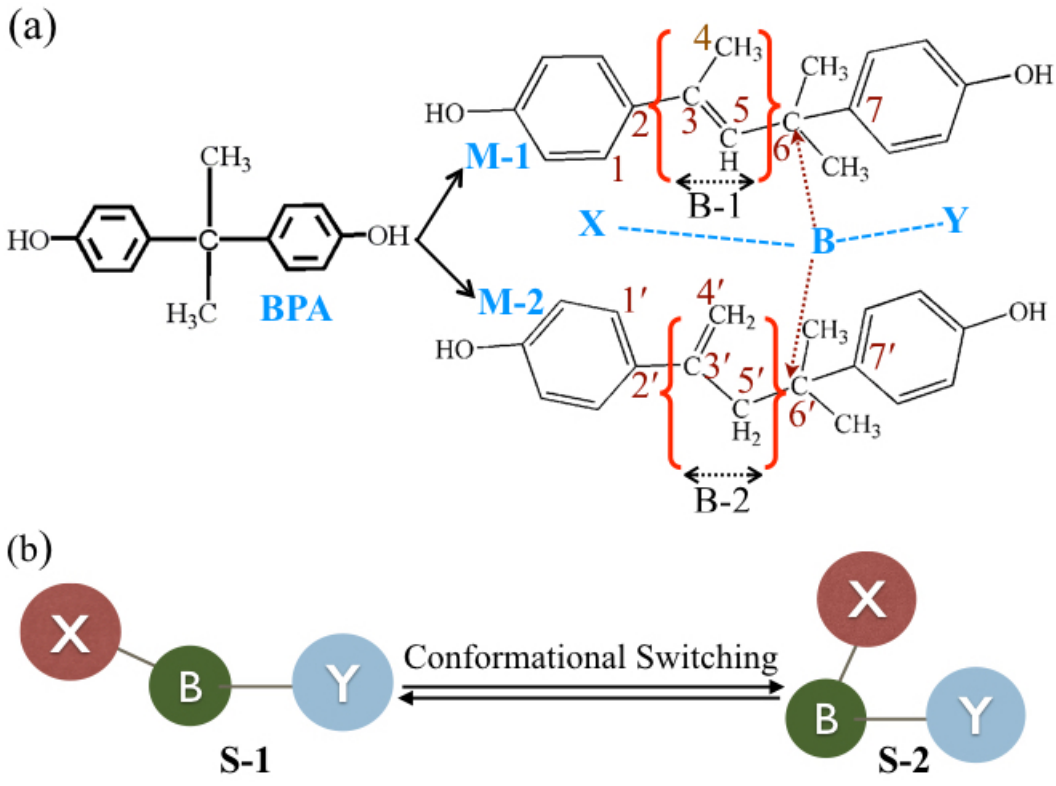

Figure 9.1: Molecular Structures of BPA and its metabolites (M-1 and M-2). X and Y are the terminal groups, tertiary C-atom in the linker group is denoted as B. Dihedral angles containing $1-2-3-5$ $(1'-2'-3'-4')$ and $3-5-6-7$ $(4'-3'-5'-6')$ for M-1(M-2) are assigned as DH-1 and DH-2, respectively.

B-Y molecular framework. The structural dissimilarity between M-1 and M-2 (two isomers) lie in their linker's configurations, denoted as B-1 and B-2, respectively

(see Figure 9.1a). In addition to the olefinic moiety (B-1/B-2), tertiary C-atom present in linker group results in the conformational flexibility. Here, we aim to introduce the possibility for photochemical energy storage in M-1 and M-2, which originates from photo-induced structural swapping. Through the first-principles Density Functional Theory and *ab-initio* Molecular Dynamics based study coupled with electron transfer theory, we have shown that photo-cycle consists of the photo-induced electron transfer and subsequent redistribution of electron density throughout the molecular framework. Consequently, two photo-switchable conformational states: S-1 and S-2 appear (see Figure 9.1b). These two states are bounds states which give rise to photostability and reversible storage capacity for light energy. We also highlight the role of through-space intramolecular interaction in electronic transition and vice-versa, which differentiates the S-1 and S-2 states in their charge-storage/transport mechanisms.

The remainder of this chapter is organised as follows: first, we introduce the computational details, which is followed by the results and discussion on the optical response of BPA, M-1, and M-2 molecules leading to photochemical energy storage. We have carried out a thorough analysis of their photophysical properties, effect of molecular assembly, solvent and temperature. Finally, we summarise our findings.

9.2 Computational details

Quantum chemical calculations have been performed using density functional theory (DFT) as implemented in the Gaussian 09[19]suite of programme. Geometry optimization of the monomers and dimers is done using the long-range dispersion corrected energy functional, ωb97xd. Triple zeta basis set (6-311+g (d,p)) has been used for all the atoms. True local minima has been confirmed by analysing the vibrational frequencies. Time-dependent density functional theory (TDDFT) calculations are based on the same exchange functional as used in DFT calcu-

lations. Appropriateness of this level of theory has been discussed in details in the previous chapters (chapter 7 and 8, see also reference[20]). Einstein coefficient $A_{21}(s^{-1})$ for spontaneous emission process has been determined using the expression,

$$A_{21} = \frac{8\pi^2\nu^2e^2g_1}{\varepsilon_0 m_e c^3 g_2} f_{12} \tag{9.1}$$

where, oscillator strength (f_{12}) and frequency (ν) dictate the rate of emission. This formulation has been adopted to find the relative emission rate at different absorption wavelength. Fundamental gap (E_{fund}) is defined as the difference of the ionization potential and electron affinity:

$$E_{fund} = IP - EA \tag{9.2}$$

where, $IP = E(N-1) - E(N)$; $EA = E(N+1) - E(N)$. It requires the comparison between the total energy of the N-electron ground state and that of the $N \pm 1$-electron state to determine EA and IP. On the other hand, optical gap (E_{op}) is defined as,

$$E_{op} = E_{S_1} - E_{S_0} \tag{9.3}$$

where, energy of the lowest energy electronic transition ($S_0 - S_1$) is accessible via absorption of a single photon (see Figure 9.3a). In general, E_{op} is less than E_{fund}, as the electron and hole remain electrostatically bound to one another in the excited state (contrary to the ionized state). The difference of the fundamental gap and the optical gap is a measure of the exciton binding energy (binding energy of electron-hole pair), E_{EB}.

$$E_{EB} = E_{fund} - E_{op} \tag{9.4}$$

Electronic excitation and associated geometrical perturbation is dictated by electron(hole)-phonon coupling constant (λ_{e-v}) which is defined as,

$$\lambda_{e-v} = N(E_F)\sum_i \frac{1}{4\pi^2 M_i \nu_i^2}\frac{dh_{kk}}{dQ_i} \tag{9.5}$$

For molecular systems, $N(E_F)$ is the density of states at the Fermi level (per molecule and per spin). The second term represents intramolecular vibronic coupling ($\lambda_{electron(hole)}$) which is the contribution from intramolecular reorganization energy (λ_{reorg}) in carrier-vibronic coupling, as discussed in Marcus theory.[21,22]; where ν_i and M_i are frequency and reduced mass of the vibrational mode, Q_i, respectively; $\frac{dh_{kk}}{dQ_i}$ is the diagonal vibronic matrix element for the electron (hole) state k. λ_{reorg} for electron ($\lambda_{electron}$) and hole (λ_{hole}) has been calculated using the Equations 9.6-9.7:

$$\lambda_{electron} = \left(E_-^* - E_-\right) + \left(E_{an}^* - E\right) \tag{9.6}$$

$$\lambda_{hole} = \left(E_+^* - E_+\right) + \left(E_{cat}^* - E\right) \tag{9.7}$$

where, E is the ground-state energy of the optimized geometry of neutral molecule, $E_-(E_+)$ is the energy of the optimized anionic (cationic) species, $E_-^*(E_+^*)$ is the energy of the anionic (cationic) molecule at neutral geometry, $E_{an}^*(E_{cat}^*)$ is the energy of the neutral molecule at anionic (cationic) geometry. Relaxation energy (λ_{rel}) can be expressed in terms of the vibrational structure present in an ionized band and can be analysed to provide the values of the $Huang-Rhys$ factors (S_i), which in the framework of the harmonic oscillator model are related to λ_{rel} by:

$$\lambda_{rel} = \sum_i S_i h\nu_i \tag{9.8}$$

$$\lambda_{rel} = \sum_i 2\pi^2 M_i \nu_i^2 (\Delta Q_i)^2 \tag{9.9}$$

So, S_i at a particular ν_i can present a frequency-resolved picture of electron (hole)-vibronic coupling. To calculate the $S_{absorption(emission)}$ for hole, we consider the vibrational frequencies of neutral (cationic) species, the same for electron is calculated after considering the vibrational frequencies of anionic (neutral) species.

Absolute value of the transfer integral (t) for electron (hole) transfer from one unit to another is approximated as (without considering any overlap),

$$t = \frac{\varepsilon_{L+1(H)} - \varepsilon_{L(H-1)}}{2} \tag{9.10}$$

Major simplification applied is the Koopmans′ theorem (KT),[23] that is to rely on the one-electron approximation. We have verified that KT estimates are in good agreement with the results derived from electron-correlated CAS-SI (CASSCF-State Interaction) calculations. We note that the ωb97xd functional obeys the property: HOMO energy corresponds exactly to (minus) the vertical ionization potential; the electron affinity is then obtained as (minus) the HOMO energy of the N+1-electron system. We perform *ab initio* molecular dynamics (AIMD) simulations using the gaussian plane wave (GPW) method and Perdew-Burke-Ernzerhof (PBE) functional as implemented in the Quickstep module of the CP2K set of program.[24] GTH (Goedecker-Teter-Hutter) pseudopotentials[25] has been used, and valence electrons are handled using triple-ζ valence (TZV) basis set. To account for noncovalent interactions, van der Waals (vdW) corrections (DFT-D3) have been employed.[26,27]

9.3 Results and Discussion

9.3.1 Optical Response and Photo-switchable Conformational States of EDCs (BPA, M-1, and M-2)

UV-sensitivity of BPA compounds are well known. We find that optical-excitation of the ground state conformer, 'S-1' (see Figure 9.2a) at ∼250 nm leads to a stable bound state denoted as 'S-2' conformer (see Figure 9.2d), shows sharp structural distinction. In fact, UV-sensitivity (λ_{max} = 225-250 nm; see Figure 9.2b) and

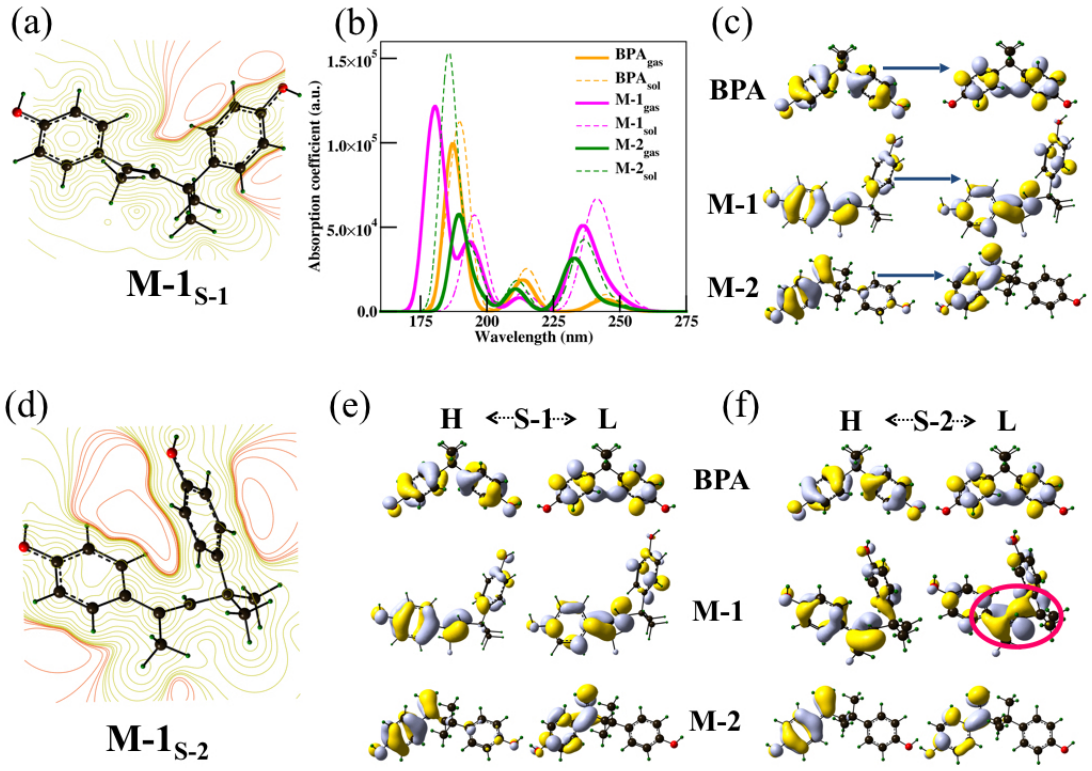

Figure 9.2: Laplacian of the contour of the electron density plots (isovalue = 0.02 e $\mathring{A}^{-3}$) are shown for (a) S-1 and (d) S-2 conformations, respectively. (b) Computed absorption spectra of BPA, M-1, and M-2 in gas-phase (represented by solid lines) and at solvated state (dotted lines) for their ground state conformation (S-1). (c) Dominant natural transition orbital (NTO) pairs for the first excited singlet states of BPA, M-1 and M-2. Frontier molecular orbitals for (e) S-1 and (f) S-2 conformations (H: HOMO and L: LUMO) are shown. Isovalue considered for all the plots are 0.03 $e\mathring{A}^{-3}$

.

optical transitions involve typically $\pi - \pi^*$ states, as evidenced by the natural transition orbitals analysis (see Figure 9.2c). We also note that polarity of the medium does not affect the absorption maxima to a great extent (Figure 9.2b), suggesting that the states involved in optical excitation remain mostly at molecular level and do not get perturbed by solvation. We find that the rate of emission is 10-15 times lesser for lower-energy transition (λ_{max} = 250 nm) compared to the transitions at λ_{max} = 225-240 nm, as obtained from the value of the Einstein coefficient for spontaneous emission (see Equation 9.1). Thus, low-energy excited state conformer (S-2) is quite stable. The conformational switching during S-1 $\rightarrow$ S-2 optical transition is driven by the alteration in dihedral angles (DH-1 and DH-2, see their definition in Figure 9.1a), as shown in Table 9.1. DH-1 determines

Table 9.1: Dihedral angles (in degree) for M-1 and M-2 at ground state conformer (S-1) and photo-excited conformation state (S-2) are given. DH-1 (DH-2) at S-1(S-2) conformer is denoted as DH-1(DH-2)$_{S-1(S-2)}$.

EDC	DH-1$_{S-1}$ (DH-1$_{S-2}$)	DH-2$_{S-1}$ (DH-2$_{S-2}$)
M-1	42° (11°)	113° (80.85°)
M-2	135°(171°)	-175° (176°)

the extended planarity of π-electronic cloud at X-component, whereas, DH-2 measures the relative alignment of two terminal groups (X and Y) with each other (see Figure 9.1). For S-1 $\rightarrow$ S-2 transformation in M-1, DH-1 reduces to zero (planarity increases) and DH-2 decreases by 32°, which results in a "half open book" like conformation (see Figure 9.2a and 9.2d). On the other hand, for S-1 $\rightarrow$ S-2 transformation in M-2, DH-1 turns out to be close to 180°, resulting in extended π-delocalisation at X-component, while DH-2 remains almost invariant. BPA exhibits the least conformational changes upon optical excitation, in comparison with M-1 and M-2. Thus, overall geometrical change after S-1 $\rightarrow$ S-2 transformation is the maximum for M-1. Reason is that the B-1 linkage in M-1 leads to electronic decoupling between two terminal π-clouds in the ground electronic state (S-1, see

Figure 9.2a, c), while, the same linkage undergoes enhanced electronic coupling in the optically excited state (S-2, see Figure 9.2d, f). Surface contour plots show the evidence for bonding overlap between two terminal groups at S-2 state (M-1_{S-2}; Figure 9.2d) which is absent in case of S-1 (M-1_{S-1}; Figure 9.2a). Thus, modulation of dihedrals can result in a significantly different chemical bonding for S-1 and S-2 conformers. Hence, B-1 acts as an asymmetric thread or wire. As a result, the excitation energy transfer (EET) in M-1 leads to two photo-switchable conformers (S-1 and S-2) with distinct spatial structure, electronic structure and chemical bonding.

9.3.2 Photophysical Properties

We have estimated two kinds of transport gaps, namely, the optical gap (E_{op}) and fundamental gap (E_{fund}), involved in the excitation spectrum (see Equation 9.2 and 9.3 in computational details and Table 9.2). E_{op} at S-1 state is comparable for M-1 and M-2 (4.91 eV). However, vertical photo-excitation from S-1 leads to a photo-excited state which upon relaxation results in S-2 conformer exhibiting a huge photochromic shift (2 eV) especially for M-1. This is because of the extended electronic coupling between two terminal π-clouds.

Table 9.2: Optical gap, E_{op}(eV); absorption maxima, λ_{max} (nm); transition dipole moment (f); fundamental gap, E_{fund} (eV); exciton binding energy, E_{EB} (eV); Reorganisation energy (eV) for electron ($\lambda_{electron}$) and hole (λ_{hole}) are given for two different states of M-1 and M-2.

State	E_{op} (λ_{max})	E_{fund}	E_{EB}	λ_{hole}	$\lambda_{electron}$
M-1_{S-1}	4.91 (252)	6.81	1.90	0.93	1.16
M-1_{S-2}	2.95 (419)	6.81	3.86	-	-
M-2_{S-1}	4.96 (250)	7.31	2.35	0.72	0.93
M-2_{S-2}	4.00 (311)	7.31	3.31	-	-

Nevertheless, significant E_{fund} and moderate E_{op} results in high exciton binding energy (E_{EB}; see Equation 9.4), as shown in Table 9.2. In this regard, knowledge of the carrier-vibration coupling (λ_{e-v}; see Equation 9.5 in computational details) is

necessary to understand the microscopic picture behind conformational switching associated with electronic excitation. At the molecular level, λ_{e-v} is determined from the intramolecular reorganization energy (λ_{reorg}) as prescribed in Marcus theory,[21] where λ_{reorg} provides a direct link between the geometrical feature and electronic coupling (see Equation 9.6 and 9.7). We find that both the M-1 and M-2 exhibit high electron (hole) reorganisation energy ($\lambda_{electron(hole)}$) at S-1 state (see Table 9.2). Moreover, the uncorrelated e-h pair *i.e.* weakly bound e-h pair (loose exciton) is stabilised in case of M-1(see Table 9.2). These excitons cannot recombine because the ground state (S-1) and photoexcited state (S-2) adopt different conformational space. This can impart the ability to store the photo-chemical energy through photo-induced variation in conformation (S-1 versus S-2). Hence, relative stability of S-1 and S-2 states is imperative to quantify the photo-chemical energy storage.

9.3.3 Photochemical Energy Storage: Quantitative Estimation

We estimate the difference in enthalpy and free energy between S-1 and S-2 states ($\Delta H_{storage}$ and $\Delta G_{storage}$; see Figure 9.3a) to quantify the energy-storage during the photo-excitation (see Table 2). Such quantities are analogous to the "packing heat" for crystalline organic solids.[28] We note that, storage capacity is maximum in case of M-1 ($\Delta G_{storage}$ ($\Delta H_{storage}$) = 0.97 (0.88) eV/mol), which is almost twice that of M-2 and nearly ten times that of BPA. Effect of conformational switching is reflected in normal mode displacement (ΔQ), as shown in the schematic presentation in Figure 9.3a. As mentioned earlier, M-1-like molecular structure is associated with huge geometrical distortion (ΔQ) after photo-excitation. We find that M-1 exhibits opposite polarities ($X^{\delta+} - B - Y^{\delta-}$) on the two terminal groups separated via bridge atoms (see Table 9.3). This is in contrast to

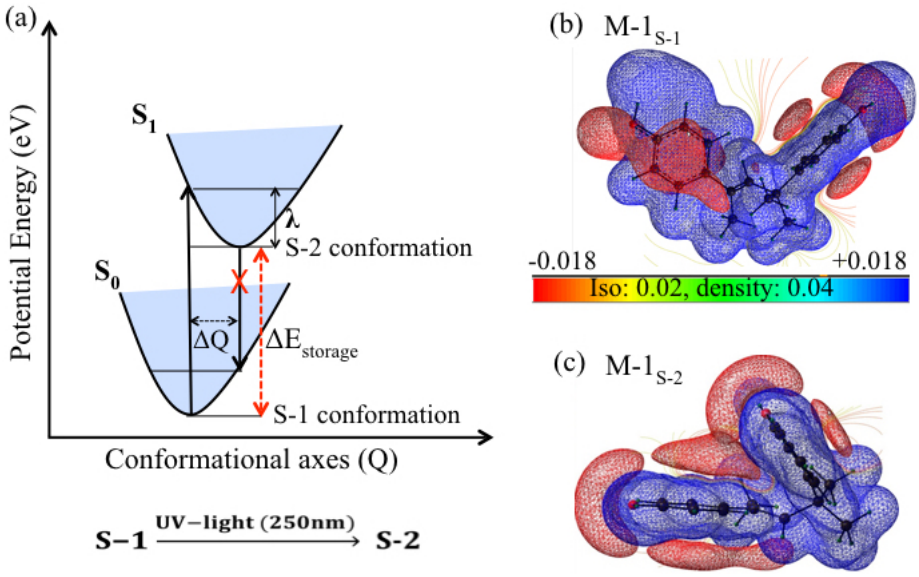

Figure 9.3: (a) Sketch of potential energy surfaces related to optical excitation, showing the vertical transitions, the normal mode displacement (ΔQ) and the reorganisation energy (λ). Conformers are labelled as S-1 and S-2, the electronic states are represented by conventional way of representation (S_0 and S_1) Net energy storage for S-1 to S-2 switching is shown as $\Delta E_{storage}$. Electron densities are presented through the molecular electrostatic potential (ESP) surface for M-1 at S-1 (b) and S-2 conformations (c). Red and blue colour represents the electron rich and poor centre, respectively. At the S-1 conformation (density isovalue = 0.04), negative ESP regions decrease, and the electron traps are partly filled. For S-2 conformation the molecular surface has a continuous ESP (density isoval = 0.01) along the conjugated backbone.

the features found in the case of BPA and M-2. However, in case of M-1, partial charges on two terminal groups are less (± 0.10-0.20) and delocalised over the molecular framework. This implies that considerable photo-energy storage

Table 9.3: Estimate of $\Delta H_{storage}$, and $\Delta G_{storage}$ in eV/mol) by BPA, M-1 and M-2. Partial charges on X and Y fragments (as denoted in Figure 9.1), at S-1 (Q_{S-1}) and S-2 (Q_{S-2}) conformers.

System	$\Delta H_{storage}$ ($\Delta G_{storage}$)	$\mathbf{Q}_{S-1}$	$\mathbf{Q}_{S-2}$
BPA	-0.10 (-0.16)	X:(+0.10); Y:(+0.10)	X:(+0.09);Y:(+0.09)
M-1	-0.88 (-0.97)	X:(+0.16); Y:(-0.09)	X:(+0.21); Y:(-0.09)
M-2	-0.49 (-0.62)	X:(-0.17); Y:(-0.11)	X:(-0.09); Y:(-0.11)

through S-1→S-2 conversion (in M-1) is not solely driven by electrostatic interaction. ln fact, the molecular orbitals in S-2 reveals that "half open book" like conformation allows significant orbital overlap between two terminal groups (see

Figure 9.2f, marked with red circle), which leads to stabilisation of the excited state and results in huge red-shift in optical transition. Secondly, the M-1_{S-1} has the electron-trapping nature, while M-1_{S-2} facilitates the migration of charge carrier (electron) through the conjugated channel, as evidenced from the molecular electrostatic potential map (see Figure 9.3b,c). Accordingly, S-2 conformer accommodates charges to attain long-range electron or hole hopping.[29] Thus, B-1 bridge acts as a conductor or resistor depending on whether it is excited or in the ground state, respectively. In fact, B-1 bridge facilitates forward excited-state ET, but effectively prevents recombination in the reverse process which is associated with through-space mechanisms.[30] Such behaviour is reminiscent with the previous experimental observation too.[31,32] From preceding discussion, charge-carrier storage/transport property of M-1 shows sharp contrast while transforming from ground state (S-1) to "half open book" like conformer (S-2).

9.3.4 Effect of Solvent and Intermolecular Interaction

To understand the dynamical behaviour of the molecular assembly in presence of water solvent, we have carried out *ab initio* molecular dynamics simulation up to 10 ps. The time scale is reasonable, since the charge carriers realize a dynamically disordered potential landscape at sub-100 fs timescale.[33] We find that H_2O molecules help to separate out the molecular assembly after stabilisation of water cluster within the intermolecular space (see Figure 9.4). Thus, intermolecular interaction weakens in presence of H_2O solvent, which can play a crucial role to impart the molecular nature of the water solvated M-1 system.

However, in the absence of solvent, intermolecular interaction determines the nature of molecular aggregation. We note that non-planarity of the M-1 molecular-surface does not allow extended π-stacking. Therefore, the molecular assembly is only possible if the M-1 units can interact in end-on fashion (D-3), as shown in

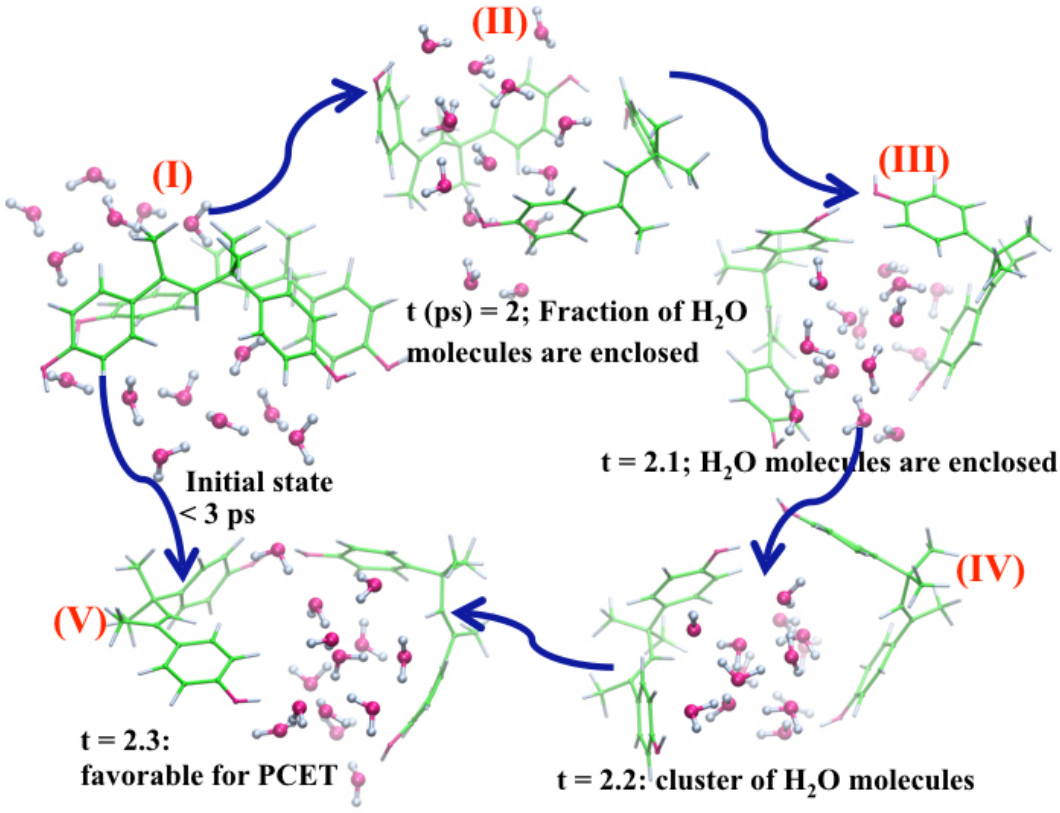

Figure 9.4: Snapshots at different times for M-1 dimer in the presence of explicit water solvent are shown. Conformational dynamics leads to isolation of dimers into monomers (step-III-V).

Figure 9.5a. However, the D-3 configuration is thermodynamically less favourable (binding energy (E_b) being slightly positive; +0.04 eV/mol). On the other hand, M-1 dimers with D-1 and D-2 configurations are thermodynamically stable (E_b: -0.20 and -0.15 eV/mol, respectively). For D-1 dimer, the interaction between two monomeric units are based on aromatic $(C-H/O-H)-\pi$ type, whereas, for D-2, there is the maximisation of $\pi-\pi$ interactions with two nearly parallel aromatic rings. In brief, intermolecular interaction avoids any extended self-assembly (D-3); instead, it leads to the formation of D-1/D-2 dimers.

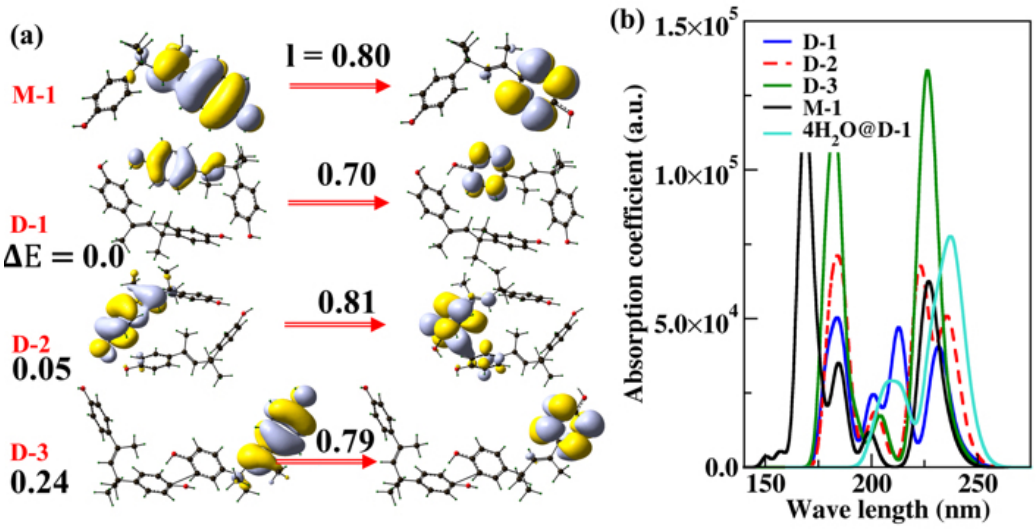

Figure 9.5: (a) Different dimer forms of M-1 (D-1, D-2, and D-3) and their relative stability (ΔE) with respect to the most stable form (D-1), along with the dominant natural transition orbital (NTO) pairs for the first excited singlet states. Initial state is on the left; the final state is on the right, associated eigenvalues (l) of NTOs are also given. (b) Computed absorption spectra of M-1, D-1, D-2 and D-3 in gas-phase and in explicit water medium are shown.

9.3.5 Fate of Charge-carriers in Photo-switchable conformers

M-1 dimers also exhibit similar UV-light sensitivity like monomeric M-1 molecule (see Figure 9.5b). D-1 and D-3 configurations favour intramolecular $\pi \rightarrow \pi^*$ transitions (see NTOs in Figure 9.5). However, D-2 dimer has transition orbitals from both the monomeric units, due to the proximity of aromatic π-electronic clouds from two terminal units. Nevertheless, characteristic features of the NTOs are dependent on the relative orientation of the monomeric units. This can control the intermolecular charge transfer integral at different dimer configurations. We employ the "energy splitting in dimer" (ESD) method[34–38] to find the quantitative estimation of the charge transfer integral (t; see Equation 9.10). Although, thermodynamic stability of D-1 and D-2 are comparable, the ratio of $t_{electron}$ to t_{hole} alters drastically for two configurations (see Table 9.4). For D-1, $t_{electron} <<$

Table 9.4: Transfer integrals for different configurations of M-1 dimer (in meV).

Transfer integral	Dimer configurations		
	D-1	D-2	D-3
$t_{electron}$	8	70	97
t_{hole}	182	102	6

t_{hole}, whereas, for D-2, $t_{electron}$ and t_{hole} are almost equal in magnitude. In contrast, dimerization in end-to-end fashion (D-3) which has been discussed previously as the thermodynamically less feasible configuration, imparts a surprisingly different behaviour when $t_{electron} >> t_{hole}$. Hence, depending on the mode of intermolecular interaction, transfer integral for electron and hole get modulated. Notably, the magnitude of $t_{electron}/t_{hole}$ (0.008-0.18 eV, see Table 9.4) is smaller than the electron/hole reorganisation energy ($\lambda_{electron/hole}$ = 0.93-1.16 eV, see Table 9.2) at S-1 conformer. Thus, charge localization is favourable in S-1 conformer due to the formation of small polaron. Hence, the charge carriers remain localised on particular conformational space until a favourable molecular configuration for charge transfer occurs dynamically. There is spectroscopic evidence supporting such localization of the charge carrier within one or a few molecules[39] as found in M-1. In practice, the most studied crystalline semiconductors based on large conjugated molecules, like, pentacene exhibits modest nuclear reorganization energy (∼0.1 eV)[40] which is similar or smaller than the average intermolecular charge-transfer integral ($\leq$ 0.12 eV)[41], leading to the charge delocalization. Behaviour of S-1 conformer of M-1 molecule is in contrast to these systems. Thus, the main point is that M-1 shows two different charge-transport (transfer) behaviour at two photo-switchable states, where charge confinement prevails at ground state (S-1 conformer); and charge-delocalisation happens at photo-excited state (S-2 conformer).

9.3.6 Effect of Temperature

Besides reorganisation energy, finding the $Huang-Rhys$ factor, S_i, (see Eq. 9.8-9.9 in computational details) can present a frequency-resolved picture of electron (hole)-vibronic coupling (see Figure 9.6). Description of specific vibrational modes contributing to the carrier-vibronic coupling (S_i), is shown in Figure 9.6.

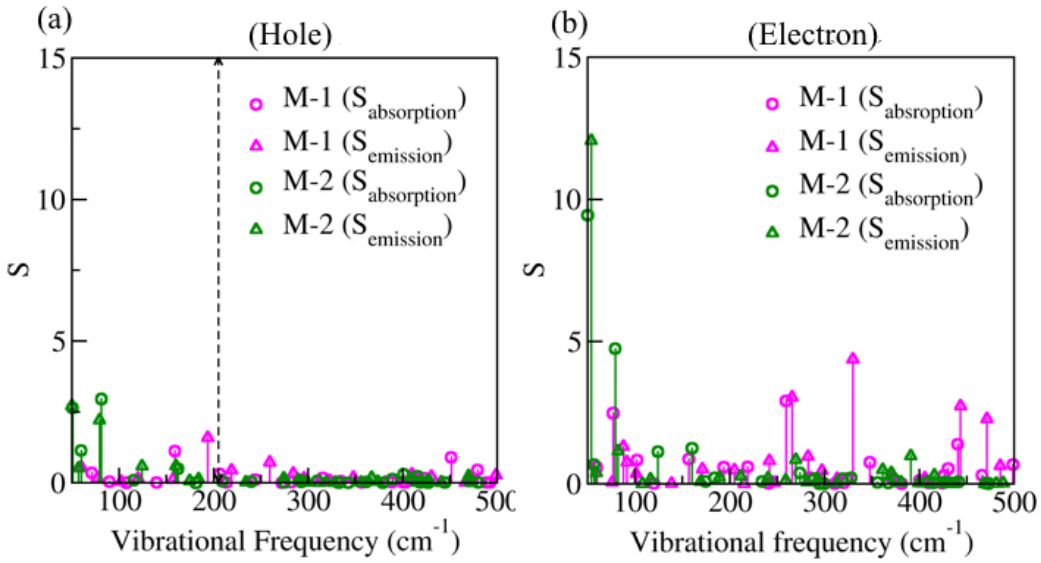

Figure 9.6: $Huang-Rhys$ factors (S) related to the first ionisation band of M-1 and M-2 as a function of the frequency of the vibrational modes for hole (a) and electron (b).

The important outcome of this analysis are: (1) at low T, there are some modes coupled to electron and hole mobility (Figure 9.6a). These are the floppy modes of vibration ($\nu < 200$ cm^{-1}), comprising of the whole molecular framework. At higher temperature ($200 < \nu < 500$ cm^{-1}), a considerable number of vibrational modes couple to electron mobility which is more than that of hole. We also find that high frequency modes, such as, aromatic C=C (1000-1500 cm^{-1}) and C-H bond stretching vibrations (> 3000 cm^{-1}) participate in carrier vibronic coupling. (2) As the electron vibronic coupling strength (S-factor) is always higher than that of hole vibronic coupling, hole mobility is higher than the electron. This trend is in line with what is commonly observed in organic semiconductors. (3) While

comparing M-1 with respect M-2, carrier-vibration coupling (S-factor) is much lesser for M-2 molecular framework. In fact, the electronic rearrangement affects the M-1 framework more than the M-2 structure which results in a very different conformational state (S-2) upon optical excitation of M-1. So, the photo-excited state of M-1(S-2) is very different from the ground state conformer of M-1 (S-1), which is not that prominent in case of BPA and M-2.

Thus, a frequency-resolved picture of electron (hole) vibronic coupling allows us to examine how excited electrons lose energy to specific modes of vibration and how the temperature affects the electron/hole mobility. Most importantly, high-frequency vibrational modes ($> 200\ cm^{-1}$) mainly dictate the electron phonon coupling of M-1. This indicates that electrons interact strongly with intramolecular modes which can result in high-field effects. Distribution of carrier vibronic coupling elements over a wide range of frequency domain proves that carrier transport can be tuned through a wide range of temperature. Difference in the distribution of electron and hole vibronic coupling elements indicates difference in the temperature dependence of hole and electron mobilities.

9.4 Conclusions

In summary, first principles study demonstrates the photo-excited state of Bisphenol derivatives as stable bound states, which prevents the light-assisted radicalisation or photo-decomposition of EDCs (BPA, M-1, and M-2). We emphasise that an appropriate bridge between two terminal phenol groups rectify electronic coupling/decoupling between two ends. B-1 bridge in M-1 exemplifies such an excellent asymmetric wire which allows the swapping between two conformers: S-1 (ground state) and S-2 (photo-transformed state). S-1→S-2 switching results in substantial photochemical energy storage ($\Delta H_{storage}$ ($\Delta G_{storage}$) = 0.88 (0.97) eV/mol). These features originate from the proximity-induced through-space in-

teraction in the S-2 conformer via alteration of the dihedrals. We also note that, for the S-1 conformer, intermolecular charge transfer integral ($t_{hole/electron}$) is much lesser compared to reorganisation energy ($\lambda_{hole/electron}$), which results in charge localisation. In contrast, S-2 conformer exhibits extended charge delocalisation due to strong electronic coupling between two terminal aromatic rings. Thus, S-1 and S-2 conformers follow dissimilar charge-storage/transport mechanism and are detectable through optical responses. Accordingly, we conjecture that optical response of BPA-compounds is not only of environmental interest but also of designing a technologically relevant molecular material. The results presented here opens up a new frontier in designing an efficient optoelectronic material with M-1 like configuration. Still, there is room for finding a suitable template exhibiting optimum chemical interaction with EDCs to achieve large-capacity and long lifetime for solar energy storage.

References

[1] A. V. Krishnan, P. Stathis, S. F. Permuth, L. Tokes, and D. Feldman, Endocrinology **132**, 2279 (1993).

[2] N. Olea, R. Pulgar, P. Pérez, F. Olea-Serrano, A. Rivas, A. Novillo-Fertrell, V. Pedraza, A. M. Soto, and C. Sonnenschein, Environmental Health Perspectives **104**, 298 (1996).

[3] A. R. Spurr, Journal of Ultrastructure Research **26**, 31 (1969).

[4] A. M. Calafat, Z. Kuklenyik, J. A. Reidy, S. P. Caudill, J. Ekong, and L. L. Needham, Environmental Health Perspectives pp. 391–395 (2005).

[5] A. Atkinson and D. Roy, Environmental and Molecular Mutagenesis **26**, 60 (1995).

[6] D. Roy, M. Palangat, C.-W. Chen, R. D. Thomas, J. Colerangle, A. Atkinson, and Z.-J. Yan, Journal of Toxicology and Environmental Health Part A **50**, 1 (1997).

[7] N. Ben-Jonathan and R. Steinmetz, Trends in Endocrinology & Metabolism **9**, 124 (1998).

[8] J. K. Pandey, K. R. Reddy, A. P. Kumar, and R. Singh, Polymer Degradation and Stability **88**, 234 (2005).

[9] J.-H. Kang, F. Kondo, and Y. Katayama, Toxicology **226**, 79 (2006).

[10] M.-M. Russew and S. Hecht, Advanced Materials **22**, 3348 (2010).

[11] M. Irie, Chemical Reviews **100**, 1683 (2000).

[12] C. Bechinger, S. Ferrer, A. Zaban, J. Sprague, B. A. Gregg, et al., Nature **383**, 608 (1996).

[13] A. Grinthal and J. Aizenberg, Chemical Society Reviews **42**, 7072 (2013).

[14] K. Vandewal, A. Gadisa, W. D. Oosterbaan, S. Bertho, F. Banishoeib, I. Van Severen, L. Lutsen, T. J. Cleij, D. Vanderzande, and J. V. Manca, Advanced Functional Materials **18**, 2064 (2008).

[15] M. Lenes, M. Morana, C. J. Brabec, and P. W. Blom, Advanced Functional Materials **19**, 1106 (2009).

[16] D. Gust, T. A. Moore, and A. L. Moore, Accounts of Chemical Research **34**, 40 (2001).

[17] R. M. Metzger, Chemical Reviews **103**, 3803 (2003).

[18] J. R. Heath and M. A. Ratner (2003).

[19] M. Frisch, G. Trucks, H. B. Schlegel, G. Scuseria, M. Robb, J. Cheeseman, G. Scalmani, V. Barone, B. Mennucci, G. Petersson, et al., Inc., Wallingford, CT **200** (2009).

[20] S. Banerjee and S. K. Pati, ACS applied Materials & interfaces **7**, 23893 (2015).

[21] R. A. Marcus, Angewandte Chemie International Edition in English **32**, 1111 (1993).

[22] R. A. Marcus, Reviews of Modern Physics **65**, 599 (1993).

[23] T. Koopmans, Physica **1**, 104 (1934).

[24] J. Hutter, M. Iannuzzi, F. Schiffmann, and J. VandeVondele, Wiley Interdisciplinary Reviews: Computational Molecular Science **4**, 15 (2014).

[25] S. Goedecker, M. Teter, and J. Hutter, Physical Review B **54**, 1703 (1996).

[26] S. Grimme, S. Ehrlich, and L. Goerigk, Journal of Computational Chemistry **32**, 1456 (2011).

[27] L. Goerigk and S. Grimme, Physical Chemistry Chemical Physics **13**, 6670 (2011).

[28] N. R. Neale, Nature Chemistry **6**, 385 (2014).

[29] R. Glaeser and R. S. Berry, The Journal of Chemical Physics **44**, 3797 (1966).

[30] A. Stockmann, J. Kurzawa, N. Fritz, N. Acar, S. Schneider, J. Daub, R. Engl, and T. Clark, The Journal of Physical Chemistry A **106**, 7958 (2002).

[31] K. M. Gaab, A. L. Thompson, J. Xu, T. J. Martínez, and C. J. Bardeen, Journal of the American Chemical Society **125**, 9288 (2003).

[32] A. L. Thompson, K. M. Gaab, J. Xu, C. J. Bardeen, and T. J. Martínez, The Journal of Physical Chemistry A **108**, 671 (2004).

[33] V. Coropceanu, R. S. Snchez-Carrera, P. Paramonov, G. M. Day, and J.-L. Brdas, The Journal of Physical Chemistry C **113**, 4679 (2009).

[34] J. Hutter, M. Iannuzzi, F. Schiffmann, and J. VandeVondele, Wiley Interdisciplinary Reviews: Computational Molecular Science **4**, 15 (2014).

[35] V. Lemaur, D. A. da Silva Filho, V. Coropceanu, M. Lehmann, Y. Geerts, J. Piris, M. G. Debije, A. M. van de Craats, K. Senthilkumar, L. D. A. Siebbeles, et al., Journal of the American Chemical Society **126**, 3271 (2004).

[36] O. Kwon, V. Coropceanu, N. Gruhn, J. Durivage, J. Laquindanum, H. Katz, J. Cornil, and J.-L. Brédas, The Journal of Chemical Physics **120**, 8186 (2004).

[37] G. R. Hutchison, M. A. Ratner, and T. J. Marks, Journal of the American Chemical Society **127**, 16866 (2005).

[38] K. D. Jordan and M. N. Paddon-Row, The Journal of Physical Chemistry **96**, 1188 (1992).

[39] P. J. Brown, H. Sirringhaus, M. Harrison, M. Shkunov, and R. H. Friend, Physical Review B **63**, 125204 (2001).

[40] S. T. Bromley, M. Mas-Torrent, P. Hadley, and C. Rovira, Journal of the American Chemical Society **126**, 6544 (2004).

[41] A. Troisi and G. Orlandi, The Journal of Physical Chemistry B **109**, 1849 (2005).

10

Summary & Outlook

The central theme of this dissertation has been to elucidate the role of surface chemistry in the modification of electrochemical and charge transport properties of two dimensional as well as bulk materials. We have employed a combination of first-principles density functional theoretical calculations, modelling and Boltzmann transport theory in our analysis. Three major topics of research is detailed in the thesis, namely, anodic behaviour of layered materials, finding carrier mobility in two dimensional semiconductors and steric control, removal and application of BPA-based molecular systems.

The anodic behaviour of boron sheets (BSs), borocarbonitrides (B_xN_z) and black phosphorus has been elucidated for Li, Na and Mg-ion rechargeable battery in chapter 2, 3 and 4 respectively. The α_1 and α_1-AA polymorphs of BS have been found to show optimum anodic behaviour, based on their electronic structure and Li adsorption/desorption properties. Li-saturation confers the theoretical estimate of the capacity as 383 $mAhg^{-1}$, which is higher than that of the conventional graphitic electrode. We also studied the effect of variation in the shape of B_xN_z-domain and B-N charge-imbalance in $B_xC_yN_z$ layers towards their potential as anode material for Na-ion battery. Two-dimensional $B_xC_yN_z$ with

nitrogen-excess trigonal B_xN_z-domain (T_N) meets the requirements for a superior anode for Sodium ion Battery (SIB). Monolayer T_N-sheet can store Na(Li) which results in specific capacity as high as 810(668) $mAhg^{-1}$. The average open circuit voltage is found to be 1.25 V vs. Na/Na^+ for a wide range of chemical stoichiometries of Na_xT_N. The enhanced electronic transport and fast diffusion kinetics of the Na-ions is particularly found in the T_N-anode, which in turn results in high power efficiency in SIB, even better than that of graphite electrode in conventional LIB. Charge-storage upon layer-wise accumulation of Na-ions on the T_N-surface is also appealing for application in sodium-ion capacitors, as an alternative to lithium-ion capacitors. We also have demonstrated Black phosphorous as anode in Magnesium-ion Battery. The results suggest that black phosphorus could be used as an anode material in three phases with varying capacity in each phase with optimum anodic voltage. This material is found to be perfect Mg-ion anode with reduced Mg-diffusion barrier as well.

In next two chapters (in chapter 5 and 6), we have developed Boltzmann Transport mechanism in deformation potential limit and have studied charge transport properties of borocarbonitrides ($B_{2.5}CN_{2.5}$, BCN, BC_4N) and phosphorene. Due to topological defect, while $B_{2.5}CN_{2.5}$-I exhibit higher electron mobility, $B_{2.5}CN_{2.5}$-II show higher hole mobility. In chapter 6, we find that tri-layer black phosphorus offers itself as appropriate anisotropic carrier transport material which possesses both the directional as well as electron-hole anisotropy.

In chapter 7, 8 and 9, we focus on bisphenol A (BPA) based molecular systems and the effect of molecular surface chemistry on their reactivity. In chapter 7, we explore the effects of solvent polarity and the nature of radical intermediates on reaction pathways of metabolic activation. Computational study is then used to examine the interaction of BPA based molecular systems with the surfaces of ma-

terials for its removal from the environment in chapter 8. The results suggest that MoS_2 could be effective for the same in a reversible manner, while graphene acts as a strong absorber. Chapter 9 describes work on the photochemical properties of BPA derivatives. It has been shown that B-1 bridge in M-1-structure acts as an asymmetric wire and leads to photo-induced switching between two conformers (S-1 and S-2). These two conformers follow dissimilar charge-storage/transport mechanism with detectable optical responses.

In brief, we have established the role of surface structure in periodic as well as molecular systems to determine the chemical reactivity, electrochemical and charge-transport properties, in this thesis. Most importantly, such studies provide access to atomistic details which is not readily accessible to experimentalists. Recently, the experimental advancement has given rise to a library of new elemental, binary and ternary layered systems with precise control over their surface-structure. Our developed methodology would be able to predict microscopic details for their applications in advanced devices.